Quantitative Dopamine Imaging in Humans using Magnetic Resonance and Positron Emission Tomography

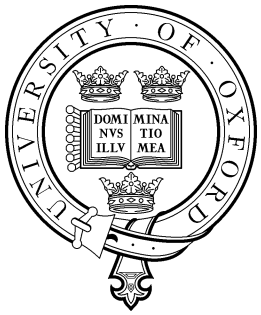

Andri Tziortzi

Wolfson College

University of Oxford

A thesis submitted for the degree of

Doctor of Philosophy

Trinity 2013

Quantitative Dopamine Imaging in Humans using Magnetic Resonance and Positron Emission Tomography

Andri Tziortzi

Wolfson College, University of Oxford

A thesis submitted for the degree of Doctor of Philosophy

Trinity term 2013

Abstract

Dopamine is an important neurotransmitter that is involved in several human functions such as reward, cognition, emotions and movement. Abnormalities of the neurotransmitter itself, or the dopamine receptors through which it exerts its actions, contribute to a wide range of psychiatric and neurological disorders such as Parkinson's disease and schizophrenia. Thus far, despite the great interest and extensive research, the exact role of dopamine and the causalities of dopamine-related disorders are not fully understood.

Here we have developed multimodal imaging methods, to investigate the release of dopamine and the distribution of the dopamine D2-like receptor family *in-vivo* in healthy humans. We use the [^{11}C]PHNO PET ligand, which enables exploration of dopamine-related parameters in striatal regions, and for the first time in extrastriatal regions, that are known to be associated with distinctive functions and disorders. Our methods involve robust approaches for the manual and automated delineation of these brain regions, in terms of structural and functional organisation, using information from structural and diffusion MRI images. These data have been combined with [^{11}C]PHNO PET data for quantitative dopamine imaging.

Our investigation has revealed the distribution and the relative density of the D3R and D2R sites of the dopamine D2-like receptor family, in healthy humans. In addition, we have demonstrated that the release of dopamine has a functional rather than a structural specificity and that the relative densities of the D3R and D2R sites do not drive this specificity. We have also shown that the dopamine D3R receptor is primarily distributed in regions that have a central role in reward and addiction. A finding that supports theories that assigns a primarily limbic role to the D3R.

D.Phil. Supervisors

Professor Roger N. Gunn

Dr. Mark Jenkinson

D.Phil. Examiners

Professor Alexander Hammers

Professor Heidi Johansen-Berg

Acknowledgements

First and foremost I would like to thank my supervisors Professor Roger Gunn and Dr. Mark Jenkinson. Thank you both for your guidance throughout the project and for being a constant source of support and reassurance. I am grateful for our excellent collaboration and the unprecedented agreement between us on every single aspect of this thesis, which have definitely made my degree a joy. Roger, I will always be grateful and eternally indebted to you for the continuous support and the countless opportunities you have offered me, which have enriched my research and career. I owe you a lot. Mark, thank you so much for giving me the opportunity to work within a first class and cutting-edge scientific environment, for your excellent advise throughout my DPhil and for your encouragement during the moments of self-doubt.

I am greatly thankful to Dr. Graham Searle and Dr. Ilan Rabiner, from whom I have learnt a great deal about PET imaging. Especially you, Graham, for being the ``definition'' of a great colleague. Special thanks to Dr. Paul Shotbolt and Dr. David Erritzoe who readily shared data and adjusted their study protocols in order for me to acquire the extra MRI sequences that I needed for my DPhil.

During this project I had the privilege to get to know and collaborate with Professor Suzanne Haber. Thank you for having me in your lab and for sharing your in-depth knowledge and valuable time on the microscope.

I also owe a great deal to the highly skilled members of FMRIB. Dr. Ricarda Menke was always very friendly and willing to give advice on multiple aspects of my research. Dr. Saad Jbabdi, Dr. Gwen Douaud, Dr. Stamatis Sotiropoulos and Dr. Tim Behrens, many thanks for your excellent advice on diffusion tractography. Dr. Karla Miller, for helping to optimise an MRI sequence during my first year and Dr. Anderson Winkler for his willingness to help at any given occasion (stats, figures,

get home safely in the early hours). Stamatis Sotiropoulos, Anderson Winkler and Courtney Bishop for their friendship. Further, I would like to thank Mrs. Sue Field and Mrs. Marilyn Goulding for handling my conference expenses and the IT people both at FMRIB (David Flitney and Duncan Mortimer) and GSK (Jonathan Rosalski and Omer casher) for helping me out with computer and software issues.

I am heartily thankful to Dr. Guo Qi, Dr. Cristian Salinas and Dr. Chris Long. You have been both excellent friends and colleagues. Qi, you deserve an extra thank you for the great travels after the conferences and especially for always being pleasant and supportive.

I am very beholden to Mr. Petros Pantelides, for his help and guidance throughout the years. I cannot omit thanking my friends Elina, Georgia, Maria, Markella, Skevi and especially Ioanna who helped me maintain my sanity in Oxford. Hitherto, that was the time that I needed you the most and you were there for me.

I would like to thank Harry, with whom the DPhil journey began and I will always be thankful for his unwavering support, encouragement and his heart-warming advise.

Last, but by no means least, I would like to thank my beloved family. My adorable Dad, who kept reminding me during this time that he wants a grandchild and not another “piece of paper” -- this is, by the way, his way of describing my degree. My beloved brother and grandmother but mostly my precious Mom, who gave me strength during this arduous period. Thank you for everything you have given me, for the unconditional love and for always being right by my side.

November 10, 2012

Oxford, UK

To the people who ...

teach me the real value in life,

those who ameliorate my present,

and those who inspire my future.

November 10, 2012

Oxford, UK

Contents

1 Introduction **1**

1.1 Molecular imaging of dopamine 4

1.2 Thesis outline 6

1.3 Journal publications and conference proceedings 10

1.3.1 As a first author 10

1.3.2 As a co-author 11

1.3.3 Conference papers 12

1.3.4 Oral presentations at international conferences 12

1.3.5 Conference abstracts 13

1.4 Awards - Grants 16

2 Brain Anatomy and Dopamine **17**

2.1 Brain 18

2.1.1 Ventricular system 18

2.1.2 Cerebellum 18

2.1.3 Brainstem 20

2.1.4 Forebrain 21

2.2 Neuroanatomy 27

2.2.1 Neuron 27

2.2.2 Synapse 28

2.2.3 Neurotransmitters 29

2.2.4 Receptors 30

2.3 Dopamine 30
2.3.1 Dopamine synthesis and release 31
2.3.2 Dopamine transporter 32
2.3.3 Dopamine receptors 32
2.3.4 Dopamine Pathways 34
2.4 Amphetamine 34

3 Brain Imaging – MRI and PET 36
3.1 MRI 38
3.1.1 Basic principles of Magnetic Resonance Imaging 38
3.1.2 Structural MRI 40
3.1.3 Diffusion MR imaging 41
3.2 PET 52
3.2.1 PET physics 53
3.2.2 Data correction and image reconstruction 54
3.2.3 PET quantification 56
3.2.4 Assessing synaptic neurotransmission with PET 64
3.2.5 Dopamine radioligands 65
3.3 Multimodal brain imaging for image analysis 67
3.3.1 Registration methods 68
3.3.2 Regions of interest segmentation methods 69

4 Development of region of interest guidelines for quantification of subcortical dopamine 73
4.1 Introduction 73
4.2 ROI guidelines for the manual delineation of subcortical regions of interest 74
4.2.1 Guidelines for ROIs defined on MRI images 75
4.2.2 Guidelines for ROIs defined on PET images 79
4.3 Automated method for the definition of the subcortical ROIs 80

4.4 Robustness, reproducibility and reliability of subcortical ROIs 84
4.4.1 Material and methods 84
4.4.2 Results 87
4.4.3 Discussion 92

5 Connectivity-based subdivision of the striatum and pallidum 96
5.1 Introduction 96
5.2 Basal ganglia connections 98
5.3 Connectivity–based subdivision of the striatum 102
5.3.1 Materials and methods 103
5.3.2 Results 110
5.3.3 Discussion 119
5.4 Connectivity–based subdivision of the pallidum 123
5.4.1 Materials and methods 124
5.4.2 Results 127
5.4.3 Discussion 130

6 Quantification of dopamine D2R and D3R distribution with [^{11}C]PHNO 134
6.1 Introduction 134
6.2 Materials and methods 140
6.2.1 Subjects 140
6.2.2 Data acquisition 140
6.2.3 Image preprocessing 141
6.2.4 Structural-based definition of ROIs 142
6.2.5 Connectivity-based subdivisions of the striatum and pallidum 142
6.2.6 Assessment of the performance of the connectivity-based atlases 143
6.2.7 Derivation of the parameters of interest - BP_{ND} and D3R/D2R contribution to the total [^{11}C]PHNO specific signal 144
6.3 Results 147

6.3.1 Distribution of [^{11}C]PHNO in the structural subcortical regions 147
6.3.2 Distribution of the [^{11}C]PHNO in the connectivity-based functional subdivisions of the striatum and pallidum 156
6.4 Discussion 162

7 Dopamine release within the anatomical and functional subdivisions of the BG following d-amphetamine stimulation 169
7.1 Intoduction 169
7.2 Materials and methods 170
7.2.1 Subjects 170
7.2.2 Data acquisition 171
7.2.3 Connectivity-based subdivision of the striatum and pallidum . 172
7.2.4 Structural subdivision and definition of the striatum and pallidum 174
7.2.5 Quantification of dopamine release 175
7.3 Results 176
7.3.1 Dopamine release in striatum 176
7.3.2 Dopamine release in pallidum 182
7.4 Discussion 185

8 Correlation of the Nigrostriatal dopaminergic pathway and dopamine PET measurements 193
8.1 Introduction 193
8.2 Materials and methods 196
8.2.1 Subjects 196
8.2.2 Data acquisition 197
8.2.3 Image analysis for PET and MRI 198
8.3 Results 201
8.4 Discussion 203

9 Conclusions and future directions **207**

9.1 Future objectives 212

9.1.1 Investigate non-linear registration algorithms for spatial normalisation 212

9.1.2 Acquisition of arterial input function for the analysis of the [^{11}C]PHNO studies 212

9.1.3 Optimisation of structural T1-weighted images 213

9.1.4 Correlation of PET measurements with the strength of the nigrostriatal pathway 214

Bibliography **215**

List of Figures

1.1 PET and structural MRI images 2

1.2 A road map for the structure of the thesis 7

2.1 The ventricular system 19

2.2 The central nervous system 19

2.3 The brain 21

2.4 Cortical anatomy 22

2.5 Basal ganglial nuclei 23

2.6 Anatomy of the striatum 24

2.7 The structure of a neurone 28

2.8 Neurotransmission at the synapses 29

2.9 Dopamine pathways 35

3.1 T1, T2 and PD MRI image contrast 41

3.2 Effect of diffusion gradients on the diffusion weighted signal 44

3.3 Diffusion tensor derived images 46

3.4 Diffusion-based tractography 49

3.5 Fibre bundle geometries, diffusion tensors and PDDs 51

3.6 PET: Detection of annihilated photons 54

3.7 Source of noise in PET 56

3.8 Compartmental model configurations. 58

3.9 Reference input models. 64

4.1 Subcortical ROI guidelines 76
4.2 Anatomical atlas 83
4.3 ROIs overlaid on [^{11}C]PHNO BP_{ND} 88
4.4 ROI reproducibility: DICE coefficient 89
4.5 ROI reproducibility: BP_{ND} variability 91
4.6 DICE coefficient Vs ROI size 92

5.1 Connections of the basal ganglia: "direct pathway" and "indirect pathway" 99
5.2 Models of cortical–subcortical information processing 100
5.3 Schematic representation of the striatal and pallidal functional organisation in primates 102
5.4 Connectivity–based striatal subdivision: methods overview 103
5.5 Cortical subdivision 109
5.6 Striatal–cortical projections 111
5.7 Population connectivity maps of striatum 114
5.8 Connectivity–based striatal subdivision in 4 subjects 115
5.9 Connectivity–based population striatal atlas 116
5.10 Cortical–striatal projections – effect of threshold 117
5.11 Cortical–striatal projection overlaps 118
5.12 Connectivity–based subdivision of the pallidum: methods overview . 123
5.13 Anatomy of the pallidum and ROI definition 125
5.14 Population connectivity maps of pallidum 129
5.15 Connectivity–based pallidal subdivision in 4 subjects 130
5.16 Connectivity–based population pallidum atlas 131
5.17 Striatal–pallidal projections – effect of threshold 131

6.1 [^{11}C]PHNO TACs and SRTM model fits in anatomical ROIs. 148

6.2 [^{11}C]PHNO parametric BP_{ND} images at baseline and after administration of GSK598809 150
6.3 [^{11}C]PHNO BP_{ND} at baseline and after administration of 75 and 175 mg GSK598809 152
6.4 [^{11}C]PHNO displacement against concentration of GSK598809 in the SN, Hypo, VST, TH, GP and VP_{SI} 153
6.5 [^{11}C]PHNO displacement against concentration of GSK598809 in CD and PU 154
6.6 Summary of the [^{11}C]PHNO BP_{ND}: total, D3R and D2R BP_{ND}. 155
6.7 [^{11}C]PHNO TACs and SRTM model fits in functional ROIs. 158
6.8 [^{11}C]PHNO displacement against GSK598809 plasma concentration in the connectivity-based subdivisions of the striatum 160
6.9 [^{11}C]PHNO displacement against GSK598809 plasma concentration in the connectivity-based subdivisions of the pallidum 161

7.1 Methods: Striatum-Pallidum functional subdivision 173
7.2 [^{11}C]PHNO and [^{11}C]Raclopride BP_{ND} before and after administration of d-amphetamine 178
7.3 Dopamine release and %COV in striatum 179
7.4 Dopamine release %COV Vs ROI size 182

8.1 Substantia nigra – striatal connections in primates 195
8.2 Substantia nigra ROI defined on a white matter nulled image 199
8.3 Substantia nigra ROI guideline landmarks 199
8.4 Age versus the a) total number of samples (TNS) and b) BP_{ND} 202
8.5 Correlation of the nigrostriatal pathway "strength" with [^{11}C]PHNO BP_{ND} 203

List of Tables

3.1 Dopaminergic D2-like receptor PET radioligands 67

4.1 Guidelines for the substantial nigra ROI 80
4.2 Structural ROI name abbreviations 81
4.3 Structural ROI size 93

5.1 Striatal–cortical projections: volume and percentage contribution to the total striatal volume 112
5.2 Pallidal–striatal projections: volume and percentage contribution to the total pallidum volume 128

6.1 Concentrations of D2R and D3R binding sites and densities in the subcortical areas of the human brain. Table adapted from Gurevich et al. [71] 135
6.2 Concentrations of D2R and D3R binding sites and densities in the subcortical areas of the human brain. Table adapted from Murray et al. [135] 137
6.3 Characterisation of the [^{11}C]PHNO signal in the structural defined ROIs: f^{D3R}_{PHNO}, BP^{PHNO}_{ND}, D3R BP_{ND} and D2R BP_{ND} 151
6.4 Comparison between connectivity-based subdivisions obtained with an atlas and with subject's own subdivisions. 156
6.5 Characterisation of the [^{11}C]PHNO signal in the connectivity-based functional subdivisions: f^{D3R}_{PHNO}, BP^{PHNO}_{ND}, D3R BP_{ND} and D2R BP_{ND} . . . 159

7.1 Quantification of dopamine release within the connectivity-based functional subdivisions of the striatum 177
7.2 Quantification of dopamine release within the connectivity-based functional subdivisions of the pallidum 184

Chapter 1

Introduction

The brain is the most complex and the most important organ in the human body. It initiates, processes, executes and maintains numerous functions essential for physical survival and others that give rise to consciousness, memories and emotions. The brain contains billions of neurones that transfer information between brain regions and to the rest of the human body. In the brain, the information is encoded in electrochemical signals that are transmitted via the release of biomolecules known as neurotransmitters. One important neurotransmitter that has a direct impact on everyday life is dopamine. Dopamine is involved in cognitive, sensorimotor, emotional and reward processes, and is also implicated in several neurological and psychiatric disorders such as Parkinson's disease, schizophrenia and addiction. The involvement of dopamine and the proteins through which dopamine exerts its actions (dopamine receptors) in these key processes and diseases makes dopamine and the dopamine receptors an important target for research and drug discovery. Thus far, despite the great interest and extensive research, the exact role of dopamine and the causalities of dopamine-related disorders are not fully understood.

In this thesis, we explore dopamine and the D2-like receptor family, in the human brain via a multimodal imaging approach using positron emission tomography (PET) and magnetic resonance imaging (MRI). In PET, a positron emitting radioactive ra-

dioligand can be injected into subjects, which enables the *in–vivo* visualisation and quantification (figure 1.1,A) of a neurotransmitter and its receptors. MRI on the other hand, uses the magnetic properties of protons to provide high resolution images of both the anatomy and physiology of the brain (figure 1.1,B).

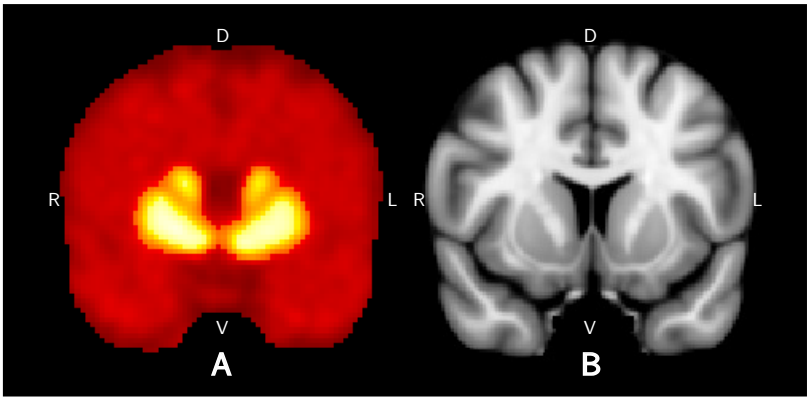

Figure 1.1: A) PET and B) structural MRI images. R=right; L=left; D=dorsal; V=ventral.

Until recently, the *in–vivo* investigation and successful quantification of dopamine and the dopamine D2-like receptor family has been restricted mainly to one brain region the striatum. This is primarily due to the radioligands available, which give sufficient signal for quantification only in the striatum, where these receptors are highly expressed. Moreover, the D2-like family consists of the D2R, D3R and D4R, and previously available radioligands did not allow a distinction between the receptor subtypes of the D2-like family. Knowledge of each receptor's distribution will help in understanding their function and their involvement in brain disorders. The recent development of [^{11}C]PHNO as a radioligand, which binds preferably to the D3R, enables for the first time, imaging of the D3R and the D2R in extrastriatal regions and the distinction of these two subtypes. In recent years, there has been great interest in imaging the D3R, both to study their implication in conditions such as addiction and schizophrenia and also to aid in development of drugs that interact with the D3R. In addition, the increased sensitivity of [^{11}C]PHNO could offer advantages in detecting

fluctuations in endogenous dopamine levels as dopamine is expected to compete more efficiently with an agonist radioligand.

Observations from recent studies that investigate the release of dopamine in the brain, suggest that dopamine might have a functional rather than a structural specificity. That means that dopamine is selectively released in brain areas that execute specific functions. Confirmation of the functional specificity of dopamine will help understand the role of dopamine and its involvement in neurological disorders where certain functions are impaired. This will have consequences for the design, analysis and interpretation of future dopamine studies in normal conditions and pathophysiology. These observations, together with the importance of dopamine in health and disease, combined with the recent introduction of [^{11}C]PHNO were the stimulus for developing the research questions and goals of this thesis.

The overarching aim of this work is to explore the regional distribution of the D2R and D3R sites and assess the functional specificity of dopamine. In this thesis, methods have been developed to facilitate the study of dopamine and the D2-like receptor subtypes, in the structural and connectivity-based functional subdivisions of the human brain. Region of interest (ROIs) guidelines, tailored to structural MRI information, have been developed to allow a reproducible and robust segmentation of the striatal and extrastriatal brain regions. In addition, diffusion weighted imaging data (DWI) are employed to study the striatal-cortical and pallidal-striatal anatomical connections and in turn, obtain the functional subdivisions of the striatum and pallidum. These methods are subsequently applied to [^{11}C]PHNO PET data acquired before and after the administration of pharmacological challenges, including a D3R antagonist compound and the dopamine releasing agent amphetamine.

Moreover, in quantitative PET imaging studies there is often a relatively high inter–subject variability in the ligand-receptor binding measurements. One hypothesis about this variability is that any differences in the PET signal might be attributed to differences in the receptor densities among subjects. Using DWI MRI and [^{11}C]PHNO PET, we explore whether there is an association between the nigrostriatal pathway potency that could impact the density of the dopamine D2-like receptors and explain the inter–subject variability in PET measurements.

1.1 Molecular imaging of dopamine

Molecular imaging enables the assessment of the biochemical and physiological processes in the living brain. PET is the first imaging modality that has been used for quantitative molecular imaging and since the early 1980's it has become an integral and indispensable tool for the study of dopamine. The subsequent introduction of single photon emission computed tomography (SPECT) — an imaging modality that also requires the injection of a radioligand — has further broadened the use of molecular imaging techniques for the study of dopamine. To the best of our knowledge, the first *in–vivo* dopamine study in humans was performed by Wagner and colleaques [185] in 1983. They demonstrated for the first time that [^{11}C]-N-methylspiroperon and PET can be used to study the distribution of dopamine receptors in the human brain. Subsequantly, Farde and colleagues [58] injected [^{11}C]Raclopride, a radioligand that has a high selectivity for the D2-like receptors, into healthy humans and showed that radioligands with sufficient selectivity for the target of interest and with favourable kinetics (rapid association and disassociation between the ligand and the target) can be used for quantitative measurement of the dopaminergic system.

The ability of PET and of selected radioligands to image and quantify acute changes in extracellular dopamine levels, was demonstrated in the early 1990's. In 1990 Dewey et

al. [46] employed benztropine, a dopamine uptake inhibitor, and reported a reduction in the striatal uptake of [^{18}F]-N-methylspiroperidol. Two imaging studies followed, one in baboons with the D3R/D2R ligand [^{18}F]-N-methylspiroperidol [45] and the other in humans with [^{11}C]Raclopride [60]. These studies acquired imaging data before and after the administration of amphetamine and showed that amphetamine, which induces release of dopamine, and which, in turn, competes with the ligand, decreased the measured PET signal. The principle that underlies the competitive binding paradigm is: changes in the synaptic dopamine levels results in changes in the number of receptors that are occupied by the neurotransmitter and this leads to changes in the number of available receptors for the ligand to bind. For example, increased levels of dopamine, increases the number of the receptors occupied by the neurotransmitter and reduces the availability of receptors for the ligand to bind. Therefore the PET signal, which corresponds to ligand-receptor binding, drops. The use of this technique has been validated and has been used extensively to study dopamine. In 1998 Koepp and coworkers [104] measured the release of dopamine after a non-pharmacological stimulus that involved a video–game playing. This study effectively demonstrated that PET is sensitive enough to measure small changes of dopamine levels and enables the monitoring of the dopamine system under physiological conditions. The high sensitivity of PET in quantifying low material concentrations is the essential advantage of the modality over other functional techniques. For example, according to Grunder [67] magnetic resonance spectroscopy (MRS) allows for assessment of GABA only in concentrations up to 10^{-3} M whereas PET can detect as low as 10^{-9} M to 10^{-12} M.

PET has been used extensively as an imaging tool to investigate the implication of dopamine in a range of neurological and psychiatric conditions. For example patients with schizophrenia have been studied with both the dopamine releasing agent amphetamine and the a-MPT depletion paradigm. The findings indicate that patients with schizophrenia have increased levels of synaptic dopamine as compared to healthy

controls [2, 112, 3]. In contrast, studies with amphetamine or methylphenidate in patients with addiction or Parkinson's disease have shown that there are decreased synaptic levels of dopamine as compared to healthy controls [121, 126, 184, 105, 147].

Understanding the functional role of dopamine and knowledge of the distribution of the dopamine receptors has helped the discovery and development of drugs for several dopamine-related diseases. PET can aid drug discovery via biodistribution or competition studies. In biodistribution studies the drug itself is labeled with a radioactive molecule and this is injected into the subject. The aim in these types of studies is to assess whether the drug enters the brain, monitor the distribution and measure the concentration-time course of the drugs in tissues of interest. In competition (or occupancy) studies, a radioligand with a high selectivity for the therapeutic target of interest is used in the absence and presence of a cold dose of the compound under investigation. Competition studies can be used for dose ranging as they allow a direct assessment of the relationship between the concentration of the drug in the plasma and the occupancy of the target. The benefits of using PET in drug discovery are such that nowadays pharmaceutical companies consider PET imaging routinely and at the earliest stages of new drug development [128].

1.2 Thesis outline

The structure of the thesis is illustrated in the road map shown in figure 1.2. Before presenting our methodological developments, applications and findings, chapters 2 and 3 introduce some background information that will help the reader understand basic concepts that are essential for a comprehensive understanding of the thesis. Chapters 4 and 5 present the methodological developments of this thesis while chapters 6 to 7 apply these methods to [^{11}C]PHNO PET and MRI data sets to characterise both the distribution of the D2-like receptors and dopamine release. In chapter 8 we explore potential correspondence between the potency of the nigrostriatal pathway

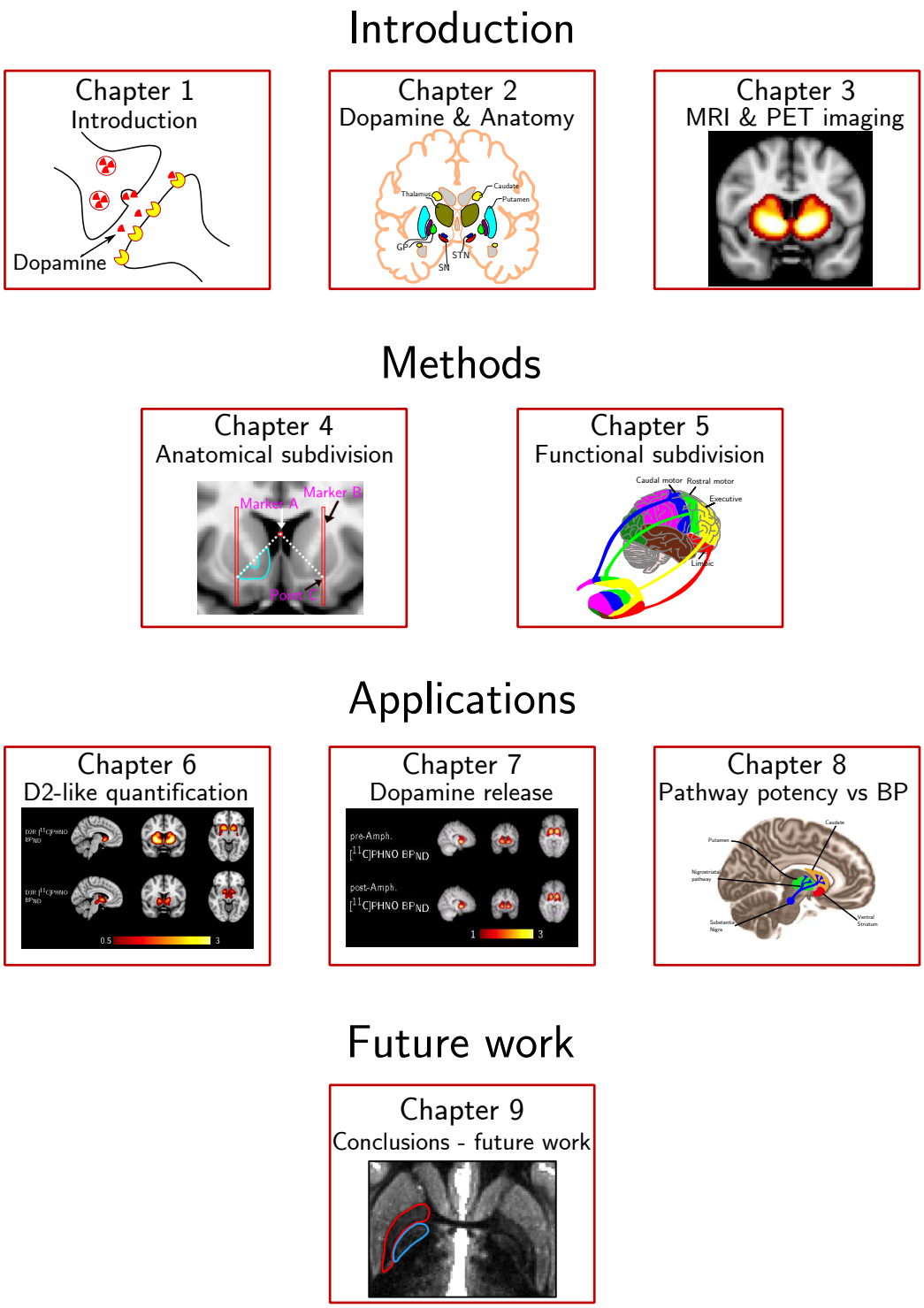

Figure 1.2: A road map for the structure of the thesis.

and the density of the dopamine receptors measured with PET. Finally, chapter 9 summarises the results and discuss future perspectives.

Chapter 2 introduces the reader to basic brain anatomy and the anatomy of the functional unit of the central nervous system, the neurone. In this chapter, particular emphasis is given to the neurotransmitter dopamine and the dopamine receptors through which dopamine exerts its actions. A concise description of the dopaminergic pathways, their origin, projections and the implication of each pathway for specific functions is presented. At the end of the chapter we introduce amphetamine, a psycho-stimulant agent that is used here as a means to provoke and measure dopamine neurotransmission.

In **chapter 3** the basic principles of the magnetic resonance imaging and positron emission tomography physics are presented. A synopsis of the structural and diffusion weighted MR imaging modalities are given as well as a brief introduction of diffusion tractography methods. An overview of the PET image reconstruction and data correction methods are also covered in this chapter. In order to quantify the *in–vivo* PET signal, which results from the radioligand-receptor interactions, pharmacokinetic compartmental modelling is used. A review of compartmental modelling methods is presented as well as an explanation of the experimental paradigm which allows the *in–vivo* assessment of synaptic neurotransmission. Furthermore, we summarise the dopaminergic PET ligands and outline their binding characteristics with regard to the D2-like receptors. To conclude this chapter, we introduce the registration algorithms that have enabled the fusion of multimodal information and the current literature on brain segmentation methods.

[^{11}C]PHNO is the first radioligand that has a higher selectivity for the D3R receptors and can also image extrastriatal D3R/D2R sites. In **chapter 4** we develop a set of

region of interest guidelines to segment the relevant anatomical regions. As manual ROI delineation is both time consuming and a labour intensive procedure we constructed an anatomical atlas, wherein the subcortical regions are defined according to these guidelines. This atlas enables automated definition of the ROIs with immediate benefits for the resource and time required. Lastly, we investigate the robustness and reproducibility of the manual ROIs and the performance of the automated approach.

Anatomical regions in the human brain can be approached with regard to their cytoarchitectonical or functional organisation. The cytoarchitectonic organisation of anatomical regions can be obtained from high resolution structural MRI images. Therefore, nowadays it is common practice in PET studies to acquire a structural MRI image to help identify the cytoarchitectonical differentiated regions (chapter 4). However, the functional organisation is not readily available and more advanced analysis approaches are required for their subdivision. The functional organisation of a region is determined from the connections with other brain regions. With diffusion weighted imaging and probabilistic tractography methods it has been possible to identify the connectivity profile of brain regions and determine their functional organisation. In **chapter 5** probabilistic tractography is used to estimate the striatal–cortical and the pallidal–striatal connections in order to subdivide the striatum and pallidum according to their connections.

Until recently, PET radioligands did not have sufficient selectivity to enable imaging of the individual subtypes of the D2-like family of dopamine receptors and therefore they were only informative for the distribution of the D2-like receptors as a whole. The introduction of [^{11}C]PHNO ligand, which has a preferential affinity for the D3R sites, enables for the first time an investigation of both the D2R and D3R receptor distributions. In **Chapter 6** we acquired [^{11}C]PHNO data in healthy volunteers scanned before and after the administration of a selective D3R antagonist compound. Using

a competition model we were able to characterise the distribution of each receptor subtype and estimate their relative densities in the human brain.

Observations in PET studies suggest that the release of dopamine is not explained by the cytoarchitecture of the anatomical regions but rather seems to be aligned with the functional organisation of these regions. In **chapter 7** we use [^{11}C]PHNO and [^{11}C]Raclopride PET data acquired before and after the administration of the dopamine releasing agent amphetamine, to examine the functional specificity of dopamine release in striatum and pallidum.

Chapter 8 examines whether there is a correlation between the potency of the nigrostriatal pathway and the density of the D2-like receptors as measured with [^{11}C]PHNO PET. Probabilistic tractography is used to both identify the dopaminergic nigrostriatal pathway and assess its potency.

In **chapter 9** we summarise and critically review our developments and findings and we discuss their limitations. Finally we outline some future perspectives that have emerged from the limitations of this work and from the necessity to further address dopamine related issues under the framework of multimodal imaging.

1.3 Journal publications and conference proceedings

1.3.1 As a first author

1. Connectivity–based functional analysis of dopamine release in the striatum using Diffusion Weighted MRI and Positron Emission Tomography. Tziortzi A. C., Haber S. N., Searle G. E., Tsoumpas C., Long C., Shotbolt P., Douaud G., Jbabdi S., Behrens T., Rabiner E. A., Jenkinson M., Gunn R. N. Cereb Cortex, 2013

2. Imaging dopamine receptors in humans with [11C]-(+)-PHNO: Dissection of D3 signal and anatomy. Tziortzi A. C., Searle G., Tzimopoulou S., Salinas C., Beaver J., Jenkinson M., Laruelle M., Rabiner E. A., Gunn R. N. Neuroimage, vol. 54, pp. 264-277 2011

1.3.2 As a co-author

1. Mathematical modelling of [^{11}C]PHNO human competition studies. Searle, G. E., Beaver, J. D.,Tziortzi, A. C., Comley, R. A., Bani, M., Ghibellini, G., Merlo-Pich, E., Rabiner, E.A., Laruelle, M., Gunn, R.N. Neuroimage, vol. 68C, pp. 119-132, 2012

2. Within-subject comparison of [^{11}C]PHNO and [^{11}C]Raclopride sensitivity to acute amphetamine challenge in healthy humans. Shotbolt P., Tziortzi A. C., Searle G. E., Colasanti A., Van der Aart, J., Abanades S., Plisson, C., Miller, S. R., Huiban, M., Beaver J. D., Gunn R.N., Laruelle M., Rabiner E. A. J Cereb Blood Flow Metab, vol. 32, pp. 127-136, 2012

3. Advances in biomathematical modeling for PET neuroreceptor imaging. Gunn R.N., Guo Q., ,Salinas C. A., Tziortzi A. C., Searle G. E. Drug Discovery Today: Technologies, vol. 8, pp.45-51, 2012

4. Endogenous opioid release in the human brain reward system induced by acute amphetamine administration. Colasanti A., Searle G. E., Long C. J., Hill S. P., Reiley R. R., Quelch D., Erritzoe D., Tziortzi A. C., Reed L. J., Lingford-Hughes A. R., Waldman A. D., Schruers K. R., Matthews P. M., Gunn R.N., Nutt D. J., Rabiner E. A. Biol Psychiatry, vol. 72, pp. 371-377, 2012

5. Orbitofrontal connectivity with resting-state networks is associated with midbrain dopamine D3 receptor availability. Cole D. M., Beckmann C. F., Searle G. E., Plisson C., Tziortzi A. C., Nichols T. E., Gunn R.N., Matthews P. M., Rabiner E. A., Beaver J. D. Cereb Cortex, vol. 22, pp. 2784-2793, 2012

6. Imaging dopamine D3 receptors in the human brain with Positron Emission Tomography, [^{11}C]PHNO, and a selective D3 receptor antagonist. Searle G., Beaver J., Comley R., Bani M., Tziortzi A., Slifstein M., Mugnaini M., Wilson A., Merlo-Pich E., Houle S., Gunn R., Rabiner E., Laruelle M. Biol Psychiatry, vol. 68, pp. 392-399, 2010

1.3.3 Conference papers

1. MRI–DTI and PET multimodal imaging of dopamine release within subdivisions of Basal Ganglia. Tziortzi A. C., Searle G., Tsoumpas C., Long C., Shotbolt P., Rabiner E., Jenkinson M. and Gunn R.N. International Conference on Image Optimisation in Nuclear Medicine(OptiNM). Journal of Physics: Conference Series, vol. 317, pp. 1-3, 2012

2. Spatial-temporal pharmacokinetic model based registration of 4D brain PET data. Jiao, J., Searle G., Tziortzi A., Salinas C., Gunn R.and Schnabel, J., 2^{nd} International MICCAI. vol. 7570, pp. 100-112, 2012

1.3.4 Oral presentations at international conferences

1. 60^{th} SNM Annual Meeting, 8-12 June, 2013, Vancouver, Canada.

2. XXVIth International Symposium of Cerebral Blood Flow, Metabolism and Function & XIth International Conference on Quantification of Brain Function with PET. 20-23 May, 2013, Shanghai, China.

3. 18^{th} Annual Meeting of the Organisation for Human Brain Mapping, 10-14 June, 2012, Beijing China

4. 58^{th} SNM Annual Meeting, 4-8 June, 2011, San Antonio, Texas, USA

5. International Conference of Image Optimisation in Nuclear Medicine. 23 - 26 March, 2011, Ayia Napa, Cyprus

6. 8^{th} International Symposium on Functional Neuroreceptor Mapping of the Living Brain, 22-24 July, 2010, Glasgow, UK

7. 56th SNM Annual Meeting, 13-17 June, 2009, Toronto, Canada

1.3.5 Conference abstracts

1. Quantification of dopamine release and dopamine D3R in the functional subdivisions of the human pallidum. Tziortzi A. C., Searle G, Rabiner E. A., Jenkinson, M., Gunn R. N. 60^{th} SNM Annual Meeting, 8-12 June, 2013, Vancouver, Canada.

2. Quantification of D3R receptors and dopamine release in the functional subdivisions of the pallidum. Tziortzi A. C., Searle G, Douaud G., Rabiner E. A., Jenkinson, M., Gunn R. N. XXVIth International Symposium of Cerebral Blood Flow, Metabolism and Function & XIth International Conference on Quantification of Brain Function with PET, 20-23 May 2013, Shanghai, China

3. A positive correlation between the potency of the nigrostriatal dopaminergic pathway and receptor density measured with [^{11}C]PHNO PET. Tziortzi A. C., Erritzoe D., Menke R., Rabiner E. A., Jenkinson, M., Gunn R. N. XXVIth International Symposium of Cerebral Blood Flow, Metabolism and Function & XIth International Conference on Quantification of Brain Function with PET, 20-23 May 2013, Shanghai, China

4. Imaging of dopamine D3R receptors in alcohol dependence using [^{11}C]PHNO-PET, and selective D3Rreceptor blockade. Erritzoe D., Tziortzi A. C., Searle G., Gunn R. N., Beaver J. D., Nutt D. J., Bani M., Merlo-Pich E., Rabiner E. A., Lingford-Hughes A. British Neuroscience Association, 7-10 April 2013, London, UK

5. Quantification of dopamine release within the connectivity-derived functional subdivision of striatum. Tziortzi A.C., Haber S. N., Searle G., Tsoumpas C.,

Long C., Shotbolt P., Behrens T., Rabiner E. A., Jenkinson M., Gunn. R. N., 9*th* International Symposium on Functional Neuroreceptor Mapping of the Living Brain, 9-11 August, 2012, Baltimore, USA

6. *In-vivo* imaging of dopamine D3R receptors in alcoholism using [^{11}C]PHNO –PET, and a selective D3R receptor antagonist. Erritzoe D., Tziortzi A. C., Bargiela D., Searle G., Gunn R. N., Beaver J., Waldman A., Nutt D. J., Bani M., Merlo-Pich E., Rabiner E. A., Lingford-Hughes A. 9*th* International Symposium on Functional Neuroreceptor Mapping of the Living Brain, 9-11 August, 2012, Baltimore, USA

7. Quantification of dopamine in the human striatum in anatomical and connectivity derived subdivisions. Tziortzi A. C., Haber S. N., Searle G., Tsoumpas C., Long C., Shotbolt P., Rabiner, E. A, Gunn R.N., Jenkinson M., 18th Annual MMeeting of the Organisation for Human Brain Mapping, 10-14 June, 2012, Beijing China

8. *In-vivo* imaging of dopamine D3R receptors in alcoholism using Positron Emission Tomography, [^{11}C]PHNO, and a selective D3R receptor antagonist. Erritzoe D., Tziortzi A., Bargiela D., Searle G., Gunn R. N., Beaver J., Waldman A., Nutt D. J., Bani M., Merlo-Pich E., Rabiner E. A., Lingford-Hughes A., Society of Biological Psychiatry, 29 May -2 June, 2011, Prague, Czech republic

9. A Diffusion Tensor IImaging (DTI) and [^{11}C]PHNO Positron Emission Tomography (PET) study to measure dopamine release within the functional subdivisions of the basal ganglia. Tziortzi A. C., Searle G., Long C., Shotbolt P., Rabiner E. A., Jenkinson. M, Gunn R.N., 58th SNM Annual Meeting, 4-8 June, 2011,San Antonio, Texas, USA

10. A combined Diffusion Tensor Imaging (DTI) and [^{11}C]PHNO Positron Emission Tomography (PET) study to quantify Dopamine D3R/ D2R receptors in Pal-

lidum. Tziortzi A. C, Douaud, G., Shotbolt P., Bishop, C., Searle G., Laruelle M., Rabiner E. A., Jenkinson M., Gunn. R. N., 8^{th} International Symposium on Functional Neuroreceptor Mapping of the Living Brain, 22-24 July, 2010, Glasgow, UK

11. Within-subject comparison of the sensitivity of [^{11}C]PHNO and [^{11}C]Raclopride to amphetamine induced changes in endogenous dopamine in healthy humans. Shotbolt P., Tziortzi A., Miller S., Van der Aart J., Abanades S., Plisson, C., Huiban M., Beaver J., Gunn R.N., Laruelle M., Rabiner E. A., 8^{th} International Symposium on Functional Neuroreceptor Mapping of the Living Brain, 22-24 July, 2010, Glasgow, UK

12. PET imaging of dopamine D3 receptors in humans with [^{11}C]PHNO: dissection of [^{11}C]PHNO signal using two highly selective D3 antagonists. Searle G., Beaver J., Iavarone, L., Comley R., Bani M., Tziortzi A. C., Slifstein M., Wilson A., Gunn R.N., Rabiner E. A., Laruelle M., 8^{th} International Symposium on Functional Neuroreceptor Mapping of the Living Brain, 22-24 July, 2010, Glasgow, UK

13. Dopamine D3 receptor availability explains orbitofrontal connectivity with cognitive networks. Cole D., Beckmann C., NicholsT. Searle G., Tziortzi A., Gunn R. N., Matthews P, Rabiner E., Beaver J., 16^{th} Annual mMeeting of the Organisation for Human Brain Mapping, 6-10 June, 2010, Barcelona, Spain

14. PET imaging of dopamine D3 receptors in humans with [^{11}C]PHNO validated with a selective D3 antagonist. Searle G., Beaver J., Comley R., Bani M., Tziortzi A., Slifstein M., Mugnaini M., Wilson A., Merlo-Pich E., Houle S., Gunn R., Rabiner E., Laruelle M. 57^{th} SNM Annual Meeting ,5-9 June, 2010, Salt Lake City, USA

15. Amphetamine–induced endogenous opioid release measured in the human brain with [^{11}C]carfentanyl PET. Colasanti A., Searle G., Hill S., Reiley R., Tziortzi

A. C., Gunn R.N., Schruers K., Nutt D., Rabiner E. A., 23^{th} European College of Neuropsychopharmacology Meeting, August 28^{th}, September 1^{st}, 2010, Amsterdam, The Netherlands

16. Imaging the dopamine D3R / D2R receptor with [^{11}C]PHNO: Development and validation of manual and automated regional analyses. Tziortzi A. C., Searle G., Tzimopoulou, S., Beaver J., Rabiner E. A., Gunn R.N., 56^{th} SNM Annual Meeting, 13-17 June, 2009, Toronto Canada

1.4 Awards - Grants

1. BBSRC/GlaxoSmithKline Industrial Partnership Studentship in the Department of Clinical Neurology (4 Year Award: 10/2009-10/2013).

2. GlaxoSmithKline Clinical Imaging Centre STRIVE award for Excellence in Science, London, U.K., 2011

3. Society of Nuclear Medicine, 2011 travel grant.

4. Wolfson College, 2012 travel grant.

5. Guarantors of Brain, 2012 travel grant.

6. XXVIth International Symposium of Cerebral Blood Flow, Metabolism and Function & XIth International Conference on Quantification of Brain Function with PET, 2013 travel grant.

7. Part of this work was included in the HIGHLIGHT session of the 60^{th} SNM Annual Meeting, 8-12 June, 2013, Vancouver, Canada.

8. Part of this work was considered for the Brain Imaging Council Young Investigator Award at the 60^{th} SNM Annual Meeting, 8-12 June, 2013, Vancouver, Canada.

Chapter 2

Brain Anatomy and Dopamine

The nervous system is a complex network that receives, interprets, processes and conveys essential information for the normal functioning of the human body. The functional units of the nervous system are the neurones or nerve cells and the glial cells. The human nervous system is divided into the central nervous system (CNS) and the peripheral nervous system (PNS). The PNS connects the limbs and the internal organs with the CNS and is subdivided into somatic and autonomic. The somatic division contains the sensory neurones that detect stimuli from the skin, the joints and the muscles and informs the CNS. The autonomic division contains the neurones that receive information from the glands, viscera and other internal structures and helps regulate the body's functions.

The CNS consists of the brain and the spinal cord. The spinal cord serves as a canal for the transmission of sensory information to the brain and motor information from the brain to the rest of the body. The brain, or encephalon, is the fundamental part of the CNS and is the most complex and among the least understood organs in the human body. It contains billions of neurones that are interconnected to facilitate the basic everyday actions and the most advanced functions. This chapter gives a brief introduction to the basic neuroanatomy of the human brain and covers the neurotransmitter dopamine and the associated dopamine receptors.

2.1 Brain

The brain consists of three major divisions: the cerebrum, or forebrain, the cerebellum and the brainstem. Running through these three anatomical compartments are fluid-filled cavities, called the ventricular system. The forebrain consists of two hemispheres, the left and right, which are relatively symmetrical, and it is the most developed part of the CNS, being involved in the planning, execution and control of both basic and ingenious functions.

2.1.1 Ventricular system

The ventricular system consists of four ventricles that are interconnected by narrow channels (figure 2.1). The four ventricles are: a) the lateral ventricle, b) third ventricle c) fourth ventricle and d) the cerebral aqueduct. The lateral ventricles extend from the brain's midline into the brain hemispheres. The third ventricle is located in the midline of the brain, between the right and the left diencephalon (see section 2.1.4). The fourth ventricle is a cavity between the brainstem and the cerebellum and the cerebral aqueduct is the bridge between the third and the fourth ventricles. The fluid in the cavities is the cerebrospinal fluid (CSF) and serves multiple roles such as to protect the brain, excrete waste and enable chemical communication within the brain. CSF is produced by the choroid plexus, a structure located in the ventricles.

2.1.2 Cerebellum

The cerebellum contains approximately 50% of the brain's neurones and takes up less than 10% of the total brain volume [103]. The cerebellum is located at the bottom of the brain, posterior to the brainstem and is connected with other parts of the brain through the pons (figure 2.2). A medial structure, the vermis, separates the cerebellum into two symmetric hemispheres. Each hemisphere consists of a grey matter area, the cerebellar cortex, and beneath this are the four deep cerebellar nuclei and the white matter with the characteristic "tree-like" branching pattern (for

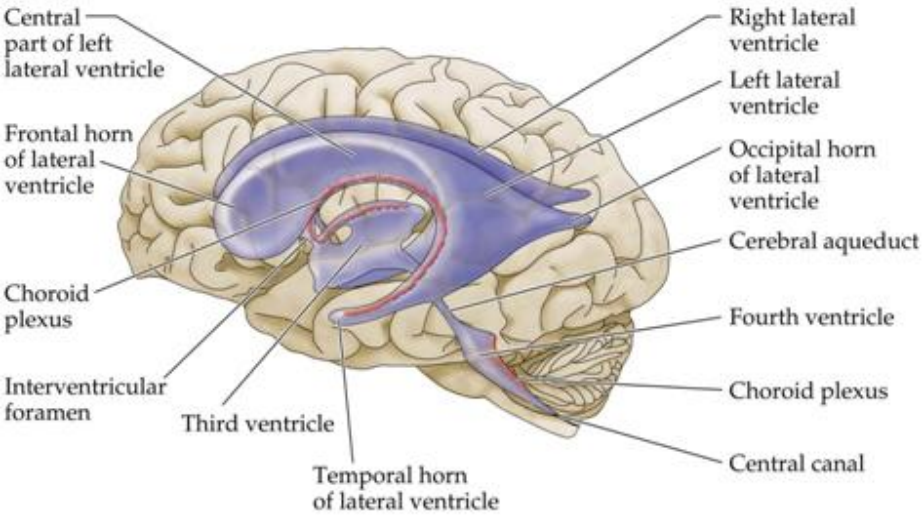

Figure 2.1: The ventricular system. Image courtesy of www.rci.rutgers.edu

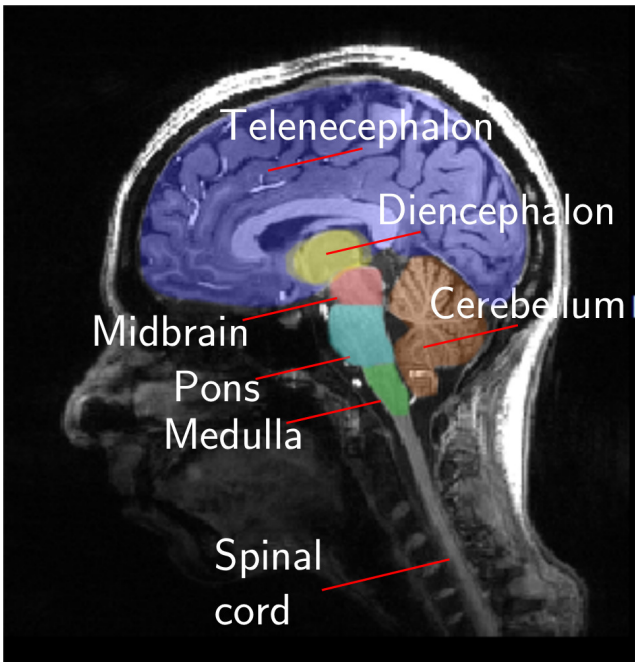

Figure 2.2: The central nervous system

information about the grey and white matter see section 2.2.1). The cerebellar cortex is a highly folded structure and these folds, called folia, are organised into ten groups termed the cerebellar lobules. This structure is essential for motor coordination, for posture and balance maintenance and influences muscle activity and muscle tone.

2.1.3 Brainstem

The brainstem is located at the base of the brain and is the structure that connects the forebrain with both the cerebellum and the spinal cord. It contains a number of important nuclei that are involved in vital autonomic body functions such as the control of blood pressure, respiration and heartbeat. The brainstem is a conduit for several major tracts that convey sensory and motor information between the forebrain and the spinal cord. Almost all of the cranial nerves originate or pass through the brainstem. Due to the numerous ascending and descending neurones that go through the brainstem and the important nuclei that reside in this area, small lesions may have profound implications.

From ventral to dorsal, the brainstem is composed of three parts: the medulla, the pons and the midbrain, or mesencephalon (figure 2.2). The mesencephalon contains the substantia nigra (SN) and the ventral tegmentum area (VTA), two regions where the dopaminergic pathways emerge (see section 2.3.4). SN, a member of the basal ganglial nuclei, consists of the substantia nigra compacta (SNc) and substantia nigra reticulata (SNr). The two components of the SN are connected in different ways to the other parts of the brain: the SNc is connected to the pedunculopontine nucleus and the thalamus whereas the majority of neurones in the SNr are dopaminergic and send their axons to the striatum. Neurones in the VTA send their axons mainly to the nucleus accumbens of the striatum and the frontal lobe.

2.1.4 Forebrain

The forebrain consists of the telencephalon and the diencephalon (figure 2.2), which comprises of the thalamus and hypothalamus. The telencephalon coarsely consists of an outer grey matter layer, termed the cortex, which overlays an inner layer of white matter and a deeper layer of subcortical grey matter nuclei (figure 2.3). The terms white matter and grey matter are introduced in section 2.2.1.

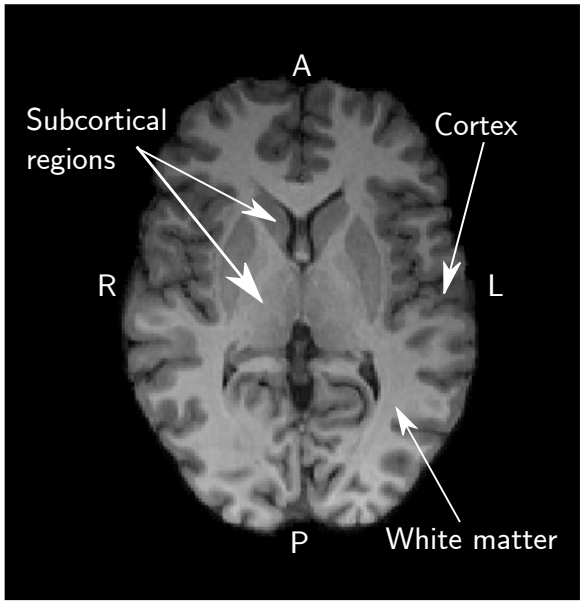

Figure 2.3: The brain. A structural MRI image from a representative subject. R=right; L=left; A=anterior; P=posterior

Cortex

Cortex is the surface of the brain and is a highly folded region. The elevated convolutions on the surface are called gyri and the furrows are termed sulci. The gyri and the sulci divide the surface of the brain into four anatomical areas: the frontal, parietal, occipital and temporal lobes (figure 2.4). Two structures, the insula and the cingulate gyrus, although they are not located on the surface of the brain, are considered as cortical regions. The insula lies beneath the frontal, parietal and temporal lobes

whereas the cingulate cortex is in the medial surface, superior to the corpus callosum (see section 2.1.4) and below the frontal, parietal and occipital lobes. The following paragraphs in this section, provide an overview of the basic high-level functional roles of the cortical regions although these functions are not exclusive.

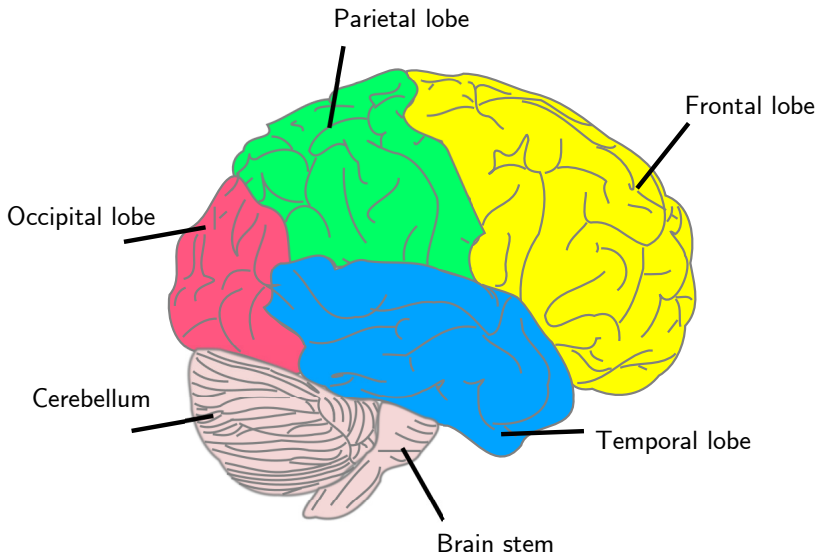

Figure 2.4: Cortical anatomy

The frontal lobe is considered to be the most evolved part of the brain. Different areas of the frontal lobe are considered to be involved in executing specific functions. For instance, the posterior part of the frontal lobe, the precentral gyrus, contains the primary motor cortex, which is involved in the execution of movements. Anterior to the precentral gyrus is the premotor areas, which are involved in planning movements and in motor decision making, whereas the ventromedial prefrontal cortex it is considered a limbic area, which means that is engaged in emotion and reward. Much of the frontal lobe is executive cortex, which means that it is involved in planning, working memory, attention, problem solving and other cognitive processes.

The parietal lobe is separated from the frontal lobe by the central sulcus and from the occipital lobe by the parietoccipital sulcus. The parietal lobe contains the primary

somatic sensory cortex (postcentral gyrus) that processes sensory information. Other areas within the parietal lobe are involved in visuospatial and limbic information processing. The occipital lobe contains the primary visual cortex and is mainly involved in visual perception. The temporal lobe is a multifunctional structure and is involved with functions such as understanding and processing of language, emotional stability and processing of auditory information. In the medial surface of the temporal lobe lies the amygdala and hippocampus. The amygdala is involved in emotions and the hippocampus in spatial memory and navigation. The insula cortex is known to be associated with pain whereas the anterior cingulate gyrus is associated with emotions and reward processes.

Basal ganglial

The basal ganglial (BG) is a set of anatomical nuclei that are situated bilaterally at the base of the forebrain (figure 2.5). The BG consists of the striatum, pallidum, subthalamic nucleus and the substantia nigra, which is located in the mesencephalon and has been described in section 2.1.3.

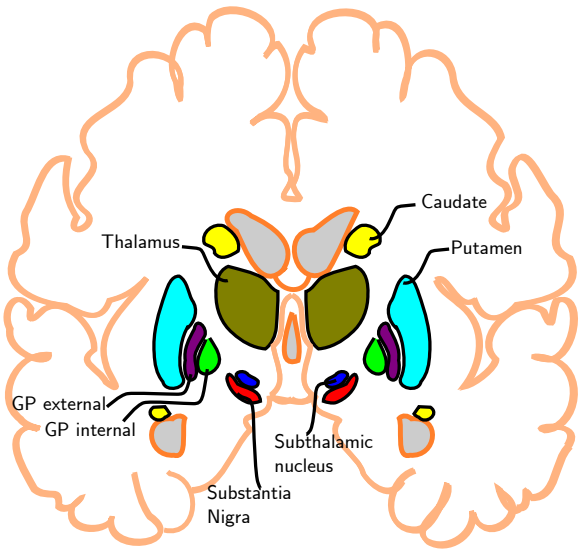

Figure 2.5: Basal ganglial nuclei

The largest component of the BG complex is the striatum (figure 2.6). The striatum consists of the caudate nucleus (CD), the putamen (PU) and the nucleus accumbens (NAC). The CD is a C–shaped structure that lies lateral to the lateral ventricles. The CD consists of three components: the head, that is the anterior part of the structure; the body; and the posterior part of the CD, the tail. Lateral to the caudate is the internal capsule, a white matter area that is spatially segmented into the anterior limb, the genu and the posterior limb. The anterior limb of the internal capsule separates the CD from the PU, in the area rostral to the anterior commissure (for anterior commissure see section 2.1.4) whereas the posterior limb separates the PU and the pallidum from the body and tail of the CD and the thalamus (see section 2.1.4). Although the internal capsule separates the CD and PU, the two structures are linked through grey matter cell bridges (figure 2.6). The NAC is situated rostral to the anterior commissure, ventral to the internal capsule, where the PU and CD are joined. Anatomically, the NAC consists of the shell and the core and together with the anterior ventromedial CD and PU it comprises the ventral striatum (VST).

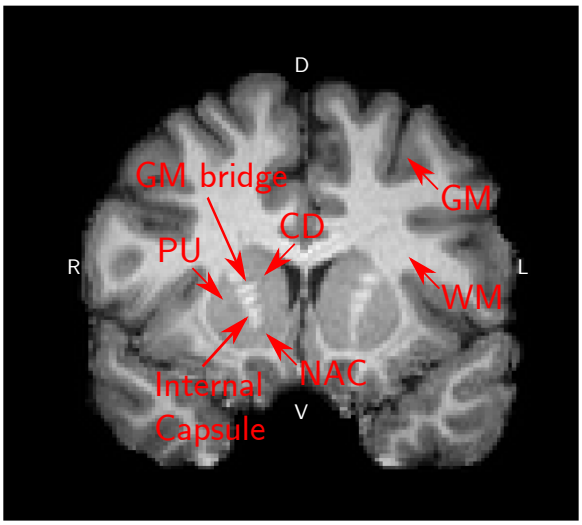

Figure 2.6: Anatomy of the striatum. A structural MRI image from a representative subject. CD: caudate; PU:putamen; NAC: nucleus accumbens; GM: grey matter; WM: white matter; R=right; L=left; D=dorsal; V=ventral.

The pallidum together with the PU are known as the lenticular nucleus. The pallidum consists of the ventral pallidum (VP) and the globus pallidus (GP) which is further subdivided into the internal segment (GP_i) and the external sement (GP_e). The GP is separated from the VP by a white matter bundle, the anterior commissure. The subthalamic nucleus is the least studied structure of the BG complex, and its function is not fully understood. As its name suggests it is located ventral to the thalamus and dorsal to the substantia nigra.

The BG nuclei receive projections from the cortex and brainstem and are related to a variety of functions. At first, the BG were considered primarily a motor structure, which along with the cortex, plan and coordinate motor functions. The projections they receive from cognitive and limbic regions together with findings from functional and lesion studies, indicate that the BG also plays a central role in cognition, motivation and emotion. The incoming information in the BG is processed in a dually organised system permitting both parallel and integrative information processing [73, 141]. The parallel processing hypothesis assumes that functional information from distinct cortical areas is processed independently while, on the other hand, the integrative hypothesis assumes that functional information from distinct cortical areas is converging and integrated in the BG [73, 141]. Recently, popular theories have implicated the BG in action selection, that is, the BG would be the arbiter of which of several possible behaviours is executed at a given time.

BG dysfunction is implicated in several neurological and psychiatric disorders including Parkinson's disease, schizophrenia, Huntington's disease, obsessive–compulsive disorder, major depressive disorder etc. Damage to the neuronal projections to the BG or neuronal losses within the BG itself may cause problems with the control of speech, movement, posture, memory, behavioural and cognitive function.

Diencephalon

The diencephalon consists of the thalamus and hypothalamus. The thalamus receives information from the BG and, in turn, sends signals back to the cortex. Anatomically, it is subdivided into cytoarchitectonically discrete nuclei that can also be approached from a functional perspective, as they have distinct connections. The thalamus is involved in numerous functions including learning, memory, emotions, cognition, movement planning and sensory integration.

The hypothalamus has a crucial role in processing the information from the autonomic nervous system and producing the behaviours necessary for the survival, such as drinking and feeding. In addition, the hypothalamus integrates emotional information and visceral and environmental stimuli in order to organise the body's response and control the secretion of hormones. Anatomically, the hypothalamus consists of numerous small nuclei located in the periphery of the third ventricle.

Commissures

The two hemispheres of the brain are connected through three white matter bundles, termed the commissures. The largest commissure in the human brain is the corpus callosum and it is subdivided into the rostrum, genu, body and splenium. The corpus callosum connects mainly the cortical lobes of the two hemispheres. The other two white matter bundles, which are substantially smaller, are the anterior commissure and posterior commissure. The anterior commissure connects the temporal lobes and the amygdala while the posterior commissure connects the mesencephalon and diencephalon.

2.2 Neuroanatomy

2.2.1 Neuron

The neurones and the glial are the functional units of the CNS. Neurones respond to stimuli, by generating electrical impulses called action potentials, which are propagated throughout the neurone and along its axon. Anatomically, a neurone consists of the dendrite, the cell body or soma, the axon and the axon terminals (figure 2.7). The dendrites and the cell body, are the receptive components of a neurone. The cell body also processes the received signals, which in turn are conducted through the axon to the axon terminals. In most neurones, the axon is intermittently covered by a lipid-rich membrane, the myelin sheath. The myelin sheath, provides electrical isolation for the axon and, in conjunction with the nodes of Ranvier (gaps where the axon is not covered with myelin sheath) help the action potentials to propagate faster, more effectively, and travel long distances. The axon of the neurone, excluding electrical signals, transports material from the cell body to the axon terminals (anterograde transport) and from the axon terminals back to the soma (retrograde transport). Depending on their functionality, neurones vary in size, shape and complexity.

The glial cells constitute about 85% of brain cells and they play an important role in supporting the neurones, structurally and metabolically. Glial cells are classified into either microglia or macroglia. Microglia respond to infections of the nervous system by destroying invading microorganisms, removing debris and promoting tissue repair [124]. Macroglia consist of three different cell types that have different support and nutritive functions: the oligodendrocytes, astrocytes and ependymal cells. Briefly, the oligodendrocytes form the myelin sheath, the astrocytes, the most abundant cells in the human brain, have important structural and metabolic functions and the ependymal cells cover the fluid-filled cavities of the nervous system and regulate the flow of

chemicals from these cavities.

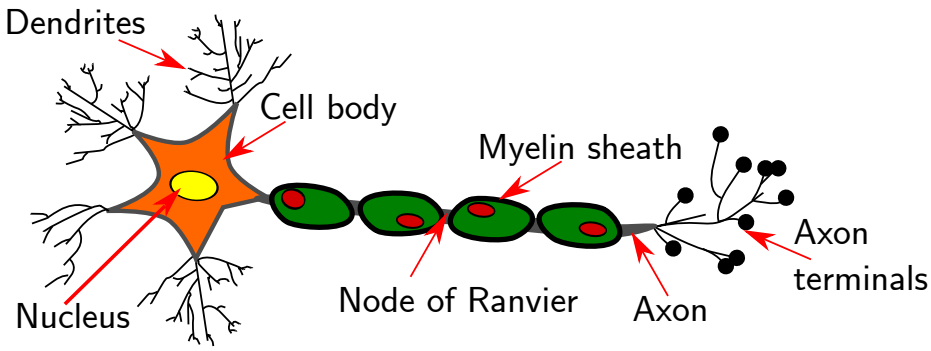

Figure 2.7: The structure of a neurone. A neurone comprises of a cell body, multiple dendrites, an axon and axon terminals

In the brain, the areas that predominately contain cell bodies of the neurones and glial are termed grey matter, whereas the regions that predominately contains the myelinated neuronal axons constitutes the white matter (figure 2.6). The white appearance of white matter is due to the presence of the myelin sheath that surrounds the axons of the brain.

2.2.2 Synapse

A synapse is the intercellular area between neurones where signals are propagated and this permits neurones to communicate (figure 2.8). The synapse consists of three elements: a) the pre-synaptic terminal; b) the synaptic cleft; and c) the post-synaptic neurone. There are two classes of synapses. The first class is the electrical synapse where the neurones communicate with a direct flow of electrical current from the presynaptic neurone to the postsynaptic dendrite. The second class is the chemical synapse and this constitutes the majority of synapses found in the human brain. In the chemical synapse, the neurones communicate via the release of chemical agents called neurotransmitters. On arrival of an action potential to the axon's terminal, the pre-synaptic ending is depolarised and in turn, the neurotransmitters that are stored in the synaptic vesicles of the pre-synaptic neurone are released in the synaptic cleft

and these bind to the post-synaptic receptors. This chemical signal, upon binding, is converted into an electrical signal post-synaptically, which can depolarise (excitatory post-synaptic potentials) or hyperpolarise (inhibitory post-synaptic potentials) the neurone.

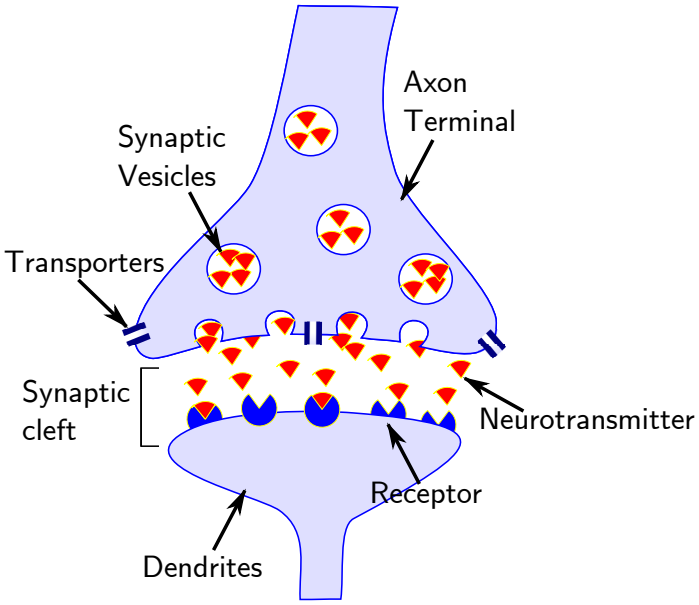

Figure 2.8: Neurotransmission at a synapse.

2.2.3 Neurotransmitters

Neurones in the human brain communicate with each other, for the most part, by releasing chemical messengers called neurotransmitters. Acetylcholine was the first neurotransmitter that was identified and the early criteria for a chemical to be classified as a neurotransmitter, were based on acetylcholine. However, new findings that suggest that neurones can also communicate via their cell bodies, axons and dendrites has put this definition under question. It is broadly accepted that a neurotransmitter is a chemical molecule that exhibits two types of physiological action on the target cell: a) opening or closing of ion channels (fast action) and b) metabolic alteration of the target cell (slow action). However, a more liberal definition proposed by Cowan [40] states that "a transmitter is a molecule, released by neurones or glia, that phys-

iologically influences the electrochemical state of adjacent cells". Presently, we know of at least 100 neurotransmitters belonging to diverse chemical classes including the biogenic amines, amino acids, gases and peptides [40]. Some neurones can release more than one neurotransmitter with the frequency of the stimulus, being the determining factor for the selection of the neurotransmitter to be released. Excitatory neurotransmitters depolarise the post-synaptic neurone and provoke the generation of action potentials. Glutamate, is the principal excitatory neurotransmitter and is found in the majority of brain synapses. Inhibitory neurotransmitters hyperpolarise the post-synaptic neurone and inhibit the generation of action potentials. GABA is the principal inhibitory neurotransmitter involving 25-30 % of brain synapses [40].

2.2.4 Receptors

Receptors are complex proteins that are located on the pre- and post-synaptic membranes of neurones or in the cytoplasm and are activated upon the binding of a molecule. A molecule that binds to a receptor is called a ligand and it can fully activate (agonist ligands) or partially activate (partial agonist ligands) the receptor or inhibit (antagonists) further biological responses. Receptors located on the presynaptic neurone are termed autoreceptors and they can affect the neuronal firing rate and regulate the synthesis and release of the neurotransmitter in response to changes in the extracellular neurotransmitter levels. A receptor can bind to only one neurotransmitter. However, a neurotransmitter can bind to many different receptors, inducing different biological effects upon activation of each receptor subtype.

2.3 Dopamine

Dopamine belongs to the catecholamines, a group of hormones or neurotransmitters produced by the amino acid tyrosine. Until the late 1960's the perception of dopamine was that it serves as a precursor for the other two catecholamines, epinephrine (adrenaline) and norepinephrine (noradrenalin). At that time, Arvid

Carlson made the seminal discovery that dopamine is a neurotransmitter in its own right. For his work on dopamine and its effects on Parkinson's disease Carlson received the 2000 Nobel prize in physiology and medicine.

In the last thirty years dopamine has been extensively studied and this research has advanced our understanding of this complex system in both the normal and diseased brain. Dopamine exerts its myriad of actions on the neurones it innervates, both directly and via dopamine receptors. Dopamine controls pleasurable reward, cognition, attention and emotions and also regulates movements. Abnormalities of the neurotransmitter itself, or its receptors, contribute to a wide range of psychiatric and neurological disorders such as Parkinson's disease and schizophrenia, where one or more of the aforementioned functions are impaired.

2.3.1 Dopamine synthesis and release

The synthesis of dopamine begins with tyrosine, which is synthesised in the liver by phenylalanine and is also found abundantly in dietary proteins. Tyrosine crosses the blood brain barrier and subsequently is transported into the dopaminergic neurones where it is converted to the dopamine precursor levodopa (L-DOPA) by the cytosolic enzyme tyrosine hydroxilase, the main enzyme that can limit dopamine synthesis. Dopamine is formed by the decarboxylation of L-DOPA and after its synthesis is either converted to norepinephrine by the enzyme called dopamine β-hydroylase or it is stored in the synaptic vesicles for subsequent release. Upon the arrival of an action potential in a dopaminergic neurone dopamine is released in the synaptic cleft where it can bind post-synaptically to dopamine receptors or pre-synaptically to the autoreceptors and/or the membrane dopamine transporters (DAT). The presynaptic binding sites (autoreceptors and membrane transporters) are responsible for regulating dopamine release and synthesis.

2.3.2 Dopamine transporter

After the synthesis and release of dopamine in the synaptic cleft, neurotransmission is terminated by the re-uptake of dopamine back into the cytosol through the dopamine transporter (DAT). Through this mechanism, DAT, regulates the synaptic concentration of dopamine and the level of dopamine receptor activation. However, the uptake mechanisms of DAT can be reversed, enabling transportation of dopamine in both directions. For example, it is believed that amphetamine binds to DAT and stimulates the release of dopamine into the synaptic cleft. Moreover, DAT, has been implicated in the reinforcing actions of psychostimulants, such as cocaine, which bind to DAT with high affinity and block the re-uptake process. In the human brain, DAT was found in areas with established dopaminergic circuitry and with a dense and heterogeneous distribution in the striatum [38].

2.3.3 Dopamine receptors

Dopamine exerts its actions through at least five distinct but closely related G protein-coupled receptors (GPCRs) that are categorised into two families, the D1-like family and the D2-like family, on the basis of biochemical and pharmacological (i.e preferential affinity to agonists and antagonists) evidence. The D1-like family comprises the D1R and D5R and activates the enzyme adenylate cyclase. The D2-like family exerts an inhibitory influence on adenylate cyclase and consists of the D2R, D3R and D4R.

The D1R is the most widespread dopamine receptor and is expressed at higher levels than any other dopamine receptor [133]. D1R mRNA is distributed in the striatum, thalamus, hypothalamus and in cortical regions. The second member of the D1-like family, the D5R, is found at considerably lower levels than the D1R and it is predominately localised in the hippocampus and hypothalamus, and at lower levels in the striatum.

The D2R are found in brain regions that receive major dopaminergic projections. The highest density of D2R mRNA is detected in the caudate, putamen and nucleus accumbens. D2R mRNA is also found in dopaminergic cell bodies in the mesencephalon, suggesting a presynaptic as well as postsynaptic role for the D2R. D2R are also found, at lower concentrations, in the frontal cortex, cingulate cortex, amygdala, hippocampus and temporal lobe [133, 130, 131].

Regional analysis of the D3R and D4R sites indicates that these receptors are at lower concentrations and are more narrowly distributed in comparison to the D2R sites. D3R mRNA is expressed predominantly in the nucleus accumbens, pallidum and hypothalamus and at considerably lower levels in the caudate and putamen. The D3R were also found, at low expression levels, in the hippocampus and cortical subregions of the medial temporal lobe [27, 166]. Like the D2R, the D3R, are also found in the substantia nigra and ventral tegmental area, a finding that indicates that D3R are also autoreceptors, serving as feedback for the regulation of dopamine synthesis and dopamine release. D4R is highly expressed in the frontal lobe, amygdala, hypothalamus, hippocampus and mesencephalon, with lower concentrations found in the striatum.

The D2R and D3R types exist in interconvertible states of low and high affinity for dopamine [122, 163]. However, the difference in affinity of dopamine for the two states of the D3R is similar and it is justifiable to consider them as the same [163]. Dopamine demonstrates a different preferential affinity for each receptor subtype. Specifically, for the D1-like family, dopamine has a higher affinity for the D5R [172] whereas with regard to the D2-like family, dopamine has higher selectivity for the D3R, followed by the D2R^{high} and the D2R^{low}.

Through these receptor subtypes dopamine exerts different functions. Specifically, the D1R and the D2R interact to determine locomotion, whereas the D3R inhibit locomotion [87, 168]. The D1R and D2R mediate learning and memory and are also involved in the reinforcing effects elicited by addictive drugs. More specifically, the D2R initiate the reinforcing effects and the D1R plays a permissive role [133]. The D2R are also thought to have a central role in psychosis as the clinically effective antipsychotics block these receptors. The regional distribution of the D3R has led to the hypothesis that they mediate dopaminergic control of limbic and executive functions [164]. Nevertheless, the specific functional role of the D3R, and of the D4R and D5R, remains largely unknown.

2.3.4 Dopamine Pathways

The dopaminergic cells are located in the mesencephalon (SN and VTA), and in the hypothalamus. The axons of the dopamine cells are organised into four pathways, namely the nigrostriatal, mesolimbic, mesocortical and tuberoinfundibular. The nigrostriatal pathway originates in the SN and innervates the CD and PU. This pathway is thought to be involved in movement disorders such as Parkinson's disease. The neurones of the mesolimbic pathway have their soma in the VTA and project to the VST, amygala and hippocampus. This pathway is involved in reward and addiction. The mesocortical pathway transmits dopamine from the VTA to the prefrontal cortex and is involved in motivational and emotional responses. Finally, the tuberoinfundibular pathway originates from cells located in the hypothalamus and transmits dopamine to the pituitary gland, regulating the secretion of prolactin. Figure 2.9 shows the three dopaminergic pathways that originate from the mesencephalon.

2.4 Amphetamine

Amphetamine was discovered at the end of the 19th century and was used as a drug for the treatment of sleep disorders such as narcolepsy and attention-deficit

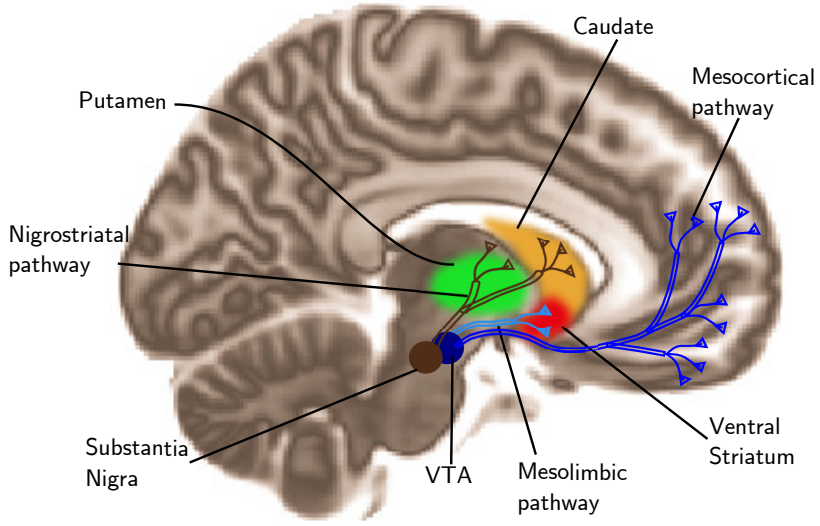

Figure 2.9: Dopaminergic pathways that originate from the mesencephalon

hyperactivity disorder. However, due to its addictive nature, it was classified as a schedule II drug by the United Nations in 1971. A schedule II drug is classified as one that has a high potential for abuse, has a currently-accepted medical use, is used under severe restrictions, and has a high possibility of severe psychological and physiological dependence (www.drugs-forum.com). In molecular imaging research, amphetamine is widely used as a means to measure dopamine transmission in healthy and diseased cohorts. Amphetamine induces dopamine release by reverse transport of dopamine from the cytoplasmic pool to the synapse through the dopamine transporter DAT [111] and it has been shown that there is a dose dependent effect [113]. To characterise the effect of amphetamine in relation to the doses administered, two studies have been performed with simultaneous microdialysis and SPECT or PET imaging [29, 113]. Both studies elegantly demonstrated that a large increase in extracellular dopamine release is associated with a relatively small effect on the tracer's binding following amphetamine. Nevertheless, a linear correlation between microdialysis and receptor-ligand binding measurements was established which supports the usefulness of this paradigm in imaging studies in order to non-invasively assess dopamine release [111].

Chapter 3

Brain Imaging – MRI and PET

Medical imaging techniques such as PET and MRI have enabled the investigation of anatomy and function of the living human brain in both health and disease. MRI is an imaging modality that is sensitive to the magnetic properties of protons, which are in turn used to provide information about the anatomy and physiology of the human brain. MRI has a broad range of applications including high resolution imaging of anatomical information, the study of changing neuronal activity (functional MRI (fMRI)), the diffusion of water molecules in biological tissues (DWI) and the levels of different metabolites in body tissues (spectroscopy). The versatile information provided by MRI, combined with no known side effects from the use of the magnetic field, have rendered MRI as one of the most widely used imaging modalities. In contrast, PET does not have as good spatial resolution as MRI but its unique strength relies on the robust and well validated quantitative estimates of *in–vivo* function. PET uses the decay properties of positron-emitting radioactive biomolecules to map human brain function. From the very beginning of molecular imaging PET has been an integral tool for studying brain physiology and more recently for understanding pharmacokinetics and pharmacodynamics of CNS drugs in drug development, in addition to its heavy use in oncology and cardiology. During the last two decades there has been a tendency for PET-MRI multimodal imaging applications to increase as a result of the distinctive yet complementary information that these two imaging modalities provide.

Multimodal imaging is the sequential or simultaneous acquisition of two or more types of images of the same subject. Multimodal imaging has been made feasible either by the development of combined instrumentation or through the evolution of advanced image co-registration software. The first multimodal imaging instruments were PET/CT and SPECT/CT scanners, with the two modalities combined in a single gantry system to allow sequential image acquisition. SPECT (Single Photon Emission Computed Tomography) is an alternative molecular imaging modality that uses longer lived single photon emitting isotopes. It has lower sensitivity and resolution compared to PET. CT (Computed Tomography) is a diagnostic imaging modality that uses a combination of X-rays to produce detailed anatomical images of the body and the brain, although the soft tissue contrast in brain, is considerably lower than the contrast obtained by MRI. The strengths of PET and MRI modalities have recently led to the construction of hybrid PET/MRI systems that facilitate the simultaneous acquisition of both sets of images. Combining PET and MRI in one apparatus is challenging due to interferences of the magnetic field on the positron range and other technical problems, which in turn can compromise the capabilities and strengths of the two modalities in contrast to when they are used separately.

In this thesis we have used sequential multi-modal PET and MRI, acquired from different imaging equipment, to study dopamine *in–vivo*. In this chapter we introduce the basic principles of the two imaging modalities. At the end of this chapter we introduce image processing methods and in particular registration methods that have enabled the fusion of information obtained from the two modalities. Finally we give a brief review of different approaches for the segmentation of region of interest (ROI) in the human brain.

3.1 MRI

MRI began in 1946 and is widely used as a diagnostic tool as well as in clinical and preclinical research. MRI is based on findings from two independent groups (Bloch and Purcell groups [23, 148]) who demonstrated that nuclei with an odd number of protons have an intrinsic magnetic moment and when placed in an external magnetic field (B_0), they tend to line up with that field and precess with a frequency proportional to the (B_0). An MRI scanner establishes a homogeneous B0 field within the scanner bore, and it is into this bore that the subject is placed when they are being scanned.

For full body human MRI scanners, the B_0 ranges from 0.5 T to 7 T with the 3T being the most widely used for research and the 1.5T for clinical applications. 7T scanners have been recently introduced and at the moment are mainly used for research with a limited number of clinical applications. The advantage of the 7T scanner is the high signal to noise (SNR) and contrast to noise (CNR) ratios. The high magnetic field benefits MRI spectroscopy, functional MRI and techniques that exploit susceptibility induced contrast [180]. In the following sections we introduce the basic principles of MRI, we present structural and diffusion MRI and we discuss tractography methods.

3.1.1 Basic principles of Magnetic Resonance Imaging

Nuclei with odd numbers of protons have an intrinsic magnetic moment, which is associated with the quantum spin property of the nucleus. Only these nuclei can be used for MRI as nuclei with even numbers of protons do not have a net magnetic field since their protons are paired and they effectively cancel each others magnetisation. Hydrogen is the atom that is mainly used for MRI due to its abundance in the human body. When the patient is placed in the MRI scanner, the magnetic moment of the nucleus tends to align with B_0, giving rise to a net magnetisation (M_0), which is

proportional to the number of hydrogen atoms. The net magnetisation precesses about the axis of the B_0 at a rate expressed by the *Larmor equation*:

$$\omega = \gamma \, B_0 \tag{3.1}$$

where γ is the gyromagnetic ratio, a constant characterising the nucleus under investigation, and B_0 is the strength of the external magnetic field. An RF pulse can then be used to perturb the alignment of the net magnetisation, by the application of a magnetic field, B_1, perpendicular to B_0. If the frequency of the RF pulse matches the precession frequency (equation 3.1) then a resonance occurs [31]. The net magnetisation precesses about the new net magnetic field (vector sum of B_0 and B_1) and upon termination of the RF pulse the net magnetisation slowly returns to its original alignment (relaxation). The precession of the net magnetisation in the transverse plane produces the signal that is measured by the MRI scanner. The measured signal is a function of, the density of the protons and of the two relaxation constants, T1 and T2. The T1 and T2 vary according to tissue type and are used to construct images that provide different types of tissue contrast.

In addition to tissue contrast, MRI can produce signal intensities that depend on other properties such as the diffusion of water molecules (diffusion MRI) and local blood oxygen-level depended changes (fMRI). Other MRI sequences include MRI angiography, that produces images of the blood vessels (figure 3.1, bottom left image), inversion-recovery pulse sequences, which are used to null signal from selected substances such as fluids (FLAIR sequence) or white matter (FGATIR sequence), susceptibility-weighted sequences, which measure the susceptibility differences (degree of magnetisation in response to an external magnetic field) between tissues, and many others.

3.1.2 Structural MRI

As mentioned above, one of the most important advantages of MRI over the other imaging modalities is the high spatial resolution and its ability to provide versatile soft tissue contrast. For structural imaging, tissue properties such as T1, T2 and proton density along with the pulse sequence determine the MRI signal and the fact that the properties are different in different tissues gives rise to tissue contrast. Tissue contrasts, are otherwise termed tissue "weighting". For instance, the T1-weighted image shows differences in the T1 relaxation time. T1 is the longitudinal relaxation time and refers to a time constant that characterises the required time for the net magnetisation to realign back to the external magnetic field. The T1-weighted images provide a good contrast between the white matter, grey matter and CSF. On a typical T1-weighted image (figures 2.6, 3.1 bottom left) the bright areas (high intensity) correspond to the white matter, the intermediate intensities to the grey matter and the nearly black areas to the CSF. T1-weighted is the standard structural image modality acquired of gross visualisation of the brain anatomy. In this thesis the T1-weighted images are employed for the delineation of the cortical and subcortical ROIs. In addition due to the high contrast between the white matter, grey matter and CSF the T1-weighted images are also employed to segment the brain into these components, to enable the image registration (see section 3.3.1) across or within subjects or to the MNI brain template (http://www2.bic.mni.mcgill.ca/).

Other parameters of interest are the transverse magnetisation time constant, T2, and time constant T2*. The T2-weighted image depicts CSF as bright whereas white matter is darker than the grey matter. This MRI sequence is particularly useful for imaging pathology, such as edema. The T2* reflects variations in both B_0 and local magnetic field inhomogeneities in the tissue. The proton density (PD-weighted) sequence detects the signal that comes from differences in the amount of available

spins, which is generally proportional, in the brain, to the density of water (figure 3.1). PD-weighted images provide good depiction of anatomical regions, such as the SN, which are not shown on the standard T1-weighted images. Here the PD-weighted images are used to provide information about the location and the size of the SN region.

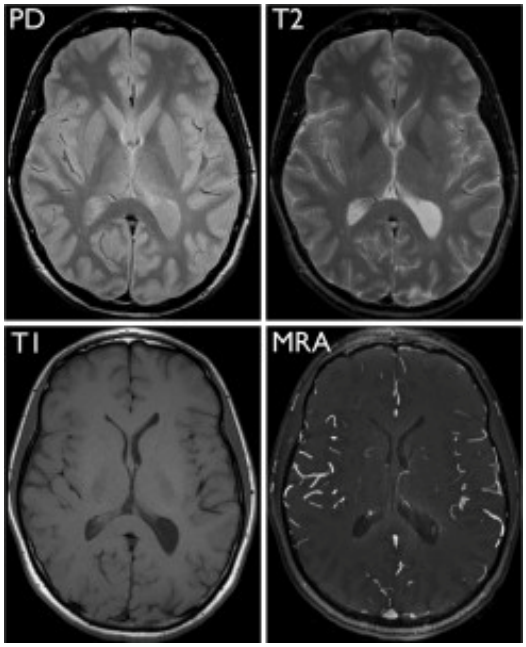

Figure 3.1: MRI images, with different contrasts, acquired at the same level in the same volunteer. Proton density (PD, top left), T1-weighted (T1, bottom left), T2-weighted (T2, top right), and MR angiography (MRA, bottom right). Image courtesy of http://blog.radiology.ucsf.edu/

3.1.3 Diffusion MR imaging

Diffusion is the random motion of molecules due to their thermal energy, which occurs even in thermodynamic equilibrium. This perpetual motion of the molecules, which results in mass transport, is termed Brownian motion and is named after Robert Brown, a botanist who first reported this motion. Einstein, reportedly unaware of Brown's research, determined how far a particle travels in a given time interval.

According to Einstein, the mean square displacement of a molecule in a homogeneous material, due to its Brownian motion, is given by:

$$\langle \chi^2 \rangle = 2\,D\,\tau \tag{3.2}$$

where $\langle \chi^2 \rangle$ is the mean square displacement, D is the diffusion coefficient, and τ the elapsed time.

Diffusion imaging is an *in–vivo* technique that allows quantitative assessment of diffusion processes in biological systems. In a homogeneous substance, molecules move along the three dimensions isotropically. In a biological tissue, the diffusivity of the substance along a certain direction or directions can be restricted or completely blocked due to the present of hindrances including cell membranes and macromolecules. Diffusion imaging can detect and quantify this anisotropy in the diffusion of the molecules within the tissue and can therefore give information about the biological microstructure.

The ability of MRI to probe the structural environment of biological tissues was first recognised by Edwin Hahn [79]. Hahn reported reduction of the measured MRI signal, which was attributed to dephasing of the spins due to translational diffusion. Since then MRI sequences have been developed to be sensitive and able to record the diffusion of molecules. These MRI sequences can detect translational motion, by utilising additional magnetic gradients. These diffusion encoding gradients make the MRI signal sensitive to water diffusion.

As mentioned above, according to the Larmor equation 3.1 the precessional frequency is proportional to strength of the magnetic field. After a given time, spins will acquire a certain phase depending on their location. Typically, this phase is reversed

by application of a gradient of the same magnitude but of opposite polarity [91]. If the molecules remain at the same position the net phase will be zero. However, if the molecules move, they will experience a different magnetic field and will precess at a different frequency according to equation 3.1. This will result in a net phase change that will depend on net displacement [94]. Since diffusion is a random translational motion, the molecules will experience differential displacements and therefore a distribution of phases, which leads to a loss of signal coherence and therefore a reduction of signal magnitude [94]. The reduction of the signal is proportional to the apparent diffusion coefficient but is only sensitive to molecular displacements along the direction of the gradient. Therefore, anisotropic diffusion can be detected by observing variations in the diffusion signal when the direction of the diffusion encoding gradients is changed [114]. The change of the MRI signal due to the diffusion is given by:

$$\frac{I_2}{I_1} = exp(-b\,ADC)) \tag{3.3}$$

where b is the "b-value", which is proportional to the square of the gradient strength and the duration of the gradient pulse and characterises the level of sensitivity to diffusion. ADC is the apparent diffusion coefficient, an estimate of the theoretical diffusion coefficient (equation 3.2). I_1 is the MRI signal intensity when no diffusion encoding gradient is applied (i.e. b-value =0) whereas I_2 is the MRI signal measured when a diffusion encoding gradient is applied ($b - value \neq 0$). Thus, to quantify the diffusion at least two signal measurements are required; normally one without gradient and one with an applied gradient.

Figure 3.2 shows diffusion–weighted images of a human brain in which the diffusion encoding gradient changes direction. In areas where the signal remains unchanged the ADC is equal along all directions, and diffusion in that area is isotropic. Dark

areas have high ADC whereas bright areas have low ADC.

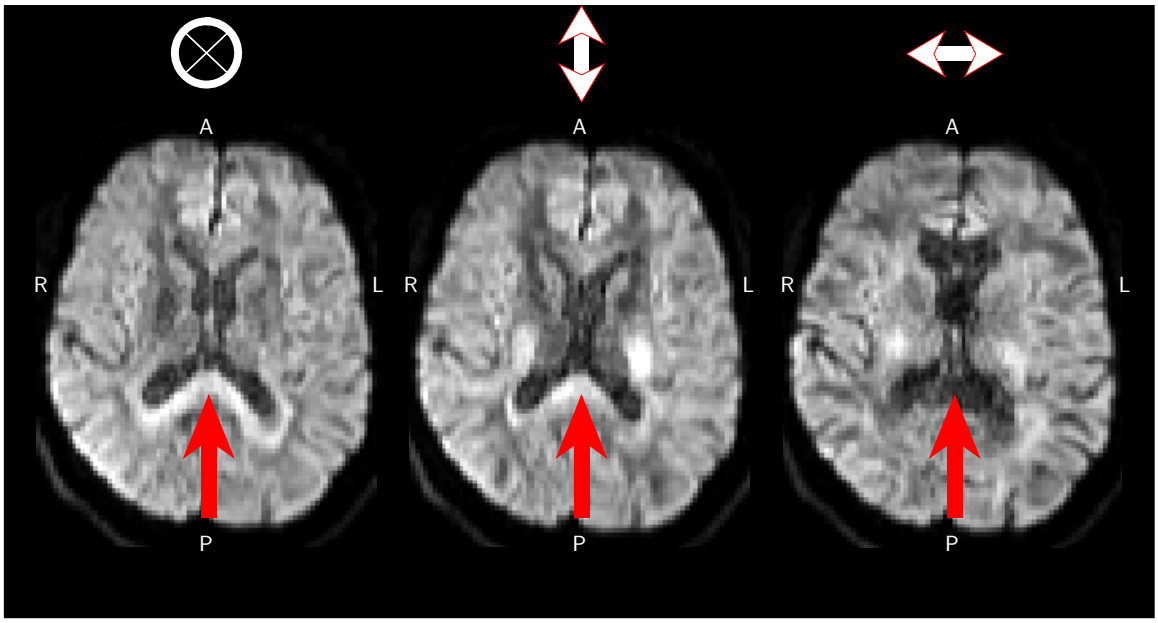

Figure 3.2: Effect of diffusion gradients on the diffusion weighted signal in a single subject. The arrows at the top of the figure show the direction of the gradient. The red arrows show the splenium of the corpus callosum. Dark areas have high apparent diffusion coefficient (ADC) whereas bright areas have low ADC. R=right; L=left; A=anterior; P=posterior

Since the measured ADC depends on the direction, the introduction of a model that can characterise diffusion in 3D was essential. The diffusion tensor model was introduced (equation 3.4), and assumes that diffusivity in different directions is not uniform. In short, this model is a symmetric matrix that characterises the ADC in 3D [94].

$$D = \begin{bmatrix} D_{xx} & D_{xy} & D_{xz} \\ D_{xy} & D_{yy} & D_{yz} \\ D_{xz} & D_{yz} & D_{zz} \end{bmatrix} \tag{3.4}$$

The diagonal elements of the tensor matrix correspond to diffusion displacements along the x, y and z axis, whereas the off-diagonal elements correspond to the correlation between displacements along those orthogonal axes [94]. However, the estimation

of ADCs along the principal axes of a local coordinate system (local tissue fiber tract orientation) are of interest. Therefore, the diffusion tensor could be diagonalised and its diagonal elements, which correspond to the three diffusivities along the principle axes, are calculated. These values are termed eigenvalues (λ_1, λ_2, λ_3) and the orientation of the principle axes eigenvectors (ε_1, ε_2, ε_3). The largest eigenvalue corresponds to the principal eigenvector, which in turn corresponds to the orientation of the tensor and is typically associated with the principal fibre orientation of the underlying tissue structure. Therefore, the diffusion tensor determines both the magnitude of the diffusion anisotropy and the likely orientation of the principle fibre [37].

A number of diffusion-relevant scalar magnitudes can be estimated from the diffusion tensor. The most widely used measures are the mean diffusivity (MD) and the fractional anisotropy (FA). These measures are given by the following equations:

$$MD = \frac{D_{xx} + D_{yy} + D_{zz}}{3} = \frac{\lambda_1 + \lambda_2 + \lambda_3}{3} \tag{3.5}$$

$$FA = \sqrt{\frac{3\sum_{i=1}^{3}\left(\lambda_i - \bar{\lambda}\right)^2}{2\sum_{i=1}^{3}\lambda_i^2}} \tag{3.6}$$

FA is zero (0) for isotropic diffusion ($\lambda_1 = \lambda_2 = \lambda_3$) and one (1) for anisotropic diffusion ($\lambda_1 \neq 0$, $\lambda_2 = \lambda_3 = 0$). Figure 3.3 shows three diffusion tensor derived images.

Diffusion image artefacts

In diffusion MRI there are physiological noise and system-related artefacts that contribute to bias and variability in the diffusion MRI measurements. Physiological noise includes head motion and cardiac pulsation. Head motion can be minimised by ensuring that the patient is comfortable and padded appropriately during image acquisition

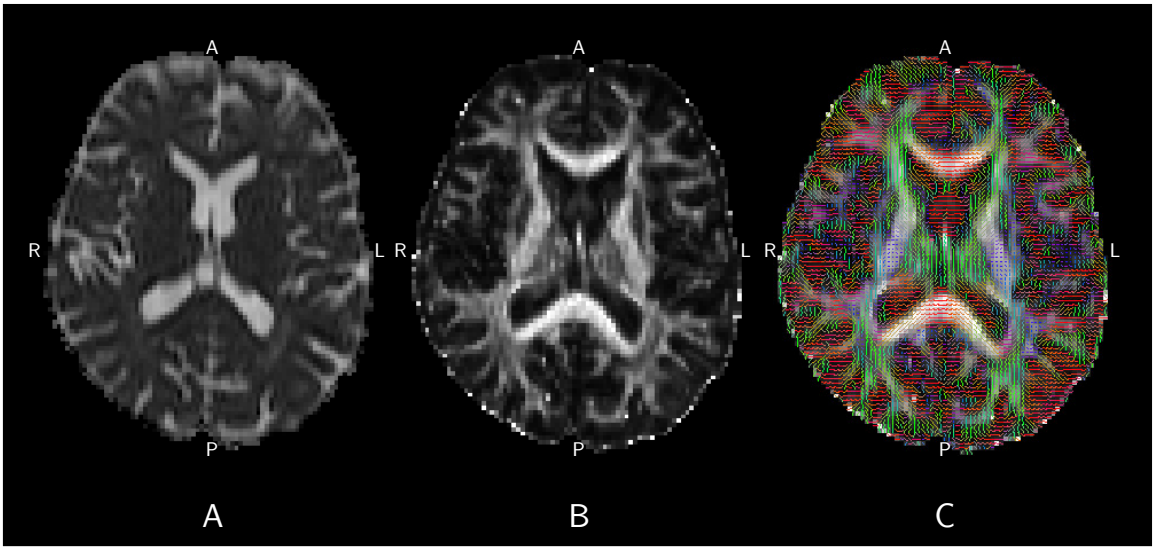

Figure 3.3: Diffusion tensor derived images in a single subject. A) mean diffusitivity, B) fractional anisotropy and C) the principle tensor eigenvector overlaid on a fractional anisotropy image. The latter is colour-encoded by orientation. Left-right is shown in red, anterior-posterior in green and ventral-dorsal in blue. R=right; L=left; A=anterior; P=posterior

and also can be rectified post acquisition by realignment of the 4D diffusion data using registration methods (for registration see section 3.3.1). Cardiac pulsation during the systolic part of the cardiac cycle causes pulsation of the brain which results in signal loss (signal dropout) that is particularly prominent in certain regions such as the mesencephalon, ventricles and other regions that are at the interface between tissue and CSF. Cardiac pulsation affects the tensor parameters (eigenvalues, eigenvectors) and diffusion tensor-derived images due to the corruption of the DWI images by the signal dropouts and due to local mis-registration from the brain moving during the cardiac cycle [95]. Cardiac pulsation effects can be partially controlled or limited by triggering the acquisition from the heart cycle of the subject (cardiac gating) or by removing the artifactual data [95, 94].

System-related artefacts affect significantly, the diffusion tensor and the estimated ADC. These artefacts result in geometrical or intensity distortions that are caused by inhomogeneities of the static B_0, concomitant fields, or due to eddy currents [95]. Im-

age distortion is the misplacement of signal as the assumption of a linear relationship between frequency and position is violated due to magnetic field inhomogeneities. In diffusion imaging, large and rapidly changing magnetic field gradients are used, which give rise to eddy currents that in turn produce unwanted magnetic fields. Eddy current-induced distortions are different for different gradient directions and result in mis-registrations within the DWI data sets. One approach to correct eddy current distortions is to register (see section 3.3.1) the diffusion data to a reference non-diffusion image. According to Pierpaoli [95], eddy currents contribute also to additional diffusion sensitisation, which is impractical to quantify and correct, and therefore is not accounted for in the calculation of the b-value.

Geometric distortions due to B_0 inhomogeneities or concomitant fields, degrade the anatomy of the image but they do not introduce major errors in the estimation of diffusion parameters. This is due to the fact that each voxel has the same, or similar, B_0-induced distortion in each acquisition, although the distortions are very different at different points in space, and signal intensities used to compute the tensor at that location are scaled by the same factor [95]. However, it is important to correct for these distortions as it is important to have anatomical correspondence with structural data and also because they can potentially affect diffusion-based tractography. Although uncorrected data will have the correct fiber orientation at each voxel the estimated fiber trajectories (see section 3.1.3) will be anatomically incorrect. One efficacious approach to correct these distortions is the acquisition of two DWI data sets with their gradients reversed (i.e blip-up – blip-down) [10, 35]. The two DWI data sets will have distortions of equal magnitude but in opposite directions. This method allows the distorted signal to be corrected as the displacement can be calculated from the two data sets.

During the acquisition of all data in this thesis, to avoid or minimise the aforementioned artefacts, the volunteer's head was constrained and brain volumes were realigned post-acquisition in order to minimise the motion artefacts. Software components from the FSL llibrary [90] were used to correct for eddy currents and geometric distortions. The corrections aim to improve the diffusion tensor fit, the DWI -derived quantitative estimates and the anatomical correspondence between the DWI and structural MRI images.

Diffusion tractography

Diffusion-based tractography identifies white matter pathways in the human brain and enables studying of the human brain connections *in–vivo*. Before the development of diffusion-tractography methods, neuronal connections were studied only in non-human primates with tracing techniques. Tracing studies enable the visualisation of the axonal transport of a tracer from (anterograde) or towards (retrograde) a neurone's cell body, and are informative about the neuronal connections between brain regions. This is an invasive procedure which necessitates the sacrifice of the animal and therefore is not applicable to humans. On the contrary, diffusion-based tractography, is a non-invasive method that obtains information from the diffusion MRI images. Specifically, diffusion-based tractography estimates 3D white matter fiber tracts, by incorporating information from the preferred diffusion direction of water molecules from a starting or "seed" region. The main assumption that underpins tractography is that the direction of the principal eigenvector within a voxel is aligned with the orientation of the white matter bundle [37]. In order to reconstruct the white matter bundles or estimate the connectivity profile of an area there are numerous algorithms and tractography approaches can be classified into two categories, deterministic or probabilistic.

In deterministic tractography, a white matter tract or a streamline is generated by connecting adjacent voxels on the basis of the best estimates of the underlying fiber orientation. The criteria that two voxels are to be connected in order to form a streamline are: a) adjacent voxels whose principal diffusion directions form an angle smaller than a predetermined value (curvature threshold); and b) adjacent voxels whose anisotropy value is higher than a predetermined value (anisotropy threshold). If the angle is bigger or the anisotropy is smaller than the predetermined threshold the streamline is terminated or rejected. Figure 3.4 shows an example of a streamline defined with a deterministic tractography method. Deterministic tractography has been successfully used to identify and delineate major white matter pathways. However, prior anatomical knowledge of the pathway is necessary in order to perform the *in–vivo* identification of a white matter bundle. Normally, two anatomical ROIs are given and only streamlines that pass through these ROIs are retained. One weakness of deterministic tractography methods is that errors accumulate along the streamline and it is therefore likely to reconstruct white matter pathways that are less anatomically meaningful.

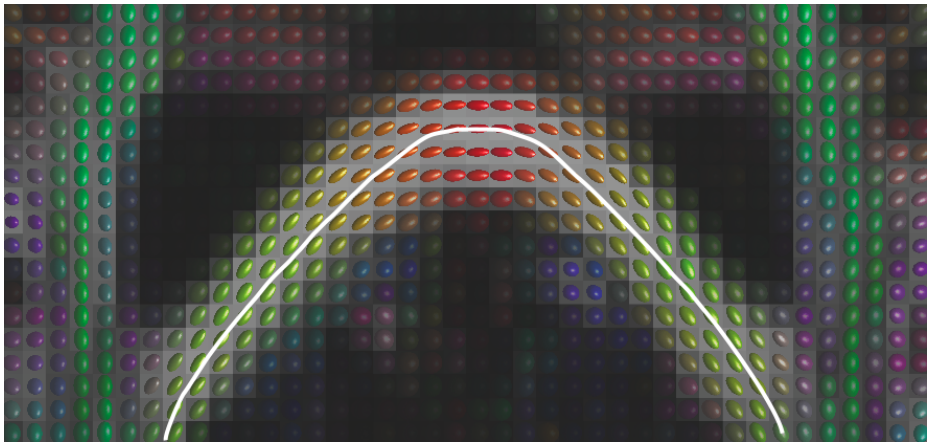

Figure 3.4: Diffusion image showing the diffusion tensor at each voxel. The long axis of each tensor shows the direction of the principal eigenvector. The white line shows a streamline obtained by connecting a set of pixels based on the principle diffusion directions. Image courtesy of www.humanconnectome.org

Probabilistic tractography, on the other hand, estimates the uncertainty in fiber orientation, takes into account this uncertainty and, for a given pathway, provides the user with the "confidence level" they should have in the results together with information about the impact of potential errors. According to Behrens and colleagues [18] probabilistic tractography estimates represent the following: given the data and the model, I have x% confidence that the route of least hindrance to diffusion from seed point A passes through region B. Or, alternatively, it represents an assessment of the confidence in whether a pathway or a connection exists. In contrast to deterministic tractography, probabilistic tractography methods are able to track through regions of high uncertainty instead of terminating or rejecting pathways.

In probabilistic tractography we incorporate the uncertainty in the tracking process, and instead of discrete estimates of fiber orientation, probability density functions (PDFs) are estimated in order to capture the distribution of possible fiber orientations within each voxel [95]. Subsequently a deterministic approach, such as the streamline process, is run on the data multiple times with each streamline sampling, for each run, randomly from the PDF sample at each voxel [95]. This procedure will provide a quantitative indication of the confidence level that the trajectory exists and the degree of the dispersion.

Probabilistic tractography methods are robust to noise and therefore there is no need for stopping criteria as errant pathways will have low probability values. However, a curvature constraint can be applied in order to prevent samples tracking back on themselves and artificially increasing the probability values [18]. Accurate estimation of white matter fiber bundles depends on several factors and tractography methods are prone to errors. A major source of errors is image noise, which does not allow an accurate estimation of the principal diffusion direction. Another source that can

lead to tractography errors is the local complexity of the white matter anatomy itself. In a voxel that contains white matter there are numerous fiber bundles some of which might have different geometry or different configuration (fanning fibers). For example, within a voxel there might be crossing, bending or kissing fibers (figure 3.5), which can lead to a similar estimated oriented tensor. This, makes the identification, recovery and reconstruction of the correct pathways challenging as it is hard to distinguish between different fiber bundle geometries.

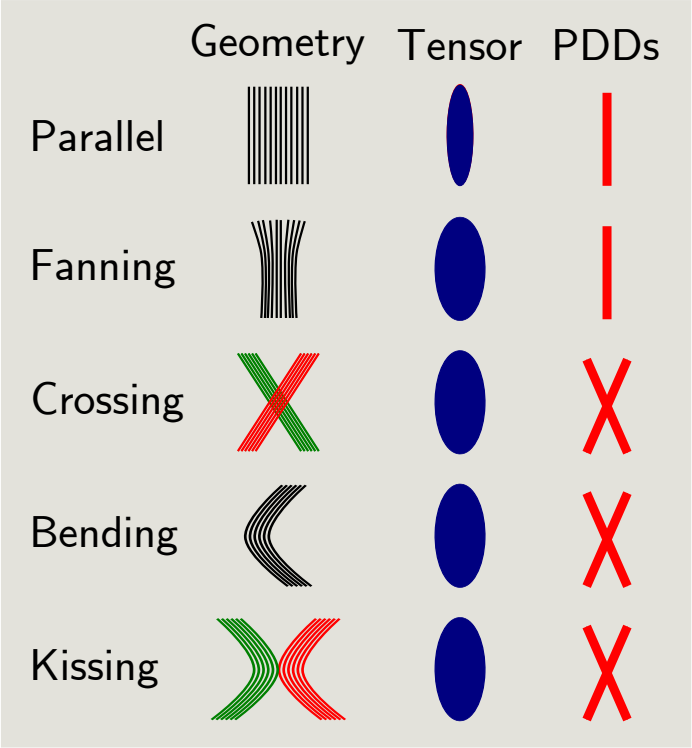

Figure 3.5: Fibre bundle geometries with the corresponding diffusion tensors and the principal diffusion directions (PDDs)

Several methods have been proposed in both deterministic and probabilistic tractography to allow modeling of more fiber bundle directions or models that can distinguish between crossing and spreading or fanning fibers in a given voxel. Although these techniques can improve the accuracy of the tractography the detailed geometry within a voxel remains ambiguous and the estimated pathway might still not

accurately represent the underlying ground truth [19, 88]. Nevertheless, the more complex algorithms, which model a number of principle directions, have improved substantially the qualitative tractography results, by revealing tracts unseen in simple models and reducing the amount of false negative connections [19]. Other fundamental limitations of tractography methods are that they are unable to determine the polarity/direction (afferent or efferent) of the fibre bundle and can not determine the termination points of the projections. If this information was available, could be potentially used to inform the tractography methods and improve the false negative and false positive results. In this thesis we have employed probabilistic tractography algorithms provided by the FSL software library [90]. The probabilistic method was chosen over a deterministic approach because of its advantages, which are mentioned above.

3.2 PET

PET is a molecular imaging technique that allows measurement of biochemical and physiological processes of the living body. PET is used as a diagnostic imaging tool in specialities including cardiology, oncology and neurology as well as in treatment planning and evaluation. Although it is an expensive imaging modality, its power to quantitatively characterise biological systems has established it as a powerful scientific tool in medicine and biology.

In PET, a radioactive molecule, termed radiotracer (or radioligand if it binds to a particular target), is injected into the subject. The radioligand distributes in the body of the subject and, assuming it can reach the relevant tissues, primarily concentrates in the tissue areas where the biochemical target manifests itself. A radioligand can target pre– or post–synaptic receptors, transporters, enzymes, glial cells and other molecules that are involved in protein synthesis and cell proliferation. It is the choice

of the labeled molecule that determines what can be imaged. The radioligand used for PET imaging emit positrons (β^+), which upon annihilation with an electron produces two collinear photons (γ-rays), which in turn, are recorded by the two independent detectors within the PET scanner. The location and the number of detected γ-rays is reconstructed into 3D images which inform about the distribution and the absolute concentration of the radioligand. Application of appropriate bio-mathematical models then permits quantification of the target itself.

There are two modes of PET data acquisition: static or dynamic. Static is the acquisition of a single PET frame. Static images are acquired in most clinical applications such as in oncology and neurology and will usually be of 10-30 min in duration. However, for a detailed and fully quantitative characterisation of the radioligands behaviour (uptake, metabolism, binding), dynamic data are required. A fully quantitative dynamic PET scan involves a scan duration of 60-120 min (for C11 and F18) and involves a series of consecutive temporal frames (20-40). Absolute quantification of the tracer also requires an appropriate input function. A plasma input function derived from arterial blood sampling during the scan is often treated as the gold standard but it is particularly invasive. Thus, much investigation has taken place to avoid arterial blood sampling whilst maintaining quantitative accuracy. Therefore, alternative analysis methods have been developed, which aimed to derive the input function from the reconstructed image data and from regions in the brain devoid of the target [24, 42]. In the following paragraphs we give a brief introduction of the basic PET physics, PET data correction and an overview of the methods for quantification.

3.2.1 PET physics

A PET radioligand constitutes a molecule, which is labelled with a positron emitting radioisotope. The PET isotopes are produced with a particle accelerator known as cyclotron and for brain imaging the most widely used are: ^{15}O (half-life: 2 min),

^{13}N (half-life: 10 min), ^{11}C (half-life: 20 min) and ^{18}F (half-life: 110 min). The radioligands decay by the process of positron emission. Each emitted positron travels a short distance before annihilating with a nearby electron. The travelling distance depends on the initial energy of the emitted positron and the surrounding material. According to the conservation of energy and momentum laws, the annihilation results in the instantaneous generation of two photons of equal energy (i.e. 511keV) travelling in opposite directions. PET detects such photon pairs occurring in a certain time window ("coincidence events"), and locates the origin of annihilation along the volume joining the two detectors, known as the Line of Response (LOR) (figure. 3.6).

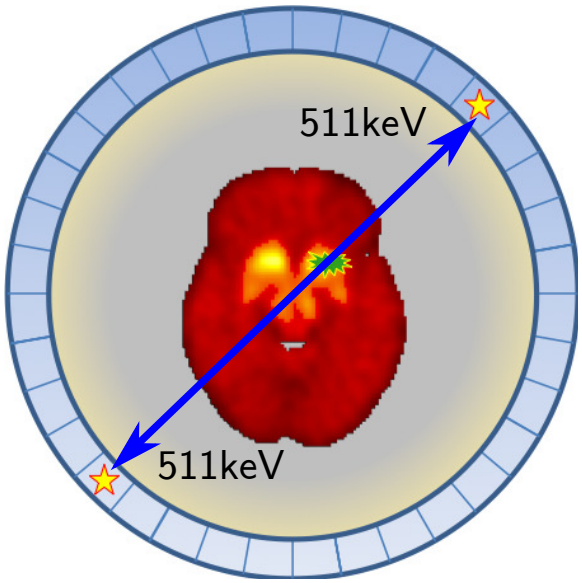

Figure 3.6: PET ring detectors record a pair of 511 keV photons emitted after annihilation. The two crystals that detect the photons define the line of response (LOR)

3.2.2 Data correction and image reconstruction

Several physical effects can occur, which result in inexact recordings of the "coincidence events", leading to a background noise and inaccurate quantification. A major source for such errors is the Compton scatter which accounts for up to 30 % of the discrepancies (figure 3.7). After the annihilation event the emitted photons may interact with the tissue and change direction (Compton scatter). This change in direction

will result in misplacement of the actual origin of the annihilation. Another source of noise comes from random coincidences (figure 3.7). Random coincidence events occur when a pair of photons are classified as a "coincidence event" but in fact the two photons are the product of two independent annihilations.

Another factor that affects the number of recorded events and hence the signal of PET is the attenuation effect. Attenuation is the effect where the photon is absorbed in the tissue before it reaches the detector. Attenuation is spatially varying and depends on the tissue density along the LOR and the distance the photon will have to travel to reach the detector. To correct for this, on modern PET-CT scanners, a CT scan is acquired and converted into an attenuation map that enables correction. All these sources of error (scatter, randoms and attenuation) are corrected for as part of the image reconstruction.

After recording the location of the true and apparent annihilations the data are processed to provide information about the spatiotemporal distribution of the radioligand. This process is termed image reconstruction. There are two types of reconstruction algorithms: analytic and iterative. The filter back projection (FBP) is an analytic algorithm that is widely used in neuroreceptor imaging, and has been used in this thesis for the reconstruction of the brain PET data as it does not compromise quantitative information and it is computationally fast. This reconstruction algorithm has the disadvantage of introducing streak artefacts at low signal to noise ratios (SNR). These artefacts can be reduced by filtering, which in turn, will reduce the image resolution. In the iterative reconstruction methods the image is constructed by an iterative optimisation procedure that estimates the image concentration that is most consistent with the acquired data. The advantage of this reconstruction method is that the images do not contain streak artefacts and look clearer [177]. However, the disadvantage is that after a number of iterations the noise becomes very prominent

especially in low SNR areas . Another disadvantage is the non-uniform resolution and convergence throughout the image. Moreover, to ensure convergence, a large number of iterations must be performed which can be very slow, especially for dynamic studies with many frames [176]. These reconstructions are favoured in clinical FDG-PET imaging in oncology were the detection of tumors is the goal rather than absolute quantification of activity.

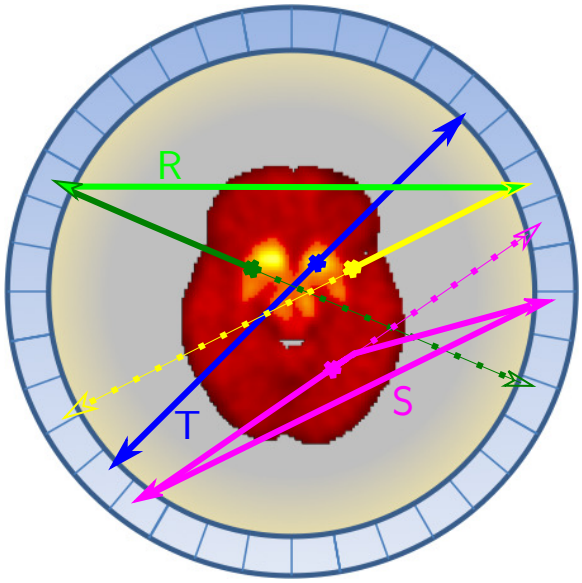

Figure 3.7: Simple illustration of true (T), random (R) and scattered (S) coincidences.

3.2.3 PET quantification

After acquisition and correction of the PET data, the final step is to assign meaningful physiological values to the measured spatiotemporal kinetic behaviour of the radioligand. For quantitative assessment of radioligand binding, the experiments must be performed under tracer conditions. At tracer conditions (ligand occupies no more than around 5–10 % of the target), the radioligand does not perturb the system under investigation. Quantitative analysis methods for radioligand–receptor binding scans are categorised into: kinetic, equilibrium, and graphical. In this chapter we introduce the kinetic approach, as this is the underlying framework for all methods

and it is the one which is applied for the quantitative analysis of the PET data in this thesis.

Compartmental modelling

PET measures the total radioactivity signal in a tissue over time and does not differentiate between the different binding states of the radioligand. The radioligand can be in three different states in a tissue: a) specifically bound to the target of interest; b) bound to other targets like lipids in a non-satuarable manner (nonspecific binding); and c) unbound or free. One approach, to quantitatively characterise the ligand's binding, is to consider each binding state as a compartment. In each compartment the concentration of the tracer is assumed to be homogeneous at all times. Therefore, the total tissue radioactivity, can be configured into a three-tissue compartment (3TC) model (figure 3.8,a). This model includes the parent tracer concentration in plasma (C_P) and 3 tissue compartments: a free tissue compartment containing the unbound tracer (C_F), a nonspecifically bound compartment (C_{NS}) and a specifically bound compartment (C_S). The C_P consists of the free and the bound tracer and only the free can cross the blood brain barrier (BBB) to enter the tissue. The ratio of the free and whole plasma concentration is known as the free fraction in plasma (f_P). The six micro–parameters (rate constants: $K_1$to k_6) describe the influx and efflux rates of the radioligand between compartments. In particular, K_1 and k_2 describe the influx and efflux of the radioligand between the plasma compartment (C_P) and the tissue compartment respectively. The k_3 and k_4 describe the transport between the free and specifically bound compartments and k_5 and k_6 describe the transport between the free and the nonspecifically bound compartments. For this compartmental model six parameters must be estimated and often the model fit is not reliable and is prone to individual large errors for the estimated micro-parameters.

Two simplified versions of the 3TC model have been proposed, the two-tissue compartment model (2TC) and one-tissue compartment model (1TC). The 2TC (figure 3.8,b), assumes that the free and the non-specific compartments are indistinguishable due to rapid equilibrium. The combined compartments, are now called the non-displaceable compartment. The free fraction of the ligand in the tissue (f_{ND}) is estimated as the ratio between the free tracer concentration and that of the whole non-displaceable compartment. Similarly, when the specifically bound and the non-displaceable compartments equilibrate rapidly, they are merged into one compartment and this is know as 1TC (figure 3.8,c).

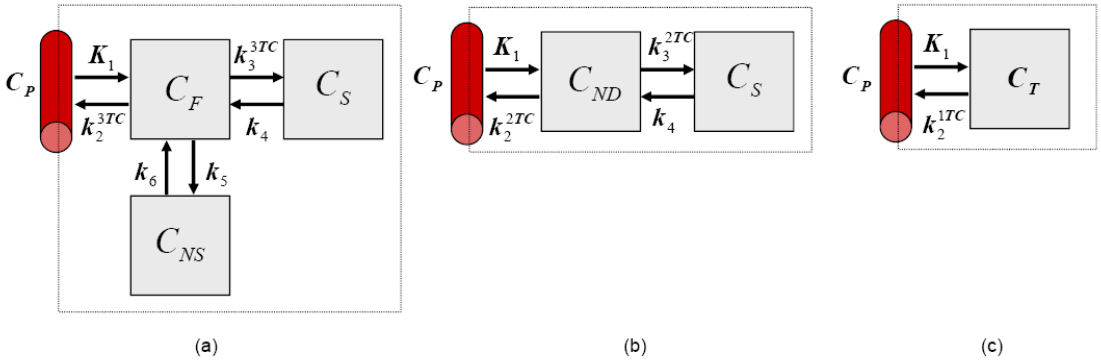

Figure 3.8: Compartmental model configurations. (a) Three-tissue compartment model. (b) Two-tissue compartment model (c) One-tissue compartment model. Image courtesy of [70]

In addition to the PET imaging data, which can determine the concentration of the radioligand in the tissue, the concentration of the tracer in the plasma may be required for full quantification (plasma input function). The plasma input function measurement requires the measurement of arterial blood samples during the scan and is an invasive procedure. Arterial blood is often withdrawn continuously for the first part of the scan in order to acquire a good description of the rapidly changing tracer concentration in plasma, and then discrete samples are taken until the end of the scan. For example, for a scan that lasts 90 min continues blood data is taken

for the first 15 min and then discrete blood samples are withdrawn at 5, 10, 15, 20, 25, 30, 40, 50, 60, 70, 90 minutes post-injection. From these data the whole blood activity curve for the total scan duration is generated. To derive the plasma input function the discrete samples are centrifuged to obtain the plasma component and the plasma-over-blood activity ratio is estimated. The whole blood activity curve is multiplied with this ratio to generate the total plasma activity curve. However, the plasma activity measurement consists of both the parent radioligand and any radio-labelled metabolites. Using high performance liquid chromatography (HPLC) analysis of plasma samples it is possible to measure the fraction of total plasma activity that corresponds to the parent (parent fraction). The product of the parent fraction curve and the total plasma activity curve generate the metabolite corrected plasma curve, which is then used as the input function for the kinetic analysis. However, as the acquisition of arterial blood samples is uncomfortable for the patient and can pose health risks, alternative reference tissue models have been developed with the view to avoiding arterial sampling. These models are introduced in section 3.2.3.

The mathematical solution of PET tracer compartmental models with a plasma input function can be obtained from the following general equation described by Gunn and colleagues [68]:

$$C_T(t) = (1 - V_B)H_{TP}(t) \otimes C_P(t) + V_B C_B(t) \tag{3.7}$$

where $C_T(t)$, $C_P(t)$ and $C_B(t)$ are the concentrations in target tissue, plasma and arterial blood respectively; $H_{TP}(t)$ denotes the impulse response function for the system and V_B is the fractional blood volume component.

The appropriate compartmental model is fitted to the time activity curves (TAC), that is, the radioactivity concentration within a tissue over time. The individual

micro–parameters are estimated by minimising the residual sum of squared errors using nonlinear least squares. Different criteria such as the Schwarz and Akaike criteria [109] can be employed for the selection of the appropriate model. These criteria objectively determine which model is the most appropriate by weighing the quality of model fit against the model complexity (described by the number of model parameters). A model is preferable if it produces a better fit and / or uses fewer model parameters [156]. However, in practise, the appropriate compartment model is dictated by the PET tracer and the physiological and biochemical properties of the system.

Macro-parameters

The individual micro-parameters are informative about the tracers kinetics but can be difficult to estimate accurately in the presence of noise. Therefore a direct assay of the ligand–receptor binding directly from these rate constants is not reliable. The macro-parameters, which are a function of the micro-parameters, are used instead for estimates of the ligand-receptor binding interactions. For reversible radioligands, the macro-parameters include the volume of distribution (V_T) and the binding potential (BP_{ND}). Reversible is defined as a ligand that binds to the target and readily dissociates over the scan duration.

The *in–vivo* investigation of ligand–receptor interactions is based on *in–vitro* receptor binding concepts, and the equilibrium binding reaction between the receptors and the free ligand. The "Michaelis-Menten" equation for the receptor–ligand binding is:

$$R + F \underset{k_{off}}{\overset{k_{on}}{\rightleftharpoons}} B \tag{3.8}$$

where k_{on} $(nM^{-1}\,min^{-1})$ and k_{off} $(min^{-1}\,)$ are the association and dissociation rate

constant respectively, R is the concentration of available receptors, B is the concentration of the ligand–receptor complex (bound receptor) and F is the free concentration of the radioligand. Thus, B_{max} is the total concentration of receptors and B_{max} = R + B. K_D is the equilibrium dissociation rate constant, or the reciprocal of the affinity of the ligand for the receptor and is defined as:

$$K_D = \frac{k_{off}}{k_{on}} \tag{3.9}$$

At equilibrium equation 3.8 leads to B(K_D + F) = F B_{max}. Under tracer conditions ($F \ll K_D$), this yields,

$$BP = \frac{B}{F} = \frac{B_{max}}{K_D}. \tag{3.10}$$

The term binding potential (BP) for *in–vivo* ligand–receptor binding studies was introduced by Mintun and colleagues [132], and is the ratio of specific binding at equilibrium to some other reference concentration. Three reference concentrations have been considered and they involve a particular subscript to identify them: a) the free radioligand in tissue (BP_f); b) the total parent radioligand in plasma (BP_p); and c) the non-displaceable radioligand in tissue (BP_{ND}). BP_{ND} is the most widely used as it does not require arterial blood sampling and is relatively easy to implement whereas the BP_f and BP_p require the acquisition of blood. BP_{ND} can be described in terms of its density, affinity and non-specific binding components as;

$$BP_{ND} = f_{ND}\frac{B_{max}}{K_D} \tag{3.11}$$

The application of these reference tissue methods and the different binding potential outcome measures rely on the availability of a reference region which is a tissue that

is devoid of the receptor of interest.

In imaging studies the volume of distribution (V_T) is defined as the ratio of the concentration of the radioligand in the tissue to the concentration in plasma at equilibrium:

$$V_T = \frac{C_T}{C_P} \tag{3.12}$$

The total tissue V_T is the sum of the volume of distribution of the individual components:

$$V_T = \frac{C_T}{C_P} = V_F + V_{NS} + V_S = V_{ND} + V_S \tag{3.13}$$

$$V_S = \frac{C_S}{C_P} \tag{3.14}$$

$$V_{ND} = \frac{C_{NS}}{C_P} \tag{3.15}$$

Because specific binding equals $V_S = V_T - V_{ND}$ then BP_{ND} can be estimated indirectly from the volume of distributions if there exists a reference region:

$$BP_{ND} = \frac{V_T - V_R}{V_R} = DVR - 1 \tag{3.16}$$

where DVR is the ratio between the total volume of distributions of the target and the reference tissue. The relationship between the macro– and micro–parameters can be deduced from the solution to the compartmental model differential equations [68] which for the 2TC yield the following relations:

$$V_T = \frac{K_1}{k_2}\left(1 + \frac{k_3}{k_4}\right) \tag{3.17}$$

$$V_{ND} = \frac{K_1}{k_2} = \frac{f_p}{f_{ND}} \tag{3.18}$$

$$BP_{ND} = \frac{k_3}{k_4} \tag{3.19}$$

Reference tissue model

Reference tissue models are constructed in the same compartmental modelling framework as plasma input models and use a reference region to avoid arterial blood sampling and permit the estimation of BP_{ND}. Parallel model equation relating the tissue and reference regions as functions of the plasma activity are combined to remove the presence of the plasma term. This yields an equation which describes the tissue time course as a function of the reference tissue time course and the micro-parameters which can characterised in terms of the impulse response of the system [68]:

$$C_T(t) = H_{TP}(t) \otimes C_R(t) \tag{3.20}$$

where $C_R(t)$ is the concentrations in the reference tissue and $H_{TP}(t)$ is the impulse response function. A schematic diagram of the full reference tissue model (FRTM) and the simplified reference tissue model SRTM is shown in figure 3.9. For the FRTM the target tissue is described by a 2TC model whereas it is described by a 1TC model in the SRTM. For both models the reference tissue is described by 1TC.
Under the assumption that the target tissue and the reference tissue have the same V_{ND}, the equations are written as follows:

$$\begin{aligned} \frac{K_{1T}}{k_{2T}} &= \frac{K_{1R}}{k_{2R}} \\ R_1 &= \frac{K_{1T}}{K_{1R}} \end{aligned} \tag{3.21}$$

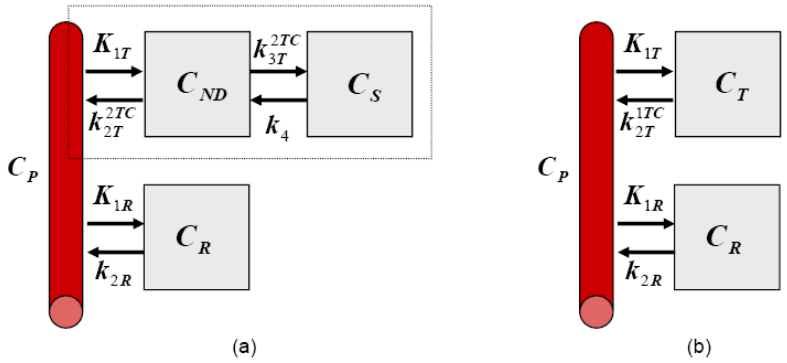

Figure 3.9: Reference input models. (a) Full reference tissue model (FRTM) (b) Simplified reference tissue model (SRTM). Image courtesy of [70]

where R_1 is the influx ratio between the target and the reference tissue. The quantitative agreement between BP_{ND} estimates derived from full plasma kinetic models and the SRTM has been evaluated for a range of different radioligands [123, 136, 142, 108]. The results show that the SRTM BP_{ND} values can be underestimates of the true values when the tissue data convincingly require more than 1TC or have a significant blood volume contribution to their overall activity. The SRTM model also lends itself easily to robust parametric imaging through the use of basis functions methods [69].

3.2.4 Assessing synaptic neurotransmission with PET

Over the last decades PET has been successfully used to measure acute synaptic fluctuations of dopamine *in–vivo*. The principle underlying this research is explained by a theoretical framework that we refer to as the occupancy model. This model, postulates that the synaptic neurotransmitter level determines the number of receptors available for binding by the radioligand and this facilitates direct measurement of synaptic dopamine transmission. Specifically, the model predicts that stimuli that increase synaptic dopamine concentration will result in increased occupancy of receptors by the neurotransmitter, which results in reduced availability of dopamine receptors for binding of the radioligand [110]. The typical experimental paradigm to

assess synaptic neurotransmitter levels involves at least two PET scans. The first scan, called the "baseline" or "resting" scan, estimates the number of available receptors in a baseline condition. The second scan, described as the "challenge" scan, estimates the number of available receptors after the neurotransmitter system has been perturbed either by a pharmacological challenge or a stimulating task. Differences in BP_{ND} between the "baseline" and the "challenge" scans are interpreted as changes in endogenous neurotransmitter levels.

3.2.5 Dopamine radioligands

Neurochemical dopamine targets, such as dopamine transporters, dopamine receptors and dopamine synthesis, have been studied *in–vivo* with the aid of molecular imaging (PET and SPECT). The investigation of each of these parts of dopamine neurochemistry requires the development of a specific imaging probe (typically a radioligand). In order to be a successful radioligand, an imaging probe has to penetrate the BBB, requires an ideal affinity and selectivity for the target, and favourable kinetics in order to image and quantify the target. Affinity is a measure of how well the ligand binds to the target and affects the *in–vivo* SNR and the reversibility of the kinetics. A successful ligand requires sufficient affinity for the target, although a very high affinity is not always optimal and can cause problems associated with irreversible kinetics.

In practise, most radioligands bind to more than one target and therefore sufficient selectivity is required. Selectivity is the ratio of the ligands affinity to a given target to that of another and *in–vivo*, a 30-fold selectivity is considered satisfactory given an equivalent target density. Moreover, the characteristics of the plasma input function and the ligand's metabolic profile can also be important factors. A good neuroimaging ligand will either have no metabolites or its metabolites do not cross the BBB.

For dopamine, there are a number of radioligands that have successfully been developed to image pre– and post–synaptic dopamine function. Radioligands for the dopamine transporter include: [^{11}C]PE2I, [^{11}C]-β-CFT, [^{11}C]-β-CIT and [^{11}C]-β-CIT-FE. To study the dopamine metabolic pathway the most commonly used tracer is [^{18}F]FDOPA, which acts at the intraneuronal level. For the post–synaptic assessment there are several radioligands for both the D1-like and the D2-like receptor families. For the D1-like receptor family the most widely used are [^{11}C]NNC112, [^{11}C]SSH23390, which also bind to the serotonin $5HT_2$ receptors and can image both striatal and cortical regions.

Table 3.1 shows the dopamine radioligands that are used for the D2-like receptor family. The [^{11}C]FLB457 and [^{18}F]fallypride ligands have a high affinity of the D2-like receptors and have the potential to image low–density extrastriatal D2-like receptors. However, quantification of striatal binding with these ligands is problematic as the kinetics are very slow. For example ^{18}[F]fallypride approaches equilibrium in the striatum after 2 hours. The other radioligands can provide quantitative estimates for the dense D2-like receptor population in the striatum. However, as they have equal affinity for the D3R and D2R, they are only informative about the abundant D2R sites. The exception is [^{11}C]PHNO, which due to its high selectivity for the D3R enables measurement of the D3R receptor population.

[^{11}C]PHNO was first synthesised in 1984 [96] and at that time it was considered as a potent D2-like receptor agonist. The agonist profile of [^{11}C]PHNO originally led to it being investigated as a potential treatment for several neurological diseases including Parkinson's and it reached Phase II clinical trials. Although clinical trials showed that [^{11}C]PHNO had significant anti-Parkinson effect, other agents such as levodopa had a superior therapeutic action [4] and it was withdrawn. In 2005 Wilson and colleagues [188] synthesised [^{11}C]PHNO as a potential agonist radiotracer for imaging

the *in–vivo* D2R^{high} in preclinical species and in humans [65, 187, 188]. The first data demonstrated that the distribution of the radioligand was different from other D2R agonist and antagonists ligands with a distinctive high accumulation in the GP and SN and also there were qualitative differences between the kinetics of the striatum and GP. An examination of the effects of the D3R preferring compound BP897 on [^{11}C]PHNO led Narendran and colleagues [138] to discover the preferential affinity of [^{11}C]PHNO for D3R over the D2R. A recent study by Gallezot and collaborators [64] measured the affinity of [^{11}C]PHNO for D2R and D3R in the living primate brain and they found that it had a 25–48 fold higher affinity for the D3R.

Table 3.1: Dopaminergic D2-like receptor radioligands. The second column shows the pharmacological profile of each ligand and the third column the *in–vivo* regional distribution in humans reported from PET and SPECT studies.

Ligand	Pharmacological properties	Regional distribution
[^{18}F]fallypride	Antagonist	Striatum, pallidum, amygdala, hippocampus, thalamus, substantia nigra, anterior cingulate and prefrontal cortex
[^{11}C]FLB457	Antagonist	Cortex,thalamus, substantia nigra, ventral anterior cingulate, amygdala, hippocampus
[^{11}C]Raclopride	Antagonist	Striatum
[^{11}C]Spiperone	Antagonist	Striatum
[^{123}I]IBZM	Antagonist	Striatum
[^{11}C]NPA	Agonist	Striatum
[^{11}C]MNPA	Agonist	Striatum
[^{11}C]PHNO	Agonist	striatum, pallidum, substantia nigra, thalamus, hypothalamus

3.3 Multimodal brain imaging for image analysis

In the following sections we give a brief introduction to the registration algorithms that have made feasible the integration of information from MRI and PET imaging, in

addition to correcting for within-modality motion. Finally we provide an overview of the region of interest (ROI) brain methodology, which has evolved over the years as a consequence of multimodal imaging approaches.

3.3.1 Registration methods

Registration refers to the process of spatially aligning two images so as to achieve anatomical or functional correspondence. The registration can be within or between subjects and within or between modalities. Within modality registration (intra-modality) corresponds to the alignment of images acquired with the same modality, whereas inter-modality registration involves the alignment of images from different modalities (e.g., T1-weighted MRI to [^{11}C]PHNO PET).

There are three main types of registration methods that are classified according to the type of deformation and the number of degrees of freedom (DOF) employed, to achieve the required spatial correspondence: a) rigid; b) affine or linear and c) non-linear. The DOF determines the flexibility of the different types of deformation that the image will undergo in order to be spatially transformed to match a reference image. The higher the DOF, the more flexibility that the deformation model has. Rigid registration is the simplest registration method and has 6 DOF (3 rotations about the x, y, z axes (pitch, roll, yaw) and 3 translations along the x, y, and z axes). Rigid registration is broadly used for intra-subject, inter– and intra–modality image alignment. Intra-modality registration is particularly useful in longitudinal studies where we want to monitor, for instance, structural changes or the growth of a lesion, whereas inter-modality registration is important for applications where structural (i.e. T1-weighted, DWI) and functional data (fMRI, PET) of the same subject are acquired. Rigid registration is also employed as a standard preprocessing step to correct for motion, between the temporal frames of a dynamic scan. Correction for subject movement is essential, especially for long scans such as for[^{11}C]PHNO and

[^{11}C]Raclopride, which last approximately 90 and 60 minutes respectively. Motion correction allows for a better model fit to dynamic data and increases the sensitivity of estimation of parameters of interest, such as BP_{ND} and V_T.

Affine registration employs 12 DOF, the 6 DOFs for translation and rotation plus 3 scalings and 3 shears. Affine algorithms are sometimes used for registration when there is not enough information in the images to support non-linear registration. On the other hand, to match the brains with high precision, non-linear registration algorithms are required. The non-linear algorithms can have from thirteen up to several million DOF. Non-linear registration is used for inter–subject registration or for the registration of a subject's brain to an average template such as the Montreal Neurological Institute (MNI or ICBM152) template and vice versa. The selection of the appropriate registration algorithm for inter–subject alignment will depend on the quality of the imaging data and the purpose of the study.

Registration algorithms calculate a "cost function" in order to assess the correspondence between the images to be registered. The lower the cost function the better the alignment. Different types of "cost function" exist and should be carefully selected for each task. For example the "least squares" and "normalised correlation" cost functions are suitable for intra–modality registrations, the "correlation ratio" for registering any MRI modalities, whereas the "mutual information" and the "normalised mutual information" cost functions are suitable for inter–modality registrations.

3.3.2 Regions of interest segmentation methods

An ROI is an area that has been delineated on an image manually or automatically using computer software. ROIs may enclose an anatomical structure and are used to provide quantitative estimates of the enclosed area, or used to perform volumetric or shape analysis. Over the years, the definition of ROIs has advanced substantially due

to the need for precise and reproducible measurements and the need to accelerate the analysis time and minimise resources used. In addition, functional studies such as fMRI and PET have demonstrated that anatomical ROIs are not always the most suitable approach to quantify the activated areas. Therefore, ROIs that attempt to approach the functional organisation of the cortical and subcortical regions are sought.

In the early days of molecular imaging the ROIs were defined on the PET images alone. Due to the limited spatial resolution of PET, some regions that were known to be anatomically distinct were lumped together. Subsequently, the advent of registration algorithms and the standard practice of acquiring high quality anatomical data advanced the segmentation practices. Since then, guidelines for the manual delineation of cortical and subcortical ROIs and semi–automated and automated softwares for the definition of these regions have been developed. Manually defined ROIs are time consuming, labour intensive, require expert knowledge and introduce a certain degree of subjectivity. Nevertheless, manual segmentation is considered the gold standard technique due to the high intra– and inter–operator reproducibility.

The automated and semi-automated methods are more objective and enable the analysis of large data sets in a timely manner. Semi-automated methods such as region-growing methods involve the placement of a starting point and the ROI then grows and deforms according to the local anatomy. The placement of the starting point, requires user intervention and basic knowledge of the anatomy and this can impact the end result.

Fully automated methods involve the spatial normalisation of anatomical atlases [57, 81, 5] and more complex methods that use active shape and appearance models [144]. The latter uses a model of each structure that has been constructed/trained from a data set of manual segmentations. The model is applied to the subject's image

and then using image and anatomical characteristics such as the intensity and shape, constructs a segmented structure. The atlas-based methods take advantage of the non-linear registration techniques. To obtain the atlas-based segmentations a brain or a brain template such as the MNI template, to which the atlas is aligned, is required. The brain is non-linearly registered to the subject's image, and the transformation parameters obtained are applied to the anatomical atlas to match the subject's anatomy. Anatomical atlases are constructed from manually segmented ROIs obtained from one or multiple subjects. Heckemann and colleagues [83] found that the performance of the atlas-based approaches can be improved, by propagating multiple atlases, combining multiple segmentations and using a decision fusion approach.

For the subcortical ROIs the majority of these atlases are segmented into, CD, PU, NAC, TH and pallidum. As reported in chapter 2, pallidum and TH consist of smaller nuclei. However, the two regions are each segmented as a whole, since their nuclei are not clearly distinguished on standard T1-weighted images, which are normally employed for the manual segmentation of these regions. Behrens and colleagues [20, 92], using DWI and probabilistic tractography, segmented the human thalamus based on cortical connectivity information and the proposed subdivisions correspond to thalamic nuclei. From this data set a population-based atlas of the human thalamus has been constructed.

As each brain region has a distinctive pattern of connections, which to some extent determine the region's functional role, several cortical and subcortical regions have been defined or subdivided using this principle. Some studies have shown that there is good similarity between the borders identified using tractography and various other methods such as histology, functional MRI and structural imaging [88]. Despite the errors in tractography methods, parcellations of grey matter areas using tractography, has been proven a successful approach. According to Jbabdi et. al [88] to tell apart

two brain regions on the basis of their connections, it is not necessary to determine the full connection pattern but finding a subset of the connectivity pattern is sufficient to distinguish them.

Chapter 4

Development of region of interest guidelines for quantification of subcortical dopamine

4.1 Introduction

In the early days of PET, methods for the delineation of subcortical ROIs were immature. ROIs were crudely defined on integral (summed dynamic image) or parametric PET images, by placing circles around or within the anatomical structures; or at best, subcortical regions such as the CD, PU and NAC were lumped together into a single ROI. These approaches were not ideal and led to underestimation or overestimation of the true biological signals. The development of registration algorithms that enabled alignment of images from different modalities (e.g. PET and MRI) allowed, for the first time, a more detailed and precise delineation of subcortical regions. Afterwards it became common practice, along with the PET data, to acquire high resolution T1-weighted structural MRI images to facilitate the manual or automated delineation of ROIs.

The dopamine D2-like family of receptors is distributed primarily in the subcortical regions of the brain. These subcortical structures are relatively small and the current automated techniques for their ROI delineation are not consistently precise.

The performance of the automated methods depends on the image quality, the resolution of the MRI data, the subject's anatomy, health status and the properties of the automated algorithm itself. Therefore, for the quantification of subcortical PET data, the current gold–standard approach for the delineation of ROIs is by manual segmentation.

Guidelines have been developed for the manual definition of subcortical ROIs [5, 54, 127, 129] and some of them have been tailored to accommodate observations of functional studies. For instance, instead of simply subdividing the striatum into CD, PU and NAC, Drevets [54] subdivided the striatum into dorsal and ventral components in order to best quantify the release of dopamine after the administration of amphetamine. With the recent advent of the agonist PET ligands [^{11}C]PHNO and [^{11}C]NPA, which have a preferential affinity for the D3R, there is a need for refinement of the existing guidelines and in addition a need for the development of guidelines for regions that have not been studied before such as the ventral pallidum. In this chapter a set of guidelines, for the manual delineation of the subcortical D2R and D3R rich regions, is presented. For optimal analysis, the ROI guidelines should accurately capture the area of interest, be reproducible and minimize operator–dependence. Moreover, since manual delineation is time consuming we have also developed an anatomical subcortical atlas to automate the definition of the subcortical ROIs. The performance of the automated method is quantified and presented in section 4.4.

4.2 ROI guidelines for the manual delineation of subcortical regions of interest

Subcortical ROIs relevant to the examination of dopamine and dopamine receptors were identified from autoradiography, PET studies and the localisation of the dopaminergic tracts [71, 80, 100, 118, 135, 138, 150, 155, 167, 169, 173]. A set of guidelines for the definition of these dopamine relevant regions was developed to balance the

need to accurately encompass the region of interest and ensure the quality and reproducibility of the analysis. The guidelines are applicable to structural MRI images with a good contrast between the structure of interest and their surroundings. For SN, due to its small size and location, the registration between PET and MRI around this area is not optimal, the ROI is defined on the PET integral image using a fixed ROI size. Apart from the traditional subdivision into CD, PU and VST the striatum is subdivided into smaller sub–regions in order to accommodate findings about the distribution of dopamine receptors.

The guidelines are developed for images in MNI space and are applicable only to images in this space. The following rules were applied during manual ROI delineation:

1. The outer limit of an anatomical structure, as defined in anatomical books [55], acts as the boundary for an ROI.

2. If reliable tracing of a portion of an ROI could not be performed, this portion is excluded.

4.2.1 Guidelines for ROIs defined on MRI images

Caudate (CD): is drawn wherever visible on the coronal plane. The inferior border of the caudate is defined by the VST and care should be taken not to include cerebrospinal fluid from the ventricles (figure 4.1: B-F). The anterior commissure AC subdivides the caudate into pre-commissural (preCD) and post-commissural (posCD) regions.

Putamen (PU): is defined on the transverse plane and it is traced on all slices where dense grey matter can be clearly observed and differentiated from surrounding structures (figure 4.1: J-L). On the most ventral slices where the AC divides the PU into two regions, the ROI includes only the grey matter that is anterior to the AC. The

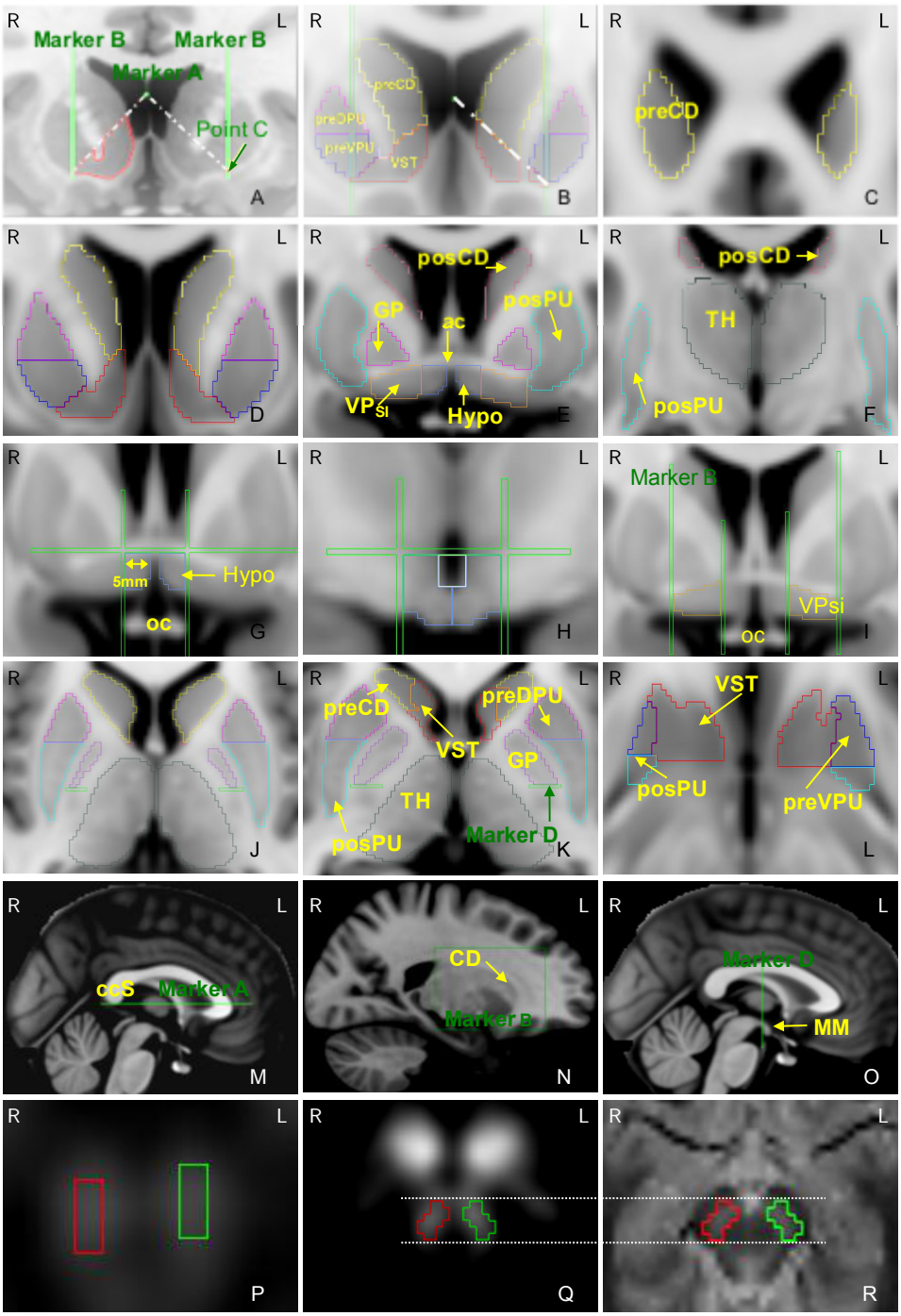

Figure 4.1: Guidelines for the manual delineation of subcortical ROIs on MRI (A-O) and substantia nigra/ventral tegmental area on PET (P-R) in a representative subject. R=right; L=left.

PU is traced as a single ROI and subsequently it is subdivided into pre–commissural dorsal PU (preDPU), pre–commissural ventral PU (preVPU) and post–commissural PU (posPU) regions by providing the position of the AC and the posterior commissure (PC). The AC subdivides the PU into pre–commissural and post–commissural regions while the PC subdivides the pre–commissural PU into dorsal and ventral sections (figure 4.1B, D, J-L).

Ventral striatum (VST): Several studies have shown that there is not a definitive anatomical, histological or histochemical distinction between NAC, CD and PU. Therefore, the dorsal boundary of the VST is defined so as to include the NAC, the pre–commissural medial CD and the rostral-ventral PU in order to be consistent with the functional anatomy of the VST as defined in primate tracing studies and human connectivity studies [25, 116, 52, 76, 39, 78, 74, 141]. The dorsal boundary is defined by connecting two points, marker A and point C on the coronal plane (figure 4.1A). These two points are predefined by the placement of two 3D markers (markers A and B) on the sagittal plane (figure 4.1M-N). Marker A: a horizontal line intersecting the most ventral part of the splenium of the corpus callosum (ccS) is placed on the most mid-sagittal slice. Sometimes there are two or three slices which can be described as the "most mid-sagittal slice" and in this case the operator is advised to select the one where the thalamus is the smallest. In the coronal view, marker A appears as a single voxel in each slice (figure 4.1A) and this voxel will be used for the definition of the dorsal boundary of the VST. Marker B: moving from lateral to medial in each hemisphere, a rectangle is placed on the first slice where the grey matter of the head of the CD can be clearly seen. In a coronal view this will appear as a voxel width column. The inferior intersection of this column with grey matter, of PU within this column, is defined as point C (figure 4.1A-B). VST tracing begins when point C comes into view, up to the slice where the anterior commissure connects the two hemispheres. However, there are occasions when the thin white matter layer which separates the

VST from the sub-callosal gyrus and/or the septal nuclei can not be observed, making it infeasible to sample the VST up to the AC. Any white matter (e.g. the internal capsule) should be excluded from the ROI. Figures 4.1B,D-E show the VST delineation on three representative rostral to caudal slices.

Globus pallidus (GP): takes its name from its pale appearance, which makes its delineation difficult and susceptible to misclassification since it is hard to discern from its surroundings. The GP ROI consists of both the external and internal GP since the subdivision is not feasible on most MRI sequences. GP delineation is performed on the transverse plane, dorsal to ventral (figure 4.1J-K), and it is defined up to the slice where the AC connects the two hemispheres. To increase the reproducibility of the tracing and exclude areas which might be misclassified (such as the corticospinal tract), a 3D marker (marker D) is placed on the most mid-sagittal slice. This is a vertical line intersecting the posterior surface of the mammillary body (MM) which becomes the posterior boundary of the GP on the transverse plane (figure 4.1O).

Ventral Pallidum / Substantia Innominata ($\mathbf{VP_{SI}}$): The ventral pallidum is not easy to define in humans as there is no sufficient contrast with the surrounding regions and also there is an admixture of the ventral pallidum and substantia innominata in the area under the AC. For this reason the proposed guidelines refer to a single ventral pallidum/substantia innominata ROI. The VP_{SI} is defined on the coronal plane (figure 4.1E,I). The tracing starts at the slice where the AC connects the two hemispheres and stops at the slice where the AC does not separate the GP from the VP_{SI} (~ 3 slices on a $1 \times 1 \times 1\,mm$ MRI). The medial boundary is a vertical line intersecting the medial edge of the optic chiasm (OC) and it is placed on the first slice where the AC interconnects the two hemispheres, as viewed on a coronal plane, and copied onto the subsequent slices of interest. Marker B (see VST definition and figure 4.1N) is the lateral boundary. The superior boundary is the white matter of the AC and the

inferior boundary is the CSF or white matter. The VP_{SI} is the grey matter that can be sampled within these boundaries. However, due to the complicated anatomy of this area, the ROI might include regions such as the anterior perforated substance or the septal nuclei. There are cases when this region cannot be clearly defined due to signal dropout and partial volume effects. Care should be taken in order to exclude PU, GP and CD grey matter.

Thalamus (TH): is drawn on all of the transverse slices that are visible and drawing ends just before the superior colliculi becomes visible (figure 4.1J-K). The dorsal boundary changes between the lateral ventricle and a thin layer of white matter. The internal capsule and the third ventricle are the lateral and medial boundaries respectively. The inferior boundary is either the CSF of the ventricles or the white matter of the fornix. The ROI should contain the full grey matter area so as to include the entire thalamic nuclei.

Hypothalamus (Hypo): is traced on the coronal plane and tracing starts from the first slice where the AC connects the two hemispheres up to the slice where the mammillary bodies (MM) are joined. Marker D (figure 4.1O) can be used as the caudal boundary of this delineation. A dorsal and a bilateral boundary are defined to enable the tracing of the region (figure 4.1G-H). The dorsal boundary is a horizontal line that intersects the inferior part of the AC and it is copied on all slices of interest. The lateral boundary is defined on a sagittal slice $5\,mm$ bilateral from the first medial slice where the Hypo can be observed.

4.2.2 Guidelines for ROIs defined on PET images

Substantia nigra (SN): is located in the midbrain and is a small region with no clear cut boundaries. Due to its small size and potential mis-registration issues between the PET and MRI images, the SN ROI is defined on the PET integral image. However, the

size of a given anatomical structure as determined from a PET image could be affected by the minimum and maximum intensity values, as well as by the physiological and pharmacological conditions of the experiment. Fixed size ROIs (right and left) are used in order to minimise variability induced by these factors. The ROIs are placed on five successive transverse slices (2 mm thickness) vertically centred on the maximal PET signal in the SN. The sizes of the ROIs are given in table 4.1. In each of the five selected transverse slices, a rectangle of the specified size is placed over each of the two hotspots, with default rotation as specified in table 4.1, though modifications to the angle are permitted if this results in improved alignment. The size of the ROIs and the proposed angles are based on information acquired from the PD weighted MRI images where the SN can be seen (figure 4.1R).

Table 4.1: ROI size and orientation for the substantia nigra. These ROIs are placed on a 2 × 2 × 2mm PET image. The magnitudes are in the following order: width × height in mm, angle in degrees. The first slice corresponds to the most ventral ROI placement while the fifth to the most dorsal ROI placement.

ROI No.	Right hemisphere	Left hemisphere
1^{st} ROI	4 × 8, 0°	4 × 8, 0°
2^{nd} ROI	4 × 10, 0°	4 × 10, 0°
3^{rd} ROI	6 × 12, 25°	6 × 12, -25°
4^{th} ROI	6 × 12, 25°	6 × 12, -25°
5^{th} ROI	4 × 10, 25°	4 × 10, -25°

Table 4.2 shows the full and abbreviated ROI names for the subcortical regions.

4.3 Automated method for the definition of the subcortical ROIs

The automated delineation of ROIs is achieved by the non-linear deformation of an anatomical atlas into the space of each individual. The subcortical ROIs of the atlas were manually defined on the non-linear ICBM152 template according to the guidelines proposed in section 4.2 and this allows for a direct comparison between manual

Table 4.2: First column shows the ROI full name, and second column the abbreviated ROI name

Region name	ROI abbreviation
Ventral pallidum/substantia innominata	VP_{SI}
Globus pallidus	GP
Ventral striatum	VST
Pre-commissural ventral putamen	preVPU
Pre-commissural putamen	prePU
Putamen	PU
Pre-commissural dorsal putamen	preDPU
Post-commissural putamen	posPU
Pre-commissural caudate	preCD
Caudate	CD
Post-commissural caudate	posCD
Hypothalamus	Hypo
Substantia nigra	SN
Thalamus	TH

and automated methods. The atlas consists of a total of 119 regions (figure 4.2). The cortical regions are a modification of the Harvard–Oxford atlas. The Harvard–Oxford atlas consists of 48 probabilistic maps derived from 37 healthy subjects aged between 18-50 years old. To create the atlas, each subject's T1-weighted image was affine-registered to the ICBM152 template with FLIRT [89] and subsequently the images were segmented according to the guidelines developed at the Center for Morphometric Analysis [1].

To create the atlas some of the probability maps were combined to create larger anatomical regions; whilst others were subdivided to reflect functional organisation using anatomical landmarks. Specifically, the superior frontal gyrus, the middle frontal gyrus, the inferior frontal gyrus pars triangularis and opercularis were combined to create the dorsolateral frontal cortex that was subsequently subdivided into anterior and posterior regions. The dorsolateral cortex anterior to the cingulate gyrus is classified as the anterior dorsolateral ROI. The frontal pole region dorsal to the rectus gyrus was also merged with the anterior dorsolateral cortex. The frontal pole ven-

tral to the rectus gyrus was combined with the frontal orbital cortex and this area was then subdivided into medial (rectus gyrus and medial orbital gyrus) and lateral orbitofrontal regions. The paracingulate and the anterior division of the cingulate gyrus were merged into one region and were subsequently subdivided into anterior cingulate (anterior to the genu of the corpus callosum) and dorsal anterior cingulate. The lateral occipital cortices (inferior and superior divisions) were combined with the occipital pole into one region. Four cortical regions (precuneous cortex, angular gyrus, superior parietal lobule and occipital pole) from the original Harvard–Oxford atlas were redefined on the ICBM152 template. After the subdivision or merging of the regions a threshold was applied to the probability map of each structure to achieve the best possible fit to the ICBM152 template. After the threshold was applied some of the regions overlapped and there were also brain areas that were not structurally classified as a member of the atlas ROIs ("holes"). To resolve this, these areas were identified and then corrected manually according to the anatomical organisation of the ICBM152 template.

The subcortical regions were defined on the non-linear ICBM152 template following the guidelines developed here while for the thalamus the thalamic connectivity atlas [92] was used. Finally, the cerebellum and the brainstem were manually defined combining information from the SUIT [51] and ICBM152 templates. The brainstem is subdivided into three areas: mesencephalon, pons and medulla. The cerebellum consists of three regions: a) dorsal cerebellum; b) ventro–lateral cerebellum; and c) medial cerebellum. Medial cerebellum includes structures such as the vermis and uvula. The subdivision of the cerebellum into the aforementioned areas is useful for PET studies where the cerebellum is used as reference region. For example, exclusion of the dorsal part of the cerebellum is recommended if there is a need to avoid spill–over effects from neighbouring high signal in the occipital cortex.

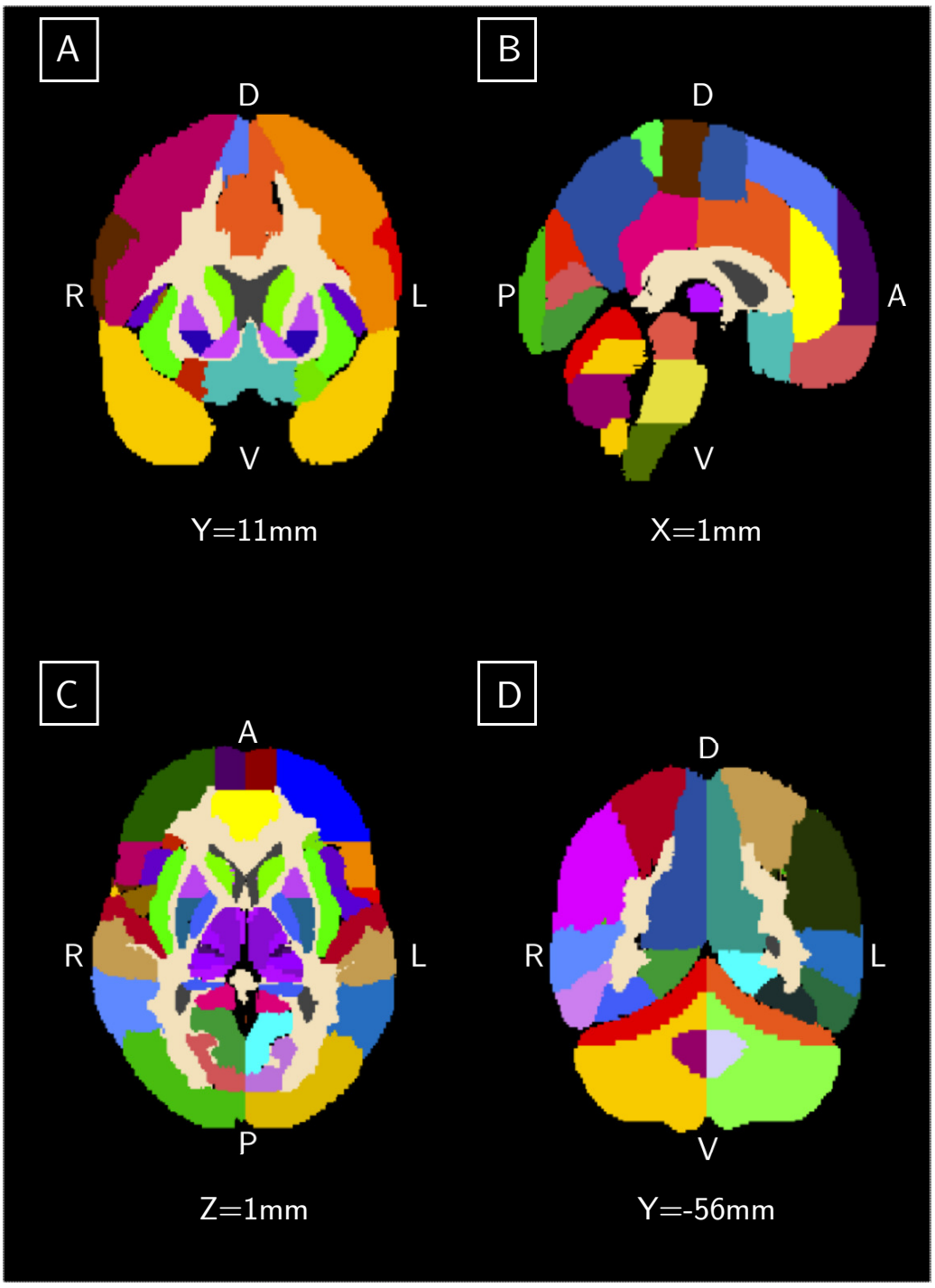

Figure 4.2: Anatomical atlas. Cortical regions are a modification of the Harvard–Oxford atlas, subcortical ROIs were defined on the ICBM152 template following the guidelines developed in section 4.2 and the thalamus was replaced by the thalamic connectivity atlas [92]. R=right; L=left; A=anterior; P=posterior; D=dorsal; V=ventral

.

4.4 Robustness, reproducibility and reliability of subcortical ROIs

To investigate the robustness and reproducibility of the manually-defined ROIs the intra– and inter–operator agreements were examined. Moreover, to provide a benchmark for the ROI reproducibility, striatal ROIs were defined and compared with a method developed previously at Columbia University PET Centre for imaging the D2R with [^{11}C]Raclopride [127, 129]. Hereafter, the guidelines we developed will be abbreviated as MAN I and the Columbia guidelines as MAN II. The regions defined automatically using the anatomical atlas were compared with the ROIs defined manually with MAN I.

4.4.1 Material and methods

Subjects and imaging data acquired to investigate the reproducibility

Nineteen healthy male volunteers had baseline [^{11}C]PHNO PET and MRI scans. All scans were conducted at the Centre of Addiction and Mental Health in Toronto, Canada and subjects provided written informed consent. For each subject a baseline [^{11}C]PHNO PET scan was acquired on a Siemens Biograph HiRez XVI PET tomograph (Siemens Healthcare). Subjects were positioned in the scanner and movement was minimised by using a custom-made thermoplastic facemask together with a head-fixation system (tru-scan imaging, Annapolis, Maryland). Subjects were injected with a single intravenous bolus of [^{11}C]PHNO between 235–368 MBq (mean = 307.2, SD = 40.6) with specific activity ranging between 23.3–38.6 GBq $/\mu mol$ (mean = 32.24, SD = 4.58) at the time of injection. The mass of injected [^{11}C]PHNO was between 2–2.6 μg (mean = 2.36, SD = 0.13) and the radiochemical purity of the compound was 97.7–99.9 (mean = 99.4, SD = 0.6). Following bolus administration of [^{11}C]PHNO, dynamic emission data were acquired for 90 minutes ($1 \times 30s$, $8 \times 15s$,

$3 \times 1min$, $5 \times 2min$, $5 \times 5min$, and $5 \times 10min$). A low dose CT scan (effective dose = 0.2 mSv) was also acquired and used for attenuation correction and model–based scatter correction. The dynamic images were reconstructed using Fourier rebinning and a 2D filtered back projection algorithm with a ramp filter at the Nyquist cut–off frequency [43]. T1-weighted MRI images were acquired on a GE Medical system Signa EXCITE HD, 1.5T. The structural T1-weighted images (acquired in the axial plane: FSPGR − IR PREPPED, TR = 4320 ms, TE = 1842 ms, flip angle = 20°, slice thickness = $0.78 \times 0.78 \times 1.5mm$) were acquired to enable definition of the subcortical ROIs.

Image analysis

The MRI and PET images of each subject underwent a series of spatial processing steps. The non-brain voxels from the MRI were removed using the FSL Brain Extraction Tool [165] and the extracted brain was rigidly registered to the nonlinear ICBM152 template (http://www2.bic.mni.mcgill.ca/) using SPM5 (Wellcome Trust Centre for Neuroimaging) to bring subjects into a similar orientation and facilitate manual ROI delineation. Regional analysis was performed with both manual and automatically–delineated ROIs (MAN I, MAN II and AUTO). For the manual ROI delineations, the MRI was made isotropic to the smallest voxel size of the original image ($0.79 \times 0.79 \times 0.79\,mm$) in order to obtain the best possible visual quality. For the automated method, the non-linear ICBM152 template was non-linearly warped with SPM5 to the high resolution T1-weighted MRI of each individual. The deformation parameters derived were then applied to the anatomical atlas, using the nearest neighbour interpolation method, to bring this into the individual subject's space. Finally, the MRI image, the ROIs and the warped anatomical atlas were resampled to match the PET image resolution ($2 \times 2 \times 2\,mm$). PET images were corrected for motion by realigning each frame to a reference frame, using mutual information as a cost function, and then these were registered to the T1-weighted image. [^{11}C]PHNO binding potential (BP_{ND}) estimates were obtained after applying the basis function implemen-

tation of the SRTM model [69] to the dynamic PET data to derive parametric images of BP_{ND} (parameter bounds in terms of non-decay corrected data: $\Theta_3^{min} = 0.0008\,s^{-1}$ and $\Theta_3^{max} = 0.5\,s^{-1}$, c.f. [69]).

Agreement and reproducibility metrics

The reproducibility of the manually defined ROIs and the level of agreement between the manually and automatically derived subcortical ROIs were examined. The manually–delineated ROIs are treated as the "gold–standard". Nevertheless, it is understood that manual delineation is subjective as it depends on the operator's knowledge of anatomy and attention to the guidelines. To examine the reproducibility of manual delineation, ROIs were delineated by two operators, twice each on two separate occasions (at least 1 month apart) according to the aforementioned guidelines. The same procedure was followed for both MAN I and MAN II, in order to provide a benchmark for the performance of MAN I in terms of reproducibility and the time taken to delineate the striatal structures. The first metric calculated was the DICE coefficient which measures the degree of ROI volume overlap between two ROIs [50],

$$\text{DICE} = 2 \cdot \frac{|\text{ROI}_1 \cap \text{ROI}_2|}{|\text{ROI}_1 + \text{ROI}_2|} \cdot 100\% \tag{4.1}$$

where $\cap$ is the intersection of the ROI volumes and ranges from 0 to 1. Thus the DICE coefficient ranges from 0%, for ROIs with no overlap up to 100 % for identical ROIs. The intra– and inter–operator ROI overlap was calculated for MAN I and MAN II. The second metric calculated was the variability of BP_{ND} which is a measurement of reproducibility that depends both on the geometrical ROI overlap and the local dopamine receptor landscape,

$$Variability\ BP_{ND} = 2 \cdot \left| \frac{BP_{ND}^{ROI1} - BP_{ND}^{ROI2}}{BP_{ND}^{ROI1} + BP_{ND}^{ROI2}} \right| \cdot 100\% \tag{4.2}$$

The intra–operator and inter–operator variability of BP_{ND} were calculated for MAN I and MAN II.

To measure the degree of agreement between MAN I and MAN II, the intra class correlation coefficient (ICC) for the BP_{ND} values obtained with the two methods was also calculated. The ICC was calculated as:

$$\text{ICC} = \frac{\text{BSMSS} - \text{WSMSS}}{\text{BSMSS} + \text{WSMSS}} \tag{4.3}$$

where BSMSS is the mean sum of squares between subjects and WSMSS is the mean sum of squares within subjects.

The automated approach (AUTO) was compared with the MAN I approach by calculating the inter–method DICE coefficient (subcortical regions only, excluding thalamus) and the inter–method variability of BP_{ND} using equations 4.1 and 4.2 respectively. Thalamus was excluded from this comparison as in the atlas we used the connectivity-based thalamus and not a thalamus delineated according to the guidelines developed in section 4.2.

4.4.2 Results

We have presented guidelines for the definition of dopamine relevant ROIs (MAN I) including Hypo, SN, striatum, GP, VP_{SI} and TH. Figure 4.3 shows the delineation of ROIs on the MRI and PET images for a number of characteristic slices. To delineate the whole set of ROIs for one subject using MAN I takes approximately 5 hours for an experienced operator with striatum and GP being the most demanding ROIs in terms of complexity and time taken.

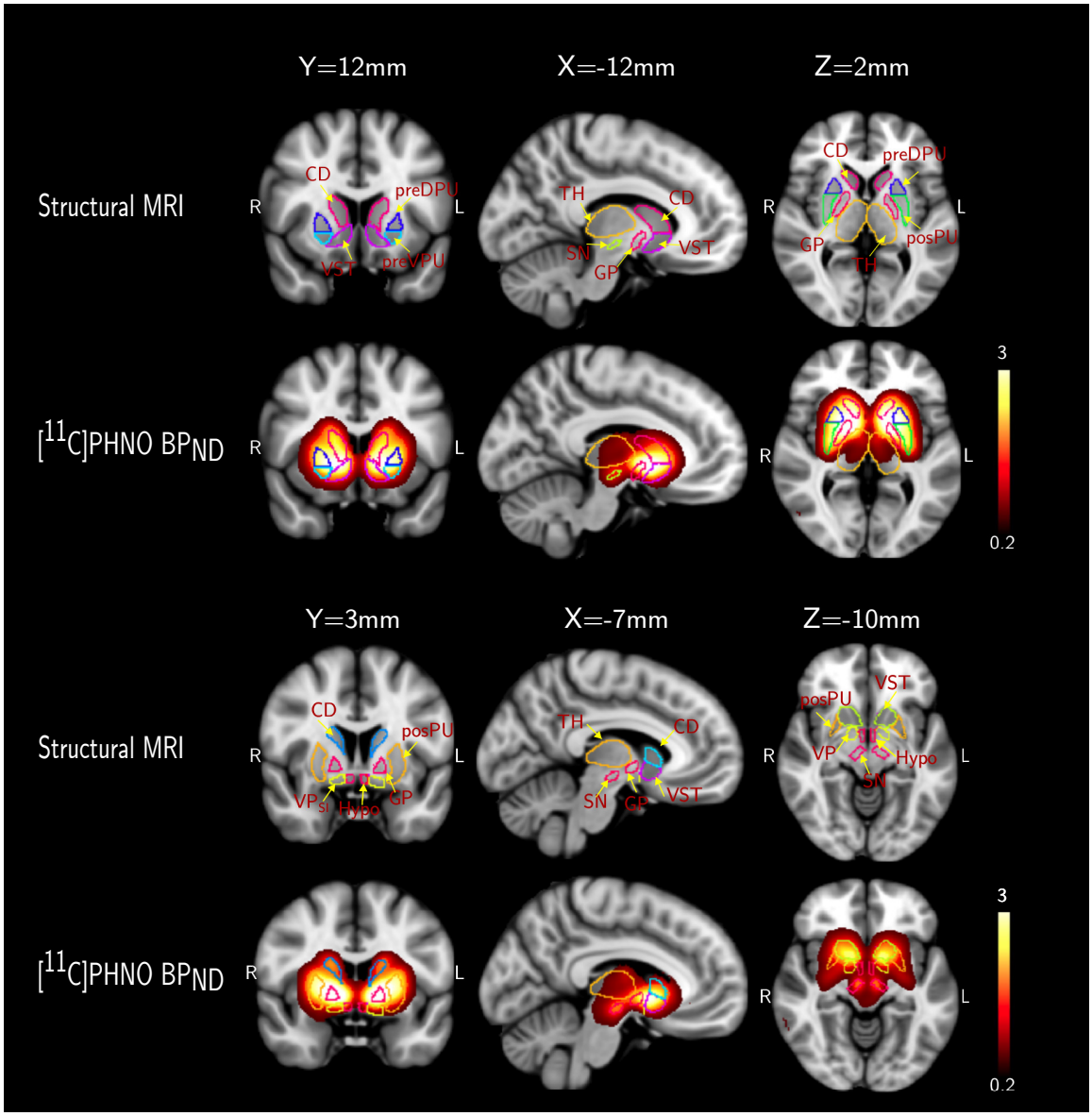

Figure 4.3: ROIs overlaid on [^{11}C]PHNO BP_{ND} parametric images and onto the T1-weighted MNI template in the pre–commissural (first 2 rows) and the post–commissural striatum (bottom rows). R=right; L=left;

The reproducibility of the manual ROIs was assessed in terms of ROI volume overlap (DICE) and BP_{ND} variability. The average intra–operator DICE across ROIs for MAN I was $88 \pm 6\,\%$ with the lowest DICE value obtained in VP_{SI} and the highest value in TH (figure 4.4). To provide a benchmark of reproducibility for MAN I, striatal ROIs were defined with the MAN II method. MAN I requires between 2 to 3 hours to delineate the striatum while MAN II takes between 2:30 to 3:30 hours. The intra–operator DICE for MAN I and MAN II respectively were $88 \pm 2\,\%$ versus $78 \pm 3\,\%$ for VST $90 \pm 1\,\%$ versus $87 \pm 1\,\%$ for PU and $91 \pm 1\,\%$ versus $88 \pm 1\,\%$ for CD (figure 4.4).

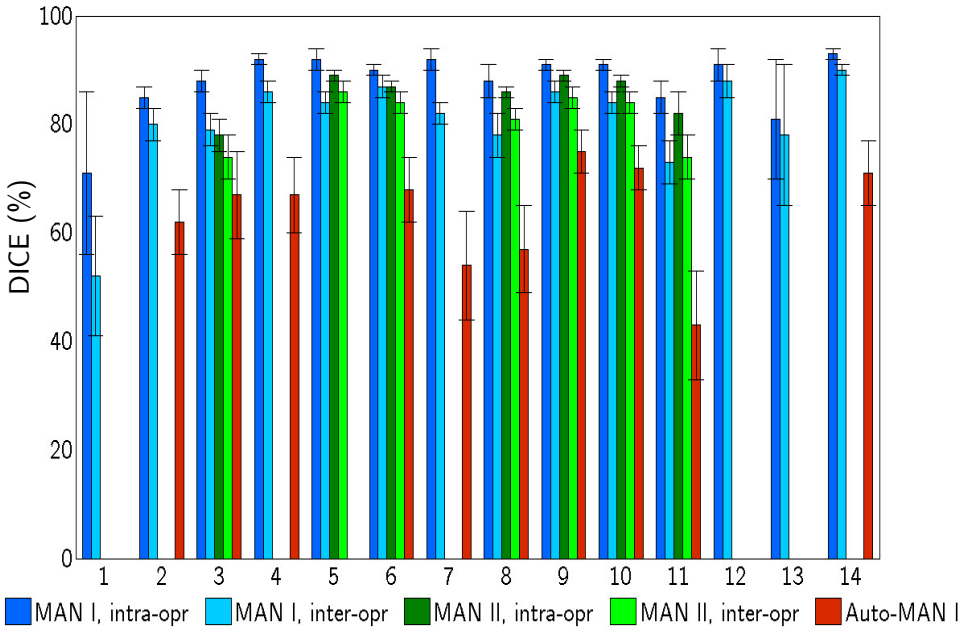

Figure 4.4: ROI volume overlap quantified in terms of the DICE coefficient: MAN I and MAN II (intra–/inter–operator) and the volume overlap between automated and MAN I. Numbers correspond to the following regions 1=VP_{SI}, 2=GP, 3=VST, 4=preVPU, 5=prePU, 6=PU, 7=preDPU, 8=posPU 9=preCD, 10=CD, 11=posCD, 12=Hypo, 13=SN, 14=TH.

The average inter–operator DICE for MAN I was $81 \pm 10\,\%$ with the lowest DICE obtained for VP_{SI} and the highest for TH (figure 4.4). In the striatum the inter–operator DICE values for MAN I and MAN II were $79 \pm 3\,\%$ versus $74 \pm 4\,\%$ for VST, $87 \pm 2\,\%$

versus $84 \pm 2\,\%$ for PU and $84 \pm 2\,\%$ versus $84 \pm 2\,\%$ for CD (figure 4.4). As with the intra–operator DICE, the inter–operator DICE for MAN I was higher than for MAN II but overall both methods provide highly reproducible results. The DICE coefficients for all regions are shown in figure 4.4. To assess the similarity between MAN I and MAN II we estimated the volume overlap (DICE), between the ROIs defined with the two methods and the values obtained were: VST $= 66 \pm 4\,\%$, CD $= 87 \pm 1\,\%$ and PU $= 81 \pm 1\,\%$.

The average intra–operator BP_{ND} variability across ROIs defined with MAN I was $2.6 \pm 1.2\,\%$ with the lowest BP_{ND} variability obtained in the CD and the highest in the SN (figure 4.5). The intra–operator BP_{ND} variability for the striatal regions obtained with MAN I and MAN II, respectively, was $1.4 \pm 1\,\%$ and $1.7 \pm 1.5\,\%$ for the VST, $1.7 \pm 1.3\,\%$ and $0.8 \pm 0.7\,\%$ for the PU and $1.2 \pm 1\,\%$ and $2 \pm 1.5\,\%$ for the CD. The average inter–operator BP_{ND} variability for MAN I across ROIs was $6.8 \pm 4.8\,\%$ with the lowest variability coming from the VST and the highest from the VP_{SI}. The inter–operator BP_{ND} variability for MAN I and MAN II for the striatal regions was: VST $2.3 \pm 2.8\,\%$ (MAN I) and $4.9 \pm 3.4\,\%$ (MAN II); PU $3.5 \pm 1.3\,\%$ (MAN I) and $1.9 \pm 0.9\,\%$ (MAN II); and CD $6.2 \pm 2.7\,\%$ (MAN I) and $6.4 \pm 1.5\,\%$ (MAN II). In figure 4.5 the BP_{ND} variability is displayed for all regions.

In addition to ROI volume overlap, the agreement between MAN I and MAN II was assessed by estimating the ICC for the BP_{ND} values obtained with the ROIs defined with the two methods, giving: VST ICC $= 0.87$, CD ICC $= 0.97$ and PU ICC $= 0.91$.

The performance of the automated method that employs a non–linear warp of the anatomical atlas was assessed and the automatically defined ROIs were compared with the ROIs delineated manually with MAN I. The comparison between the automated method and MAN I gave an average DICE coefficient for the gross anatomical regions

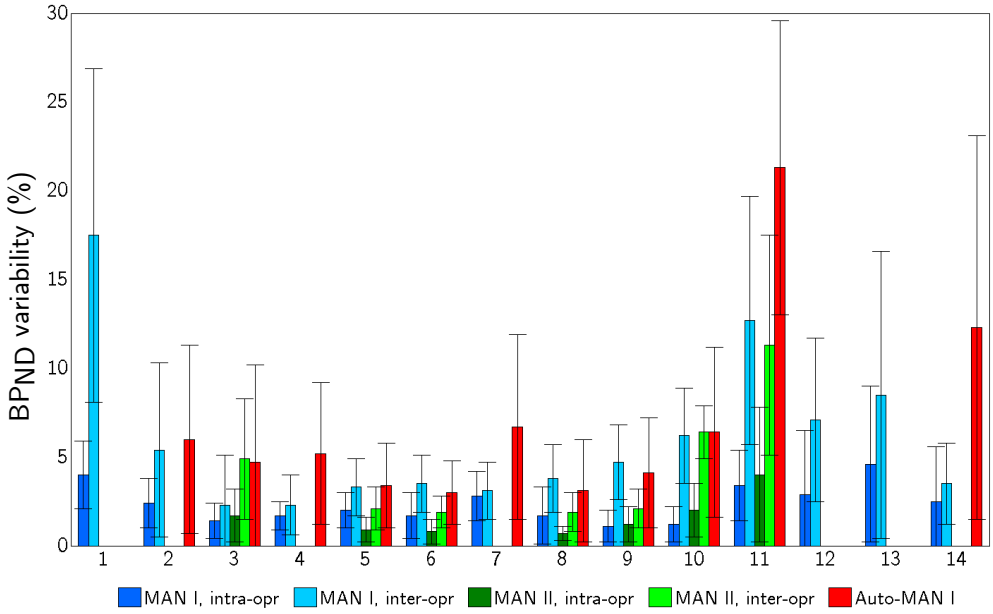

Figure 4.5: [^{11}C]PHNO BP_{ND} variability for methods: MAN I and MAN II (intra–/inter–operator) and for automated vs MAN I. Numbers correspond to the following regions 1=VP_{SI}, 2=GP, 3=VST, 4=preVPU, 5=prePU, 6=PU, 7=preDPU, 8=posPU 9=preCD, 10=CD, 11=posCD, 12=Hypo, 13=SN, 14=TH.

such as CD, PU, VST and GP of approximately $70 \pm 4\,\%$ (figure 4.4). For striatal subdivisions (preCD, posCD, posPU, preDPU, preVPU) the average DICE is $65 \pm 4\,\%$. The DICE for posCD and preDPU is lower and this might be due to the smaller size of these ROIs. The inter–method BP_{ND} variability was $4.9 \pm 1.4\,\%$ across all ROIs (excluding posCD which had high BP_{ND} variability). The inter–method DICE and BP_{ND} variability values for all regions are shown in figure 4.4 and 4.5 respectively.

To assess the relation between volume overlap and ROI volume (table 4.3), the DICE coefficients for the manual (MAN I, intra– and inter–operator) and automated approaches were plotted against the ROI volume in figure 4.6. For ROI volumes above $0.5\,cm^3$ DICE is relatively constant for the manual approach, although the DICE does drop off for the GP. The GP is a mixture of grey and white matter and this texture complicates delineation. DICE coefficients for the automated method also depend on

the size of the ROI (table 4.3). Smaller regions yield lower DICE values and this is consistent with mis–registration effects having bigger consequences for smaller regions.

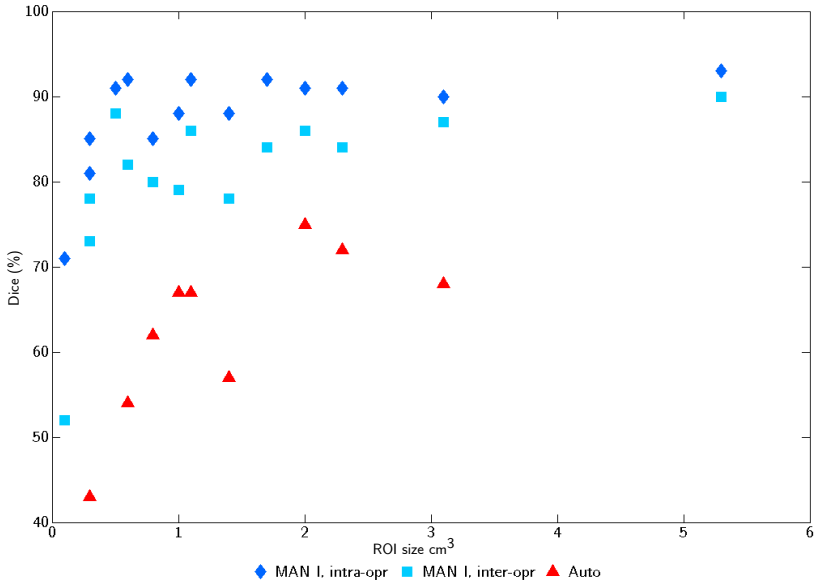

Figure 4.6: DICE coefficient as a function of ROI size. DICE was obtain for MAN I intra– and inter–operator and for the automated/MAN I overlap. The x–axis is the mean ROI volume estimated by MAN I.

4.4.3 Discussion

We have developed robust guidelines (MAN I) for the delineation of subcortical regions relevant to dopamine. Overall MAN I performed very well, with high DICE coefficients and low BP_{ND} variability for both the intra– and inter–operator comparisons, which demonstrates the high reproducibility of the method. The guidelines have also been tested with other MRI sequences such as FLAWS [174] and FGATIR [171] and various image resolutions (0.78–1.5 mm) and they achieve similar levels of reproducibility, indicating the robustness of the method.

Table 4.3: ROI name and ROI volume. a=Fixed ROI size.

ROI name	ROI volume (cm^3)
VP_{SI}	0.1 ± 0.05
GP	0.8 ± 0.1
VST	1.0 ± 0.1
preVPU	1.1 ± 0.2
prePU	1.7 ± 0.2
PU	3.1 ± 0.3
preDPU	0.6 ± 0.1
posPU	1.4 ± 0.2
preCD	2.0 ± 0.2
CD	2.3 ± 0.3
posCD	0.3 ± 0.1
Hypo	0.5 ± 0.03
SN	0.3^a
TH	5.3 ± 0.4

As mentioned above, several studies have shown that there is not a definitive anatomical, histological or histochemical distinction between the nucleus accumbens, CD and PU. Therefore, the VST guidelines presented in this manuscript and other published guidelines are using anatomical landmarks to define the dorsal boundary of the ventral striatum. The rationale for selecting marker A and marker B in these guidelines was based on the following: a) the dorsal boundary encompasses the VST area as it is described in the literature; b) the two regions (corpus callosum and CD) that are used to define the two landmarks are less variable, at least in healthy humans, compared to the landmarks used in other methods (i.e. ventricles, internal capsule, anterior commissure) and the variability does not seem to affect the definition and reliability of the VST ROI. These criteria have been applied to more than sixty subjects and on the MNI template, and the defined VST ROI is well-matched with the area descried in the literature as limbic striatum; c) the definition of these markers is simple and reproducible and can be applied with high confidence even on low resolution data.

MAN I optimised the VST definition and the results indicate that MAN I outperformed

MAN II for both DICE and BP_{ND} variability metrics. There is a 10 % improvement in VST intra–operator DICE for MAN I over MAN II due to the more robust definition of the dorsal boundary of VST with MAN I. In particular, the definition of the dorsal boundary with MAN I involved connecting two predefined points that are placed before the tracing starts. MAN II is a more complex and subjective procedure as the operator needs to identify, on each slice, the most superior and lateral point of the internal capsule (sometimes difficult to identify) and the centre of the portion of the anterior commissure overlying the striatum. Another limiting factor for the VST definition with MAN II is that the anatomy of the area is such that sometimes the placement of the dorsal boundary with MAN II may not be optimal since it oversamples CD and/or PU.

The delineation of the PU on the transverse plane with MAN I was faster than with MAN II (defined on coronal plane) and gives the operator better control over the ROI boundaries with the GP and the clastrum. However, the delineation of the ROI on the most ventral slices can be difficult and a good knowledge of the anatomy is required in order to sample the correct region. Therefore, following the delineation of the PU on the transverse plane it is recommended that the operator switches to the coronal plane and optimises the intersection of PU and VST. It is important to note that the sub–parcellated striatal ROIs from MAN I (preVPU, preDPU, posPU, preCD, posCD) achieved similar DICE and BP_{ND} variability values compare to the gross anatomical regions (i.e. CD and PU), indicating that MAN I is highly reproducible for smaller regions. Additionally, MAN I required less time for the ROI delineation and both operators reported that MAN I guidelines were applied with increased confidence in noisier images. Overall, there was a good agreement between MAN I and MAN II which is reflected in the relatively high volume overlap between the ROIs defined with the two methods and the high ICC for the BP_{ND} values.

The performance of an automated method for the delineation of the aforementioned subcortical dopamine regions has been examined. Automated methods, such as the non–linear deformation of an anatomical atlas into the space of each individual, enables the analysis of large data sets within feasible time scales, and completely removes any operator subjectivity. On the other hand, they are susceptible to misalignment, especially for small and subcortical structures, causing misclassifications. Here the agreement between AUTO and MAN I was moderate. As expected, the inter–method DICE coefficient was not as high as the MAN I intra–method values. However, the inter–method BP_{ND} variability is similar to the inter–operator variability across regions, which indicates that the method could be used for estimation of BP_{ND} values in certain applications.

In this study we have employed SPM5 for non-linear registration, which was developed in 2005. A recent paper by Klein et al. [102] ranked this algorithm eleventh out of fourteen non-linear registration algorithms in terms of their performance with regard to cortical registration. The performance of the automated method that we presented here can improve significantly by employing other state-of-the-art non-linear registration algorithms such as FNIRT [8], SPM5 DARTEL [12], SyN [14] or ART [11] which were highly rated for their performance [102].

Chapter 5

Connectivity-based subdivision of the striatum and pallidum

5.1 Introduction

The basal ganglia (BG), and especially striatum and pallidum, have been the focus of dopamine research due to an abundance of dopamine receptors and their involvement in dopamine related diseases such as Parkinson's and schizophrenia. The BG act in conjunction with the cortex to control and execute behaviours and although their connections have been extensively studied they are still among the least understood of all brain structures. The striatum is a heterogeneous structure, which consists of three, cytoarchitectonically undifferentiated areas, the CD, PU and NAC. The pallidum consist of the globus pallidus (GP), which is structurally subdivided into GP_i and GP_e segments (figure 2.5), and the ventral pallidum (VP).

Autoradiography studies have shown that dopamine receptors are not always uniformly distributed within these traditional striatal and pallidal subdivisions [71, 169]. Microdialysis studies in rats have also shown that, following a chemical challenge, the extracellular dopamine concentration is higher in the ventral striatum than the dorsal striatum [28, 48, 49, 47]. Moreover, molecular imaging studies have demonstrated that dopamine, in response to a pharmacological or behavioural challenge, is released differentially in both the dorsal–ventral and anterior–posterior directions

[54, 127, 129]. The observed dorsal–ventral differential release could be explained anatomically by the present of the NAC. However, the anterior–posterior differentiation is not justified by anatomical criteria. These observations led researchers to seek ways of improving the methods employed for the regional quantification of dopamine.

Enhancements in the spatial resolution of PET scanners and the development of MRI and PET image co-registration methods allowed a more detailed *in–vivo* investigation of regional dopamine distribution. In 1999, Drevets and colleagues [54], incorporated information from structural MRI and developed a method that subdivides the striatum into ventral and dorsal, in order to study the amphetamine–induced dopamine release. This method was further developed by Martinez and Mawlawi [127, 129] who attempted to approach the functional organisation of the striatum, incorporating information from non human primate tracing studies, by subdividing the putamen into pre–commissural and post–commissural. Ventral striatum was classified as the limbic striatum, post–commissural PU as sensorimotor and the remaining striatum as cognitive. The aforementioned approaches, which employ anatomical landmarks to approximate the functional striatal sub–regions, were the first attempt to quantify dopamine beyond the traditional anatomical boundaries.

It is known from lesion studies that the functional characteristics of a structure are determined by the neuronal projections that it receives. In non human primates, tracing and degeneration experiments have studied the distribution of the cortical inputs [6, 72, 75, 99, 141] to the BG and the neuronal connections among the BG nuclei. These studies have shown that the BG are functionally organised into motor, executive and limbic domains and have revealed the existence of individual and overlapping cortical-striatal networks. More recently, the advent of DWI and of tractography algorithms made it possible, for the first time *in–vivo* for humans, to study the cortical–subcortical projections [25, 39, 41, 52, 115, 116, 117] demonstrating that

the human and non human primate functional topography are similar. In this chapter, we use DWI and probabilistic tractography [20] to determine the striatal–cortical and pallidal–striatal projections, in individual subjects, in order to segment the striatum and pallidum into functional subregions. To obtain the connectivity-based subdivisions of the striatum the cortex is subdivided into seven anatomical regions that are named either according to their functional specialisation or their anatomy (limbic, executive, rostral-motor, caudal-motor, parietal, occipital and temporal). Then we estimate the connection probabilities between the striatum and each cortical target and according to these probability estimates we segment the striatum. Similarly, for the subdivision of the pallidum, the limbic, executive and sensorimotor (rostral-motor, caudal-motor and parietal striatal segmentations combined into one region) striatal subdivisions were used to estimate the connection probabilities with the pallidum. The methodology presented here will be used in subsequent chapters to investigate the distribution of dopamine receptors and quantify dopamine release within these sub-regions.

5.2 Basal ganglia connections

The cortical–subcortical connections are organised into partially closed cortical–BG-thalamic–cortical loops with each structure maintaining the functional characteristics of the projective region. Striatum, GP, SN, and STN comprise the BG and the intrinsic interconnections of these nuclei create a large subcortical network for information processing. The individual constituents of the striatum are the main input nuclei of the BG and receive a direct cortical input whereas GP_i and SN_r are the two output nuclei, which project back to different cortical areas of the frontal lobe via the thalamus. The intrinsic projections of the BG are organised into two pathways, the "direct pathway" and the "indirect pathway" (figure 5.1). The "direct pathway" refers to projections from the striatum to the GP_i and SN_r. The "indirect pathway", which

provides a second route linking the striatum with GP_i and SN_r, involves the projections from the striatum to the GP_e, which in turn projects to the GP_i and STN. The STN subsequently projects to the two output nuclei (GP_i and SN_r) [149].

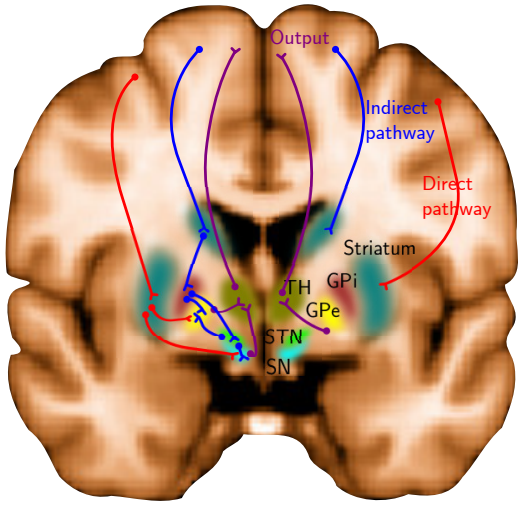

Figure 5.1: Diagram shows the "direct pathway" (red) and "indirect pathway" (blue) of the BG interconnections. GP_e: globus pallidus, external, GP_i: globus pallidus, internal, TH: thalamus, STN: subthalamus, SN:substantia nigra.

The cortical–striatal input is the first step in the transposition of the functional cortical map onto the BG nuclei [141]. While all cortical lobes project to the striatum, the frontal lobe projections occupy the bulk of the striatum. According to physiological and anatomical observations [6, 72, 141, 145] the cortical inputs are organised into parallel (segregated) and overlapping (integrated) circuits (figure: 5.2). There exist two models with regard to the processing of cortical information from these circuits: A) The parallel processing model infers that the cortical-striatal projections are organised into five functionally distinct circuits named according to the cortical target or known function: motor, oculomotor, dorsolateral prefrontal, lateral orbitofrontal and anterior cingulate. The parallel model sees the cortical projections as parallel and isolated loops that process the cortical information independently at specific and

non-overlapping zones, which then project back to the cortical area of origin via the thalamus [141]. B) The integrative processing model, in contrast, proposes that the distinct cortical loops converge in the BG. In these overlapping areas information is integrated and processed and is sent back to the cortex [141].

These models are believed to be an over-simplification of the true information processing that takes place in the BG as neither of them can entirely explain the BG function and also neither is exclusive of the other [179].

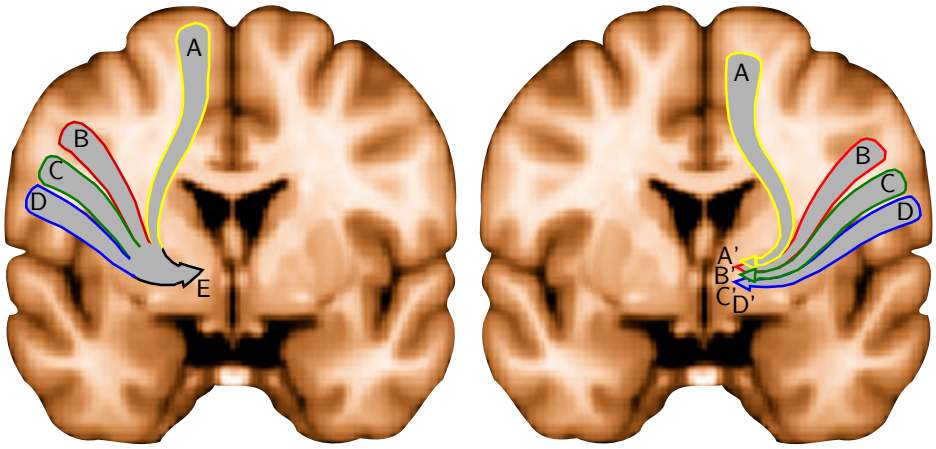

Figure 5.2: Diagrams show the two prevailing views on the processing of cortical information as it flows in the BG. Left: Integrative processing model; functional information from distinct cortical areas is converging in the BG. Right: Parallel processing model; functional information from distinct cortical areas are processed independently. Figure adapted from Parent and Hazrati [141].

Kemp and Powell [98] first suggested that the cortical–striatal projections are a point–to–point transfer with each striatal area receiving input from the nearest overlying cortical area, with only a slight overlap from the cortical projections. In 1985, Selemon and Goldman-Rakic [157] proposed that a longitudinal pattern represents most or all cortical–striatal projections without a strict point–to–point organisation. Another view of the cortical–striatal organisation is that non–adjacent cortical areas project

to adjacent striatal areas, subdividing the striatum into distinct functional sectors namely executive, limbic and sensorimotor [141, 157]. According to this theory, in non-human primates, the executive territory occupies large parts of the CD and the pre–commissural PU, the sensorimotor comprises the dorsolateral post–commissural PU and the dorsolateral rim of the head of the CD nucleus while the limbic striatum comprises the nucleus accumbens and the ventral pre–commissural parts of the CD and PU (figure 5.3) [141, 157].

Fibers from striatum arborise within the pallidum and SN transposing the striatum's functional map. At the outset, the pallidum was considered as a structure where striatal fibers intensively converge, leading to integration of the striatal functional information [84, 145]. However, new data [141] showed that neighbouring striatal cell populations do not have overlapping terminal fields in the pallidum and that the striatal–pallidal projections are highly organised into a specific pattern. Thus, the organisation of the striatal–pallidal system reflects the functional organisation of the cortical–striatal system (figure 5.3). According to Parent and Hazrati [141], neurones from the executive striatal territory project to the pre–commissural GP, the dorsomedial third of the post–commissural GP and large sectors of the SN_r. Neurones in the sensorimotor striatum project to the ventrolateral two thirds of the post–commissural GP and parts of the SN, whereas neurones originating in the limbic striatum project to the VP, the ventromedial rim of the rostral GP_e, the medial GP_i and parts of the SN_r.

In humans, results from DWI studies have shown that the human striatal functional organisation is similar to the non-human primates with distinct functional sectors and with segregated and overlapping pathways [25, 39, 41, 52, 115, 116, 117]. However, to the best of our knowledge, the functional organisation of the pallidum has not been studied. Draganski and Lenglet [52, 117] have investigated the projections from the CD and PU to pallidum but not from the functional striatal sub-regions. Therefore it

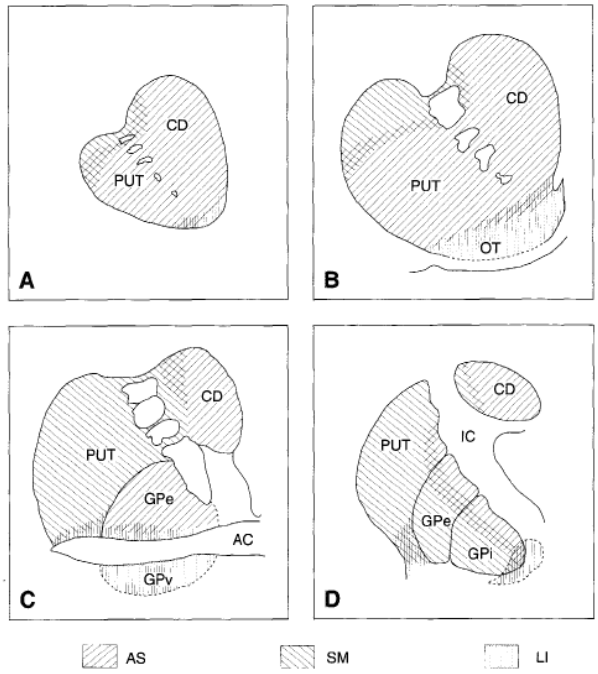

Figure 5.3: Schematic representation of the striatal and pallidal functional organisation in primates. AS: associative, SM: sensorimotor and LI: limbic territories. Figure courtesy of Parent and Hazrati [141].

is not known whether the striatum transposes its functional organisation to pallidum in a topographical manner similar to that of non-human primates.

5.3 Connectivity–based subdivision of the striatum

In this section of the thesis we subdivide the striatum, in each human subject, into functional subregions according to their cortical connections. To accomplish this step we have used DWI data and probabilistic tractography algorithms [21]. In total 26 healthy human volunteers were scanned and to achieve the connectivity-based subdivision, a two-phase procedure was applied. Phase I: the projections between the four brain lobes (frontal, parietal, occipital, temporal) and the striatum were calculated and the striatal areas associated with each lobe were established; Phase II: The frontal lobe was subdivided into four anatomical ROIs, each associated with a particular functional specialisation (limbic, executive, rostral motor and caudal motor), and

projections between these anatomical ROIs and the striatal area associated with the frontal lobe were estimated. Figure 5.4 is an overview of the processing steps applied to obtain the connectivity–based subdivisions.

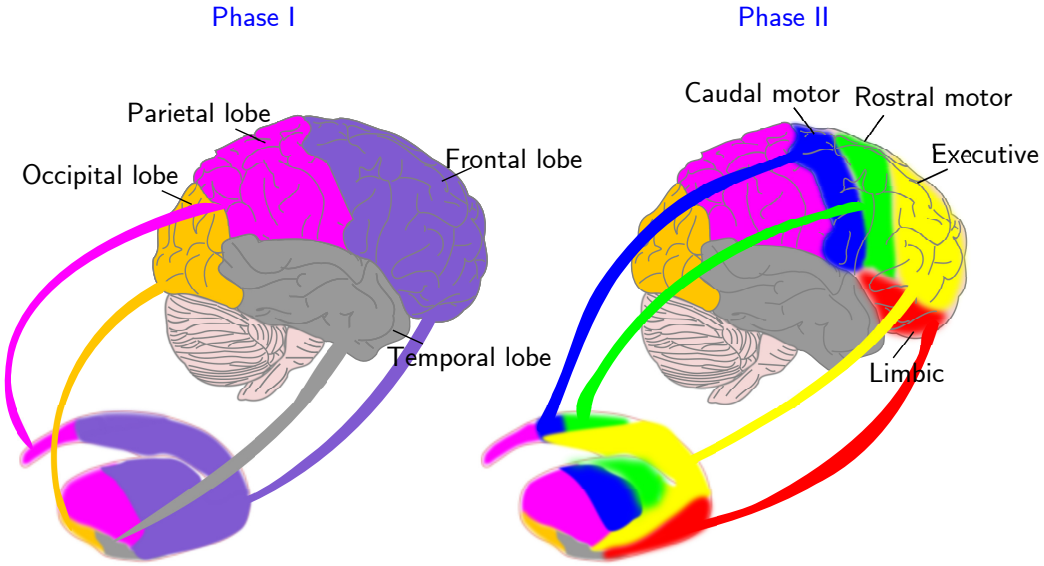

Figure 5.4: Methods overview. To obtain the connectivity-based functional regions in each subject a two-step procedure was applied: Phase I) the projections from the four brain lobes (frontal, parietal, occipital, temporal) to the striatum were calculated and the striatal areas associated with each lobe were established; Phase II) The frontal lobe was subdivided into four anatomical ROIs, each associated with a particular functional specialisation (limbic, executive, rostral motor and caudal motor), and projections between these anatomical ROIs and the striatal area associated with the frontal lobe were estimated

5.3.1 Materials and methods

Subjects

The study was conducted at the GlaxoSmithKline Clinical Imaging Centre, Hammersmith Hospital, London and was approved by Essex 1 Research Ethics Committee and the Administration of Radioactive Substances Advisory Committee (ARSAC). Twenty-six (26) healthy male volunteers were recruited aged between 25 and 60 years, free

from clinically significant illness or disease as determined by their medical history and standard laboratory tests. Each subject underwent a series of MRI scans including T1-weighted and DWI data. Subjects provided written informed consent.

Data acquisition

Data were acquired on a Siemens Tim Trio, 3T MRI scanner (Siemens Healthcare, Erlangen, Germany) with a 32–channel head coil. Two imaging protocols were used for data acquisition. For the first data set (12 subjects) the diffusion weighting was isotropically distributed along 30 directions (b-value = $1000\,\mathrm{s/mm^2}$) and a non-diffusion-weighted image (B0) was acquired at the beginning of each scan. DWI data were acquired using echo planar imaging (EPI) with TR = 9000 ms, TE = 86 ms, flip angle of 90° and voxel size of $1.875 \times 1.875 \times 1.9\,mm^3$. An isotropic T1-weighted image ($1\,mm^3$) was acquired with a magnetisation-prepared rapid gradient echo (MPRAGE) sequence (TR = 3000 ms, TE = 3.66 ms, flip angle of 9°, TI = $1100\,ms, matrix = 256 \times 192$). A parallel imaging factor of 2 was applied to enable an acquisition time of $321\,s$. For the second data set (14 subjects) the diffusion weighting was isotropically distributed along 64 directions ($b-value = 1000\,s/mm^2$, TR = $9300\,ms$, TE = $88\,ms$, flip angle of 90° and voxel size of $1.9\,mm^3$ isotropic) and a non-diffusion-weighted image (B0) was acquired at the beginning of each scan. For the acquisition of structural images the FLAWS sequence [174] was used using the ADNI-GO recommended parameters: $256 \times 192mm$ field of view (FOV), $1\,mm^3$ isotropic resolution, parallel imaging (PI) factor of 2, TI = $409\,ms$ in $321\,s$.

EPI acquisitions are prone to geometric distortions which can lead to errors in tractography [9]. To minimise this, for both datasets, two DWI image sets were acquired with the phase encoded direction reversed ("blip-up" and "blip-down" [35]),

resulting in images with geometric distortions of equal magnitude but in the opposite direction, allowing for the calculation of a corrected image [10]. Before correcting geometric distortions, each image set was corrected for motion and eddy-current related distortions using FSL tools (FMRIB software library, Oxford University http://www.fmrib.ox.ac.uk/fsl/).

Probabilistic tractography

FMRIB's diffusion toolbox (http://www.fmrib.ox.ac.uk/fsl/fdt) was used to perform probabilistic tractography [20], which allowed for up to two fiber directions in each voxel [19]. Five thousand sample tracts were generated from each voxel in the seed mask (striatum). The tractography was performed in the subjects' continuous space and the results were output in the MNI space by providing transformation parameters estimated via a two-step procedure as follows: a) the fractional anisotropy image was registered to each subject's high resolution T1-weighted image using FLIRT [89] with 6 degrees of freedom and a mutual information cost function; b) the T1-weighted image was non-linearly registered to the $1 \times 1 \times 1\, mm^3$ nonlinear MNI template with FNIRT [8]. The transformation parameters obtained from these two steps were concatenated to yield the mapping from DWI to MNI space.

Striatal functional subdivision – Phase I

The projections from the frontal, parietal, occipital and temporal cortical areas to the striatum were estimated. For each striatal voxel we calculated the probability of connection to each area as a proportion of the total number of samples from that voxel that reach any cortical area. Following this, the striatum was segmented by assigning each voxel to the lobe with which it had the highest connection probability [92]. This "hard" segmentation establishes the association of the areas in the striatum

with each lobe.

Striatal functional subdivision – Phase II

The striatal area that was found in Phase I to be associated with the frontal lobe, is subdivided into the following functional regions: a) limbic, involved in emotions, reward and motivation; b) executive, linked to executive processes such as perception, memory, reasoning and judgment; c) rostral-motor, involved in the planning and control of movements; and d) caudal-motor, involved with the execution of movements. Four frontal lobe anatomical subdivisions (described below), each associated with the aforementioned functions, were used to estimate connection probabilities within the striatal area associated with the frontal lobe. Note that these cortical ROIs are not derived from functional MRI experiments but make use of the known anatomical areas of specific brain function, as determined from the human and primate literature.

At the end of Phase I and Phase II, for each subject and for each hemisphere, seven connection maps were derived, one for each cortical target (limbic, executive, rostral-motor, caudal-motor, parietal, occipital and temporal). Since individual and overlapping cortical-striatal networks may exist, striatal voxels are either connected exclusively to a cortical target or show connectivity to multiple cortical regions. To accommodate this finding we process the connectivity maps in two different ways: a) for each subject, exclusive connectivity-based functional ROIs (CBe) were created following the procedures described by Johansen-Berg and colleagues [92]. In brief, for each striatal voxel the probability of connection to each cortical target was calculated as a proportion of the total number of samples from that voxel that reach any cortical area; next, each voxel was assigned to the cortical target with the highest connection probability. The second way of processing the connectivity maps was; b) each subject's connectivity maps were thresholded at 1%, 5% and 10% of the maximum

connectivity value to exclude noise and voxels with low connectivity values. These particular thresholds were selected on the basis that these are the most commonly used thresholds in DWI studies [20, 25, 41]. The second way creates functional subdivisions that incorporate voxels that are exclusively connected to a cortical target and voxels that concurrently connect to other cortical zones (overlapping networks). The functional areas obtained with this method will be respectively abbreviated as follows: CBo-thr1 (1% threshold), CBo-thr5 (5% threshold) and CBo-thr10 (10% threshold).

Striatal connectivity–based atlases

To create population maps of the connectivity profile of each cortical area with the striatum, for each voxel the number of subjects with a connection probability (between that striatal voxel and the cortical target) higher than 50% was estimated. These connectivity population maps were, in addition, used to create a population atlas. To create the atlas, each voxel in the striatum was assigned to the cortical target that had the majority of subjects connected to that target.

Region of interest preparation

To perform the probabilistic tractography the striatum and the cortical ROIs were defined for each subject in order to serve as the seed and target masks respectively. The striatum was manually defined on the subject's T1-weighted image and the cortical lobes were obtained from the atlas described in chapter 4. As the frontal lobe sends a massive number of projections to the striatum [25, 72, 141] and is the main driving force for its functional organisation the frontal lobe was subdivided into four anatomical regions, based on the known anatomical classification of function (figure 5.5). Details of the four frontal lobe subdivisions are as follows:

Limbic target: The structures comprising the limbic anatomical ROI are the anterior orbital gyrus, posterior orbital gyrus, medial orbital gyrus, gyrus rectus [36], and subcallosal gyrus – ventral anterior cingulate (parolfactory area - area 25). The subcallosal gyrus – ventral anterior cingulate has strong connections with the amygdala and hypothalamus and is an area where reward and emotion related activations are observed [17]. Rolls has demonstrated that the orbitofrontal cortex is involved in representing primary reinforces and has important functions in motivational behaviour and emotion [153]. The lateral orbital gyrus was excluded since several studies report that it has a different connectivity pattern and function from the medial orbital cortex [106, 186, 152]. The dorsal anterior cingulate was excluded as well from the limbic target as it has a different connectivity profile from that of the ventral cingulate and also is activated during memory related tasks [17].

Executive target: The functional map proposed by Petrides [146] was adopted to delineate areas 9, 9/46 and area 10 of dorsolateral prefrontal cortex which constituted the executive ROI. Anatomically the ROI consisted of the rostral superior and middle frontal gyri and the dorsal prefrontal cortex ($3mm$ above the mid-sagittal most anterior and dorsal tip of gyrus rectus where area 10 is situated).

Rostral-motor target: The caudal portions of lateral and medial superior gyrus, and the caudal middle and inferior frontal gyri were included in the rostral-motor target. These anatomical regions correspond functionally to rostral area 6 and area 8 and are described as premotor areas [139]. Functionally there are similarities between the anatomical subregions that constitute the rostral-motor target but lesion studies have also shown that there are distinct effects [143, 146]. However, a detailed investigation of the various subregions of the premotor target is beyond the aim of the current study therefore the areas are combined into one region.

Caudal-motor target: Includes the pre-central gyrus, which corresponds functionally to the primary motor cortex (area 4), and the caudal premotor area (caudal area 6).

To tailor the cortical masks to the subjects' individual anatomy, the subjects' segmented grey matter (GM) and fractional anisotropy (FA) images, both normalised to the MNI template, were used to mask the ROIs. The lower threshold for the GM mask was set at 0.25 and the FA mask upper threshold was set at 0.40.

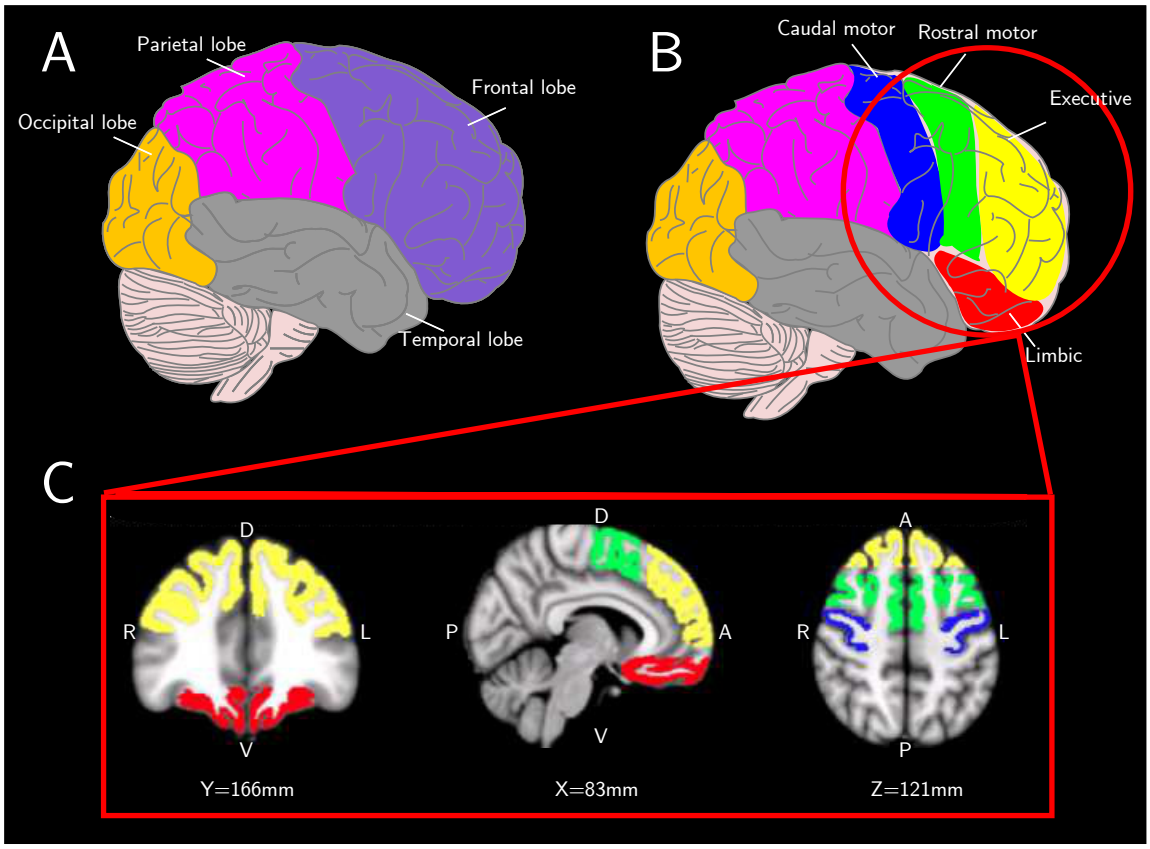

Figure 5.5: Subdivision of the cortex: A) cortical lobes; frontal lobe (purple), parietal (magenta), temporal lobe (grey) and occipital lobe (orange) B–C) The four frontal lobe targets, overlaid on the average MNI template. Yellow corresponds to the executive, red to the limbic, green to the rostral-motor and blue to the caudal-motor target mask. R=right; L=left; A=anterior; P=posterior; D=dorsal; V=ventral.

5.3.2 Results

Projections from cortical lobes - Phase I

While all cortical lobes project to the striatum, the areas that each lobe's efferent projections occupy are not equally represented. After hard segmentation of the striatum across subjects, the frontal lobe input dominates with $82 \pm 7\,\%$ of the total striatal volume (frontal lobe grey matter volume: $248 \pm 14\,cm^3$), followed by the parietal lobe with $11 \pm 5\,\%$ (parietal lobe grey matter volume: $116 \pm 7\,cm^3$), the temporal lobe with $5 \pm 5\,\%$ (temporal lobe grey matter volume: $114 \pm 3\,cm^3$) and the occipital lobe with $2 \pm 1\,\%$ (occipital lobe grey matter volume: $85 \pm 3\,cm^3$). Table 5.1 shows the volume that cortical projections occupy after the hard segmentation as well as for the CBo-thr1, CBo-thr5 and CBo-thr10 projections.

The cortical projections were estimated for each subject and the group average inputs (after hard segmentation) are shown in figure 5.6 whereas the population connectivity maps are shown in figure 5.7. The frontal lobe input occupies almost the entire CD and pre–commissural PU extending up to the post–commissural PU. Parietal lobe, the second biggest cortical input, projects primarily to the post–commissural CD and PU with scattered projections observed in the pre–commissural CD and VST (figures 5.6 and 5.7). In contrast, with input from the frontal and parietal lobes, projections from the occipital and temporal lobes are more confined (figure 5.6 and 5.7). Small interspersed projections from the temporal lobe were found in the pre–commissural CD, VST and in the ventral post–commissural PU whilst occipital projections were limited to the ventral post–commissural PU. The projections of each lobe occupy distinctive striatal areas with a significant degree of overlap observed between frontal and parietal lobes in the post–commissural PU and VST and some overlap between frontal and temporal lobes in the VST and post–commissural regions. The large number of

frontal lobe projections into the striatum confirms that these two regions interact extensively to coordinate and execute function.

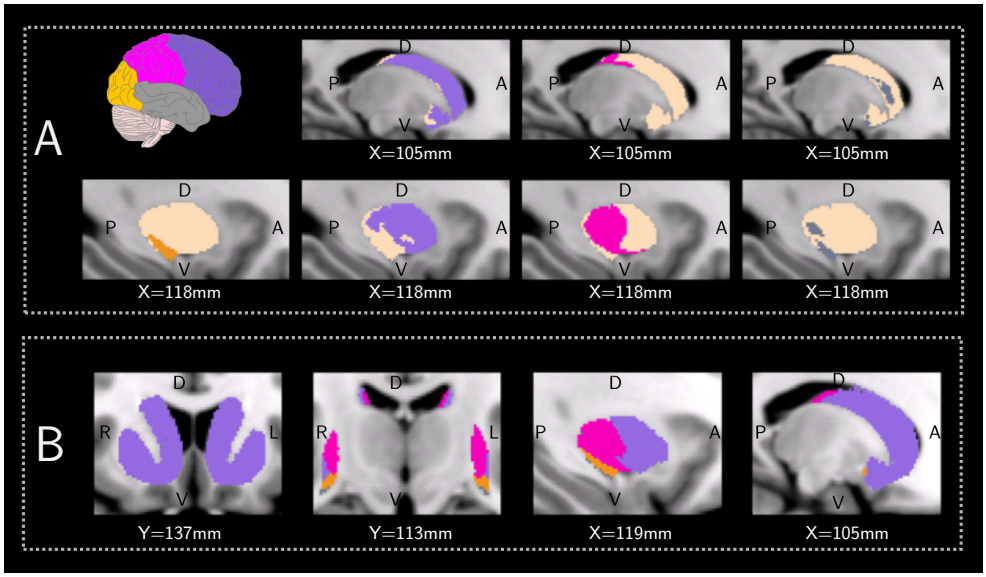

Figure 5.6: A) Group average projections (first data set) after hard segmentation, in the MNI space sagittal view, of the four cortical lobes to the striatum. Top row, left image shows the four cortical lobe subdivisions; frontal lobe (purple), parietal (magenta), temporal lobe (grey) and occipital lobe (orange). The remainder of the first row shows the projections of each lobe to the caudate and second row corresponds to projections in putamen. The beige colour corresponds to the striatal mask. B) Areas within the striatum where the connections from each lobe prevail. R=right; L=left; A=anterior; P=posterior; D=dorsal; V=ventral.

Projections from frontal lobe subdivisions - Phase II

Distinct, overlapping and bilaterally symmetric projections, from the four anatomical subdivisions of the frontal lobe (limbic, executive, rostral-motor and caudal-motor), were derived (figure 5.7) and were consistent with those obtained from non-human primate tracing studies [32, 75] and confirmatory of previous human DWI studies [52, 116]. The limbic striatum occupies the NAC and ventral pre–commissural CD and PU. Of particular interest are the patches of limbic projections observed in the ventral post–commissural PU, an area where projections from the temporal lobe and

Table 5.1: Volume and percentage contribution to the total striatal volume of the cortical projection at thresholds of 1%, 5%, and 10% (CBo methods). CBe is the volume and contribution to the striatal volume of exclusively connectivity–based ROIs (assignment of each voxel to the cortical target with the highest connection probability). Results are averaged between the left and right hemispheres.

	CBo-thr1		CBo-thr5		CBo-thr10		CBe	
Region/function	Volume (cm^3)	Contribution to striatal volume (%)	Volume (cm^3)	Contribution to striatal volume (%)	Volume (cm^3)	Contribution to striatal volume (%)	Volume (cm^3)	Contribution to striatal volume (%)
Limbic	2.42 ± 0.83	20.83 ± 7.17	1.36 ± 0.49	11.68 ± 4.23	1.03 ± 0.43	8.89 ± 3.69	2.32 ± 0.79	19.89 ± 6.70
Executive	5.86 ± 1.66	46.96 ± 14.18	3.04 ± 1.42	26.17 ± 12.37	1.97 ± 1.15	16.99 ± 10.08	5.73 ± 1.15	49.20 ± 9.49
Rostral–motor	1.67 ± 0.62	14.41 ± 5.48	0.65 ± 0.40	5.64 ± 3.44	0.36 ± 0.29	3.14 ± 2.53	1.00 ± 0.53	8.65 ± 4.51
Caudal–motor	1.67 ± 0.71	14.39 ± 6.23	0.65 ± 0.38	5.61 ± 3.37	0.33 ± 0.22	2.85 ± 1.94	0.45 ± 0.30	3.82 ± 2.59
Parietal	4.80 ± 1.56	41.30 ± 13.71	2.50 ± 1.02	21.51 ± 8.93	1.70 ± 0.71	14.63 ± 6.16	1.29 ± 0.52	11.09 ± 4.56
Occipital	1.91 ± 1.07	16.43 ± 9.17	0.69 ± 0.42	5.91 ± 3.65	0.41 ± 0.26	3.55 ± 2.28	0.23 ± 0.14	1.97 ± 1.21
Temporal	4.38 ± 1.44	37.81 ± 12.77	1.58 ± 0.76	13.71 ± 6.67	0.79 ± 0.48	6.86 ± 4.26	0.60 ± 0.60	5.16 ± 5.17

amygdala can also be found. For pre–commissural striatum, the executive projections reside in the central and dorsal striatum as opposed to the post–commissural striatum where they occupy the central and ventral zones. The rostral-motor target projects to an elongated area that occupies the dorsal tiers of PU and CD. In contrast, the caudal-motor projections are confined to the post–commissural PU with only a few low probability connections in the anterior dorsal CD. Figure 5.8 show the subdivisions with the CBe method in four representative subjects, which are symmetrical and spatially coherent across individuals, while figure 5.9 shows the population atlas. The volume and percentage contribution to the total striatal volume of the cortical projections defined with the CBo-thr1, CBo-thr5, CBo-thr10 and CBe methods are shown in Table 5.1, with the projections from the executive target occupying the greatest area. Figure 5.10 illustrates the impact of different thresholds on the topography and size of the cortical projections.

Frontal lobe overlapping projections

Tracts from the frontal lobe led to overlapping pathways (figure 5.11) and were categorised as a) limbic–executive, b) executive–rostral-motor, c) executive–caudal-motor and d) rostral-motor–caudal-motor. A threshold of 50 samples was applied to the projections and subsequently the overlapping areas were determined. The limbic–executive overlap occupies the ventral medial area of the pre–commissural CD and the posterior and ventral post–commissural PU. The location of this overlap agrees with that of non human primates as described by Haber and colleagues [75]. The executive–rostral-motor overlap is the most extensive and resides in the dorsal pre–commissural striatum and post–commissural PU. Even though it is spatially consistent with the overlaps described in primates [32], in our human study it appears to extend further. The executive–caudal-motor overlap is found only in the post–commissural striatum

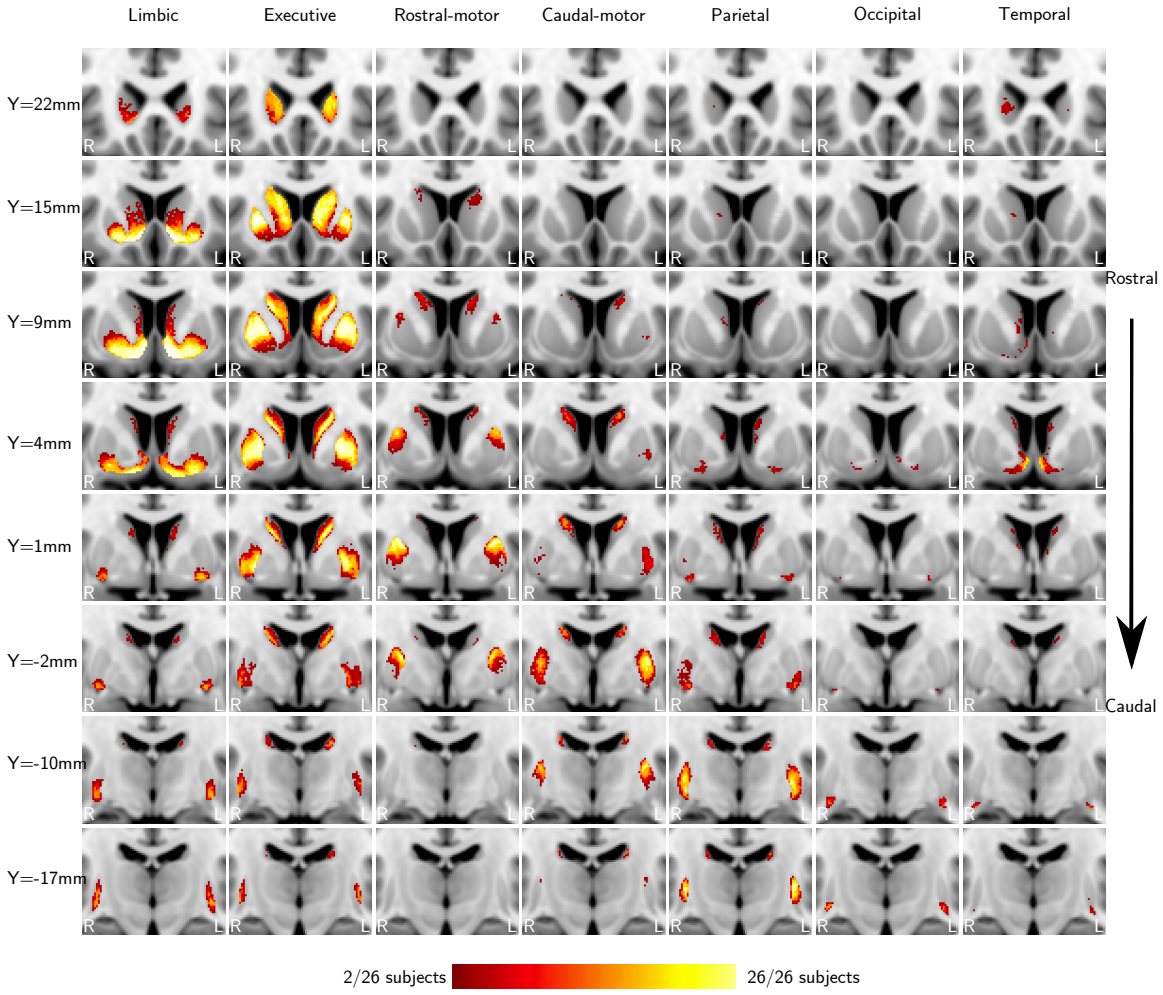

Figure 5.7: Population connectivity maps of each cortical area with the striatum. To create the maps, for each voxel the number of subjects with a connection probability (between the striatal voxel and the cortical target) higher than 50% was estimated. The connectivity maps are overlaid on the MNI template. R=right; L=left.

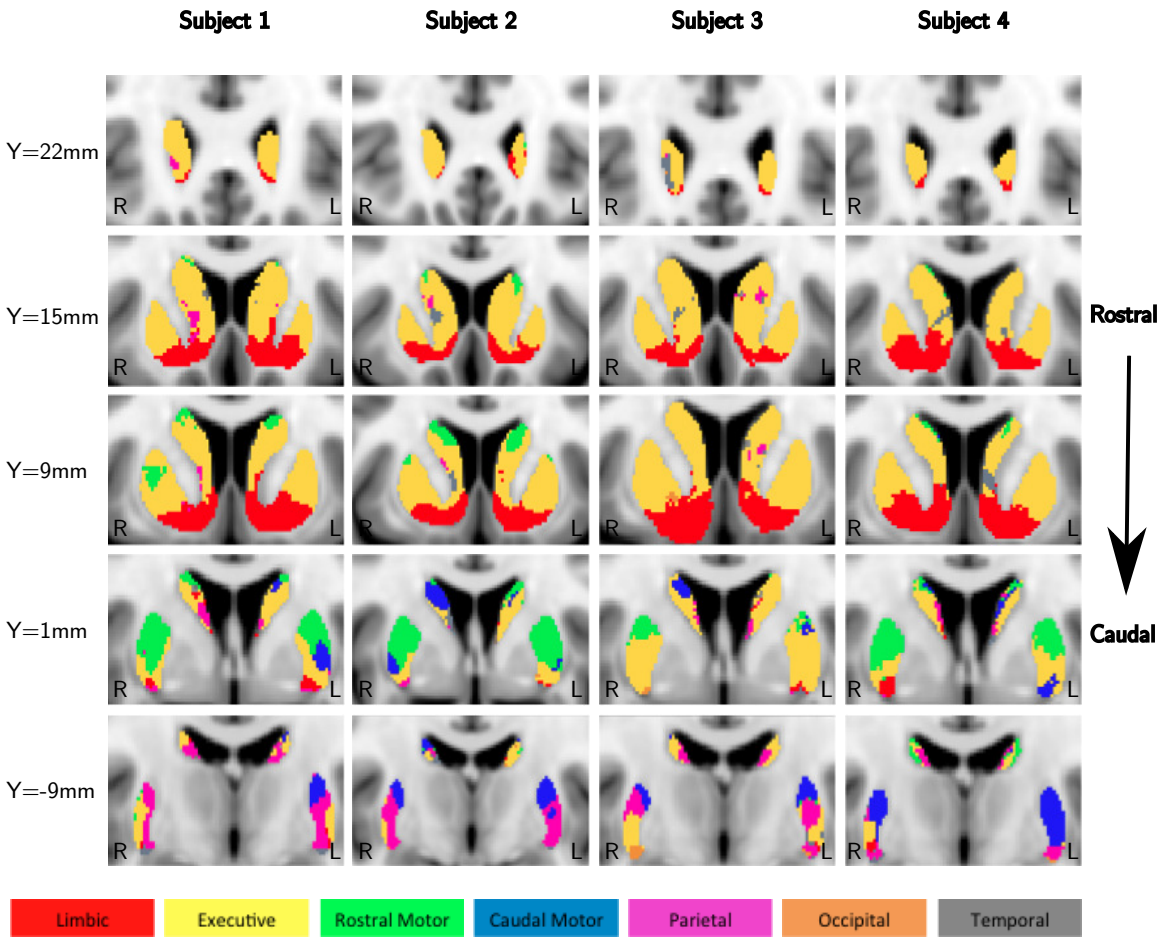

Figure 5.8: Individual functional subdivisions in four randomly selected subjects (MNI space — coronal planes). Each column corresponds to a subject starting from rostral (top row) to caudal (bottom row). To obtain the functional subdivision for each subject a two-step procedure was applied. First the projections from the four brain lobes (frontal, parietal, occipital, temporal) were calculated and each lobe's dominant area was established. Subsequently, the frontal lobe was subdivided into four anatomical regions of interest, each associated with a specific function (limbic, executive, rostral-motor and caudal-motor) and the projection of each target to the frontal lobe dominant area was estimated. Each voxel was assigned to the target that gave the highest connection probability. R=right; L=left.

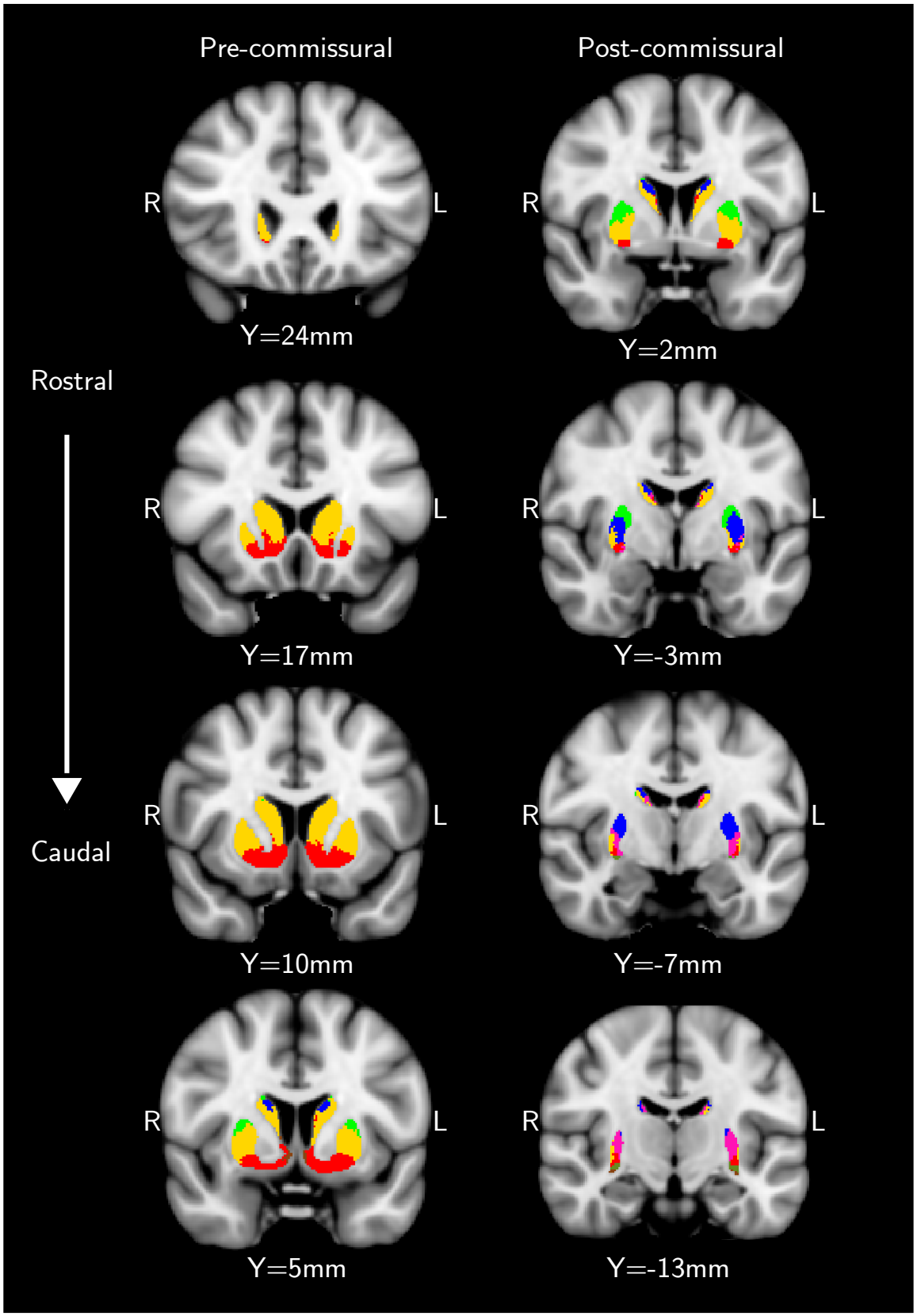

Figure 5.9: Connectivity–based population atlas of striatum overlaid on the MNI template (MNI space – coronal planes). First column corresponds to the pre-commissural and second column to post-commissural striatum. Colour-scheme is as follows: red = limbic, yellow = executive, green = rostral-motor, blue = caudal-motor, magenta = parietal, grey = temporal lobe and orange = occipital lobe. R=right; L=left.

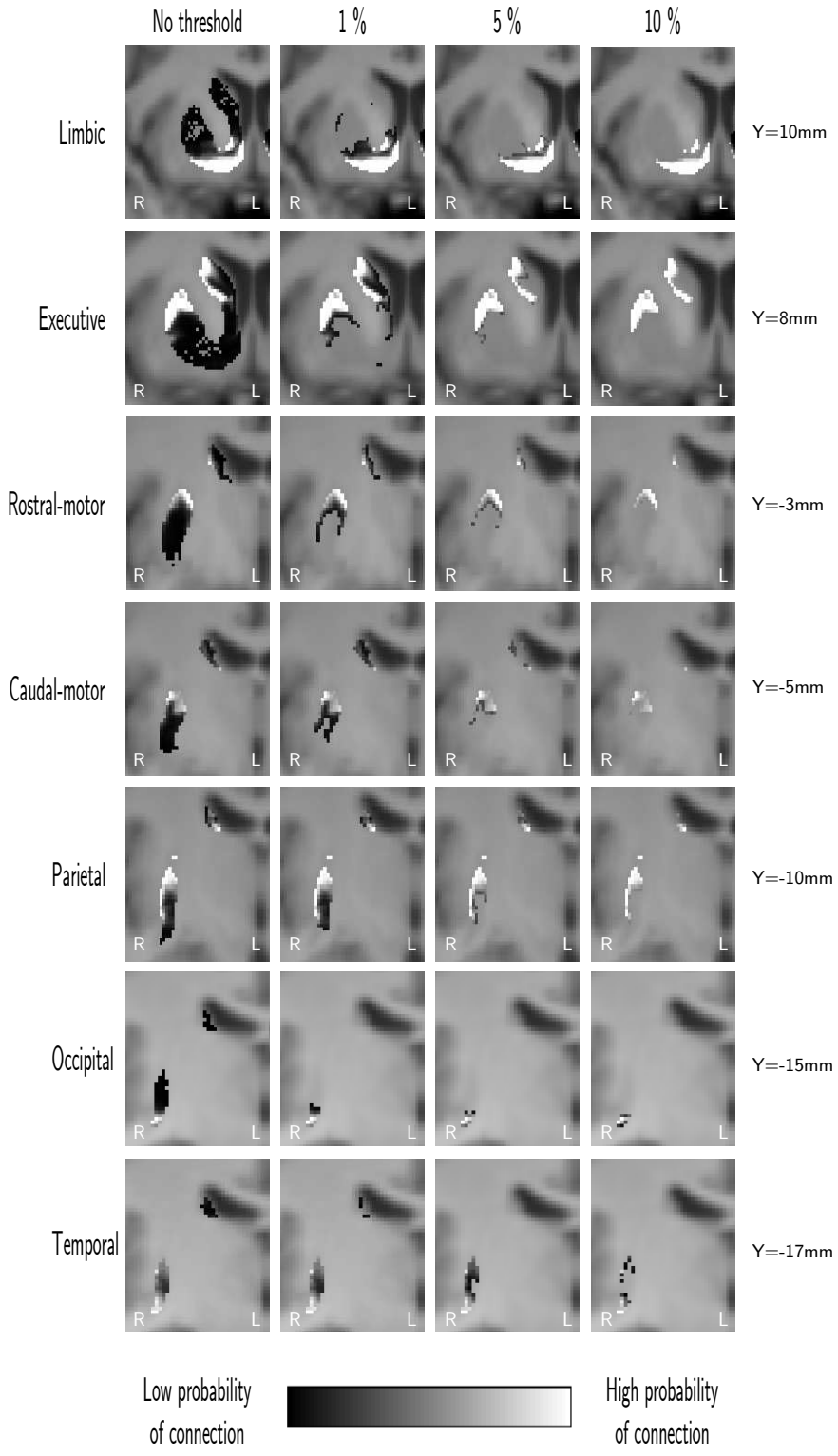

Figure 5.10: Effect of thresholds on the cortical–striatal connectivity maps in a representative subject. The first column shows the total projection from each target to the striatum. Subsequent columns show the connectivity maps after thresholded at 1%, 5% and 10% of the maximum connectivity value respectively. R=right; L=left.

and specifically in the dorsal CD and dorsal and central lateral PU. Finally, the rostral-motor–caudal-motor overlap is found in the post–commissural lateral PU. In order to examine the sensitivity of these finding to the arbitrary choice of threshold, we applied increasing levels of threshold (1 %, 5 % and 10 %) to the tractography results for each striatal projection. Although the occupied volume of the overlapping areas changed substantially from the threshold of 1 % to that of 10 % the aforementioned overlaps were preserved. This evidence and the fact that the existence and location of these overlaps have been confirmed by tracing studies, supports their use to report dopamine-related measures in the corresponding areas.

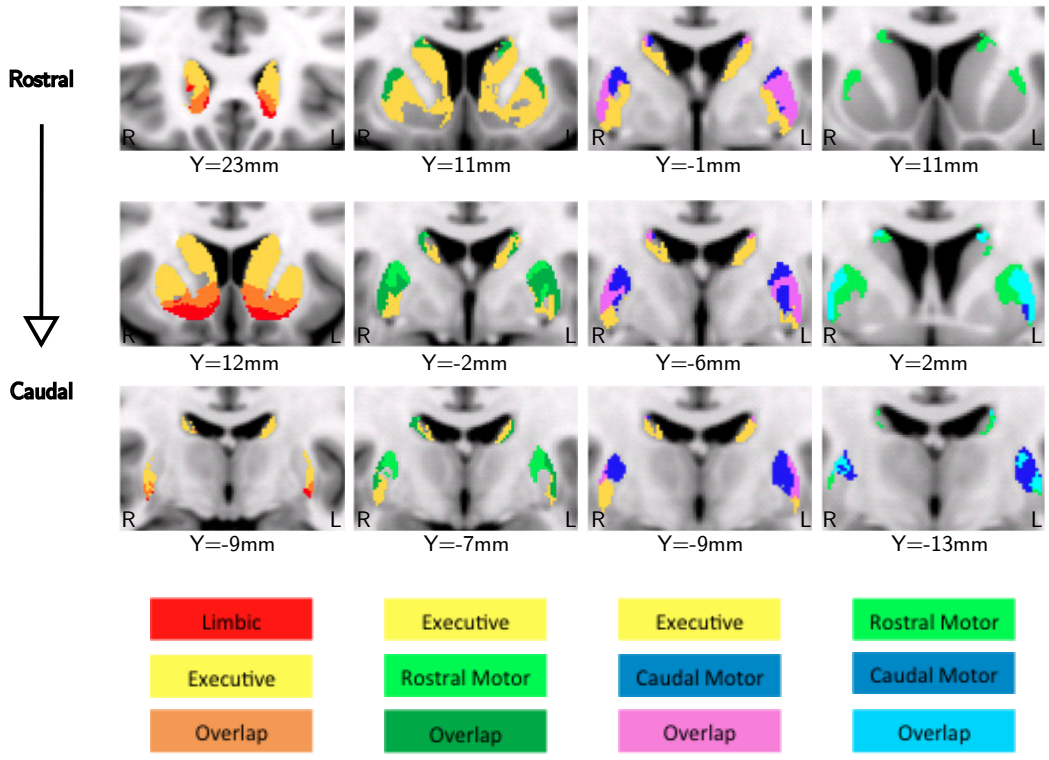

Figure 5.11: Overlapping projections in the striatum averaged across subjects and overlaid on the MNI template (MNI space – coronal planes). The columns correspond to overlaps between: i) limbic and executive (first column); ii) executive and rostral-motor (second column); iii) executive and caudal-motor (third column); and iv) rostral-motor and caudal-motor (fourth column). A threshold of 50 samples was applied to the projections and subsequently the overlapping areas were determined. R=right; L=left.

5.3.3 Discussion

Our findings show bilaterally symmetric and topographically consistent projections of the cortical targets to the striatum, which are organised into discrete and overlapping networks. The spatial consistency of the connectivity-based subdivisions is reflected qualitatively by the consistency of the functional classifications across subjects respectively (figure 5.8). For the connectivity-based functional subdivision of the striatum two diffusion datasets were used. For the first data set twelve subjects were recruited and the diffusion weighting was isotropically distributed along thirty (30) directions. For the second dataset fourteen subjects were employed and the diffusion weighting was distributed along sixty-four (64) directions. The thirty-directions datasets generally recover similar cortical-striatal pathways to those found with sixty-four-directions datasets and the functional parcellation of the striatum yields consistent results across subjects. A difference that was observed in the functional parcellations of the striatum in five out of fourteen subjects, who had sixty-four directions DWI data, was the ability to recover the cortical limbic projections to the medial wall of the caudate. These projections are detected in primate tracing studies and were not observed in any of the thirty-directions datasets in our study.

For both datasets our model assumed up to two crossing fibers per voxel. A more complex local representation of the underlying fiber architecture requires higher quality DWI data (i.e. larger number of diffusion directions). As reported by Behrens and Jbabdi [18], depending on the technique that is used to reconstruct multiple fibers it may be necessary to acquire data from fifty (50) to hundreds of different gradient orientations and therefore our thirty directions dataset might not be of adequate quality to apply such complex approaches. However, since we did not observed consistent differences between the functional segmentation of the striatum obtained with the two datasets we preserved the crossing fiber approach for all the data.

As Parent [141] reports and as shown by our study, virtually all cortical areas contribute, at varying degrees, to the cortical-striatal projections. Consequently, the projections from all cortical lobes to striatum were considered for a comprehensive examination of the functional organisation of the striatum. The frontal lobe connections are dominant contributing $82 \pm 7\%$ of the total striatal volume and are the main source that influences the functional organisation of the striatum. A detailed anatomical subdivision of the frontal lobe was performed, with each subdivision associated with a particular function, and the projections from each subdivision were estimated. As with non human primate data [75] the ventral–medial prefrontal and orbital cortices connect to the anterior ventral CD and PU, the NAC and also the ventral post–commissural PU, which in primates also receives projecting fibers from the amygdala [63]. A discrepancy we observed between our results and the primate tracing studies, is that the limbic projections do not extend to the medial wall of the pre–commissural CD in all subjects [75]. This might be due to the fact that this projection is very thin and with the current DWI resolution it has not been possible to recover it. In addition, we explored the projections of the cingulate cortex (areas 32/24) to understand if in humans this contributes to the medial limbic territory but such connections were not detected. The limbic volume contributes to $20 \pm 7\,\%$ of the total striatal volume, which corresponds well with primate limbic volumetric estimates of $22\,\%$ from tracing studies [75]. Amygdala and hippocampus complex was excluded from the limbic target. As expected, and consistent with previous human DWI studies [39] and non human primate tracing studies, projections from these structures were found in the VST area and the ventral post–commissural PU. However, in most of our subjects strong connections were also observed in the lateral anterior caudate, next to the internal capsule and also in the lateral PU parallel to the external capsule. Although termination and exclusion masks were used to investigate further these projections, the results were inconclusive and these structures were excluded

from the limbic target. In non human primates, fibers from the amygdala reach striatum via two routes (personal communication Professor Haber). The first route is via the substantia innominata–nucleus basalis, pass under the anterior commissure and reach the striatum. The second route involves fibers that ascend parallel to the external capsule. It is therefore highly possible that the discrepancy we observed here is due to crossing fibers in the anterior commissure – internal capsule and external capsule and hence the amygdala tracts follow these white matter bundles.

The executive projections occupy a large portion of the striatum and this finding contradicts the concept that striatum is primarily a motor functional region. Projections from this target were found in rostral striatum and extended in the post–commissural striatum. In our data, the probability of connections for tracts originating from the executive target showed a degree of variability in the anterior caudate. These results are in agreement with those of Lehericy and colleagues [116] who reported tracking variability across subjects in the anterior striatum. Rostral-motor projections occupy the dorsal tier of rostral striatum and extend to dorsal PU caudal to the anterior commissure. Our findings are consistent with those of non human tracing studies [72] and other DWI studies in humans [52]. The caudal-motor projections reside in the post–commissural striatum. These projections overlap with the rostral-motor projections caudal to the anterior commissure and extend further posteriorly. The pattern of cortical projections to the striatum supports the theory of elongated rostral-caudal domains [157].

For the rest of the brain, a coarse anatomical approach was followed, by estimating the projections from the entire lobe. Areas where parietal lobe projections dominate occupy $11 \pm 5\,\%$, the second biggest cortical-striatal connections, and reside mainly in the posterior striatum. In eight out of twelve subjects we observed small patches of parietal projections in the anterior striatum mainly in the central CD, a finding that

is consistent with primate studies [33]. Parietal lobe is a functionally heterogeneous structure that consists of executive, visual, somatosensory and limbic sub-regions. At first we considered parcellating the parietal lobe into anatomical subdivisions that would represent the four functions. Nevertheless taking into consideration evidence from tracing studies that: a) the visual cortex contributes the least from all the cortical regions [98, 141]; and b) the limbic areas of the parietal lobe are connected with visual and somatosensory areas [33], we decided that it is preferable to subdivide the parietal lobe only into the somatosensory area (SS) and posterior parietal (PP) area as described elsewhere [20, 25]. However, the projections from these two areas, SS and PP, show an extensive overlap, an observation confirmed by Bohanna et al. [25] and Cavada et al. [34] that did not justify the subdivision of the parietal into SS and PP. Therefore, considering parietal lobe as one entity was the most reliable choice.

Temporal and occipital lobes have limited connections with the striatum. Temporal projections in non human primates have been reported in the ventral-medial anterior CD [157] and the tail of the CD [181]. However, we did not observe projections to the tail of the CD. This discrepancy might be due to the fact that the CD ROI did not include the whole tail of the structure as the small size of the tail did not allow reliable tracing for all slices. Our cortical-striatal projections are in agreement with those reported by Bohanna et al. [25] with the exception that we did not observe any projections from the occipital lobe to the CD.

Accumulating evidence [52, 75] supports the concept of distinctive and overlapping networks in the striatum, which form the basis for reward-based learning and goal-directed behaviours. Our findings support the existence of overlapping projections throughout the human striatum, engaging striatum in integrating information between functions, via overlapping networks. Our results indicate that the executive area overlaps with all the other functional areas (limbic, rostral-motor, caudal-motor).

This suggests executive involvement in both motor and limbic functions; in other words, it points to a role for the striatum in orchestrating the top-down component of action planning and selection.

5.4 Connectivity–based subdivision of the pallidum

In non human primates, striatum sends massive projections to pallidum, imposing its functional organisation (figure 5.3). Here, we study the projections from the functional territories of striatum to pallidum in humans, using probabilistic tractography [21]. The analysis was performed in individual subjects in two steps. First the striatum was parcellated into functional territories as described in section 5.3. After the hard segmentation of the striatum (method CBe) the rostral-motor, caudal-motor and parietal subdivisions were combined to make the sensorimotor striatal territory. Finally projections to the pallidum from the limbic, cognitive and sensorimotor striatal areas were estimated (figure 5.12).

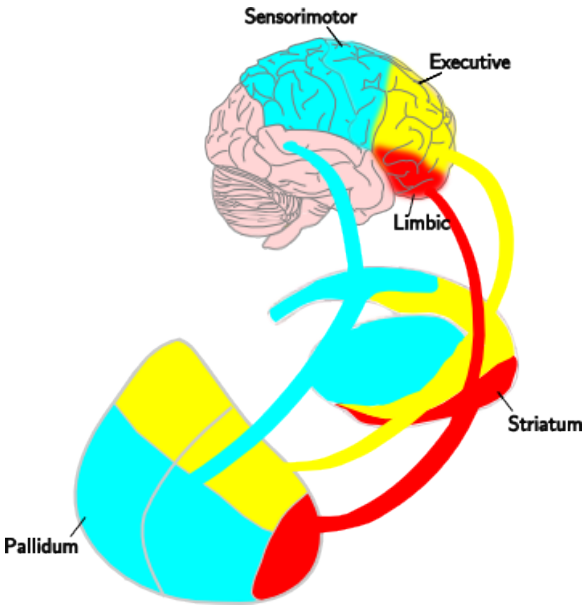

Figure 5.12: Methods overview to subdivide pallidum into connectivity-based functional regions. To obtain these subdivisions a two step procedure was followed. First the striatum was segmented according to the methods described in section 5.3. Subsequently the limbic, executive and sensorimotor motor striatal regions were defined and used to estimate the probability of connection between the pallidum and these striatal functional targets.

5.4.1 Materials and methods

Subjects, data acquisition and probabilistic tractography

Twelve healthy subjects underwent DWI scans 30 directions "blip-up" and "blip-down". The data set and the probabilistic tractography methods are described in detail in section 5.3. In brief, tractography was performed in the subjects' continuous space and the results were output in the MNI space. Five thousand sample tracts were generated from each voxel in the pallidum mask. As indicated in section 5.2 the "indirect pathway" involves the projections from striatum to GP_e, which in turn projects to the GP_i. Although the resolution of our DWI data probably would not detect such a short connections, to eliminate this probability, the pallidum mask was employed as a termination mask. Termination masks will stop the striatal projections as soon as they enter the pallidum.

Region of interest preparation

Pallidum was manually defined on each subjects' T1-weighted MRI image and comprises of GP_e, GP_i and small parts of the VP nucleus. As mentioned in chapter 4, VP is not visible on a standard T1-weighted MRI and is located below the AC an area where there is an admixture of the VP, VST and substantia innominata regions [85]. Figure 5.13 shows the pallidal ROI defined on a subjects' T1-weighted image and the pallidal subdivisions on the subject's WM–nulled image. Definition of the pallidum ROI was carefully performed to exclude the VST and substantia innominata structures.

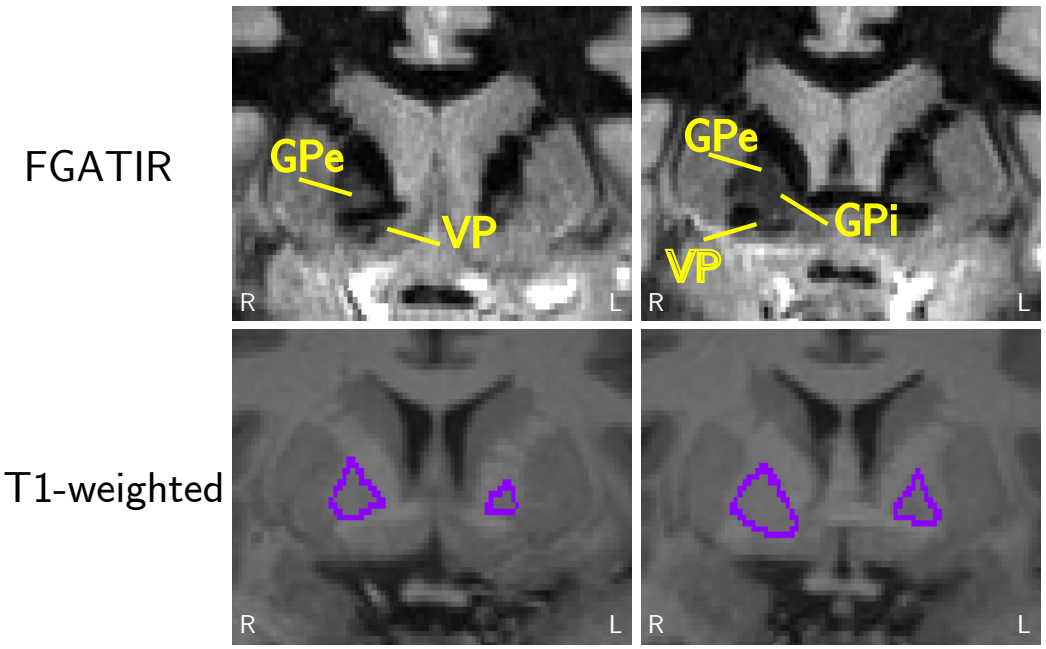

Figure 5.13: Figure shows the FGATIR image and the T1-weighted image in the same subject. First row is the FGATIR MRI image showing the 3 structural subdivisions of the pallidum, GP_e, GP_i, and VP. The bottom row shows the pallidum ROI (purple) overlaid on the subjects' T1-weighted image. R=right; L=left.

Pallidal functional subdivision

Connection probabilities from the limbic, cognitive and sensorimotor striatal territories were estimated for each individual subject. Sensorimotor area comprises of the rostral-motor, caudal-motor and parietal striatal ROIs obtained with the CBe method. We decided to use the sensorimotor area instead of the individual areas that sensorimotor area consists of, for various reasons. Firstly, a preliminary investigation showed that there was a great overlap between these regions. Secondly, as pallidum is a small structure, subdivisions into five sub-regions compromises consistency across subjects and reliability. As Traynor [175] reports increasing the number of target regions reduces the within subject reproducibility and increases the between subject variability. Third, non-human primate tracing or degeneration studies, have dealt with the sensorimotor area as a whole [61, 141] and therefore, our approach permits a "direct" comparison between the non-human and human functional organisation. Occipital

and temporal lobe projections were excluded from the analysis as they occupy small parts of the striatum and the location of these projections are not consistent across subjects after hard segmentation.

Like the cortico–striatal projections, the striatal projections to the pallidum are considered to be organised into parallel and overlapping networks [84, 141, 145]. Therefore, similar to striatum, the striatopallidal connectivity maps are processed into two ways: a) for each subject, exclusive connectivity-based functional ROIs (CBe) were created following the procedures described by Johansen-Berg and colleagues [92]; b) each subject's connectivity maps were thresholded at 1%, 5% and 10% of the maximum connectivity value to exclude noise and voxels with low connectivity values. The functional areas obtained with this method will be respectively abbreviated as follows: CBo-thr1 CBo-thr5 and CBo-thr10.

Pallidal connectivity–based atlases

Population maps of the connectivity profile of each striatal area with the pallidum were created, following the methodology described in section 5.3. However, preliminary data suggested that the striatal-pallidal connection probabilities are lower than those obtained for the cortical-striatal network. Therefore, to construct the population maps the voxels with a connection probability (between the pallidum and the striatal target) higher than 25 % and not 50 % were preserved as suggested by Johansen-berg [92]. The connectivity population maps were, in addition, used to create a pallidum population atlas with each voxel assigned to the striatal target that the majority of subjects had connections with.

5.4.2 Results

Similar to non human primate species the three striatal functional territories also send projections to the pallidum in humans. These projections are topographically organised, are bilaterally symmetric and occupy the pallidum to varying degrees. After hard segmentation of the pallidum across subjects, the executive area dominates with $63 \pm 27\,\%$ of the total pallidal area (striatal executive area volume: $5.73 \pm 1.15\,cm^3$) followed by the sensorimotor with $37 \pm 13\,\%$ (striatal sensorimotor area volume: $2.75 \pm 0.55\,cm^3$). The limbic area occupies the lesser portion of the pallidum with approximately $6 \pm 4\,\%$ (striatal limbic area volume: $2.32 \pm 0.79\,cm^3$). Table 5.2 shows the volume that striatal projections occupy after the hard segmentation (CBe) and also for the CBo-thr1, CBo-thr5 and CBo-thr10 projections.

Limbic striatum connects to the rostral pole of the GP_e, the ventro–medial tip of the pre–commissural GP_e and the ventro–medial GP_i. The executive striatum occupies the entire rostro–caudal extent of the pallidum with the highest connection probabilities observed in the dorso-medial anterior and central pallidum while low connection probabilities were found in the posterior pallidum. In contrast to the projections from the executive striatum, the sensorimotor projections reside in the ventral pre–commissural pallidum whereas post–commissuraly the sensorimotor projections occupy both the ventral and lateral pallidum. Figure 5.14 shows the population connectivity maps of the striato–pallidal projections. These maps show that the striatal projections have a distinctive pattern and at the same time they overlap extensively. Particularly in the rostral pallidum, anterior to the AC, the limbic and sensorimotor projections overlap in the ventral areas whereas the executive projections overlap with those from the limbic and sensorimotor targets in the rostral and caudal pallidum areas respectively.

Figure 5.15 shows the subdivisions with the CBe method in four representative sub-

Table 5.2: Volume and percentage contribution to the total pallidal volume of the striatal projection at thresholds of 1%, 5%, and 10% (CBo methods). CBe is the volume and contribution to the pallidum volume of exclusively connectivity–based ROIs (assignment of each voxel to the striatal target with the highest connection probability). Results are averaged between the left and right hemispheres.

	CBo-thr1		CBo-thr5		CBo-thr10		CBe	
Region/function	Volume (cm^3)	Contribution to pallidal volume (%)	Volume (cm^3)	Contribution to pallidal volume (%)	Volume (cm^3)	Contribution to pallidal volume (%)	Volume (cm^3)	Contribution to pallidal volume (%)
Limbic	0.27 ± 0.18	22.43 ± 17.84	0.12 ± 0.09	9.76 ± 8.08	0.07 ± 0.06	6.06 ± 4.87	0.07 ± 0.06	5.76 ± 4.45
Executive	0.82 ± 0.25	69.97 ± 30.72	0.50 ± 0.22	43.54 ± 26.99	0.36 ± 0.20	31.68 ± 22.72	0.73 ± 0.20	62.58 ± 26.63
Sensorimotor	0.64 ± 0.30	52.63 ± 20.44	0.31 ± 0.20	24.96 ± 13.36	0.19 ± 0.14	15.10 ± 9.65	0.45 ± 0.19	36.82 ± 12.99

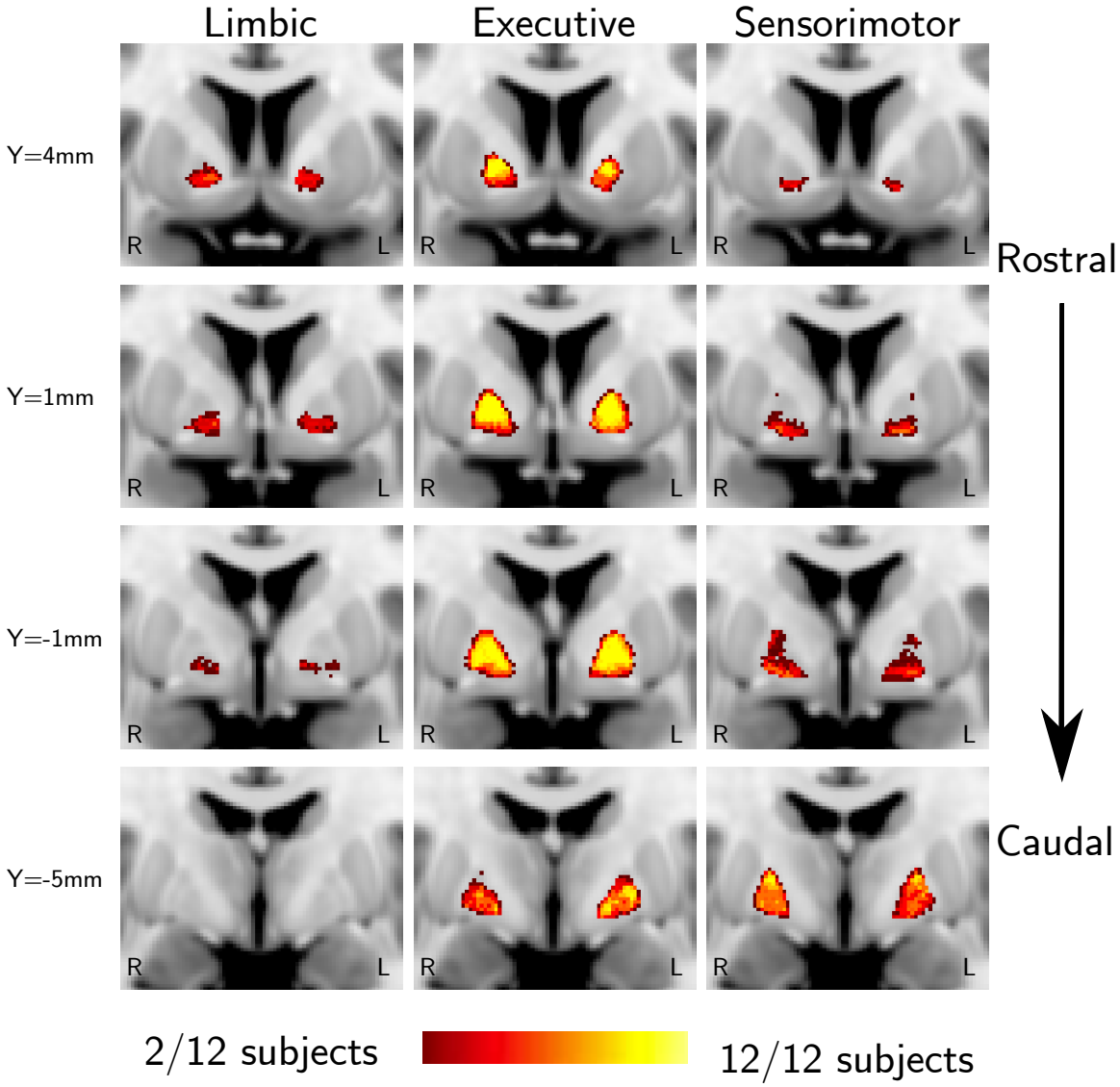

Figure 5.14: Population connectivity maps of the limbic, executive and sensorimotor areas in the pallidum, determined from the connections with corresponding striatal areas. To create the maps, for each voxel the number of subjects with a connection probability (between the pallidum voxel and the striatal target) higher than 25% was estimated. R=right; L=left.

jects, which can be seen to be symmetrical and relatively coherent across individuals, while figure 5.16 shows the population atlas. Figure 5.17 illustrates the impact of different thresholds on the topography and size of the projections that the pallidum receives from the striatum.

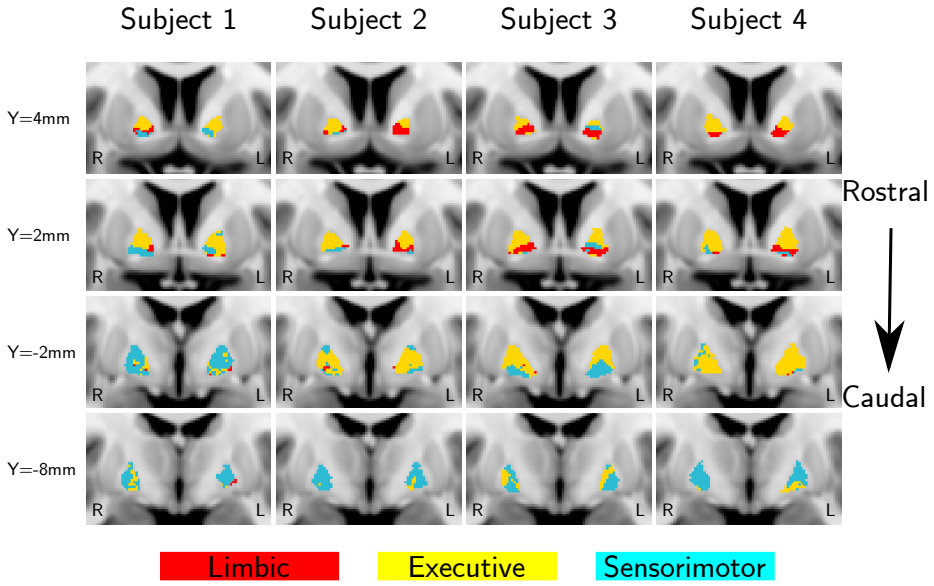

Figure 5.15: Individual functional subdivisions in four randomly selected subjects (MNI space – coronal planes). Each column corresponds to a single subject, starting from rostral (top row) to caudal (bottom row). To obtain the functional subdivision for each subject a two-step procedure was applied. First the striatum was subdivided into limbic, executive, and sensorimotor functional territories. Subsequently, the projections from each of these striatal functional territories to the pallidum was estimated. Finally, each voxel was assigned to the target that gave the highest connection probability. R=right; L=left.

5.4.3 Discussion

Our data demonstrate that the striatal projections to pallidum are topographically organised and are bilaterally symmetric. A projection is topographically organised if the spatial order of the projective fibers is reflected in the spatial organisation of the receiving fibers. As shown in figure 5.14, the limbic striatum, which is located in the ventral striatum (figure 5.7), projects to the ventral pallidum. Similarly, projections from the executive striatum, which is located throughout the striatum, projects along pallidum's rostrocaudal extent with the highest connection probabilities in the dorsal

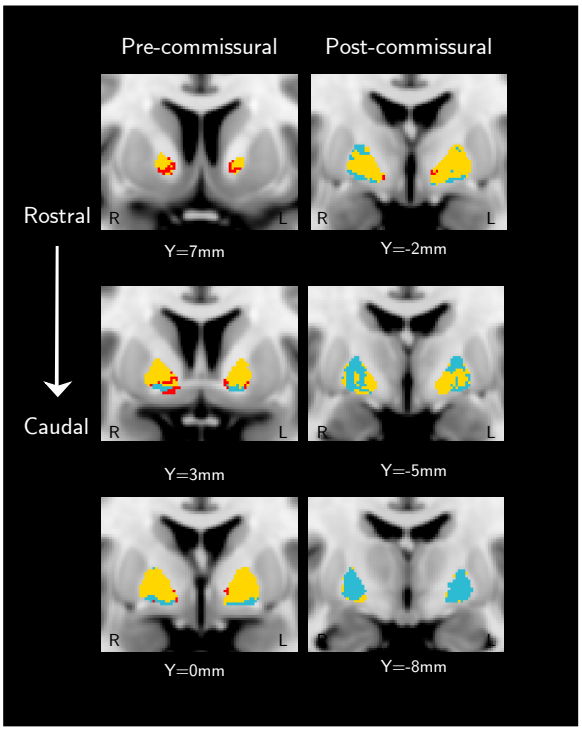

Figure 5.16: Connectivity–based population atlas of pallidum (MNI space, coronal planes). Colour-scheme is as follows: red = limbic, yellow = executive, light blue = sensorimotor. R=right; L=left.

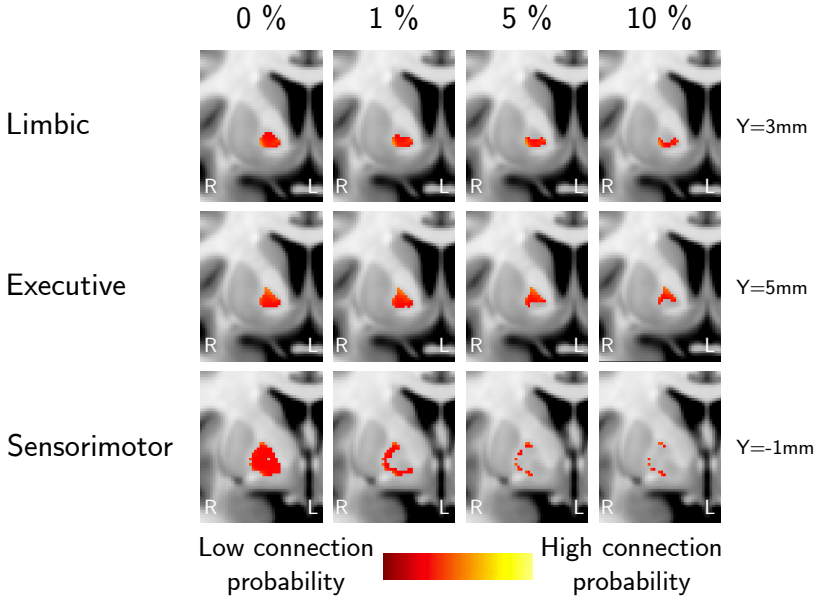

Figure 5.17: Effect of thresholds on the striatal–palital connectivity maps in a representative subject. The first column shows the total projection from each target to the striatum. Subsequent columns show the connectivity maps after thresholded at 1%, 5% and 10% of the maximum connectivity value respectively. R=right; L=left.

anterior region. The sensorimotor striatum preserves this topographical organisation with the highest connection probabilities found in the post–commissural pallidum. The topographical organisation observed in our study is also found in non-human primates [98, 99, 77, 84, 82, 141, 61].

The executive projections occupy the majority of the pallidum with $63 \pm 27\,\%$ of the total pallidal area. Similar to the striatum, the pallidum is considered a sensorimotor structure [141]. However, it seems that both striatum and pallidum, due to the large projections they receive from the executive brain regions, are principally concerned with executive information. Limbic pallidum occupies the smallest proportion with $6 \pm 4\,\%$. However, evidence from primate studies suggest that the VST, the area that corresponds to the limbic part of the striatum, projects extensively to the VP – an area which is minimally sampled in our pallidal ROI. For this reason the percentage contribution of the limbic pallidum, estimated in our study, might not be a good approximation of the actual limbic representation in humans.

Figure 5.15 shows the functional organisation of the pallidum in four representative subjects, after hard segmentation. In general, there is good agreement across subjects with ventral pre–commissural pallidum showing the greatest variability. In this area there is an overlap between the limbic and sensorimotor projections (figure 5.14) and after hard segmentation (assignment of each voxel to the striatal target with the highest connection probability), the two areas intermingle as shown in figures 5.15 and 5.16. Although there is not a direct reference for a limbic–sensorimotor overlap in the pre–commissural ventral pallidum of non-human primates, the anatomical areas that correspond to the limbic and sensorimotor functions project to the pre–commissural ventral pallidum. Specifically, VST (limbic), projects to the ventral pre–commissural pallidum [77, 141] whereas post–commissural putamen, a predominately sensorimotor

area, projects to the ventro–lateral pallidum.

Pallidum is considered an area of extensive convergence [77, 84, 82, 141, 61]. Although we have observed extensive overlaps between all three functional territories in the pallidum, we believe that our data cannot reliably speculate on their existence and location. This is due to several factors. First, the resolution of the DWI data in association with the short distances of these pathways, as they are originating from neighbouring structures, makes their recovery difficult. Therefore, the overlaps could be a technical artefact. The connection probabilities of the striatal–pallidal pathways are substantially lower as compared to the cortico–striatal probabilities. After applying the thresholds of 1%, 5% and 10%, these overlaps are either not preserved or their location is not consistent across subjects. Therefore, for the aforementioned reasons and also as data is not available in non-human primates, in order to confirm their existence and location, we are not confident about reporting. Nonetheless, executive pallidum has high connection probabilities and occupies the rostra-caudal extent of the pallidum. Therefore, we are confident about reporting that it overlaps with the limbic and sensorimotor areas. Consequently, as in the striatum, there is an executive involvement in both motor and limbic functions, pointing to a role for the BG in orchestrating the top-down component of action planning and selection.

In conclusion, using DWI data we identified the functional subdivisions of the human striatum and pallidum. The functional organisation of these structures is consistent between subjects and the human functional organisation has the same pattern with that obtained in primates with distinctive and overlapping networks.

Chapter 6

Quantification of dopamine D2R and D3R distribution with [^{11}C]PHNO

6.1 Introduction

The D3R were characterised in 1990 by Sokoloff [167], and are thought to be implicated in several neurological, psychiatric and substance–use disorders. The high concentration of D3R in brain areas linked with functional aspects of motivation and reward have made them an attractive target for the treatment of psychiatric and addictive disorders. Studies exploring the distribution of the D3R in the human brain using post-mortem tissue [71, 135] have reported a declining rostral to caudal gradient of the D3R concentration in the striatum as well as the existence of D3R in some extra-striatal locations, such as the substantia nigra and the thalamus. In the striatum the D3R are particularly enriched in the nucleus accumbens and the pre–commissural ventral putamen. D3R sites and mRNA were observed in the pallidum [71, 135] with the highest concentrations found in the internal segment of the globus pallidus and the ventral pallidum. Gurevich [71] documented the existence of D3R in the anterior ventral thalamus and throughout the hypothalamus, though at considerably lower levels than in the striatum and pallidum. Gurevich stressed the relative abundance of the D3R in the mammilothalamic tract and the mammilary bodies of the hypothalamus. Table 6.1 and Table 6.2 show the concentrations of D2R and D3R in healthy subjects obtained from autoradiography studies in healthy subjects [71, 135].

Table 6.1: Autoradiographic experiments with [^{125}I]epidepride and [^{125}I]PIPIT were carried out using concentrations of the radioligands equal their respective Kds. This makes concentrations of D2R and D3R binding sites roughly comparable, even though Bmax values were not obtained. n/d- specific binding not detected. Table adapted from Gurevich et al. [71]

Regions	**D2R receptor binding (fmol/mg)**	**D3R receptor binding (fmol/mg)**
Basal ganglia and basal forebrain		
Dorsal caudate nucleus	64.2 ± 4.5	9.65 ± 1.36
Ventral caudate nucleus	55.8 ± 4.5	13.84 ± 2.04
Dorsal putamen	67.9 ± 5.5	15.60 ± 2.72
Ventral putamen	63.9 ± 5.2	22.17 ± 3.3
Nucleus accumbens	49.3 ± 7.8	24.8 ± 3.9
Tail of caudate	48.7 ± 6.1	7.67 ± 1.09
Globus pallidus external	15.5 ± 2.8	7.37 ± 1.31
Globus pallidus internal	2.32 ± 0.55	9.34 ± 1.34
Ventral pallidum	7.35 ± 2.69	10.6 ± 3.22
Nucleus basalis	17.5 ± 12.46	3.84 ± 1.3
Thalamus		
Anteroventral nucleus	3.21 ± 0.44	4.96 ± 0.46
Mediodorsal nucleus	3.0 ± 1.23	1.53 ± 0.43
Ventral anterior nucleus	2.39 ± 0.4	2.16 ± 1.24
Ventral lateral anterior nucleus	3.05 ± 1.45	0.98 ± 0.5
Ventral lateral posterior nucleus	2.62 ± 1.29	1.37 ± 0.45
Central medial nucleus	5.42 ± 1.15	n/d
Central lateral nucleus	3.69 ± 0.92	n/d
Reuniens nucleus	3.19 ± 0.33	2.92 ± 1.4
Paracentral nucleus	2.63 ± 0.53	n/d
Ventral posterior lateral nucleus	0.98 ± 0.14	n/d
Lateral geniculate nucleus	1.54 ± 0.08	0.86 ± 0.27
Medial geniculate nucleus	1.93 ± 0.37	0.8 ± 0.29
Mammillothalamic tract	n/d	5.79 ± 0.38
Subthalamic nucleus	4.17 ± 0.69	n/d
Hypothalamus		
Medial preoptic area	8.45 ± 1.55	n/d

Continued on next page

Table 6.1 – continued from previous page

Regions	**D2R receptor binding (fmol/mg)**	**D3R receptor binding (fmol/mg)**
Dorsal hypothalamic area	5.37 ± 0.76	n/d
Anterior hypothalamic area	4.84 ± 1.9	n/d
Paraventricular nucleus	5.49 ± 1.55	1.04 ± 0.19
Dorsomedial nucleus	3.83 ± 1.58	n/d
Ventromedial nucleus	2.82 ± 0.45	n/d
Lateral hypothalamic area	4.56 ± 1.16	1.72 ± 0.39
Arcuate nucleus	8.53 ± 1.28	n/d
Posterior hypothalamic area	5.49 ± 1.55	1.84 ± 0.19
Tuberomammillary nucleus	7.86 ± 1.38	2.18 ± 0.68
Supramammillary nucleus	5.66 ± 1.1	1.87 ± 0.28
Mammillary nuclei	2.34 ± 0.73	4.32 ± 1.47
Mammillary fasciculus	n/d	5.79 ± 0.38
Amygdala		
Amygdalostriatal transitional area	10.98 ± 1.97	2.4 ± 0.03
Amygdalopiriform transitional area	n/d	1.7 ± 0.51
Central nucleus	2.64 ± 0.89	1.56 ± 0.28
Cortical nucleus	n/d	1.65 ± 0.4
Basolateral nucleus dorsolateral division	5.03 ± 2.2	2.48 ± 0.4
Basolateral nucleus dorsal division	5.69 ± 2.32	2.54 ± 0.46
Basolateral nucleus intermediate division	5.91 ± 3.0	2.35 ± 0.3
Basolateral nucleus paralaminar division	4.04 ± 3.1	1.9 ± 0.14
Basolateral nucleus ventromedial division	5.75 ± 3.5	1.77 ± 0.17
Basolateral nucleus ventrolateral division	3.64 ± 2.33	1.9 ± 0.25
Basomedial (accessory) nucleus	n/d	1.85 ± 0.22
Lateral nucleus	1.35 ± 0.45	0.96 ± 0.37
Substantia nigra and ventral tegmental area		
Substantia nigra pars compacta	15.44 ± 3.56	5.07 ± 0.64
Substantia nigra pars reticulata	9.78 ± 1.54	4.19 ± 0.18
Substantia nigra pars reticulata rostral	3.44 ± 0.52	11.33 ± 1.78
Substantia nigra pars lateralis	12.07 ± 2.73	3.1 ± 0.4
Paranigral nucleus	13.18 ± 2.83	n/d
Parabrachial pigmented nucleus	10.58 ± 1.93	n/d
Caudal linear raphe nucleus	7.69 ± 1.00	n/d

Table 6.2: The total Bmax values are for [^{125}I]epidepride binding; Bnax values for D2R and D3R receptors are estimated from displacement experiments. Values are $mean \pm \mathrm{SD}$ for a minimum of four subjects per region.Table adapted from Murray et al. [135]

Regions	**D2R receptor binding (fmol/mg)**	**D3R receptor binding (fmol/mg)**
Rostral striatum		
Caudate	116.8 ± 18	17.2 ± 4
Nucleus accumbens		
Striosome	79.1 ± 15	118.5 ± 11
Matrix	101.2 ± 9	51.0 ± 7
Ventral putamen	88.1 ± 14	$94.6 + 10$
Caudal striatum		
Caudate	155.3 ± 16	10.2 ± 7
Ventral putamen	101.3 ± 13	35.6 ± 7
Pallidum		
External	58.6 ± 17	8.1 ± 4
Internal	4.4 ± 2	47.3 ± 11
Ventral	4.5 ± 2	39.3 ± 10
Basal forebrain		
Septal nucleus	19.3 ± 4	89.4 ± 16
Islands of Calleja	17.3 ± 3	73.6 ± 16
Nucleus basalis	15.1 ± 3	76.1 ± 11
Midbrain		
Medial and A10	25.8 ± 11	63.6 ± 17
Lateral (A9)	36.7 ± 12	8.4 ± 7
A8-raphe	21.1 ± 9	3.3 ± 4
Amygdala		
Basolateral	38.8 ± 14	8.7 ± 3
Central	6.4 ± 2	51.1 ± 11
Amygdalostriatal	5.2 ± 2	62.9 ± 9

Despite these post–mortem findings, the *in–vivo* investigation of D3R had been limited due to the lack of a selective D3R PET ligand. The D3R are co-localised with the D2R sites in the brain, with the D2R expression being higher. The existing antagonist (i.e. [^{11}C]Raclopride, [^{18}F]fallypride) and agonist ([^{11}C]NPA) PET ligands bind with comparable affinity for the D3R, the D2R^{high} and the D2R^{low}, and consequently measure the total D2R signal without distinguishing between the functionally inert D2R^{low} and the functionally active D2R^{high} [187]. Agonist radioligands, similar to dopamine itself, bind predominately to the D3R and D2R^{high} sites.

The introduction of [^{11}C]PHNO [188], with its *in–vitro* 30 to 50-fold selectivity for the D3R over the D2R [62, 182] and its suitability as a promising agonist ligand for *in–vivo* imaging [65] has opened the possibility of imaging the D3R. [^{11}C]PHNO was initially introduced as a potent agonist radioligand suitable for imaging *in–vivo* the high affinity state of the D2R [187, 65]. The ligand had the expected high specific binding in the dorsal striatum, however, in comparison to other D2-like ligands it demonstrated high binding in the pallidum and ventral striatum. The characteristic distribution of [^{11}C]PHNO combined with prior knowledge of the *in–vitro* preferential affinity for the D3R sites, prompted speculations on whether [^{11}C]PHNO had a D3R component to its signal *in–vivo*. Narendran and colleagues [138], using the D3R preferring blocker BP-897 in non-human primates, demonstrated that [^{11}C]PHNO is indeed a D3R preferring radioligand *in–vivo*. A recent study has confirmed this finding and estimated a 20 to 50-fold [64] *in–vivo* preference for the D3R in non–human primates.

Further investigation of the PHNO signal was performed by Rabiner [150] with *in–vitro* investigation (autoradiography) of the [^{3}H]PHNO binding in wild-type (WT), D2R knock-out (D2RKO) and D3R knock-out (D3RKO) mice, following administration of Vehicle or SB277011 (100-fold selectivity for D3R over D2R). Autoradiography enabled the visualisation and quantification of receptors at a high anatomical resolution

and enabled the detection of molecules of interest in small quantities [107]. The binding of [^{3}H]PHNO in the WT mice, after injection of vehicle, was high in CD, PU, VST, pallidum, habenula and hypothalamus, whereas total binding in the cerebellum was low. Results after injection of SB277011 in the knock-out and in WT mice implied that D3R dominated the signal in the pallidum and extra–striatal regions, contributed to a significant proportion of the signal in the VST and only to a small proportion of the [^{3}H]PHNO signal in the CD and PU.

[^{11}C]PHNO binding was also examined *in–vivo* in non–human primates with PET at baseline conditions and following administration of SB277011 at different doses (0.5-5 mg/kg) [150]. SB277011 produced a dose dependent reduction of the [^{11}C]PHNO binding with the following order SN> TH> GP> VST> CD> PU. The [^{11}C]PHNO specific binding attributed to the D3R was: SN = 98 %, TH = 92 %, GP = 77 % VST = 57 %, CD = 33 % and PU = 21 %. These D3R contributions were derived assuming one binding site for SB277011, as binding to the D2R at such doses was assumed negligible. Graff-Guerrero and colleagues [66], following a similar approach, tried to characterise the [^{11}C]PHNO signal *in–vivo* in humans using the ABT-925 compound, which had demonstrated a 45 to 120-fold *in–vitro* selectivity for the D3R over the D2R. However, *in–vivo* the ABT-925 compound demonstrated at best a 4-fold higher affinity for D3R over D2R and this did not allow for an effective dissection of the [^{11}C]PHNO signal into its D3R and D2R components.

As has been shown from *in–vivo* and *in–vitro* studies [150, 138] the [^{11}C]PHNO binding is a mixture of D3R and D2R components whose relative contribution varies regionally. The aim of this chapter is to explore the regional [^{11}C]PHNO signal *in–vivo* in healthy humans at baseline conditions and following D3R blockade. This will enable partitioning of the regional [^{11}C]PHNO specific binding into its D2R and D3R components and characterisation of the densities and distribution of the D2-like receptors

in the brain. Regional [^{11}C]PHNO binding is examined in the subcortical dopamine–rich regions that are defined using the landmark–based guidelines developed in chapter 4. Furthermore, [^{11}C]PHNO binding was also assessed in the connectivity-based functional subdivisions of the striatum and the pallidum using probabilistic atlases constructed according to the methodology presented in chapter 5.

6.2 Materials and methods

6.2.1 Subjects

Nineteen healthy male volunteers, aged between 22 and 55 years, free from clinically significant illness or disease as determined by their medical history and standard laboratory tests, had [^{11}C]PHNO PET and T1-weighted MRI scans. The data presented here is the same cohort used in section 4.4. Studies were approved by local ethics committees and all subjects gave written informed consent. All PET scans were conducted at the Centre of Addiction and Mental Health in Toronto, Canada. Subjects were scanned at baseline and received one to three further [^{11}C]PHNO scans following the administration of a selective D3R blocker (GSK598809) at doses of 5 mg to 175 mg. GSK598809 is a selective D3R antagonist which exhibits a 100-fold *in–vitro* selectivity for the D3R over the D2R . The post-drug PET scans were scheduled to begin approximately 2 to 3 hours after administration of the GSK598809 in order to estimate occupancy shortly after the anticipated peak plasma levels. Blood samples were taken for analysis of GSK598809 plasma pharmacokinetics.

6.2.2 Data acquisition

PET

In total, 48 PET scans were acquired on a Siemens Biograph HiRez XVI PET tomograph (Siemens Healthcare). Subjects were positioned in the scanner and movement was minimised by using a custom-made thermoplastic facemask together with a head-fixation system (Tru-Scan Imaging, Annapolis, Maryland). Subjects were injected

with a single intravenous bolus of [^{11}C]PHNO between $235 - 368\,MBq$ (mean=307.2, SD=40.6) with specific activity ranging between $23.3 - 38.6\,GBq/\mu mol$ (mean=32.24, SD=4.58) at the time of injection. The injected [^{11}C]PHNO mass was between $2 - 2.6\,\mu g$ (mean=2.36, SD=0.13) and the radiochemical purity of the compound was 97.7-99.9 % (mean=99.4, SD=0.6). Following bolus administration of [^{11}C]PHNO, dynamic emission data were acquired for 90 minutes ($1 \times 30\,s$, $8 \times 15\,s$, $3 \times 1\,min$, $5 \times 2\,min$, $5 \times 5\,min$, and $5 \times 10\,min$). A low dose CT scan (effective dose=$0.2\,mSv$) was also acquired and used for attenuation correction and model-based scatter correction. The dynamic images were reconstructed using Fourier rebinning and a 2D filtered back projection algorithm.

MRI

T1-weighted images were acquired on a GE medical system signa EXCITE HD, 1.5T. The structural T1-weighted images (acquired in the axial plane: FSPGR - IR PREPPED, TR=12.008, TE=5.1160, flip angle=20°, resolution=$0.78 \times 0.78 \times 1.5\,mm$) were acquired to aid in the definition of the subcortical ROIs and for registration of the MNI template and the connectivity atlases to the subject's space.

6.2.3 Image preprocessing

The MRI and PET images of each subject underwent a series of spatial processing steps. The non-brain voxels from the MRI images were removed using the FSL Brain Extraction Tool [165] and the extracted brain was rigidly registered to the nonlinear MNI152 template using FLIRT [89] in order to bring the subjects into a similar orientation and facilitate manual ROI delineation. For the manual ROI delineation, the MRI was made isotropic to the smallest voxel size of the original image ($0.79 \times 0.79 \times 0.79\,mm$) in order to obtain the best possible visual quality (HiRes image). PET images were corrected for motion by rigidly (six degrees of freedom) realigning each frame (MCFLIRT [89]) to a reference frame defined as the average PET

baseline volume. The manually defined ROIs and the warped atlases were aligned to the PET data via a rigid registration of the HiRes MRI to the PET baseline reference frame.

6.2.4 Structural-based definition of ROIs

ROIs were manually defined on the subject's HiRes T1-weighted image following the guidelines described in chapter 4 (ROIs are listed in table 4.3). The anatomical cerebellum, which was used as the reference region for the quantification of the PET signal, was obtained from the spatially normalised anatomical brain atlas described in chapter 4. Each ROI was then applied to the dynamic PET data to derive regional time-activity curves (TACs).

6.2.5 Connectivity-based subdivisions of the striatum and pallidum

For this study DWI data were not available, therefore it was not feasible to functionally subdivide the striatum and pallidum using the subject's own DWI data and the methods described in chapter 5. To obtain the functional subdivisions of the striatum and pallidum the population connectivity atlases constructed in chapter 5 were employed and were spatially normalised to the subject's T1-weighted image via the nonlinear registration (using FNIRT [8]) of the MNI template to the subject's HiRes image.

Two versions of the connectivity-based (CB) atlases were employed. The first version involves the connectivity probability maps and will be denoted with "CBo" as in STR-CBo-limbic. In this version (CBo) each functional subdivision includes voxels that are exclusively connected (discrete network) to a cortical target as well as voxels that concurrently connect to other targets (overlapping networks) (figures 5.7 and 5.14). The second version includes the atlases that assign a sole function to every

voxel after performing “hard" segmentation (figures 5.9 and 5.16) and these atlases will be denoted with “CBe” as in STR-CBe-limbic.

Using the two versions of the atlas, the striatum was subdivided into limbic, executive, rostral-motor, caudal-motor, parietal, occipital and temporal sub-regions. In addition, the rostral-motor, caudal-motor and parietal striatal subdivisions were combined to create the sensorimotor functional area. The pallidum was also subdivided into limbic, executive and sensorimotor territories. To customise further the probabilistic atlases to each subject, the subject's segmented grey matter image, thresholded at 0.25, was employed to mask the ROIs.

The nomenclature for the connectivity-based subdivisions of the striatum and pallidum are as follows: the prefixes Str and Pal correspond to the striatum and the pallidum respectively. The middle part of the name denotes whether the exclusive atlas (CBe) or the connectivity probability maps that allow overlapping zones (CBo), were employed. Finally, the suffix denotes the functional specificity of the ROI such as Str-CBe-limbic or Pal-CBo-executive.

6.2.6 Assessment of the performance of the connectivity-based atlases

As DWI data were not available for this study, the probabilistic connectivity atlases created in chapter 5 were employed and customised to each subject's space. Data from a separate study were used to assess the correspondence between connectivity-based subdivisions defined using the subject's own DWI data and those obtained from the spatial normalisation of a connectivity probabilistic atlas.

Fourteen healthy male volunteers aged between 27 and 60 years were employed to assess the agreement between the atlas–defined and the within–subject–defined func-

tional subdivisions. The data presented here is the same cohort used in section 5.3. For each subject a range of scans were performed to acquire a T1-weighted structural MRI, 64-directions "blip-up" and "blip-down" diffusion-weighted MRI and [^{11}C]PHNO PET at baseline conditions. Additional information about the subjects and the acquisition protocols can be found in chapter 8. The connectivity-based subdivision of the striatum and pallidum were performed following the methodology described in chapter 5 and the spatial normalisation of the atlases was performed according to the methodology described in section 6.2.5. The assessment was performed in terms of the spatial overlap between the functional subdivisions by calculating the DICE coefficient using equation 4.1. In addition, the agreement in the regional baseline [^{11}C]PHNO binding was also calculated (equation 4.2).

6.2.7 Derivation of the parameters of interest - BP_{ND} and D3R/D2R contribution to the total [^{11}C]PHNO specific signal

The structural-based and connectivity-based ROIs were applied to the dynamic PET data to derive regional time activity curves (TACs) before applying the simplified reference tissue model (SRTM) [69, 108] to derive regional BP_{ND} estimates. The cerebellum was used as the reference region. Regional BP_{ND} estimates are proportional to the number of available receptors and can be described by:

$$BP_{ND} = \frac{f_{ND} B_{avail}}{K_D} \tag{6.1}$$

where f_{ND} is the free fraction of the non-displaceable ligand in the brain, B_{avail} is the density of the available receptors and $1/K_D$ is the affinity of the ligand to the receptors. Since [^{11}C]PHNO binds to D3R and D2R sites, the total [^{11}C]PHNO BP_{ND} can be described by:

$$BP_{ND}^{PHNO} = BP_{ND}^{D3R} + BP_{ND}^{D2R} \tag{6.2}$$

where BP_{ND}^{D3R} and BP_{ND}^{D2R} correspond to [^{11}C]PHNO binding to the D3R and the D2R respectively. According to equation 6.1 the total [^{11}C]PHNO binding can be expressed as:

$$BP_{ND}^{PHNO} = f_{ND}\left(\frac{B_{avail}^{D3R}}{K_D^{D3R}} + \frac{B_{avail}^{D2R}}{K_D^{D2R}}\right) \tag{6.3}$$

where B_{avail}^{D3R} is the density of the available D3R and $1/K_D^{D3R}$ is the [^{11}C]PHNO affinity for the D3R. Similarly B_{avail}^{D2R} is the density of the available D2R and $1/K_D^{D2R}$ is the affinity for the D2R sites.

The single site competition model assumes that GSK598809 binds solely to the D3R and that binding to the D2R sites is negligible and can be ignored. GSK internal studies have shown that the *in–vitro* selectivity of the GSK598809 for the D3R over the D2R is 100-fold and this justifies the selection of the single site competition model. Therefore, following administration of GSK598809, a number of D3R sites are occupied by the compound and the number of B_{avail}^{D3R} reduces proportional to the administered dose. This results in a change to the measured BP_{ND}^{PHNO}, which in a PET study is described by:

$$\Delta BP_{ND}^{PHNO} = \left(\frac{BP_{ND}^{baseline} - BP_{ND}^{GSK598809}}{BP_{ND}^{baseline}}\right) 100\,\% \tag{6.4}$$

Where $BP_{ND}^{baseline}$ is the total [^{11}C]PHNO binding at baseline and $BP_{ND}^{GSK598809}$ is the total [^{11}C]PHNO binding after the administration of the GSK598809 compound. The change in [^{11}C]PHNO BP_{ND} is related to the concentration of the GSK598809 compound

in plasma and, assuming a single site competition model, it can be described by:

$$Occupancy = X\left(\frac{C_P^{GSK598809}}{C_P^{GSK598809} + EC_{50}^{D3R}}\right) \tag{6.5}$$

where $C_p^{GSK598809}$ is the plasma concentration of GSK598809, EC_{50}^{D3R} is the plasma concentration of GSK598809 that leads to a 50% occupancy of the D3R, and X represents the fraction of radiotracer binding attributable to the binding site (i.e. D3R). In other words, X in our study corresponds to the fraction of [^{11}C]PHNO binding to the D3R and can be expressed as:

$$f_{PHNO}^{D3R} = \frac{BP_{ND}^{D3R}}{BP_{ND}^{D3R} + BP_{ND}^{D2R}} \tag{6.6}$$

Combining equations 6.4 to 6.6 and assuming a single site competition model (binding only to the D3R sites) for the GSK598809 the BP_{ND} obtained following administration of the selective D3R antagonist can be described by:

$$BP_{ND}^{post-drug} = BP_{ND}^{Baseline}\left(\frac{f_{PHNO}^{D3R}}{1 + \frac{C_p^{GSK598809}}{EC_{50}^{D3}}} + \left(1 - f_{PHNO}^{D3R}\right)\right) \tag{6.7}$$

where $BP_{ND}^{Baseline}$ and $BP_{ND}^{post-drug}$ are the BP_{ND} values at baseline and following dosing with GSK598809 respectively.

Regional f_{PHNO}^{D3R} were estimated via model fits to equation 6.7 with EC_{50}^{D3} shared between regions under the assumption that the free brain concentration and affinity of GSK598809 are homogeneous across the brain. The estimation of f_{PHNO}^{D3R} allowed the determination of the BP_{ND}^{D3R} and BP_{ND}^{D2R} using the following equations:

$$BP_{ND}^{D3R} = f_{PHNO}^{D3R}\, BP_{ND}^{PHNO} \tag{6.8}$$

$$BP_{ND}^{D2R} = \left(1 - f_{PHNO}^{D3R}\right)\ BP_{ND}^{PHNO} \tag{6.9}$$

6.3 Results

All forty-eight [^{11}C]PHNO PET scans and corresponding MRI scans from the nineteen subjects were analysed successfully to derive regional estimates of BP_{ND} and f_{PHNO}^{D3R}. After the tracer injection, three subjects reported mild nausea.

6.3.1 Distribution of [^{11}C]PHNO in the structural subcortical regions

High accumulation of [^{11}C]PHNO was observed in the striatum and pallidum whereas lower concentrations were observed in the midbrain, thalamus and hypothalamus. The concentrations within the pallidum, thalamus and striatum were not spatially homogeneous. Specifically, in the striatum a lower concentration was observed in the ventral striatum but it was notably higher than concentrations observed in studies that use other agonist (i.e. [^{11}C]NPA) or antagonist (i.e. [^{11}C]Raclopride) ligands. In the pallidum a higher accumulation was seen in the rostral and ventral pole of the pre–commissural pallidum, whereas in the thalamus a higher accumulation was seen in the anterior-medial thalamus.

In all regions, [^{11}C]PHNO concentration peaked within the first 20 *minutes* but the washout rate of the radioactivity was different between regions (figure 6.1). The fastest washout rate was in the cerebellum, whereas washout in the pallidum was more protracted. A good description of the kinetic data was achieved using SRTM at baseline and following the administration of GSK598809, with the cerebellum as the reference region. Figure 6.1 shows regional SRTM model fits for a representative subject at baseline and post 175 *mg* of GSK598809. After administration of 175 *mg* of

GSK598809 the activity in SN and Hypo reached the level of activity in the cerebellum whereas in the CD and the PU we observed the least reduction.

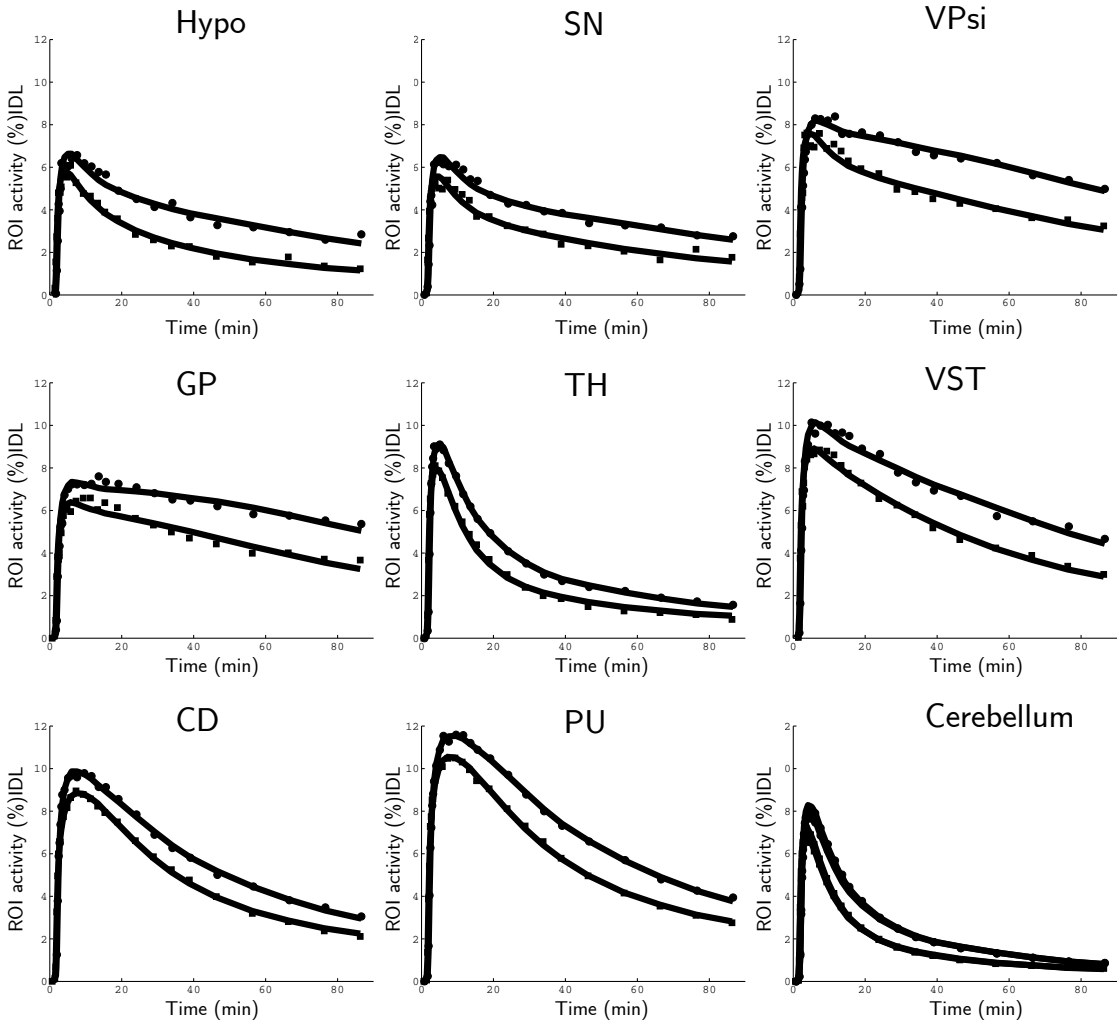

Figure 6.1: [^{11}C]PHNO TACs and SRTM model fits in one subject at baseline and after the oral administration of $175\,mg$ of the selective D3R antagonist GSK598890 in the anatomical ROIs

Following administration of the GSK598809, a regional and dose dependent reduction of the [^{11}C]PHNO signal was observed. After administration of $175\,mg$ of GSK598809, the highest reduction was observed in the SN, Hypo and pallidum, whereas in the cortical regions, CD and PU the signal was marginally reduced. In the cerebellum, which was used as the reference region, a small change was seen in the vermis. Figure

6.2 shows a parametric SRTM [^{11}C]PHNO BP_{ND} image [69], in a representative subject, at baseline conditions and following the administration of 175 mg GSK598809.

A prominent decrease in BP_{ND} was measured in the SN, Hypo, GP and VP_{SI} and a modest reduction in the TH and VST. The lowest BP_{ND} reduction was observed in the CD and PU. Figure 6.3 shows the average [^{11}C]PHNO BP_{ND} at baseline (light grey) and after administration of 75 mg (grey) and 175 mg (black) of GSK598809 in selected brain regions. In agreement with the visual observations, the largest reduction of the BP_{ND}, following 175 mg of GSK598809, was measured in the Hypo, SN and pallidum. In the striatum the BP_{ND} was reduced after the administration of 175 mg of GSK508809, whereas at doses of 75 mg the BP_{ND} was unchanged. In the striatum the largest reduction was in the VST.

The model described in equation 6.7 was fitted to the data from all subjects and regions simultaneously (figures 6.4 and 6.5). The EC_{50}^{D3} was shared between regions whereas f_{PHNO}^{D3R} was estimated for each ROI.

In table 6.3 the regional estimates for f_{PHNO}^{D3R} and $BP_{ND}^{Baseline}$ are presented. In the Hypo and SN almost the entire [^{11}C]PHNO signal is attributable to the D3R sites, whereas in the CD and PU the [^{11}C]PHNO signal is estimated to be solely due to the D2R sites. In table 6.3 the two columns on the right hand side correspond to the binding of [^{11}C]PHNO to the D3R sites (BP_{ND}^{D3R}) and the D2R (BP_{ND}^{D2R}) sites derived using equations 6.8 and 6.9. The highest concentration of D3R receptors is found in the pallidum, followed by the Hypo and SN with lower levels in the striatum and particularly in the CD and PU.

Figure 6.6 shows the total [^{11}C]PHNO and the BP_{ND}^{D3R} and BP_{ND}^{D2R} components. To create this figure the parametric SRTM BP_{ND} image generated for each scan was non-

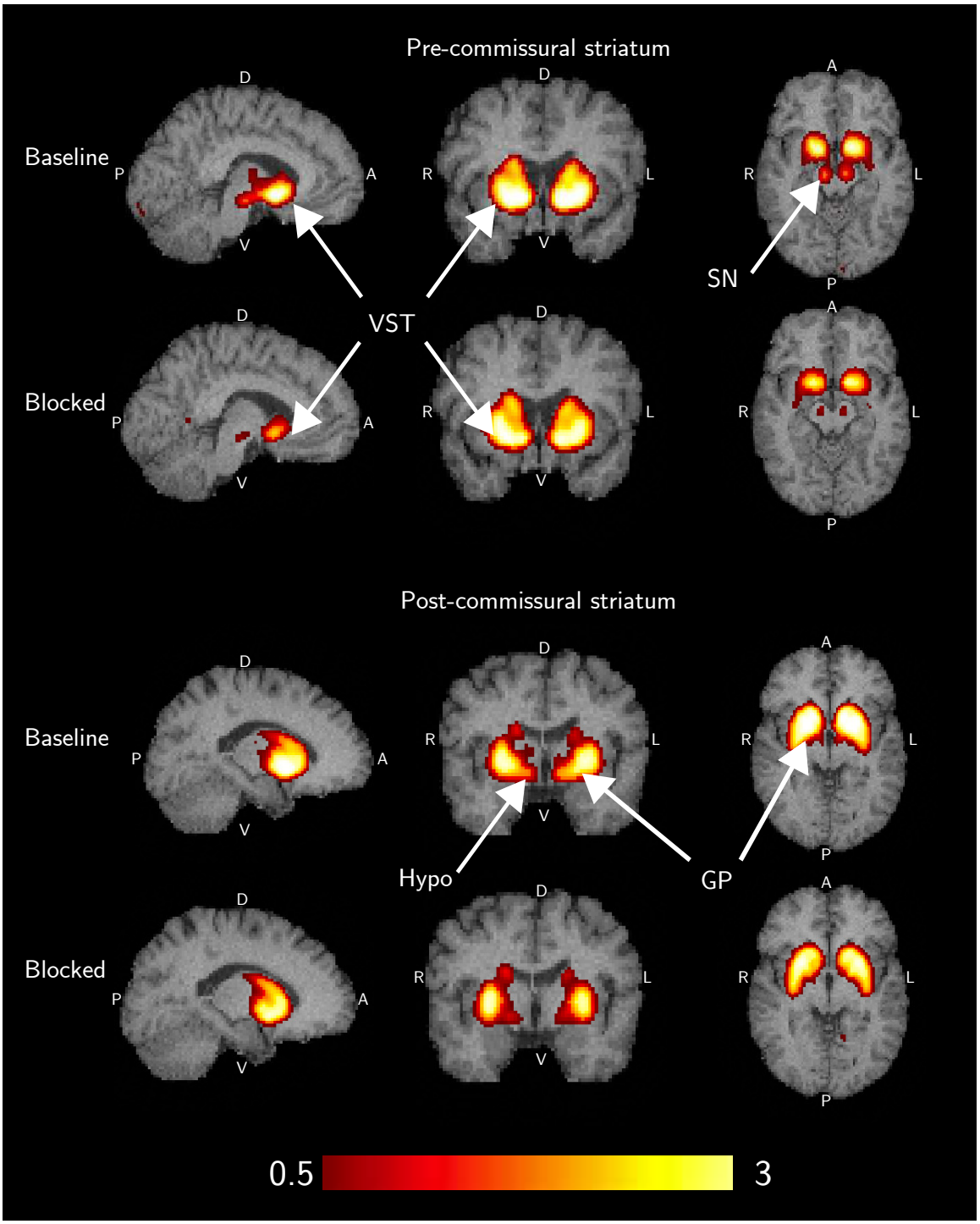

Figure 6.2: [^{11}C]PHNO parametric BP_{ND} images at baseline and after administration of $175\,mg$ GSK598809 in the pre–commissural (top set of images) and post–commissural (bottom set of images) striatum in a single subject. The top row of each set shows the BP_{ND} at baseline and the bottom row shows the BP_{ND}after the administration of the GSK598809. The image illustrates the marked change in the SN and Hypo, the moderate change in the GP and VST and the marginal change in the CD and PU. R=right; L=left; A=anterior; P=posterior; D=dorsal; V=ventral.

Table 6.3: [^{11}C]PHNO parameters estimated in the dopamine–rich subcortical structures using the model described in equation 6.7 and equations 6.9. Columns correspond to: total [^{11}C]PHNO baseline binding (BP_{ND}^{PHNO}); the fraction of baseline [^{11}C]PHNO binding that corresponds to D3R (f_{PHNO}^{D3R}); [^{11}C]PHNO baseline binding to D3R (BP_{ND}^{D3R}), and to D2R (BP_{ND}^{D2R}). Values in parentheses represent 95% confidence intervals.

Region	BP_{ND}^{PHNO}	f_{PHNO}^{D3R}	BP_{ND}^{D3R}	BP_{ND}^{D2R}
VP_{SI}	3.42 (3.30 – 3.54)	0.69 (0.59 – 0.79)	2.37	1.05
GP	2.62 (2.50 – 2.73)	0.57 (0.46 – 0.67)	1.48	1.14
Hypo	1.10 (0.98 – 1.21)	1 (0.78 – 1)	1.10	0
SN	1.04 (0.92 – 1.15)	0.92 (0.70 – 1)	0.96	0.08
TH	0.37 (0.26 – 0.49)	0.46 (0 – 1)	0.17	0.20
VST	2.48 (2.37 – 2.60)	0.19 (0.09 – 0.29)	0.47	2.01
PU	2.19 (2.07 – 2.30)	0 (0 – 0.12)	0	2.19
preVPU	2.50 (2.39 – 2.62)	0.01 (0 – 0.12)	0.04	2.47
preDPU	1.92 (1.81 – 2.04)	0 (0 – 0.14)	0	1.92
prePU	2.29 (2.17 – 2.40)	0 (0 – 0.11)	0	2.29
posPU	2.08 (1.96 – 2.19)	0 (0 – 0.13)	0	2.08
CD	1.46 (1.35 – 1.58)	0 (0 – 0.18)	0	1.46
preCD	1.53 (1.41 – 1.64)	0 (0 – 0.17)	0	1.53
posCD	1.04 (0.93 – 1.16)	0 (0 – 0.25)	0	1.04

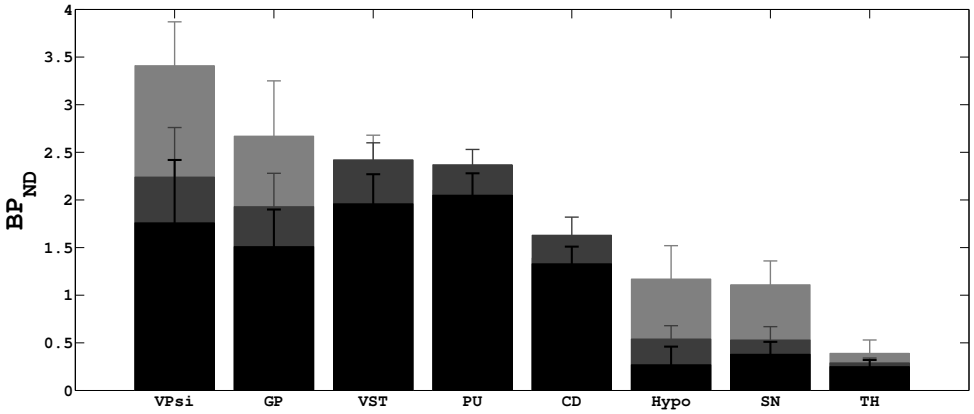

Figure 6.3: [^{11}C]PHNO BP_{ND} at baseline (light grey) and after administration of $75\,mg$ (grey) and $175\,mg$ (black) of GSK598809 in selected brain regions

linearly warped onto the MNI template. Subsequently, f_{PHNO}^{D3R} was estimated at the voxel level by fitting the single site competition model (equation 6.7) to the spatially normalised parametric images and constraining the EC_{50}^{D3} to the value estimated on a regional basis. Afterwards, using the average parametric SRTM [^{11}C]PHNO baseline BP_{ND} template and equations 6.8 and 6.9 we derived the BP_{ND}^{D3R} and BP_{ND}^{D2R} images. The distribution shown reflects the estimated regional f_{PHNO}^{D3R}. The figure shows that the majority of the signal from the Hypo, SN, VP_{SI} and GP is due to the D3R. A heterogeneous distribution is observed in the TH where a D3R signal is seen in the rostral nuclei of the thalamus. In the striatum, on the other hand, the majority of the signal is due to the D2R. In particular, in the PU and CD the signal is entirely due to the D2R, while in the VST the signal is a mixture of the D2R and D3R with the majority being D2R. The estimated values in the Hypo and SN indicate that the [^{11}C]PHNO signal is predominantly attributable to the D3R. In the VP_{SI} and GP this becomes less marked but the majority of the signal is still attributable to the D3R.

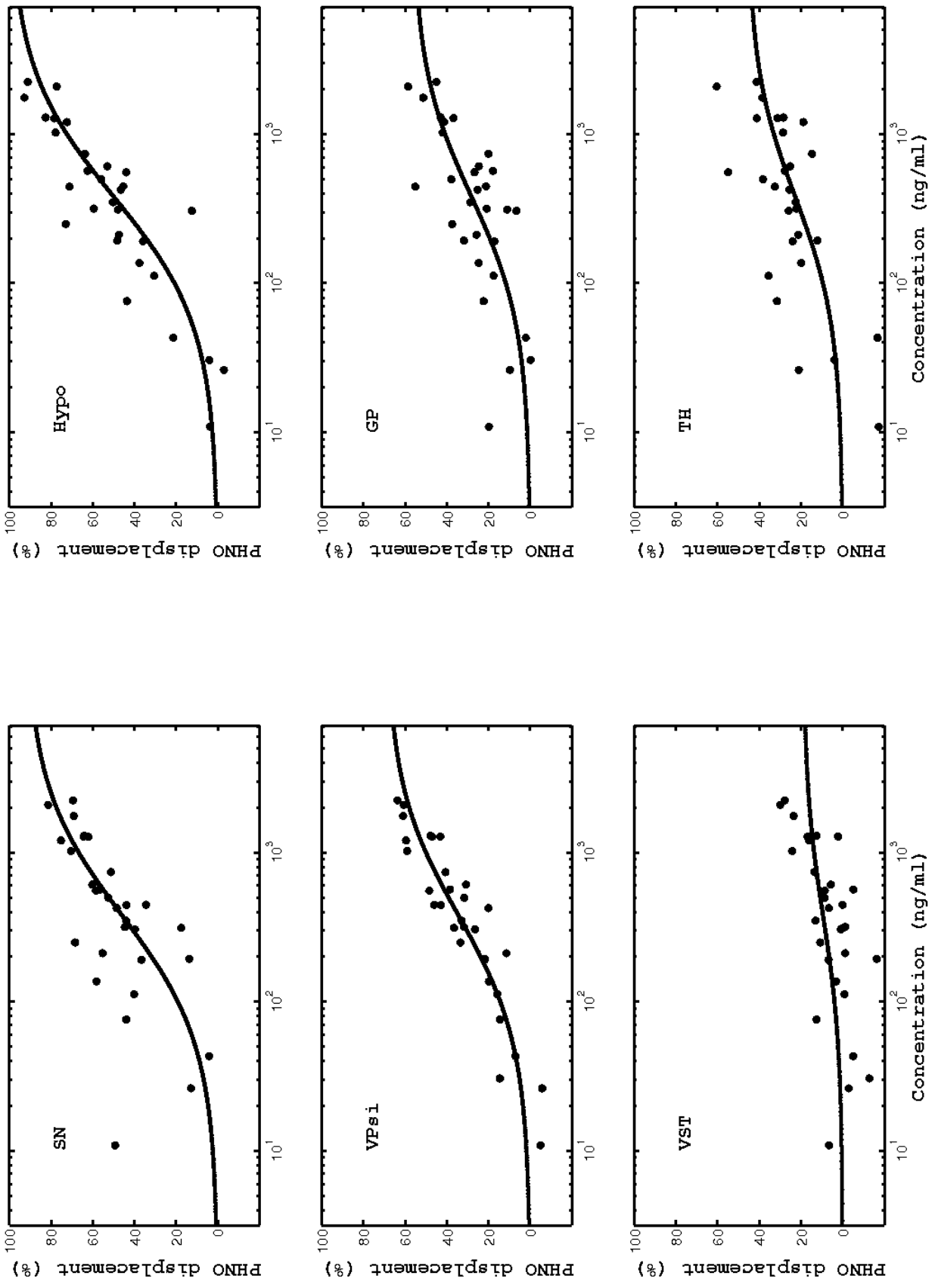

Figure 6.4: Displacement of the [^{11}C]PHNO ligand against GSK598809 plasma concentration in SN, Hypo, VST, TH, GP and VP_{SI}. Solid lines represent model fits to the measured data according to equation 6.5.

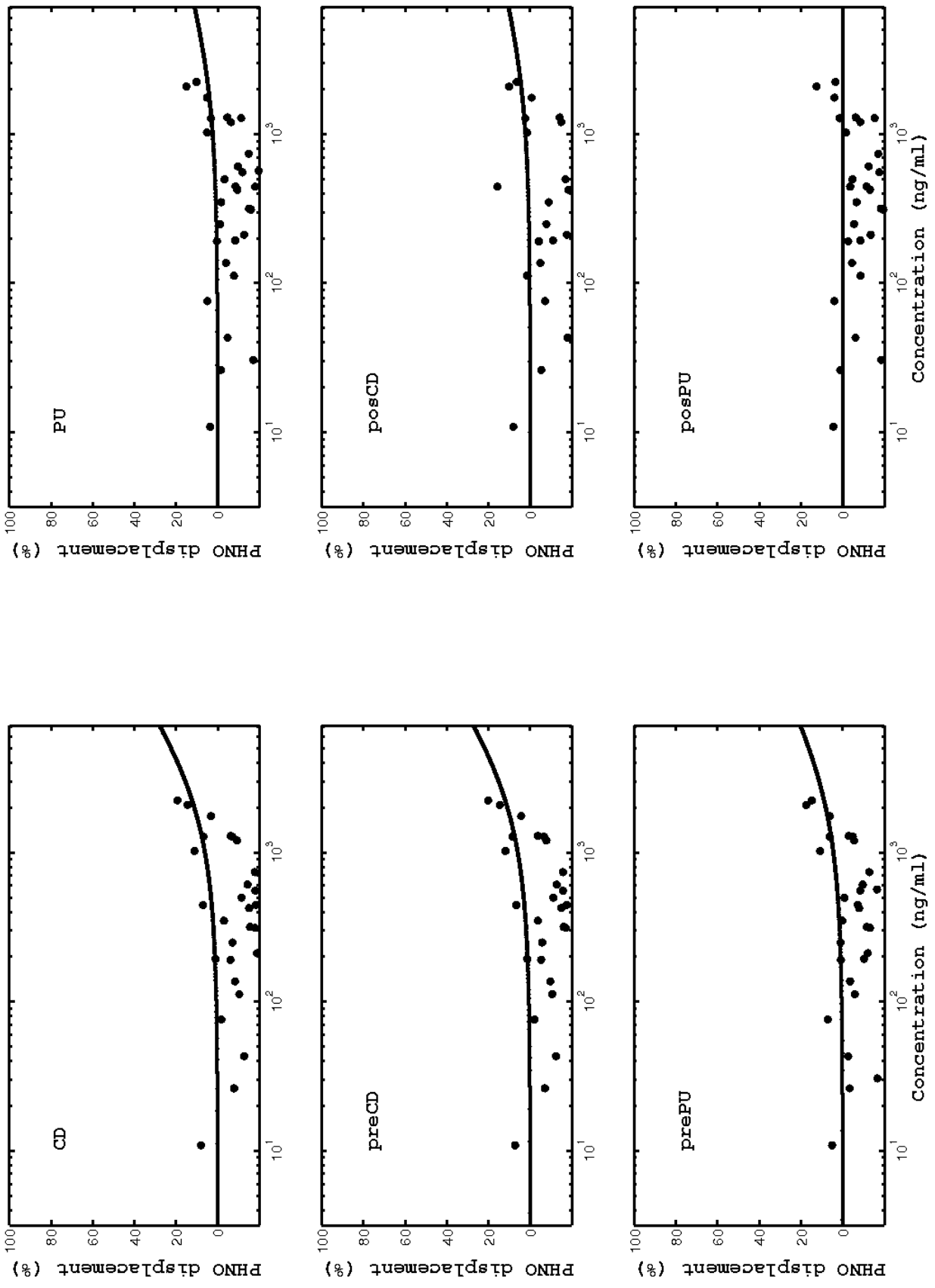

Figure 6.5: Displacement of the [^{11}C]PHNO ligand against GSK598809 plasma concentration in the CD, PU, and in their pre–commissural and post–commissural subdivisions. Solid lines represent model fits to the measured data according to equation 6.5.

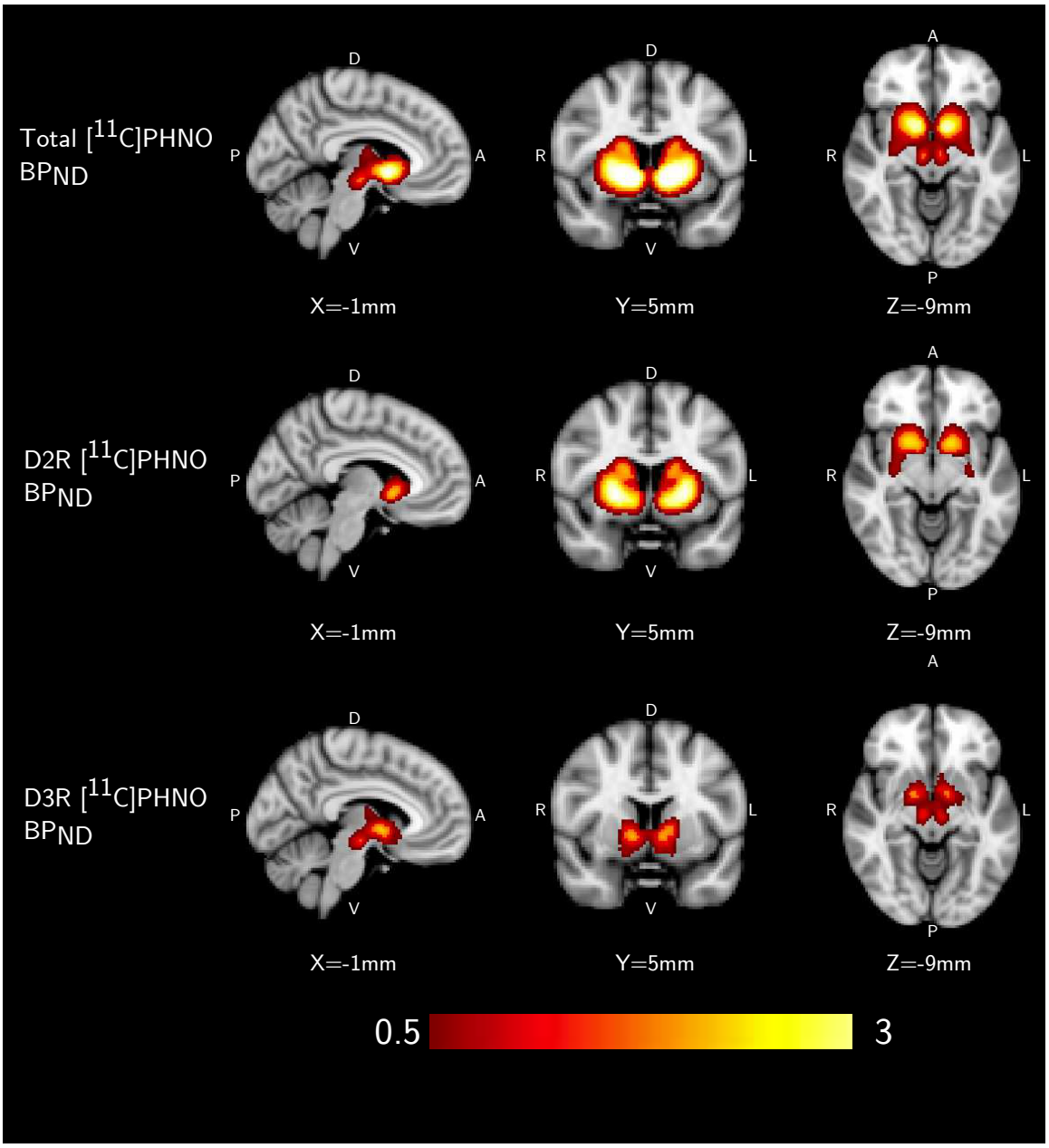

Figure 6.6: Summary of the [^{11}C]PHNO BP_{ND}: total (top), D2R (middle) and D3R (bottom) BP_{ND}overlaid on the MNI template. To create the figure the baseline and post-GSK598809 scans from all subjects were employed. R=right; L=left; A=anterior; P=posterior; D=dorsal; V=ventral.

6.3.2 Distribution of the [^{11}C]PHNO in the connectivity-based functional subdivisions of the striatum and pallidum

To characterise the [^{11}C]PHNO signal in the connectivity-based functional subdivisions of the striatum and pallidum the atlases constructed in chapter 5 were employed and spatially normalised to each subject in order to define the connectivity-based subregions. However, before we proceeded with the quantification of [^{11}C]PHNO in the functional subdivisions we examined whether the atlas subdivisions correspond well with individual subject's connectivity-based subregions. Data from another study were employed to evaluate this correspondence. The comparison was made in terms of volume overlap (DICE coefficient, equation 4.1) of the atlas–defined subdivisions and the subject's individually-derived subdivisions, and also with regard to the variability of the BP_{ND} (equation 4.2). The results of the comparison are displayed in table 6.4.

Table 6.4: Agreement between subdivisions performed with individual data-driven connectivity-based subdivisions and connectivity-based atlas.

Region	DICE(%)	BP_{ND} variability (%)
Striatum limbic	60.55 ± 6.33	1.58 ± 1.23
Striatum executive	55.37 ± 14.60	4.65 ± 3.90
Striatum rostral-motor	45.89 ± 8.38	4.20 ± 3.93
Striatum caudal-motor	35.17 ± 10.43	9.92 ± 7.66
Striatum parietal	36.75 ± 7.38	7.07 ± 3.95
Striatum sensorimotor	65.10 ± 6.45	4.95 ± 3.21
Striatum occipital	14.10 ± 15.45	22.99 ± 12.28
Striatum temporal	4.52 ± 4.51	21.86 ± 13.02
Pallidum limbic	13.22 ± 5.52	2.39 ± 2.38
Pallidum executive	50.86 ± 8.01	1.59 ± 1.32
Pallidum sensorimotor	49.56 ± 5.97	4.63 ± 3.17

For the larger subdivisions, the DICE coefficient is $\sim 50\,\%$ and the BP_{ND} variability is lower than $5\,\%$, which is at a level comparable with the BP_{ND} variability obtained for the intra and inter operator manually–defined subcortical ROIs (chapter 4). For the striatal subdivisions the DICE coefficient ranges from $4.52\,\%$ for the temporal lobe to $65\,\%$ for the sensorimotor subdivision. As there is no scientific consensus to what is considered a satisfactory DICE coefficient, for the striatum, which is a relatively big subcortical area, we set $50\,\%$ to be the lowest value. Therefore only the limbic, executive and sensorimotor areas were considered and employed for the quantification of the PET signal. The pallidum is a substantially smaller structure and a DICE of $50\,\%$ was the maximum achieved. Other than the possible low regional correlation between the atlas and the subject's own functional subdivisions, the low DICE coefficient could also be due to the small size of the pallidum (figure 4.6) and due to the fact that non-linear registration algorithms do not perform well in this area as the pallidal tissue is an admixture of white and grey matter and due to this admixture and partial volume effects the region has a low contrast which might impact the registration between the MNI template and the subject's T1-weighted image. The DICE for the limbic area of the pallidum is only $13\,\%$. As we reported in chapter 5, the limbic area of the pallidum is predominantly the ventral pallidum, which is a region that is not visible on standard T1-weighted images. Hence the pallidal ROI does not inclute this area and therefore the limbic area is very small and in some instances is comprised of only a few voxels. However, the BP_{ND} variability of the limbic pallidum is only $2.39\,\%$ and this supports the use of this region, although the results should be treated with caution. Therefore, for both the striatum and pallidum we have characterised the [^{11}C]PHNO signal in the limbic, executive and sensorimotor functional subregions.

As with the structural subdivision, the SRTM model describes the kinetic behaviour well in the connectivity-based functional subdivisions of the pallidum and striatum (figure 6.7) at baseline and following the administration of $175\,mg$ of GSK598809.

Again, different washout rates were observed with a particularly slow washout in the pallidal subdivisions as compared to the striatum.

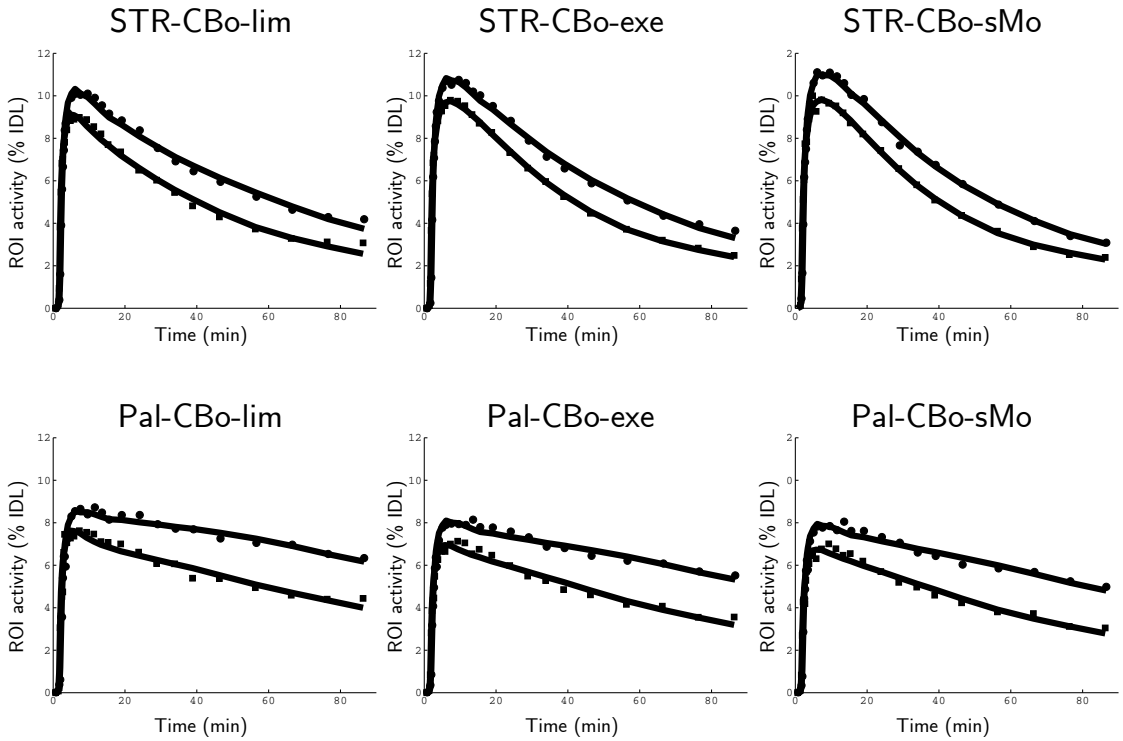

Figure 6.7: [^{11}C]PHNO TACs and SRTM model fits in one subject at baseline and after oral administration of $175\,mg$ GSK598809, using the connectivity-based functional ROIs of the striatum and pallidum

Using equation 6.7 we estimated f_{PHNO}^{D3R} and BP_{ND}^{PHNO} and from equations 6.8 and 6.9 the D3R and D2R BP_{ND} were derived for each connectivity-based functional subdivision in the striatum and pallidum. Figures 6.8 and 6.9 show the model fits, and the parameter estimates with confidence intervals are given in table 6.5.

There is a good agreement between the results derived for the subdivisions from the exclusive atlas (CBe) and from the subdivisions obtained with the connectivity probability maps (CBo) that allow overlapping zones between the functional parcellations. In the limbic striatum approximately 20 % of the [^{11}C]PHNO signal is attributable to

the D3R sites, whereas in the other subdivisions of the striatum the [^{11}C]PHNO signal is almost entirely due to the D2R sites. In contrast, in all pallidal regions the majority of the [^{11}C]PHNO signal is due to the D3R. The highest concentration of D3R is in the limbic, followed by the executive and sensorimotor. Notably, the density of the D2R sites (BP_{ND}^{D2R}) is uniformly distributed across the functional subdivisions of both the striatum and pallidum.

Table 6.5: [^{11}C]PHNO parameters estimated in the connectivity-based functional subdivisions of the striatum and pallidum using the model described in equation 6.7 and equations 6.8 – 6.9. Columns correspond to: total [^{11}C]PHNO baseline binding (BP_{ND}^{PHNO}); fraction of baseline [^{11}C]PHNO binding corresponding to D3R (f_{PHNO}^{D3R}); [^{11}C]PHNO baseline binding to D3R (BP_{ND}^{D3R}), and to D2R (BP_{ND}^{D2R}). Values in parentheses represent 95% confidence intervals.

Region	BP_{ND}^{PHNO}	f_{PHNO}^{D3R}	BP_{ND}^{D3R}	BP_{ND}^{D2R}
Str-CBo-lim	2.41 (2.31 – 2.51)	0.17 (0.06 – 0.27)	0.40	2.01
Str-CBo-exe	2.07 (1.97 – 2.17)	0.02 (0 – 0.15)	0.04	2.03
Str-CBo-sMo	2.00 (1.90 – 2.09)	0 (0 – 0.14)	0	2.00
Str-CBe-lim	2.42 (2.32 – 2.52)	0.19 (0.08 – 0.29)	0.45	1.97
Str-CBe-exe	2.01 (1.91 – 2.10)	0.01 (0 – 0.15)	0.03	1.98
Str-CBe-sMo	1.88 (1.78 – 1.97)	0 (0 – 0.14)	0	1.88
Pal-CBo-lim	3.98 (3.88 – 4.08)	0.76 (0.68 – 0.84)	3.03	0.94
Pal-CBo-exe	3.04 (2.94 – 3.14)	0.70 (0.60 – 0.79)	2.11	0.92
Pal-CBo-sMo	2.71 (2.62 – 2.81)	0.65 (0.55 – 0.75)	1.76	0.95
Pal-CBe-lim	3.61 (3.51 – 3.70)	0.72 (0.60 – 0.78)	2.60	1.01
Pal-CBe-exe	3.05 (2.95 – 3.15)	0.69 (0.61 – 0.79)	2.10	0.94
Pal-CBe-sMo	2.23 (2.13 – 2.33)	0.51 (0.40 – 0.63)	1.15	1.08

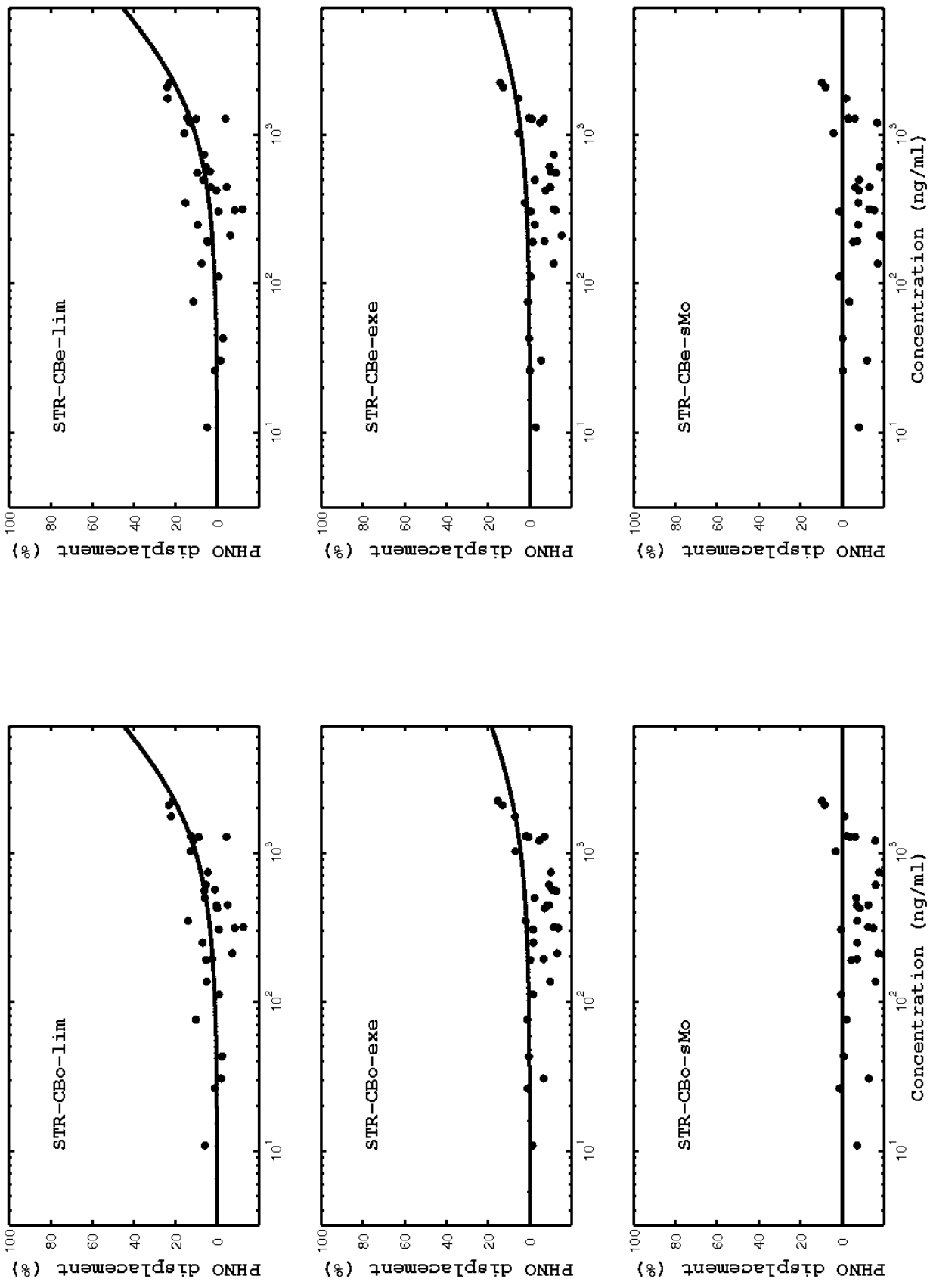

Figure 6.8: Displacement of the [^{11}C]PHNO ligand against plasma concentration in the connectivity-based subdivisions of the striatum. Solid lines represent model fits to the measured data according to equation 6.5.

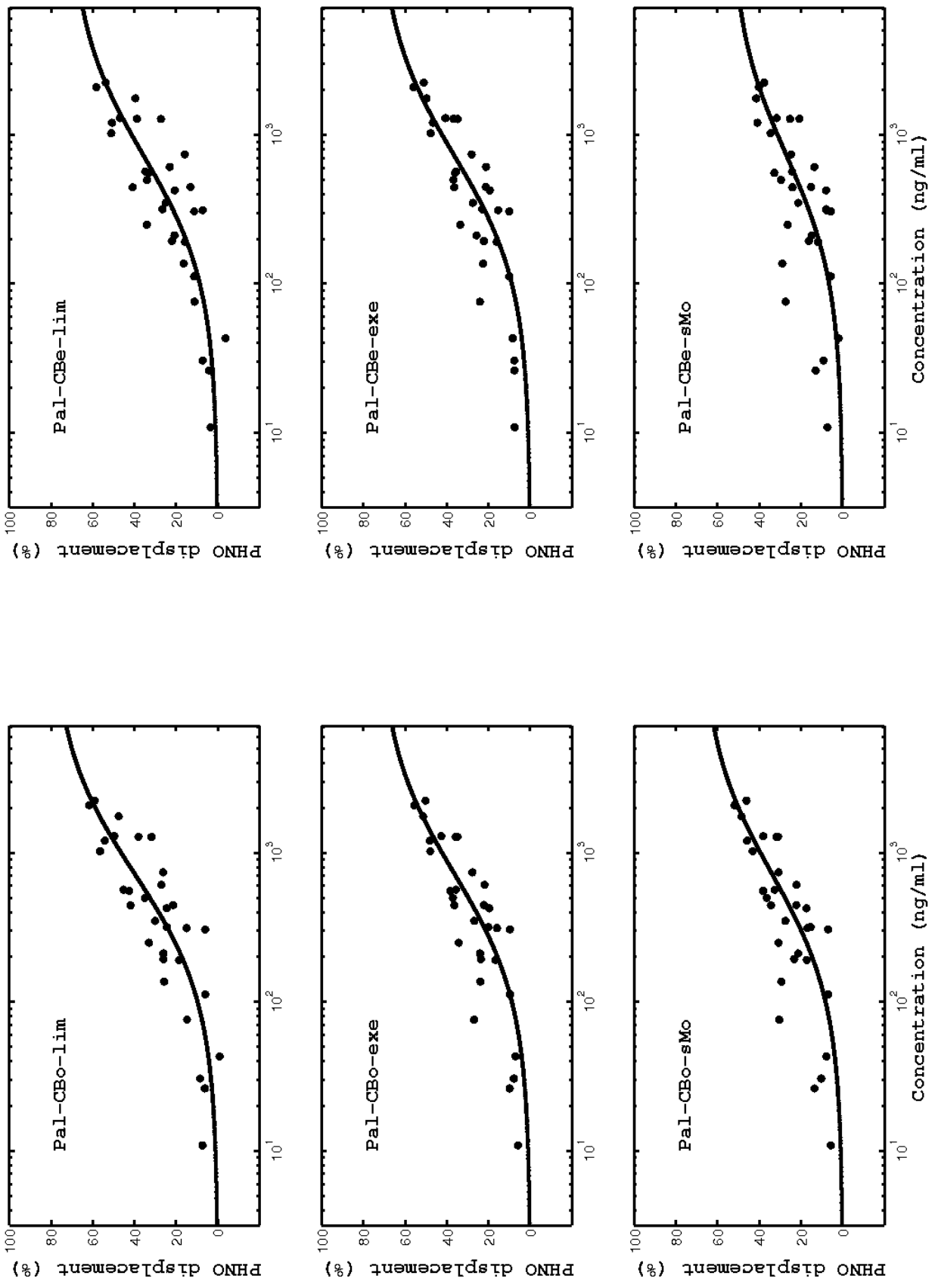

Figure 6.9: Displacement of the [^{11}C]PHNO ligand against plasma concentration in the connectivity-based subdivisions of the pallidum. Solid lines represent model fits to the measured data according to equation 6.5.

6.4 Discussion

In this chapter we have examined the distribution of [^{11}C]PHNO in healthy humans at baseline conditions and after the administration, at varying doses, of the selective D3R antagonist GSK598809. This allowed the [^{11}C]PHNO specific binding signal to be partitioned into its D3R and D2R components using equation 6.7, and provided information about the relative density of these receptors in the living human brain. For baseline conditions, [^{11}C]PHNO concentration was high in the subcortical regions, especially in the striatum and the pallidum. [^{11}C]PHNO signal was also observed in other regions such as the mesencephalon, TH and Hypo. There was no significant [^{11}C]PHNO signal in cortical regions except for some low activity in the subiculum and the parahippocampal gyrus. In VP_{SI} we measured the highest BP_{ND} (3.47) followed by the GP, whereas the TH had the lowest BP_{ND} estimates (0.37).

Although [^{11}C]PHNO has a higher preferential affinity for D3R, it is not sufficiently large to render the imaging probe completely D3R selective and thus the D2R contribution must also be considered. The contribution of each receptor type to the total [^{11}C]PHNO BP_{ND} depends on the relative regional density of the D2R / D3R sites. In order to dissect the [^{11}C]PHNO signal for each region into its D2R and D3R components, the single site model was used. This model assumes that the GSK598809 compound binds only to one site, the D3R. The results indicate that in the Hypo and SN almost the entire signal is due to the D3R receptors, whereas in the CD and PU the signal is only due to D2R. The highest concentration of D3R sites was in the pallidum and the lowest in the dorsal striatum, which has the highest concentration of D2R. The high concentration of D3R in the pallidum, coupled with the high preferential affinity of [^{11}C]PHNO for this receptor type, is consistent with the slow washout rate observed in the pallidum.

The two site model was also investigated, which assumes that the GSK598809 compound binds not only to the D3R but also to the D2R. The two site model yielded comparable results, while the Akaike information criterion was marginally better for the one site model for the estimates of BP_{ND} with the SRTM model. Nevertheless, a recent study by Searle and colleagues [156] characterised the GSK598809 compound *in–vivo* and found that the two site binding model (binding of the GSK598809 to both D3R and D2R) produced significantly better fits to the data than the single site model (D3R only). Searle and colleagues also demonstrated that the *in–vivo* selectivity of the GSK598809 compound is around 75-fold for the D3R over the D2R.

In the D3R rich regions our results are compatible to *in–vitro* [71] and *in–vivo* studies in baboons [150]. However, the f_{PHNO}^{D3R} in the D2R rich regions such as the CD and the PU is lower and the model does not seem to describe the data well (figures 6.4, 6.5 and 6.8). In particular, at high concentrations of GSK598809 the occupancy has negative values, which means that the post-challenge BP_{ND} is higher than the BP_{ND} at baseline. This may be attributed to blockade of the receptors in the reference region after the administration of the GSK598809. Rabiner and colleagues [150], who measured the arterial input function, found a dose dependent decrease in cerebellar V_T following administration of SB277011 in primates. Specifically, a decrease in cerebellar V_T of up to 28 % was measured at doses of $5\,mg/kg$ of SB277011. In our study we have estimated the SUV (ratio of tissue radioactivity concentration divided by the injected activity and the body weight) in the cerebellum and found a reduction of 13 %. In addition, the D3R parametric BP_{ND} image showed a small signal in vermis ($BP_{ND} \sim 0.25$). We have examined the occipital lobe, parietal lobe, frontal lobe, dorsal cerebellum and ventro-lateral cerebellum as potential reference regions. However, all candidate reference regions have a similar or equal signal decrease after the administration of GSK598809. Only the dorsal cerebellum shows a smaller decrease (regional BP_{ND} obtained with dorsal cerebellum is $\sim 5\,\%$ higher compared to

regional BP_{ND} obtained with the whole cerebellum). However, the small size of this region leads to poor statistics; therefore the whole cerebellum was selected for the reference region. A conclusive statement as to the suitability of the cerebellum as a reference region in human studies warrants further investigation.

In this study we have identified and quantified the D3R binding in two regions, the VP_{SI} and the Hypo, which had not been examined *in–vivo* before even though there is *in–vitro* evidence that supports the existence of D3R. [^{11}C]PHNO accumulation in the Hypo was observed in the BP_{ND} parametric images (figure 6.6). While we had some concern that the signal might be due to spill-over effects from the VP_{SI} and/or the GP, the high f^{D3R}_{PHNO} ($\sim 100\,\%$) and BP_{ND} values (1.17 ± 0.25) from both parametric and dynamic analyses in conjunction with the *in–vitro* human [169, 71] and findings in mice [150] suggests that the accumulation of [^{11}C]PHNO here is due to the presence of D3R in the Hypo. The VP_{SI} has the highest [^{11}C]PHNO BP_{ND} across regions. These results are in agreement with the *in–vitro* studies [169, 71] that have identified the ventral pallidum as a region with a high concentration of D3R. We have to point out that the VP_{SI} includes both the ventral pallidum and the substantia innominata regions, and therefore a direct comparison with the ventral pallidum data cannot be made. A high BP_{ND} signal was also observed in areas where the bed nucleus of the stria terminalis (BNST) and extended amygdala are located. The extended amygdala has been accepted as a useful concept in the investigation of drug addiction and neuropsychiatry disorders [85] making this observation important, and increasing the need to investigate the existence of D3R and D2R in this region.

The [^{11}C]PHNO signal was also characterised in the connectivity-based functional subdivisions of the striatum and pallidum. In both structures the highest f^{D3R}_{PHNO} and BP^{D3R}_{ND} were in the limbic regions. This finding is in accord with theories that assign a primarily limbic role to the D3R and justifies the efforts to target the D3R for the

treatment of addictive and other psychological disorders. In the executive and sensorimotor targets of the striatum the estimated f_{PHNO}^{D3R} is negligible. However, similar to the CD and PU, there is a dip in the occupancy estimates (figure 6.8) after administration of high doses of GSK598809, which can be explained by a blockade of the cerebellum. This could result in underestimation of the f_{PHNO}^{D3R} in the D2R rich regions.

In the pallidum, D3R were found in all functional subdivisions with the lowest estimates found in the sensorimotor region. The estimated f_{PHNO}^{D3R} in the sensorimotor pallidum, which constitutes 40% of the total pallidal volume, was comparable to the estimates for the whole GP structure (57 %). In the limbic and executive regions the average f_{PHNO}^{D3R} was around 72 %. This suggests that merging the signal from different functional subdivisions might underestimate the overall finding and this might prove an important issue when comparing healthy and diseased cohorts. The parameters of interest for the striatum and pallidum were estimated for the CBe and CBo atlases and the results were comparable. This shows that quantification within the connectivity-based subdivisions is robust. Moreover, there was an excellent correlation between [^{11}C]PHNO BP_{ND} in the limbic striatum and the VST structure. This demonstrates that our guidelines for the definition of the VST are able to effectively capture the limbic territory of the striatum.

Some limitations of this study should be acknowledged. For example, we cannot subdivide certain regions reliably with the MRI sequences acquired in this study. The *in–vitro* findings suggest that in the GP, TH and SN the D3R are not homogeneously distributed. In particular, the D3R concentration in the GP_i, SN pars reticulata and the antero-ventral thalamic nucleus is higher. Therefore a subdivision of these regions, based on functional data or anatomical data, should be considered. Advanced MRI sequences such as the FGATIR [171], should be acquired to aid in the subdivision of these regions. In addition, we did not apply partial volume correction in this

study. The subcortical regions of interest studied here have different surroundings that will impact quantifications differently. For example, the striatum is near the pallidum, which has a high specific binding, and the SN is surrounded by areas with little detectable activity. The neighbouring structures can potentially overestimate or underestimate the quantification of D3R in the region of interest due to spill-in or spill-over effects respectively.

The kinetic modelling was performed using the SRTM model to describe the data. As we have discussed, the cerebellum might not be an optimal reference region as there is some evidence for a small amount of specific binding in subregions of the cerebellum. Also, SRTM assumes just a single tissue compartment in both target and reference regions which could lead to a small bias in the estimated binding potential although these effects should be minimal for challenge–based studies where the fractional change in BP_{ND} is sought. Nevertheless, without arterial blood data it is not possible to assess whether the reduction of [^{11}C]PHNO signal in the cerebellum is due to displacement of a small amount of specific binding. The study by Searle et al. [156] used the D3R selective GSK618334 compound and acquired arterial blood data to assess the binding in the cerebellum. They discovered that the V_T values in the cerebellum were reduced to a modest degree in a dose-dependent manner, suggesting the presence of specific binding. Specifically, they derived V_T values in baseline conditions and following various doses of GSK618334 that led to plasma concentrations ranging from approximately $10\,ng/ml$ to $1000\,ng/ml$. These data showed that increasing plasma concentrations of GSK618334 led to decreasing cerebellum V_T values, with the magnitude of this decrease at the highest doses being around 20%.

Searle and colleagues [156] also applied the 1TC and 2TC models (see chapter 3) to the [^{11}C]PHNO baseline and post-drug data and found that the 2TC model produced

superior model fits in all ROIs. The BP_{ND} values derived using the 2TC model (calculated from the 2TC V_T data) were also compared with those derived from the SRTM model. As is the case for other radiotracers, the SRTM BP_{ND} values were underestimated relative to 2TC estimates, especially for higher values, but the correlation between the two was strong ($r^2 = 0.95$). However, as we are measuring the relative change in BP_{ND} between baseline and post-drug scans, the bias introduced by using the SRTM model will be small, according to Searle and colleagues, relative to the subject's discomfort and the measurement variability associated with the acquisition of the blood data.

In our study three subjects reported nausea, which is consistent with reports from other studies [134]. There is hence the possibility that the [^{11}C]PHNO doses that were administered resulted in a non-negligible fraction of the target receptors being occupied (mass dose effect). A low mass is necessary not only to avoid pharmacological or potential toxic effects but is also required in order to keep the experiment at "tracer conditions" [170], which will provide reliable quantitative estimates for the BP_{ND}. Tracer conditions refer to PET experiments where the cold ligand occupies $<$ 5-10% of the receptor/transporter target. There are two main consequences of the violation of the tracer assumptions. First, for studies involving two PET [^{11}C]PHNO scans at short time intervals (some hours apart) a carry-over effect (occupancy of the receptors by "cold" (+)PHNO) is possible, which will underestimate the BP_{ND} estimates of the second scan. Second, non-tracer amounts of (+)PHNO might not provide reliable estimates of the BP_{ND} and will underestimate any occupancy effects. Searle et al. [156] estimated that in order to achieve tracer conditions the injection of [^{11}C]PHNO would need to contain less than 0.15 μg of (+)PHNO. However, with the current radiochemistry techniques, it is difficult to produce [^{11}C]PHNO with high enough specific activity to avoid any mass dose effects.

In summary for the quantification of D2R and D3R distribution with [^{11}C]PHNO we used the SRTM model with the cerebellum as the reference region and we assumed the single site binding model for the GSK598809 compound. A recent study by Searle and colleagues [156] has explored in more detail the limitations raised here and imply the following: a) the SRTM may not be the optimal model; b) evidence for a small amount of specific binding in the cerebellum; c) GSK598809 binds to both D3R and D2R; and d) mass dose effects. However, our estimates for the D3R and D2R distribution and Searle's estimates, after correcting for the bias introduced from the aforementioned factors, were in a good agreement with the highest discrepancy observed in the D2R regions such as the CD and the PU, which is possibly attributable to the specific binding present in the cerebellum. Specifically the f_{PHNO}^{D3R} estimated in our study versus Searle's estimates were: SN: 0.92 vs 0.87, Hypo: 1 vs 0.90, VP_{SI}: 0.69 vs 0.71, GP: 0.57 vs 0.66, VST: 0.19 vs 0.39, TH: 0.46 vs 0.69, CD: 0 vs 0.21 and PU: 0 vs 0.14. In conclusion, by using a selective D3R antagonist and robust image analysis techniques it has been possible to dissect the regional D3R signal from [^{11}C]PHNO scans in humans *in–vivo*.

Chapter 7

Dopamine release within the anatomical and functional subdivisions of the BG following d-amphetamine stimulation

7.1 Intoduction

Dopamine release in subcortical regions of the brain has been extensively studied with PET and SPECT imaging using agonist and antagonist ligands (see Laruelle [110, 111] for a review). *In–vivo* studies report a differential regional dopamine release that is not explained by the cytoarchitectonic organisation of the structures. For example, Drevets and Martinez [54, 127] have reported a ventro-medial/dorso-lateral and posterior/anterior gradients of increasing dopamine release following an amphetamine challenge. This topographical pattern of dopamine release seems to be aligned with the functional organisation of these structures.

The aim of this chapter is to quantify amphetamine-induced dopamine release in the connectivity–based functional subdivisions of the human striatum and pallidum. Quantification of dopamine in the functional territories may provide new insights about dopamine function, help understand the neurochemical organisation and potentially help the development of novel therapeutic compounds and comprehension of

dopamine related neurological disorders. The first part of this chapter determines, in individual subjects, the cortical-striatal and striatal–pallidal projections to functionally parcellate the striatum and pallidum using the methodology described in chapter 5. The second part of the chapter applies these functional subdivisions to PET neurotransmission data to quantify regional dopamine release following the administration of d–amphetamine. To examine whether dopamine release has a functional or a structural specificity dopamine is also measured in the structural subdivisions of the striatum in the same subjects and the measurements are compared. PET data from two D2R/D3R dopamine ligands were investigated: the agonist [^{11}C]PHNO, which has a preferential affinity for the D3R sites [64] and the antagonist [^{11}C]Raclopride, which has equal affinity for the D2R/D3R. This permits testing of the robustness of the findings across two PET radioligands and investigation of whether the regional detection of dopamine release depends upon the relative distribution of the D2R/D3R and the ligands' preferential affinities.

7.2 Materials and methods

7.2.1 Subjects

The study was conducted at the GlaxoSmithKline Clinical Imaging Centre, Hammersmith Hospital, London and was approved by Essex 1 Research Ethics Committee and the Administration of Radioactive Substances Advisory Committee (ARSAC). Twelve healthy male volunteers were recruited, aged between 25 and 55 years, free from clinically significant illness or disease as determined by their medical history and standard laboratory tests. Each subject underwent a series of MRI and PET scans. Nine subjects completed four PET scans, two with [^{11}C]PHNO and two with [^{11}C]Raclopride in a counterbalanced order. A further three subjects received only two [^{11}C]PHNO scans as two of these dropped out of the study and the third was withdrawn because of an incidental finding. For each ligand, subjects initially received a baseline scan and

thereafter d-amphetamine was administered orally ($0.3\,mg/kg$) on an empty stomach, three hours prior to the start of the challenge scan. The two administrations of amphetamine were separated by a minimum of 6 days. Subjects provided written informed consent.

7.2.2 Data acquisition

MRI data

High resolution T1-weighted and DWI images were acquired with a 32-channel head coil on a Siemens Tim Trio, 3T MRI scanner (Siemens Healthcare, Erlangen, Germany). An isotropic T1-weighted ($1\,mm^3$) image was acquired with a magnetisation-prepared rapid gradient echo (MPRAGE) sequence (TR = 3000 ms, TE = 3.66 ms, flip angle of 9°, TI = $1100\,ms$, matrix = 256×192. A parallel imaging factor of 2 was applied to enable an acquisition time of $5:21\,min$). DWI data were acquired using echo planar imaging (EPI) (TR = 9000 ms, TE = 86 ms, flip angle of 90° and voxel size of $1.875 \times 1.875 \times 1.9\,mm^3$). The diffusion weighting was isotropically distributed among 30 directions (b-value=$1000\,s/mm^2$) and a non-diffusion-weighted image (B0) was acquired at the beginning of each scan. EPI acquisitions are prone to geometric distortions that can lead to errors in tractography [9]. To minimise this, two image sets were acquired with the phase encoded direction reversed, resulting in images with geometric distortions of equal magnitude but in the opposite direction, allowing for the calculation of a distortion corrected image [10]. Before correcting geometric distortions, each image set was corrected for motion and eddy-current related distortions. Diffusion data analysis was performed with the FSL tools [90].

PET data

All subjects were scanned on a Siemens Biograph HiRez XVI PET scanner (Siemens Healthcare, Erlangen, Germany), under baseline conditions (no d-amphetamine challenge) and three hours following the oral administration of 0.3 mg/kg of d-amphetamine.

For each scan, subjects were injected with a single intravenous bolus of [^{11}C]PHNO or [^{11}C]Raclopride and dynamic emission data were acquired continuously for 90 minutes. Six of the subjects had their two [^{11}C]PHNO scans on the same day (with at least five hours between [^{11}C]PHNO injections) whereas the other six subjects had the two scans on separate days. [^{11}C]Raclopride scans were acquired on the same day.

The PET dynamic images were reconstructed, into 26 frames ($8 \times 15\,s, 3 \times 1\,min, 5 \times 2\,min, 5 \times 5\,min$ and $5 \times 10\,min$), using a filtered back projection algorithm (direct inversion Fourier transform; DIFT) with a 128 matrix, a zoom of 2.6, and a transaxial Gaussian filter of $5\,mm$. A low dose CT scan (effective dose $0.2\,mSv$) was acquired for attenuation and scatter correction. The dynamic PET data were corrected for motion via frame–to–frame image registration and aligned with the structural T1-weighted MRI image using SPM5b (Wellcome Trust Centre for Neuroimaging, http://www.fil.ion.ucl.ac.uk/spm) with a mutual information cost function.

7.2.3 Connectivity-based subdivision of the striatum and pallidum

The connectivity-based subdivision of the striatum and pallidum (figure 7.1) was performed according to the methodology described in chapter 5. In brief, to obtain the connectivity-based functional striatal sub–territories, the connection probabilities from five cortical anatomical regions were calculated. The five cortical targets consist of four frontal lobe subdivisions (limbic, executive, rostral-motor and caudal-motor) and the parietal lobe. The parietal lobe, although a functionally heterogeneous structure consisting of somatosensory, visual, limbic and executive regions, is considered as one entity as this was the most reliable option (details in chapter 5).

For the quantification of dopamine release, the occipital and temporal lobes were not included in our analysis. As it has been shown in chapter 5, these lobes have very

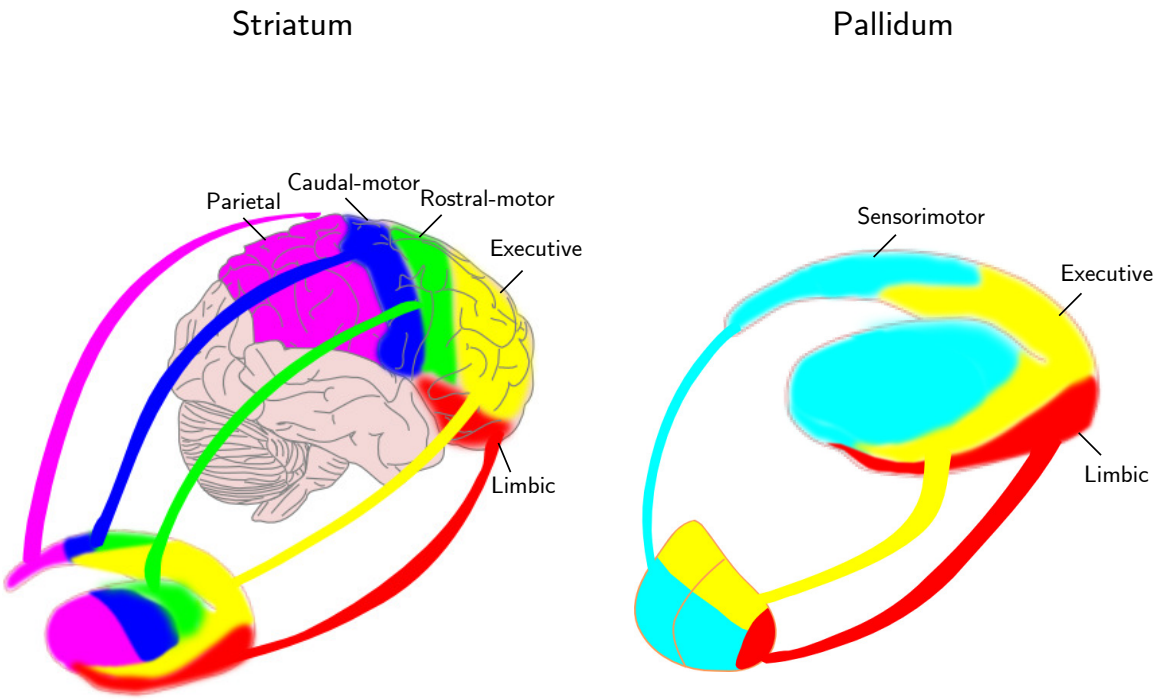

Figure 7.1: Schematic representation of the striatal and pallidal functional subdivision

confined and low probability connections (figure 5.7). After hard segmentation the occipital lobe occupies 2% of the total striatal volume whereas the temporal lobe occupies 5%. In addition, after hard segmentation, the occipital and temporal territories were not spatially consistent across individuals and therefore are not reported.

For the connectivity-based subdivision of the pallidum the connection probabilities from the limbic, cognitive and sensorimotor striatal territories to pallidum were estimated for each individual subject. Sensorimotor area comprises of the rostral-motor, caudal-motor and parietal striatal ROIs. Information about the decision to use the sensorimotor area, instead of the individual areas that sensorimotor area consists of, can be found in chapter 5.

As the cortico–striatal and the striatal–pallidal projections are organised into parallel and overlapping networks, the projections are processed in two ways: a) for each sub-

ject, exclusive connectivity-based functional ROIs (CBe) were created following the procedures described by Johansen-Berg and colleagues [92]; b) each subject's connectivity maps were thresholded at 1%, 5% and 10% of the maximum connectivity value to exclude noise and voxels with low connectivity values. The functional areas obtained with this method will be respectively abbreviated as follows: CBo-thr1 CBo-thr5 and CBo-thr10.

FMRIB's diffusion toolbox was used to perform probabilistic tractography [20]. Five thousand sample tracts were generated from each voxel in the seed mask. The tractography was performed in the subjects' continuous space and the results were output in the MNI space. For the pallidum the seed mask was also used as a termination mask in order to terminate the striatal projections as soon as they entered the pallidum, to avoid the projections from GP_e to GP_i.

The complete striatum and pallidum outlines were manually defined on the subject's T1-weighted image. The cortical masks were transferred to the subject's space after a non-linear registration of the MNI template to the subject's T1-weighted image. To tailor the cortical masks to the subject's individual anatomy, the subjects' segmented grey matter (GM) and fractional anisotropy (FA) images, both normalised to the MNI template, were employed to mask the ROIs. The lower threshold for the GM partial volume fraction was set at 0.25 and the FA upper threshold was set at 0.40.

7.2.4 Structural subdivision and definition of the striatum and pallidum

A structural-based method that uses anatomical landmarks to subdivide the striatum based on the guidelines described in chapter 4 was employed for comparison with the connectivity approach. Two structural subdivisions are produced: a) the striatum is subdivided into CD, PU and VST as described in chapter 4. The ROIs are

defined on each subject's T1-weighted image and this subdivision will be referred to as structural-based ROIs (SB); b) PU is subdivided into pre– and post–commissural as described by Martinez et al [127]. This technique was proposed in an attempt to structurally approach the functional organisation of the striatum, incorporating information from non-human primate tracing studies. Specifically, the VST is classified as limbic striatum, the post–commissural PU as sensorimotor and the pre–commissural PU with CD, as executive. These subdivisions will be referred to as structural-based functional ROIs (SBf). Unfortunately, with the T1-weighted image it is not feasible to subdivide pallidum into its structural components (i.e. GP_e, GP_i and VP) and therefore pallidum was defined as a single unified structure.

7.2.5 Quantification of dopamine release

The basis function implementation of the simplified reference tissue model (SRTM) [69, 108] was applied to the dynamic [^{11}C]PHNO and [^{11}C]Raclopride PET data, using the cerebellum as a reference region, to derive parametric images of the non-displaceable binding potential (BP_{ND}), which is proportional to the receptor availability. Each subject's pre- and post-d-amphetamine parametric images were co-registered using FLIRT [89] and then transformed into MNI space using the transformation parameters derived from non-linearly registering the subject's T1-weighted image to the $1 \times 1 \times 1\,mm^3$ nonlinear MNI template with FNIRT [8]. Subsequently the CBe, CBo-thr1, CBo-thr5, CBo-thr10, SB and SBf ROIs were applied to the [^{11}C]PHNO and [^{11}C]Raclopride BP_{ND} parametric images to calculate the regional estimates of BP_{ND}. The fractional change between baseline and post-d-amphetamine conditions then provides an index of the synaptic dopamine release as,

$$\Delta\, BP_{ND} = 100 \left(\frac{BP_{ND}^{Base} - BP_{ND}^{Amph}}{BP_{ND}^{Base}} \right) \% \tag{7.1}$$

where BP_{ND}^{Base} is the BP_{ND} in the baseline condition and BP_{ND}^{Amph} is the BP_{ND} following

the administration of d-amphetamine. The within region homogeneity index (%COV, coefficient of variation) for the dopamine release, was calculated to provide an index of homogeneity of dopamine release within each subdivision. The %COV is expressed as the ratio of standard deviation and mean and is the measure of variability of the data. When the %COV is high, it means that the data have high variability and when the %COV is low, it means the data have less variability. Less variability of dopamine release within an ROI indicates that the defined ROI describes effectively an area that has a certain biological/physiological response to amphetamine. Therefore, if the %COV within an ROI is low it corresponds to a relatively homogeneous release of dopamine across the voxels and across subjects within the region and this implies that the definition of a certain ROI describes better the physiological effects of the area.

7.3 Results

Dopamine release post d-amphetamine, in the structural and connectivity-based functional subdivisions of the striatum and pallidum was inferred from the percentage change in [^{11}C]PHNO and [^{11}C]Raclopride BP_{ND}. The magnitude of the d-amphetamine effect for both [^{11}C]PHNO and [^{11}C]Raclopride is shown in figure 7.2. Following the administration of d-amphetamine the psychological effects experienced by participants include euphoria, increased libido, alertness, restlessness and anxiety.

7.3.1 Dopamine release in striatum

The dopamine release, and the within region homogeneity index (%COV), were measured for the connectivity-based (CBo-thr1, CBo-thr5, CBo-thr10, CBe), and structural-based (SB, SBf) subdivisions of the striatum, and the results are shown in table 7.1 and figure 7.3.

Table 7.1: Quantification of dopamine release within the connectivity-based functional subdivisions of the striatum for [^{11}C]PHNO and [^{11}C]Raclopride. Bottom row is the average %COV across all functional subdivisions

	[^{11}C]PHNO				[^{11}C]Raclopride			
Threshold	CBo-thr1	CBo-thr5	CBo-thr10	CBe	CBo-thr1	CBo-thr5	CBo-thr10	CBe
Limbic	19.61 ± 6.78	21.03 ± 7.33	21.15 ± 7.50	20.75 ± 5.94	13.98 ± 6.58	13.50 ± 4.30	13.71 ± 4.07	14.01 ± 5.40
Executive	14.13 ± 4.12	13.89 ± 3.26	13.61 ± 3.16	13.87 ± 3.71	7.46 ± 3.51	5.45 ± 3.33	5.59 ± 3.03	8.48 ± 3.43
Rostral-motor	15.18 ± 2.69	14.43 ± 4.16	15.40 ± 2.99	15.70 ± 2.25	8.15 ± 4.14	7.48 ± 5.07	8.59 ± 3.91	8.95 ± 4.49
Caudal-motor	16.04 ± 2.10	16.44 ± 2.25	16.46 ± 2.97	17.47 ± 2.34	8.64 ± 2.43	8.50 ± 5.41	8.70 ± 6.50	10.23 ± 3.84
Parietal	16.32 ± 4.29	16.78 ± 4.39	16.87 ± 4.59	18.11 ± 3.68	10.49 ± 6.32	11.78 ± 4.67	11.43 ± 5.18	11.28 ± 5.49
COV% (average)	24.16 ± 8.68	24.40 ± 7.78	24.69 ± 7.01	20.69 ± 6.95	46.66 ± 11.65	52.83 ± 15.98	49.89 ± 16.45	43.07 ± 5.93

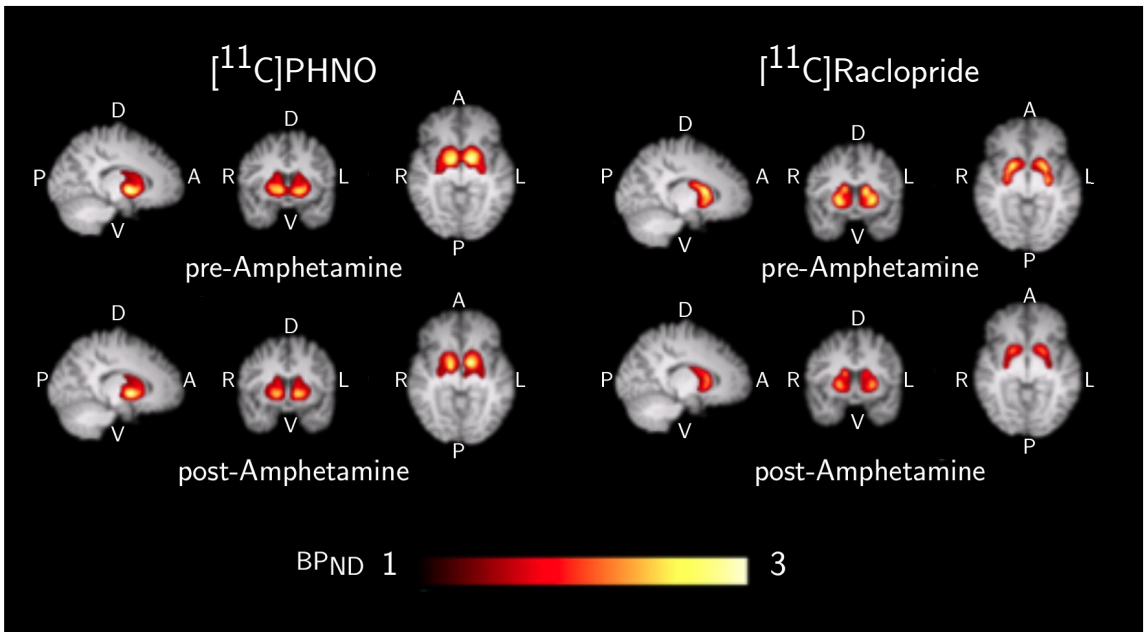

Figure 7.2: Parametric image of the [^{11}C]PHNO and [^{11}C]Raclopride binding potential (BP_{ND}) before (top row) and after (bottom row) the oral administration of (0.3 mg/kg) d-amphetamine in a single subject. R=right; L=left; A=anterior; P=posterior; D=dorsal; V=ventral.

For the connectivity-based methods a consistent pattern of dopamine release was found for the two ligands. Specifically, the highest dopamine release was measured in the limbic area followed by the parietal, the caudal-motor and rostral-motor areas. The lowest dopamine release was measured in the executive region. For each connectivity-based functional subdivision and for each ligand a statistical test (analysis of variance (ANOVA)) was performed to assess whether the mean dopamine release, estimated for a particular function (i.e limbic, executive etc) with each method (CBo-thr1,CBo-thr5,CBo-thr10, CBe), were different. Before applying ANOVA the Shapiro-Wilk test [159] was applied to test the normality of the data and the results show that the distributions are normal. The outcome of the ANOVA test demonstrated that the difference in dopamine release across methods for each function were not significant.

In addition, ANOVA was implemented to assess if dopamine is differentially released in the striatal functional subdivisions. For [^{11}C]PHNO data, the statistical analysis

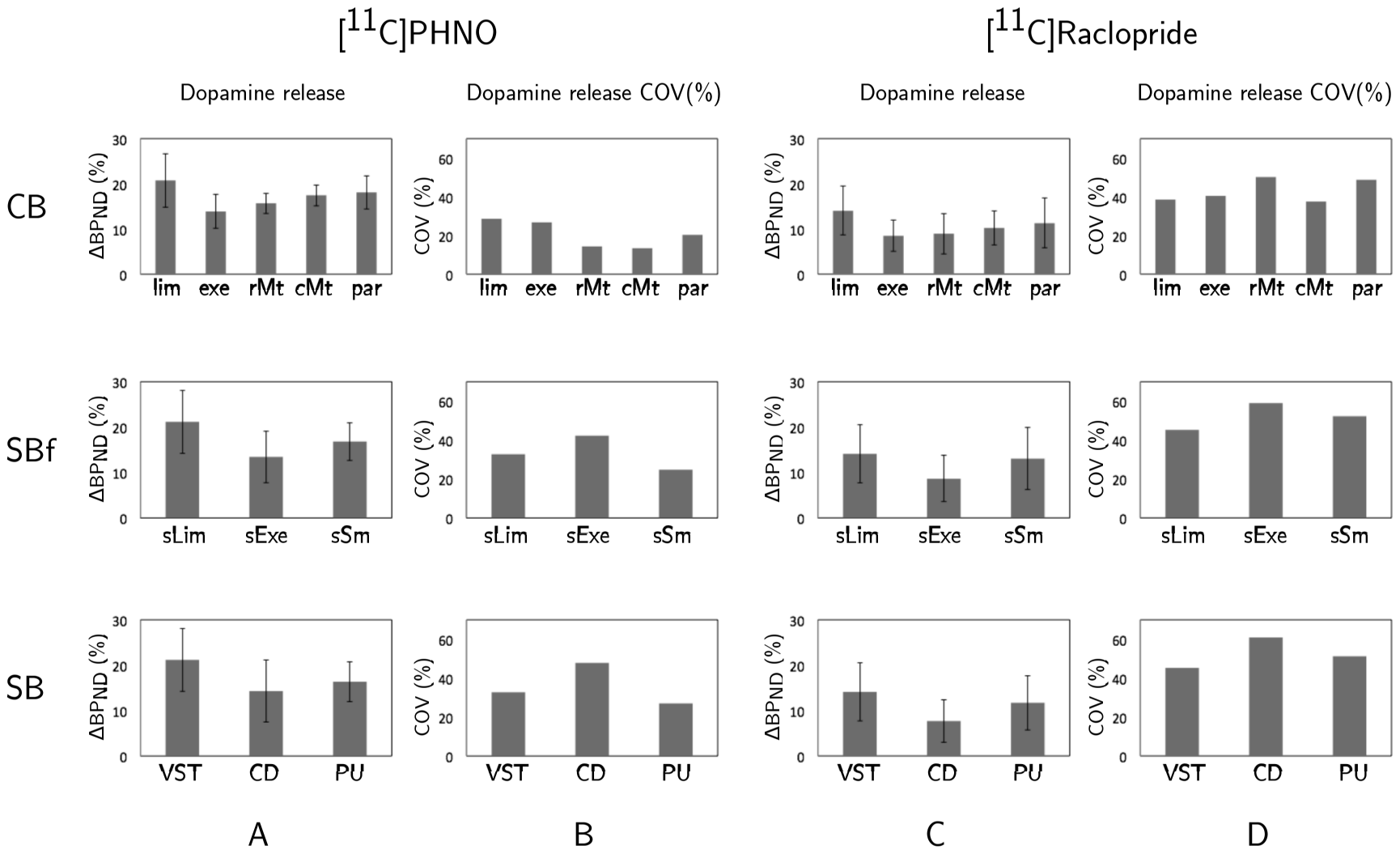

Figure 7.3: Dopamine release measured as the percentage change of [^{11}C]PHNO BP_{ND} (column A) and [^{11}C]Raclopride BP_{ND} (column C) within the exclusive connectivity-based functional regions of interest (CBe, top row), the structural-derived functional regions of interest (SBf, middle row) and the structural subdivisions of the striatum (SB, bottom row). Columns B and D correspond to the dopamine release coefficient of variation (%COV) in each region for [^{11}C]PHNO and [^{11}C]Raclopride respectively. Abbreviations correspond to: lim = limbic, exe = executive, rMt = rostral-motor, cMt = caudal-motor, par = parietal, sLim = structural-limbic, sExe = structural-executive, sSm = structural-sensorimotor, VST = ventral striatum, CD = caudate, PU = putamen.

indicated that dopamine was differentially released in the striatal functional subdivisions for all methods (p-values: CBo-thr1 = 0.043, CBo-thr5 = 0.004, CBo-thr10 = 0.005, CBe = 0.002). Multiple comparison tests with Bonferroni correction were performed, to determine which pairs of functional areas exhibit significant difference in dopamine release. All methods, except CBo-thr1, showed significant difference between the limbic – executive (p-values: CBo-thr5 = 0.02, CBo-thr10 = 0.03, CBe = 0.02) and between limbic – rostral-motor areas (p-values: CBo-thr5 = 0.04, CBo-thr10 = 0.05, CBe = 0.04). The CBo-thr1 showed a significant difference only between the limbic and executive regions (p-values: CBo-thr1 = 0.05). For [^{11}C]Raclopride the ANOVA tests show that dopamine is differentially released in the striatal functional subdivisions defined with CBo-thr5 (p-value = 0.01) and CBo-thr10 (p-value = 0.03). Specifically differential dopamine release was found in the limbic – executive pair (p-values: CBo-thr5 = 0.04, CBo-thr10 = 0.05). For the CBe (p-value = 0.09) and CBo-thr1 (p-value = 0.1) methods we did not detect a significant differential dopamine release as data did not survive the corrections for multiple comparisons.

In the SBf subdivisions the highest dopamine release was in the limbic region (VST) ([^{11}C]PHNO = 21.2±6.93%, [^{11}C]Raclopride = 14.1±6.38%) followed by the sensorimotor (post–commissural PU) ([^{11}C]PHNO = 16.8±4.17%, [^{11}C]Raclopride = 13.1±6.82%) and executive regions (CD and pre–commissural PU) ([^{11}C]PHNO = 13.4 ± 5.68%, [^{11}C]Raclopride = 8.62 ± 5.09%). These results are in agreement with those obtained by Martinez and colleagues [127] using [^{11}C]Raclopride. In the SB subdivisions of the striatum, which has been the most commonly used method to date for the quantification of striatal dopamine release, the highest release was measured in the VST ([^{11}C]PHNO = 21.2±6.93%, [^{11}C]Raclopride = 14.1±6.38%) followed by PU ([^{11}C]PHNO = 16.4±4.42%, [^{11}C]Raclopride = 11.7±5.99%) and the lowest in the CD ([^{11}C]PHNO= 14.3±6.84%, [^{11}C]Raclopride = 7.68±4.68%). Quantification with [^{11}C]PHNO indicates that dopamine is released differentially (ANOVA test) in the structural-based subdi-

visions (SBf p-value = 0.009 and SB p-value = 0.03) but no differential dopamine release was detected for [^{11}C]Raclopride. For [^{11}C]PHNO and the SBf method the limbic–executive pair showed a significant difference, whereas for the SB method the difference was only detected in the VST–CD pair.

The within region homogeneity index (%COV) for each method and each subdivision was measured (figure 7.3 B, D and table 7.1) to assess the homogeneity of dopamine release within each region. For the connectivity-based methods, the average %COV was 23.48% for [^{11}C]PHNO and 48.11% for [^{11}C]Raclopride. A higher average %COV was measured in the SBf in comparison with the connectivity-based subdivisions. In particular, the average %COV for [^{11}C]PHNO was 33.3% and for [^{11}C]Raclopride was 52.2%. For the SB, the average %COV is 35.9% for [^{11}C]PHNO and 52.5% for [^{11}C]Raclopride. As we progress from the structural subdivisions to the more sophisticated connectivity-based subdivisions, measures of dopamine release become more homogenous (lower %COV) (figure 7.3). To assess these differences the non-parametric Mann-Whitney test was implemented to compare the homogeneity of dopamine release in the CBe (limbic, executive, rostral-motor, caudal-motor, sensory) versus the structural-based ROIs (CD PU, VST (limbic), CD /pre–commissural PU (executive) and post–commissural PU (sensorimotor)). The results show that homogeneity of dopamine release was significantly higher in the CBe ROIs for both ligands ([^{11}C]PHNO p-value = 0.05 and [^{11}C]Raclopride p-value = 0.03). However, our concern was that these significant differences might be driven by the fact that some of the CBe ROIs are small in size, which might lead to lower %COVs. We explored the correlation between the %COV and the size for each ROI and no significant correlation was observed (p-value = 0.3) (figure 7.4).

According to Haber and colleagues [75] limbic–executive overlapping areas mediate incentive learning and these areas might be particularly sensitive to dopamine

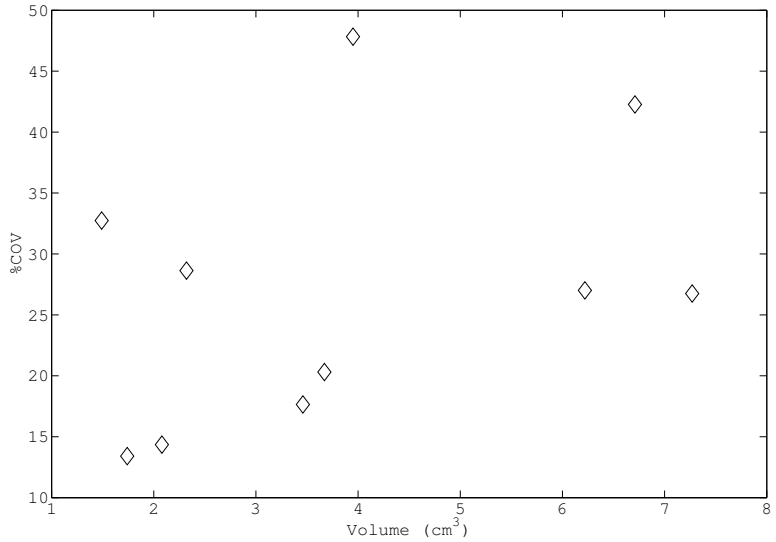

Figure 7.4: ROI volume against the %COV of dopamine release. No significant correlation was observed (p-value = 0.3).

modulation. The release of dopamine within the overlapping ROIs was quantified with [^{11}C]PHNO only, as it has been shown to provide a greater signal-to-noise than [^{11}C]Raclopride. The release of dopamine as measured by $\%BP_{ND}$ changes in the overlapping limbic–executive area was $18.2 \pm 5.39\%$ (limbic alone = $19.61 \pm 6.78\%$, and executive alone = $14.13 \pm 4.12\%$, using the CBo-thr1 method). In this experimental design we did not find any evidence that support that d-amphetamine provokes a higher dopamine release in this overlapping area. Moreover, a similar conclusion was drawn from the quantifications in the other overlapping areas. Specifically dopamine release, as measured by $\%BP_{ND}$ change, was: executive–rostral-motor overlap = $14.7 \pm 4.15\%$; executive – caudal-motor overlap= $16.2 \pm 5.05\%$; and rostral-motor – caudal-motor overlap= $16.0 \pm 4.78\%$.

7.3.2 Dopamine release in pallidum

The dopamine release and the within region homogeneity index (%COV) were measured for the connectivity-based subdivisions of the pallidum (CBe, CBo-thr1, CBo-thr5, CBo-thr10) (7.2) and pallidum as a whole. Unfortunately, subdivision of the

pallidum into its GP_e, GP_i and VP components was not feasible as the MRI sequences acquired for this study did not allow such subdivision. For the connectivity-based methods a consistent pattern of dopamine release was found for [^{11}C]PHNO and this was in agreement with the striatal pattern. In particular, the highest dopamine release was measured in the limbic area followed by the sensorimotor and the lowest release was measured in the executive region. An ANOVA test was performed to assess whether the estimated dopamine release measured with [^{11}C]PHNO for each functional subdivision differed across methods (CBo-thr1,CBo-thr5,CBo-thr10, CBe). The results did not show a significant difference across methods. Moreover, ANOVA was implemented to assess if dopamine was differentially released in the pallidal functional subdivisions. In contrast with the striatum, differential dopamine release, measured with [^{11}C]PHNO, was not detected in the connectivity-based subdivisions.

For [^{11}C]Raclopride, dopamine release did not show a consistent pattern across the connectivity-based methods. For all methods, the highest dopamine release was measured in the sensorimotor territory whereas the limbic and executive territories had a similar release with their order interchanged. Specifically, for the CBo-thr1 method, the executive region had a higher dopamine release than the limbic, whereas in the other methods the order was reversed (table 7.2). The Shapiro-Wilk test [159] was applied and the results indicate that the measurements of dopamine release were normally distributed across subjects and subdivisions. Therefore, an ANOVA test was performed to examine whether the dopamine release was significantly different between pairs of functional subdivisions. The results did not show a statistically significant difference across subdivisions, or methods for any of the pairs.

Subdivision of the pallidum into its structural components was not possible, so the structural measurement of dopamine release in the pallidum was done across the whole structure. The measured dopamine release was $10.35 \pm 10.23\%$ measured with

Table 7.2: Quantification of dopamine release within the connectivity-based functional subdivisions of the pallidum for [^{11}C]PHNO and [^{11}C]Raclopride. Bottom row is the average %COV across all functional subdivisions

	[^{11}C]PHNO				[^{11}C]Raclopride			
Threshold	CBo-thr1	CBo-thr5	CBo-thr10	CBe	CBo-thr1	CBo-thr5	CBo-thr10	CBe
Limbic	14.82 ± 8.25	17.62 ± 8.10	18.45 ± 8.65	15.64 ± 9.56	8.16 ± 5.96	9.53 ± 4.64	9.99 ± 4.23	9.55 ± 7.48
Executive	10.34 ± 9.70	10.44 ± 9.76	10.44 ± 9.88	10.71 ± 9.49	9.62 ± 5.90	9.16 ± 5.63	8.95 ± 5.58	9.01 ± 5.86
Sensorimotor	11.45 ± 10.25	12.75 ± 10.40	14.22 ± 10.29	12.33 ± 12.48	12.36 ± 6.19	12.71 ± 6.06	12.54 ± 6.13	11.94 ± 9.46
COV% (average)	79.71 ± 20.94	73.69 ± 24.72	71.27 ± 23.89	83.65 ± 20.48	61.49 ± 11.55	52.61 ± 7.70	51.20 ± 10.19	74.25 ± 7.92

[^{11}C]PHNO and $10.15 \pm 6.93\%$ with [^{11}C]Raclopride.

The %COV of dopamine release for each method and each functional subdivision was measured (table 7.2, bottom row) to assess the homogeneity of dopamine release. For the connectivity-based methods the average %COV was 77% for [^{11}C]PHNO and 60% for [^{11}C]Raclopride. A higher average %COV was measured in the whole pallidum in comparison with the connectivity-based subdivisions. In particular, the average %COV for [^{11}C]PHNO was 99% and for [^{11}C]Raclopride 68%.

7.4 Discussion

Striatum

D-amphetamine-induced reduction of the BP_{ND} has been well validated as a measure of changes in synaptic dopamine [110, 111]. To date, agonist and antagonist ligands have been used to explore dopamine release in the striatal subdivisions and pallidum, which have been defined based on structural criteria [127, 162]. Here, two PET radioligands, the agonist [^{11}C]PHNO and the antagonist [^{11}C]Raclopride have been used to quantify dopamine release, within the connectivity-based functional subdivisions of the striatum and pallidum.

In the connectivity-based functional subdivisions of the striatum the highest release of dopamine was measured in the limbic, followed by the sensory, motor and executive regions. This pattern was consistent for both ligands (table 7.1) and across all the functional subdivisions (CBo-thr1, CBo-thr5, CBo-thr10and CBe). A statistical comparison, for each function (region) separately (limbic, ececutive etc.), showed that the quantification of dopamine release is not affected by the connectivity-based method employed. The aforementioned data indicate that the connectivity-based subdivision

of the striatum is a robust method for the quantification of the PET signal. Nevertheless, the selection of an appropriate threshold is critical in order to detect regional differences in dopamine release. For [^{11}C]PHNO, which has higher sensitivity in detecting dopamine release than [^{11}C]Raclopride, all methods except the CBo-thr1 have shown a significant difference in dopamine release between the limbic-executive and limbic-rostral motor pairs. The CBo-thr1 approach applies a lower threshold of 1% to the maximum connectivity value, and this may not be large enough to exclude noise and voxels with low connection probabilities.

The cortical-striatal projections are organised into discrete and overlapping networks. The advantage of using methods that define the connectivity-based ROIs by applying a lower threshold to the connection maps over the hard segmentation method (CBe) is that it includes voxels that are both exclusively connected (discrete network) to a cortical target and concurrently connect to other targets (overlapping networks).

The SBf method, which was proposed by Martinez and colleagues [127] and endeavours to approximate the functional organisation of the striatum and, like the CBe method, assigns to every voxel a single function, has detected significant differences between the limbic and executive regions, whereas the significant differences between the limbic and sensorimotor areas found with the CBe were not preserved. This indicates that assigning an executive role to the CD/pre–commissural PU complex and a sensorimotor role to the post–commissural PU is not optimal. Nevertheless, assigning a limbic role to the VST area, which is defined using anatomical landmarks whose placements were inspired by non-human tracing studies, is a good approximation as the dopamine release was similar to that obtained with the limbic CBe method.

The biggest change in the PET signal in our study was seen in the limbic striatum followed by the sensorimotor and executive area. The magnitude of the PET signal

change, following the administration of amphetamine, is dependent on the amount of dopamine released, as well as the relative proportions of the D2-like receptors in each subdivision. Dopamine has a preferential affinity for the D3R, over the $D2R^{high}$ followed by the $D2R^{low}$ therefore a given concentration of dopamine can be expected to occupy a greater proportion of D3R and $D2R^{high}$. D3R and $D2R^{high}$ are known to be abundant in the ventral striatum area where the limbic cortex projects. This could potentially explain the higher release of dopamine detected in the limbic region. Nevertheless, the second highest level of dopamine release was measured in the sensorimotor striatal areas, which are primarily located in the post-commissural putamen where the D3R contribution to the total [^{11}C]PHNO signal is negligible (chapter 6). A similar argument could be made for the ratio of $D2R^{high}$:$D2R^{low}$ being higher in the sensorimotor than the executive striatum, leading to greater changes in signal following similar amounts of dopamine released. In order to test this, we compared the ratio of [^{11}C]PHNO/[^{11}C]Raclopride BP_{ND} for the two regions (where D3R contribution in the two regions is negligible). We found no evidence for a difference in the [^{11}C]PHNO/[^{11}C]Raclopride ratio between the two regions, suggesting that differences in the relative regional proportions of D2-like species are unlikely to be responsible for the regional pattern of BP_{ND} change seen in our data. Thus the emerging hypothesis is that amphetamine leads to a preferential release of dopamine in the limbic, followed by the sensorimotor and the executive areas.

Dopamine release is elicited in all functional sub-territories of the striatum and this is consistent with the diversity of physiological effects provoked after the administration of d-amphetamine, which includes psychological and physical effects such as euphoria, psychomotor agitation, locomotor stimulation, hyperactivity, increased libido, increased concentration. The universal striatal activation could be explained by the anatomical arrangement of the cortico-striatal and striato-nigro-striatal pathways. The cortico-striatal pathways are organized into individual and overlapping networks.

In these overlapping areas the distinct cortical loops converge and information is integrated and conveyed. The striato-nigro-striatal pathways form an ascending spiral by which information from a striatal region in transferred to other areas of the striatum. Specifically, Haber and colleagues postulate [74] that there is an interface between different striatal regions via the midbrain dopamine cells, which creates a hierarchy of information flow. Thus, the universal striatal activation could be due to a complex chain of events, beginning with motivation and progressing to cognitive and motor activations, as explained by the feed-forward organisation of the striatal network.

The homogeneity of dopamine release in the striatal subdivisions was assessed by calculating the %COV. Our data demonstrate greater homogeneity of dopamine release within the connectivity-based functional ROIs as compared to the structural subdivisions, suggesting that connectivity-based functional ROIs might be a better representation of neurotransmission relevant sub-regions of the striatum. These data provide evidence that there is an association between local dopamine release and the cortical connectivity profiles of these regions.

Our results do not indicate that d-amphetamine provokes a higher dopamine release in overlapping area. It is worth bearing in mind that d-amphetamine releases accumulated dopamine stores by reversing the dopamine transporter, and is thus a good measure of overall dopamine system integrity. Physiological dopamine release depends on the firing rate of dopamine neurones, controlled at several levels by feedback loops. Assessment of physiological dopamine release in these overlapping striatal functional areas may be assessed via performance of tasks that require multi-function engagement.

For the connectivity-based subdivision of the striatum the frontal functional subdivisions were not derived from functional MRI experiments but make use of the known

areas of specific brain function, as determined from the human and primate literature. We are not aware of how the spatial anatomical arrangements of these cortical areas are affected in different neurological and psychiatric disorders. Therefore, if this methodology is to be applied to diseased cohorts, the anatomical-functional cortical alterations should be considered.

Pallidum

In the pallidum the quantification of dopamine release, with [^{11}C]PHNO, showed a consistent pattern across all methods (table 7.2) and these were in line with findings from the striatum. The highest release was in the limbic, followed by the sensorimotor areas, whereas the lowest dopamine release was measured in the executive area. The statistical tests did not detect a significant difference across the methods employed (CBo-thr1, CBo-thr5, CBo-thr10 and CBe) for both [^{11}C]PHNO and [^{11}C]Raclopride. For [^{11}C]Raclopride though, the pattern of dopamine release was not consistent across the methods. For all methods, the highest dopamine release was detected in the sensorimotor territory and not in the limbic territory. As discussed in chapter 5, the limbic striatum projects extensively to the VP, an area that is minimally sampled in our pallidal ROI. For this reason the limbic quantification might be devalued. In view of this and given [^{11}C]Raclopride is a less sensitive ligand at detecting dopamine release, as compared to [^{11}C]PHNO, this interpretation is justifiable.

The ANOVA tests did not show a differential dopamine release across the functional subdivisions for any of the methods in pallidum. If indeed dopamine is differentially released in the functional subdivisions of the pallidum, then a number of factors could have potentially contributed to this undetected difference. As stated in chapter 5, the pallidum is considered as a structure where striatal fibers converge strongly, leading to integration of striatal functional information [84, 145]. Moreover, we have shown

in chapter 5 (figure 5.14) that there is a great overlap between the striato–palidal projections. Therefore, this substantial overlap between functional territories could potentially explain the non-differential dopamine release, as dopamine function in one territory would affect the dopamine quantification in the others. In addition, the limited resolution of PET imaging, in conjunction with the small size of the pallidum, contributes largely to signal blurring. Specifically, activity will spill-in and spill-out from high-activity and low-activity regions and this particularly influences small regions. Methods such as partial volume corrections [13, 154] or resolution recovery techniques [160, 161] could potentially improve the precision of dopamine release quantification and reveal differential dopamine release across the functional subdivisions.

With the MRI sequences acquired in this study it was not possible to subdivide the pallidum into its structural subcomponents (GP_e, GP_i, and VP). Therefore, dopamine release was measured in the pallidum structure as a whole. This means that a comparison of the homogeneity of dopamine release between the connectivity-based subdivisions and structural-based subdivisions is not equitable. In general, the %COV change in the connectivity-based subdivisions were consistent across methods for both ligands but considerably higher as compared to the striatum.

As has been mentioned before, [^{11}C]PHNO is expected to have a higher sensitivity in detecting dopamine release due to its agonist profile. A direct within-subject comparison, for both the striatal and pallidal subdivisions, has shown that dopamine release measured with [^{11}C]PHNO was higher in comparison to dopamine release measured with [^{11}C]Raclopride. Specifically, the average $\Delta BP_{ND}^{PHNO} : \Delta BP_{ND}^{Raclopride}$ across subjects and subdivisions was estimated at 1.58 ± 0.40. As mentioned before, dopamine has a preferential affinity for the D3R, over the $D2R^{high}$, and a reduced affinity for the $D2R^{low}$. Antagonists such as [^{11}C]Raclopride are not expected to show a decreased

affinity for the D2R^{low} state of the receptor compared with the D2R^{high}. Dopamine would have limited facility to compete effectively with antagonist ligands at D2R^{low} sites. In contrast, an agonist ligand, such as the [^{11}C]PHNO, is expected to compete more effectively with dopamine at the D3R and D2R^{high} sites and this justifies the increase sensitivity of the [^{11}C]PHNO ligand. Our data are consistent with previous work showing the change in binding of the D3R/D2R agonist [^{11}C]NPA to be higher than that of [^{11}C]Raclopride in awake humans [137]. As the contributions of D3R to [^{11}C]NPA binding is negligible as compared to [^{11}C]PHNO, the greater sensitivity of [^{11}C]NPA is attributed to binding to the D2R^{high} sites.

Several studies support a functional and structural decline of the human brain with age. For instance, a recent study has demonstrated an age-related decline in white matter tract integrity [183] while a PET study with [^{11}C]Raclopride has shown that there is an age-related loss of striatal D2R receptors [151]. The current study aimed to recruit a narrow age range in order to minimize age related effects. If the decline of the dopamine receptors and/or of the white matter tracts within a subject and across regions were uniform then one would expect to affect to a similar degree the connectivity-derived regions and the respective quantification of dopamine release. Nevertheless potential age related effects warrant a further investigation.

In conclusion, the use of connectivity-based functional subdivisions allows an alternative approach for the investigation of *in–vivo* dopamine release. The results in the striatum demonstrated an improvement in the evaluation of regional differences in dopamine release, with the connectivity-based methods providing greater homogeneity within each subdivision. The data also suggest that the relative regional proportions of D2-like receptors are unlikely to be responsible for this regional dopamine release pattern. Notably, the homogeneity of dopamine release was significantly higher within the connectivity-based functional subdivisions in comparison

with the structural subdivisions. These results support an association between local levels of dopamine release and cortical connectivity fingerprints.

These connectivity-based methods are not limited to dopamine and d-amphetamine challenge but could also be applied to a range of neuroscience studies in order to better understand the physical or chemical processes, or the pathophysiology, of the human brain. For example, the methodology presented can be employed to compare groups with specific function impairments, as the sensitivity, in detecting regional functional differences, is increased. Finally, this methodology can provide a tool for deep brain stimulation (DBS) surgery planning and help improve the treatment of several neurological disorders such as pain, obsessive-compulsive disorders, depression and addiction.

Chapter 8

Correlation of the Nigrostriatal dopaminergic pathway and dopamine PET measurements

8.1 Introduction

Dopamine is a neurotransmitter that is involved in several neurological conditions. Evidence suggests that some of these disorders are due to the occurrence of neurodegenerative processes in the dopaminergic pathways, which, in turn, result in dopamine dysfunction. For instance, Parkinson's disease is characterised by the degeneration of nerve cells in the substantia nigra (SN) with a subsequent decrease in dopamine transmission in the BG, the areas where dopaminergic neurones terminate. Bernheimer and colleagues [22] have shown that there is a positive correlation between the degree of cell loss in the SN compacta and the dysfunction of dopaminergic neurotransmission in the nuclei of the BG.

The existence and spatial organisations of the nigrostriatal and the striatonigral projections has been extensively studied in non human primates [140, 158, 120, 119, 74]. The mesencephalic projections that arise from the ventral tegmental area (VTA) are often referred to as the mesolimbic projections and those originating from the SN as the nigrostriatal. Haber and colleagues suggest that the VTA and the medial SN are

associated with the limbic system whereas the lateral and the ventral SN are associated with the executive and the sensory-motor systems [74].

The limbic striatum, which corresponds to the VST, receives sparse projections from the mesencephalon and projects to a relatively large region. In contrast, the dorsal striatum, receives input from a large amount of dopamine neurones and projects to a limited area (figure 8.1) [74].

In the last two decades PET imaging has investigated dopamine transmission and synthesis in healthy and diseased populations. Although the intra–subject variability is relatively low (mean difference between PET measurements under the same experimental conditions is $< 10\,\%$) the inter–subject differences can be substantially bigger due to experimental and physiological variables. Several intrinsic characteristics can potentially contribute to this inter–subject physiological variability: a) the dopamine receptor density which can be determined genetically or be subject to regulatory mechanisms [59], b) density of dopamine transporter, c) inter–individual differences in the concentration of endogenous dopamine, which can, in turn, affect the apparent affinity (Kd^{app}) in a competitive manner [59] d) age, e) sex of the subjects and f) the density/potency of the presynaptic dopamine neurones.

The aim of this chapter is to examine whether the potency of the nigrostriatal pathway, defined with diffusion-weighted magnetic resonance and image-based probabilistic tractography, is correlated with dopamine PET measurements of receptor number ($\mathrm{BP_{ND}}$). The hypothesis under investigation is that the stronger the nigrostriatal pathway is, the more receptors will be found in the post–synaptic terminals. This would achieve a balance between the level of synaptic dopamine, the number of dopamine transporters and the number of available receptors. Here, the potency of the nigrostriatal trajectory is defined as the total number of streamlines (samples) seeded from

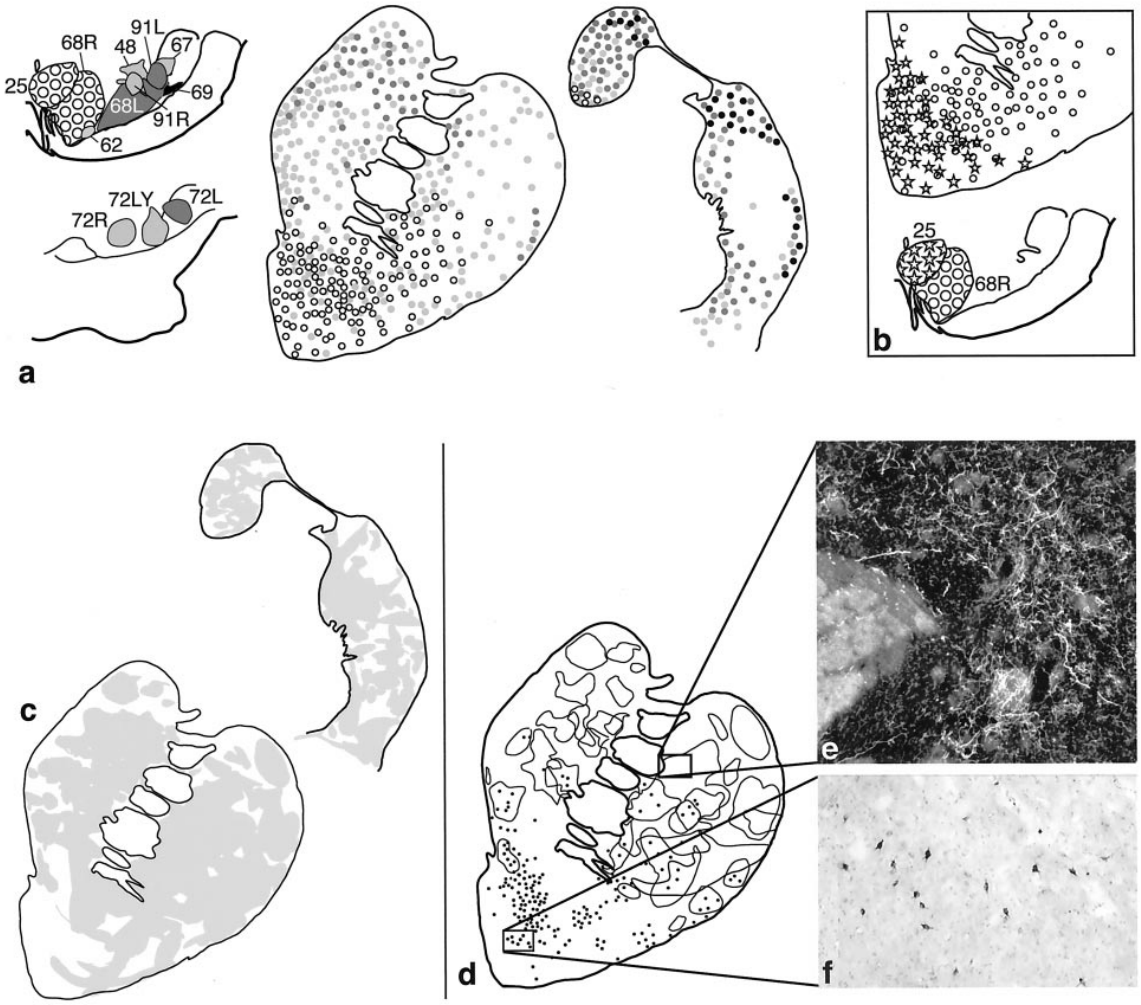

Figure 8.1: Figure courtesy of Haber and colleagues [74]. a) Collective distribution of labeled cells in the pre–commissural and post–commissural striatum after retrograde injections into the mesencephalon. Rostral (top) and caudal (bottom) drawings of the midbrain showing the location of retrograde injection sites. Shading of sites corresponds to that of the cells in the striatal schematics. One dot = 4–6 cells. b) Magnified view of VST illustrates the distribution of labeled cells at the border between the core and shell after injections into the medial SN (open circles) and VTA (stars). c) Combined chartings of terminal/fiber distributions in the striatum after all anterograde tracer injections into the midbrain. Note that fibers are distributed throughout the dorsal striatum and central striatum, whereas the VST receives a more limited projection. d) Schematic of the rostral striatum showing the distribution of labeled cells and fibers after an injection of the bi-directional tracer LY into the densocellular region of the SN. e) Dark-field photomicrograph taken from the boxed central striatum region in d showing dense LY-positive fibers, but no labelled cells. f) Photomicrograph taken from the boxed region in the VST of labeled cells (from the boxed region in d).

the SN that reach the CD and the PU.

Quantification of the connection strength is challenging even for invasive tracing techniques. It is difficult, for example, to establish whether equivalent amounts of tracer have been injected into the tissue and taken up by particular areas of interest [93]. Probabilistic tractography can estimate the level of confidence that a tract exists and connects the areas of interest [18]. The level of confidence is not directly related to the potency of the actual pathway and higher confidence does not necessarily imply a stronger connection. Nevertheless, investigators have used diffusion tensor parameters (FA, MD) and tractography measurements for intra-subject, inter-subject and across population comparisons. For example, Bartsch and colleagues [16] have shown that there is a correlation between the number of streamlines that reached the target region and impaired motor function. Specifically, the fewer samples that reach the target from the seed relative to the contralateral side, the more pronounced the motor weakness. Additionally, Bridge and colleagues [30] have calculated the total number of streamlines that reach the target in order to compare the strength of ipsilateral and contralateral tracts (lateral geniculate nucleus to human motion area tract). Therefore, we also adopt probabilistic tractography measures as a surrogate for connection strength, but we emphasise at this point that it does not correspond to the strength of the actual nigrostriatal pathway and consequently care should be taken to not over-interpret the findings.

8.2 Materials and methods

8.2.1 Subjects

The study was conducted at the GlaxoSmithKline Clinical Imaging Centre, Hammersmith Hospital, London and was approved by Essex 1 Research Ethics Committee and the Administration of Radioactive Substances Advisory Committee (ARSAC). Four-

teen healthy male volunteers were recruited aged between 27 and 60 years, free from clinically significant illness or disease as determined by their medical history and standard laboratory tests. Each subject underwent a series of MRI and PET scans including T1-weighted MRI, diffusion-weighted (DWI) MRI and [^{11}C]PHNO PET.

8.2.2 Data acquisition

Positron Emission Tomography

Each subject was scanned on a Siemens Biograph HiRez XVI PET scanner (Siemens Healthcare, Erlangen, Germany), under baseline conditions (no drug challenge). Subjects were injected with a single intravenous bolus of [^{11}C]PHNO and dynamic emission data were acquired continuously for 90 minutes. The dynamic images were reconstructed into 26 frames ($8 \times 15s, 3 \times 1min, 5 \times 2min, 5 \times 5min, 5 \times 10min$). A computed tomography (CT) scan was acquired for attenuation correction of the PET data.

Magnetic Resonance Imaging

All the MRI images were acquired with a 32–channel head coil on a Siemens Tim Trio, 3T MRI scanner (Siemens Healthcare, Erlangen, Germany). High resolution structural MRI, and in particular the two components of the FLAWS sequence [174], were acquired. FLAWS generates a T1-weighted contrast and a WM–nulled image in a single scan. T1-weighted 3D MPRAGE volumes were acquired using the ADNI-GO recommended parameters: $256 \times 192\,mm$ field of view (FOV), $1\,mm^3$ isotropic resolution, parallel imaging (PI) factor of 2, in 321s. The inversion times for the T1-weighted and the WM–nulled images were 409 ms and 1100 ms respectively. DWI data were acquired using echo planar imaging (EPI) (TR = 9300 ms, TE = 88 ms, flip angle of 90° and voxel size of 1.9 mm^3 isotropic). The diffusion weighting was isotropically distributed along 64 directions (b-value=1000 s/mm^2) and a non-diffusion-weighted image (B0) was acquired at the beginning of each scan.

8.2.3 Image analysis for PET and MRI

PET analysis

Dynamic PET data were corrected for motion via frame-to-frame image registration and aligned with the subject's structural T1-weighted MRI image using FLIRT [90]. PET data were analysed with the SRTM model [108, 69], using the cerebellum as the reference region.

MRI analysis

*Definition of the regions of interest (*ROI*)*

The SN ROI was defined manually for each subject, combining information from the subject's WM nulled [174] and B0 images. The SN ROI was defined on the transverse plane (figure 8.2). Starting from ventral to dorsal the SN delineation commences after the brainstem is disconnected from the cerebellum and ends at the slice where the marker E is placed (figure 8.3). Marker E is a horizontal line defined at the mid-sagittal slice dorsal to the mammillary bodies. Following the delineation of the SN on the transverse plane it is recommended that the operator switches to the coronal plane and optimises the delineation of the SN and excludes the subthalamic nucleus. The SN has a prominently dark appearance on the B0 image due to high iron deposition [53] and this information was used when there were doubts about parts of the SN seen on the WM–nulled image. It is important to note that the SN ROI is likely to contain a small part of the VTA as this area is adjacent to the medial SN region and projects primarily to the VST. The CD and the PU ROIs were manually defined on the subjects T1-weighted image following the guidelines described in chapter 4.

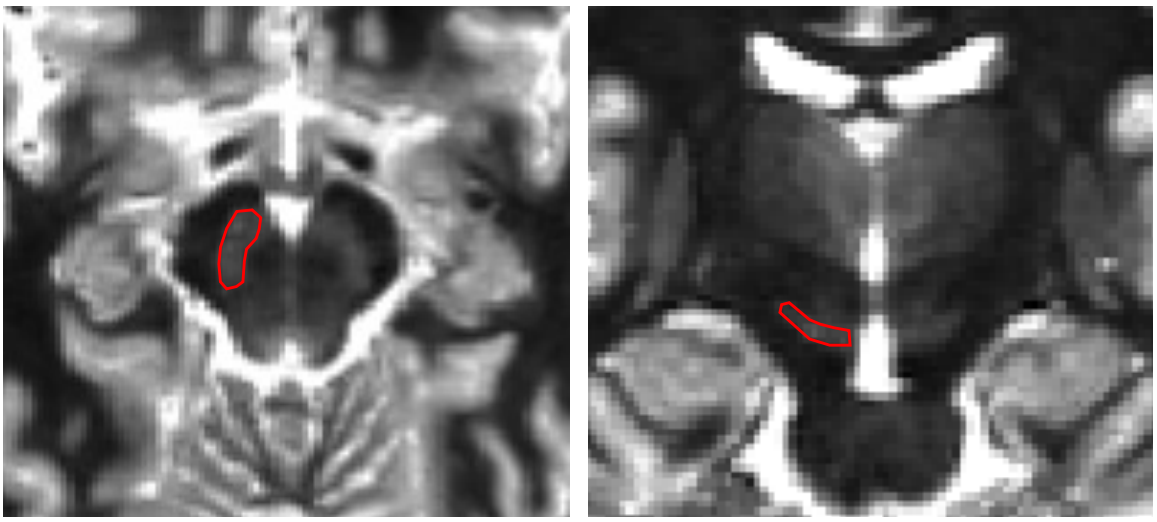

Figure 8.2: Manual delineation of the right substantia nigra region on a WM–nulled image of a representative subject. Right picture corresponds to a coronal slice and left to an axial slice.

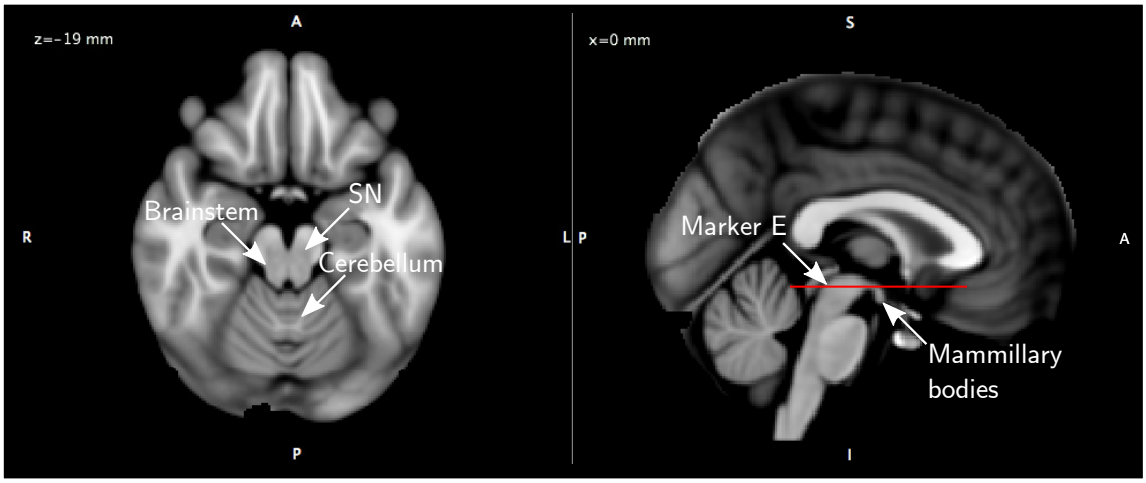

Figure 8.3: Substantia nigra ROI guideline landmarks

Creation of a SN *atlas.*

Both the size of the SN ROI and also the sampled areas of the SN structure can contribute to the estimates of the nigrostriatal potency. Therefore, in addition to the individually defined SN ROIs, a group probability map of the SN was constructed and used to estimate the potency of the pathway. To create the probabilistic SN ROI all the individual ROIs were registered to the MNI template via spatial normalisation of the subject's T1-weighted image with FNIRT. The T1-weighted image and the WM-nulled image were generated from the same acquisition, and are therefore intrinsically aligned, so there was no need for a rigid registration between these images. The non–linear transformation parameters were then applied to the SN ROIs using the nearest neighbour interpolation method. Finally, for each voxel in the mesencephalon, we assigned a number that corresponds to the number of subjects that have that voxel classified as SN in their ROI mask. The probability maps were thresholded and only the voxels that were classified as SN in at least 11/14 subjects were retained. The thresholding was performed in order to increase the probability that voxels classified as SN in the probabilistic map correspond to actual SN voxels in the majority of the subjects, and therefore minimise potential discrepancies between the probabilistic and the actual SN ROI. Henceforward, the thresholded probabilistic SN will be termed as atlas SN.

Probabilistic tractography

Diffusion data were analysed using FSL tools [90]. The following pipeline was followed for the DWI data pre-processing: i) eddy current correction and motion correction, ii) correction for geometric distortions [10] and iii) a diffusion tensor model was fitted at each voxel to estimate diffusion parameters such as FA and MD. Each subject's FA image was registered to the FMRIB58_FA high resolution template [178], which is in

the same space as the MNI standard space image. Probabilistic tractography was performed in the subjects' continuous space and the results were output in the MNI space by providing the transformation parameters estimated with FNIRT [8]. For the probabilistic tractography ten thousand (10000) samples (pathways) were generated for each voxel in the SN ROI and only those that entered the target mask were recorded. The pathway curvature threshold was set at 0.1 and pathways were terminated as soon as they entered the target masks in order to prevent them from projecting to other areas. Probabilistic tractography was run, separately for the two hemispheres, with both the subject's specific SN ROI and for the atlas SN as seed masks. The CD and the PU nuclei were used as classification targets. For each pair (SN-target), the "connection strength" was estimated as the Total Number of Samples (TNS) that were generated from the SN ROI and reached the respective target region.

Age factor

Age is one of the subject's intrinsic characteristics that could impact both the nigrostriatal pathway and the receptor density. To ensure that this factor is not overlooked, and is not responsible for potential significant correlations between the TNS and PET measurements, the relationship between age and the parameters of interest was examined.

8.3 Results

PET imaging data were successfully collected and analysed for thirteen subjects. One subject had strong side effects (nausea and low blood pressure) after the administration of [^{11}C]PHNO and was withdrawn from the study. The SRTM model was applied to the PET time activity curves to derive estimates of the BP_{ND} for the right and left CD and PU. Diffusion and probabilistic tractography analysis was successfully performed

for all subjects.

Figure 8.4 shows the age of subjects (27 – 60) plotted against the TNS and BP_{ND} for CD and PU. No significant correlation was found between age and any of the parameters studied.

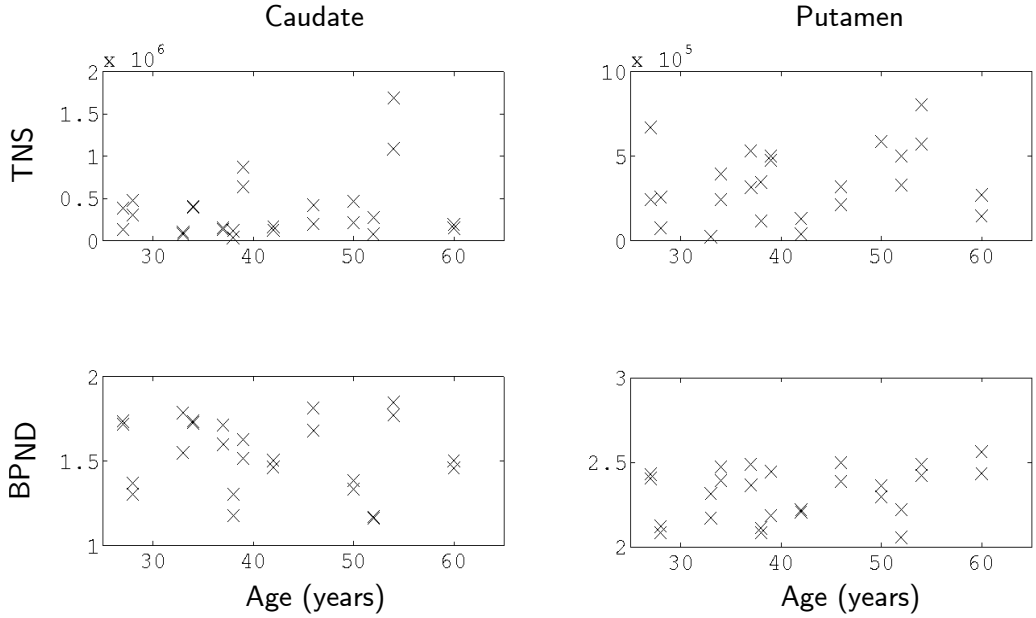

Figure 8.4: Age versus: a) total number of samples to reach the target, 1^{st} row and b) SRTM binding potential (BP_{ND}), 2^{nd} row. 1^{st} column corresponds to CD and 2^{nd} to PU. No significant correlation with age was observed ($p > 0.05$). The plots contain the values for right and left region for each subject

.

The average size of the manually–defined SN was $496 \pm 76.1\, mm^3$ and the size of the atlas SN ROI was $485\, mm^3$. The size of the seed mask (number of voxels) presumably contributes to the TNS, which might reflect the "strength" of the nigrostriatal pathway. Figure 8.5 shows the TNS (black: individual SN, red: atlas SN ROI estimates) versus BP_{ND} for CD and PU.

For both CD and PU there is a trend for positive correlation between the TNS and [^{11}C]PHNO BP_{ND} estimates. Permutation tests were performed (200000 repetitions)

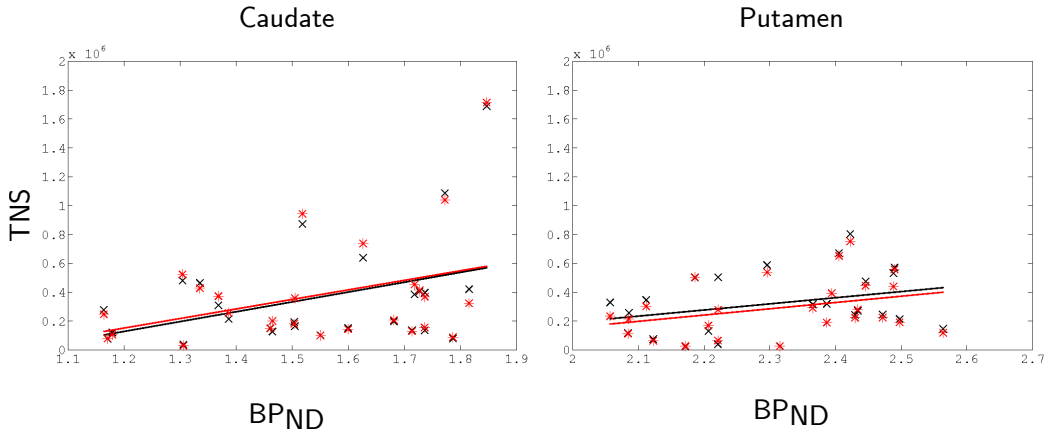

Figure 8.5: Correlation of the nigrostriatal strength (TNS) with [^{11}C]PHNO BP_{ND}. 1^{st} column corresponds to CD and 2^{nd} to PU. Black markers ($\times$) and black regression lines correspond to the measurements derived with the individual SN ROIs; Red markers ($\star$) and red regression lines to the atlas SN ROI. For the individual delineated SN the p-value for CD was p = 0.04 whereas for PU p = 0.13. For the atlas SN ROIs the CD p-value = 0.05 and for PU p-value = 0.18. SN: substantia nigra, TNS: total number of samples from substantia nigra to reach the target, BP_{ND}: binding potential.

to assess the correlation and estimate p-values. For the individual delineated SN the p-value for CD was significant for BP_{ND} (p = 0.04). For PU, although there is a trend for positive correlation the results did not reveal a significant correlation (p = 0.13). Similar results were observed for the TNS estimates calculated for the atlas SN ROI. Specifically for CD, the p-value = 0.05 and for PU p-value = 0.18.

8.4 Discussion

In this chapter we have studied the relationship between the nigrostriatal pathway strength and BP_{ND} measurement, where the BP_{ND} is proportional to the number of D2-like receptors. The strength of the nigrostriatal pathway was estimated using probabilistic tractography, by the total number of samples that were generated in the SN ROI and reached the striatum. First and foremost it needs to be emphasised that the strength of the nigrostriatal pathway, estimated with probabilistic tractography, does not correspond to the "strength" of the actual nigrostriatal pathway. Therefore, any tractography-derived measures should be interpreted with caution. Many

anatomical features of the pathway of interest (number of axons, membrane integrity, axon diameter, myelin thickness, crossing fibers, tract geometry, tract length) [93], the quality of the diffusion data and the tractography methods employed, will all contribute to this diffusion estimate.

The TNS (our surrogate for the strength of the pathway) shows a positive correlation with the [^{11}C]PHNO BP_{ND}. In physiological terms, the strength of a pathway could potentially translate into fiber integrity, larger axon diameter or fiber density. In a healthy population one explanation for this positive trend would be that the existence of more fibers is associated with the presence of more dopamine receptors and transporters, which preserve the equilibrium of the synaptic system. This is different to conditions where, due to neurodegenerative disorders or in response to an external stimuli, the system down-regulates or up-regulates the number of receptors or transporters in order to decrease or increase, respectively, its sensitivity to the stimulus.

The potency of the nigrostriatal pathway could also be governed by the dendritic arbor of the area, which in turn affects the synaptic plasticity and has an important role in the integration of information delivered by the synapses to stimulate dopaminergic activity. Synaptic plasticity is the experience-dependent change in connectivity between neurones that is believed to underlie learning and memory [86]. Changing the strength of connections between neurons is widely assumed to be the mechanism by which memory traces are encoded and stored in the central nervous system [125]. Moreover, an influential hypothesis is that addiction represents a pathological, yet powerful, form of learning and memory [97]. Hence, the potency of the nigrostriatal pathway could impact behaviours related to drug addiction and what makes certain people more vulnerable to drug abuse than others.

Despite the small sample size we observed a significant relationship for the CD and a trend for significance in the PU for both the individual and atlas SN ROIs. This implies that any correlations observed are not driven by the size of the seed mask, which due to the nature of the probabilistic tractography algorithm could potentially contribute to the TNS. For example, with bigger seed masks, more samples are generated in the seed mask and hence more samples can reach the target. Age is another factor that could potentially contribute to the correlations investigated. However, we did not observe any significant correlation between age and the measurements of interest.

The positive correlation was significant for the CD. However, for the PU this trend did not reach statistical significance. To investigate further the connection between the striatum and the SN and to understand the lack of significant correlation between the PU and TNS, we ran the tractography with the PU and the CD as the seed masks and the SN as the target. As the dorsal striatum receives a large amount of dopamine neurons but projects to a limited area [74] we expected dense projections from SN to both the CD and the PU similar to primate studies (figure 8.1b). Nevertheless, there were fewer projections to the PU in comparison to the projection to the CD. Several reasons could contribute to this. For example, SN to PU tract geometry might be more difficult or complex to track with probabilistic tractography, or the area of SN that primarily receives projections from PU might not be included in the ROI. The average size of the SN ROI defined in this study ($496 \pm 76.1\, mm^3$) is substantially smaller than that estimated by Eapen et al. ($725.7 \pm 98.37\, mm^3$) [56] in healthy participants on high resolution T2- and T2*-weighted GRADE and FEE MRI images at 7T. In this study the SN delineation stopped at a certain dorsal level to avoid sampling of the subthalamic nucleus. Additionally, it is not certain if the whole of the SN is shown on the FLAWS sequence or solely the SN pars compacta or SN pars reticulata. Therefore, if the majority of the SN that projects to the PU is excluded then this might contribute to the fact that we observe fewer projections in the PU. Probabilistic tractography

is unable to distinguish between afferent and efferent fibre tracts. As can be seen in figure 8.1a, from the striatum it is the CD nucleus that sends dense projections to the SN. Therefore, all the aforementioned evidence and also the small number of subjects could potentially justify the lack of significant correlation between PU BP_{ND} and TNS.

If the hypothesis of increased "strength" corresponding to increased dopamine receptors in the system is indeed true, then more dopamine transporters or more dopamine synthesis capacity may also be expected. This would preserve the biological equilibrium in the synapse. Experiments to investigate this hypothesis would make use of ligands that bind to the dopamine transporters, such as [^{18}F]-FECNT or ligands that measure the dopamine synthesis capacity such as [^{18}F]FDOPA. If a positive correlation with the TNS is found, with both the transporter and dopamine capacity, this could support this theory.

A future study with some or all of the following refinements would be useful for further investigation: a) more subjects to increase sensitivity; b) better MRI sequence that allows for a better delineation of the SN ROI; c) higher resolution for both PET and MRI; and finally d) novel tractography techniques [15] to estimate the connection strength. A follow–up study with these refinements is worthwhile as it would allow a deeper understanding of how the potency of the nigrostriatal pathway contributes to the PET inter-subject variability. It is encouraging that we have obtained a significant relationship between the number of receptors in the CD and the potency of the nigrostriatal pathway. If following further investigations this positive correlation is robust then, the potency of the nigrostriatal pathway, could be used as a normalisation factor in PET studies. This would allow a better intra–subject comparison (in longitudinal studies), inter–subject comparisons and comparisons between healthy and diseased groups.

Chapter 9

Conclusions and future directions

The implication of dopamine and its receptors in normal and abnormal conditions has made it an attractive target for research and drug discovery. Although components of the aetiology for some of the dopamine-related disorders have been identified, their root causes are not yet fully understood despite extensive research. The motivation in this thesis was to develop multimodal imaging methods, using PET and MRI, to investigate dopamine in humans *in–vivo*.

[^{11}C]PHNO PET is highly informative about the biochemical and physiological processes of dopamine and the D2-like receptors in the living human brain but lacks anatomical information. The anatomical information, in this investigation is obtained from the structural and DWI MRI modalities. Structural MRI is used to facilitate study of dopamine in the anatomical structures of the brain. Specifically, ROI guidelines were developed to enable the delineation of the subcortical D2-like receptor rich regions on the T1-weighted images. The guidelines were assessed in terms of intra– and inter–operator reproducibility and the results show that robust and reproducible quantifications are obtained. DWI was used to estimate the anatomical connectivity profiles of brain regions and specifically to estimate the striatal–cortical and pallidal–striatal projections to generate the connectivity-based functional subdivisions of the striatum and the pallidum. The connectivity profiles of these regions were consistent

among subjects and congruent with non–human primate data with distinctive and overlapping networks. Moreover, to speed-up the manual definition of the subcortical ROIs and to enable the use of the connectivity-based functional subdivisions of the striatum and the pallidum in studies where DWI data were not available, structural-based and connectivity-based atlases were constructed.

Exploiting the strengths of the D3R–preferring radioligand [^{11}C]PHNO and the methods developed – structural– and connectivity–based subdivisions – we aimed to explore the following objectives: a) study the distribution and relative regional densities of the D3R and D2R sites in the human brain, b) explore dopamine release after administration of the dopamine releasing agent amphetamine and c) investigate the relationship between the strength of the nigrostriatal pathway and the density of dopamine receptors. Below we critically review some of our findings, we report limitations of our investigation and in section 9.1 we indicate how this work could potentially contribute to the field.

In this thesis the [^{11}C]PHNO scans for the quantification of dopamine and the D2-like receptors were analysed with the SRTM model. Our decision was based upon an early study [65], which reported that both the 2TC and the SRTM models describe the data well and the BP_{ND} obtained with the two models are highly correlated. The advantage of the SRTM over the 2TC model is that no arterial blood sampling is required, which is invasive, uncomfortable for the patient and can introduce additional measurement variability. On the other hand, the SRTM model requires a region that is devoid of specific binding (reference region). As was proposed by Ginovart [65], the use of the cerebellum as the reference region was a suitable option for the quantification of [^{11}C]PHNO data. However, in their investigation the use of the cerebellum as a reference region was validated against quantifications obtained with plasma input functions using scans at baseline conditions. A recent study by Searle and colleagues

[156], who applied the 2TC model and used a D3R blocker, demonstrated that in certain areas of the cerebellum there is a small amount of specific binding. Moreover, they show that for [^{11}C]PHNO the SRTM underestimates BP_{ND} relative to the 2TC, especially in the high binding regions. In this thesis the cerebellum was used as the reference region and this will impact the quantification for the occupancy of the D3R receptors. However, as the dopamine related parameters are estimated as relative changes in the BP_{ND}, the introduced bias might be insignificant.

Mass dose effects are also a potential confounding factor in imaging with [^{11}C]PHNO. Mass dose effects occur when a non-negligible fraction of the target receptors are occupied by the cold ligand. For reliable and accurate quantitative estimates of BP_{ND}, the scans should be performed at tracer conditions (<10 % occupancy of the target receptor). Moreover, mass dose effects can lead to underestimation of the BP_{ND} which in turn can induce underestimation or overestimation of the relative BP_{ND} changes. Another consequence of any mass dose effect is the potential for carry-over of mass dose effects. Often, especially in challenge studies (administration of a D3R blocker, or of amphetamine etc), consecutive PET scans are performed within a short time interval. If, at the beginning of the challenge scan, a significant amount of the D3R is still occupied by the unlabelled ligand from the baseline scan, then the mass dose effect can induce errors in occupancy estimates [156]. Searle et al. [156] estimated that in order to achieve tracer conditions the injection of [^{11}C]PHNO would need to contain less than 0.15 μg of (+)PHNO. However, with current radiochemistry techniques, it is difficult to produce [^{11}C]PHNO with high enough specific activity to avoid any mass dose effects [156].

With regard to the characterisation of the [^{11}C]PHNO signal and the functional distribution of the D3R and D2R sites, the results show that in both regions, striatum and pallidum, the highest contribution to the [^{11}C]PHNO signal and the highest density of

the D3R sites, was in the limbic subdivisions. This was expected as D3R receptors are implicated in addiction and psychiatric disorders. The findings in the executive and sensorimotor subdivisions do not show a consistent pattern between the striatum and the pallidum. Specifically, in the striatum there are only D2R sites in the sensorimotor and executive zones whereas in the pallidum the bulk of the signal is due to D3R. This discrepancy between the striatal and pallidal sensorimotor and executive functional subdivisions could indicate that the D2-like dopamine receptors are aligned with the structural–cytoarchitectonic organisation of the areas and not the functional organisation.

We have explored dopamine function following the administration of d-amphetamine. The results indicate a functional specificity of the dopamine release. In other words we have demonstrated that the neurochemical architecture of dopamine is aligned with function. This has consequences for the design, analysis and interpretation of future dopamine release studies in normo- and patho- physiology. The same pattern of dopamine release was observed in both the striatum and the pallidum. Specifically, the highest release was measured in the limbic zone, followed by the sensorimotor and the executive zones. To examine whether our findings are robust, and not ligand–specific, dopamine release was also quantified with [^{11}C]Raclopride. The pattern of dopamine release in the striatum was the same and it does not seem to be affected by the D2R / D3R preferential affinities of the ligands. In the pallidum, the quantification of dopamine release with [^{11}C]Raclopride did not give the same order. Specifically, the highest dopamine release was detected in the sensorimotor and not in the limbic area. As we discussed in chapter 7, we believe that this is due to the lower sensitivity of the [^{11}C]Raclopride ligand to detect dopamine fluctuations and that in small regions, such as the limbic pallidum, the quantification is particularly noisy.

In chapter 7, the connectivity-based functional subdivisions were applied to PET data for the quantification of dopamine release. This methodology is not limited to the investigation of endogenous dopamine release and could be of value in other neurotransmitter systems such as those involving opioids and the serotonin. The improved regional discrimination of this method can be of value in group comparisons, where the detection of specific functional differences are explored. For example, in a study where non-depressed, non-demented, dopaminergic drug-naive patients with early-stage Parkinson's disease were compared relative to matched–controls [26] the authors found a bilateral decrease of [^{11}C]PHNO in the VST area but not in the PU, the area that post-commissuraly is primarily involved in motor functions. In studies like this our methods could be applied and potentially reveal group differences that otherwise are lost due to the methods used for regional quantifications.

The striatum of the human brain has highly differentiated neurochemical architecture. The connectivity-based method proposed in this thesis can also be used to study the distribution of neurotransmitters in individual subjects and understand the neurochemical organisation. Such capability may help the development of novel therapeutic compounds and enhance the evaluation of novel radiopharmaceuticals. This methodology may also provide a valuable tool for deep brain stimulation surgery planning, helping to improve the treatment of a variety of disorders such as pain, motor, obsessive-compulsive disorders, depression and addiction. For example, probabilistic tractography could be applied in individual subjects before surgery to identify where the specific impaired function is expressed in certain structures. This a–priori knowledge could potentially help locate the best target for implantation of electrodes and increase the efficacy of the deep brain stimulation treatment.

9.1 Future objectives

9.1.1 Investigate non-linear registration algorithms for spatial normalisation

The spatial normalisation of anatomical atlases into an individual subject's space is one of the most commonly used methods for definition of cortical and subcortical ROIs. In this thesis we have utilised SPM5 to perform the non-linear registration of our anatomical atlas. Specifically, the normalisation was between the MNI template and the subject's T1-weighted image and the transformation parameters were then applied to the atlas using the "nearest neighbour" method for interpolation. Although the results were satisfactory, using improved non-linear registration algorithms could substantially increase the performance of the spatial normalisation. A recent investigation by Klein and colleagues [102] has shown that a number of state-of-the-art non-linear registration algorithms perform significantly better than the SPM5 algorithm.

Another approach that improves the automated definition of the ROIs is the multi–atlas propagation technique [7, 44, 83]. This method performs a non-linear registration of multiple individual atlases to the subject's space. Subsequently, it combines information from the multiple propagated labels to create the segmentations. The "majority vote rule" as described by Kittler [101] is used to assign each brain voxel to a label. This technique, combined with a state-of-the-art registration algorithm, could substantially improve the automatic segmentation.

9.1.2 Acquisition of arterial input function for the analysis of the [^{11}C]PHNO studies

In chapter 6 the analysis of the [^{11}C]PHNO data was performed using the SRTM model and the cerebellum as the reference region. However, visual inspection of the BP_{ND}

parametric images and the SUV values at baseline conditions and after the administration of the D3R blocker GSK598809 indicate that the cerebellum is not devoid of D2-like receptors, as there is a dose-dependent reduction of the binding. This impacts the estimates of the BP_{ND}, especially in the high binding regions, and the estimates of regional f_{PHNO}^{D3R}, particularly in the low D3R regions. Full quantitative analysis of [^{11}C]PHNO uptake using a measured arterial input function should be undertaken in order to estimate the regional effects of GSK598809 and to justify whether the cerebellum or subregions of the cerebellum or other cortical regions are appropriate to be used as reference region.

9.1.3 Optimisation of structural T1-weighted images

In this thesis we have quantified the release of dopamine in the structural and functional regions of the basal ganglia, hypothalamus and thalamus. For regions such as the striatum we have developed guidelines for its subdivision into VST, CD and PU. The remaining regions consist of several anatomical nuclei as well, but it was not feasible to develop guidelines to further subdivide them due to the lack of structural MRI information, as the contrast and resolution of the current structural MRI images are not sufficient to allow delineation of such small nuclei. The development of sequences such as FGATIR [171] and FLAWS [174] – where the white matter is nulled – look promising for enabling the subdivision of structures such as the pallidum and the thalamus. Moreover, the advent of 7T MRI scanners can potentially allow a more refined delineation of these regions and could also enable their subdivision. For instance Eapen and colleagues [56], using high resolution MRI at 7T, developed sequences that provided a good contrast between midbrain regions and allowed a refined segmentation. We believe that it is imperative to employ sequences with such detailed anatomical information and use them along with PET imaging and resolution recovery techniques [13, 160, 161] for a detailed investigation of the anatomical specificity of dopamine.

9.1.4 Correlation of PET measurements with the strength of the nigrostriatal pathway

In chapter 8 we investigated whether the strength of the nigrostriatal pathway, as defined by probabilistic tractography, correlates with PET measurements that are proportional to the receptor density (BP_{ND}). The hypothesis is that the stronger the capacity of the nigrostriatal pathway, the higher the number of receptors and hence the higher the PET measurement would be. We believe that if this hypothesis proves to be correct then it will have a direct effect on the analysis of PET studies. For example, in studies of group comparisons or intra–subject longitudinal studies, this parameter should be considered and potentially used as a normalising factor.

The nigrostriatal pathway consists of dopaminergic neurons that originate in the SN and reach the dorsal striatum i.e. the CD and PU. In this thesis we found a positive correlation for both the CD and the PU, but it reaches significance only for the CD and the BP_{ND} measurement. Although there is some evidence that could potentially explain the lack of significant correlation for the PU (described in detail in chapter 8) the issue should be explored further. For example, inclusion of additional subjects or the acquisition of higher quality DWI could potential increase the sensitivity and provide better assessment. Moreover, the same experimental setting, with a ligand that images the dopamine transporter and shows a positive correlation with the capacity of the nigrostriatal pathway, would confirm and support the correctness of such a hypothesis.

Bibliography

[1] Center for Morphometric Analysis, Massachusetts General Hospital. http://www.cma.mgh.harvard.edu, Date of access: 6/Jul/2013.

[2] A. Abi-Dargham, R. Gil, J. Krystal, R. M. Baldwin, J. P. Seibyl, M. Bowers, C. H. van Dyck, D. S. Charney, R. B. Innis, and M. Laruelle. Increased striatal dopamine transmission in schizophrenia: confirmation in a second cohort. *The American Journal of Psychiatry*, 155(6):761–7, Jun 1998.

[3] A. Abi-Dargham, J. Rodenhiser, D. Printz, Y. Zea-Ponce, R. Gil, L. S. Kegeles, R. Weiss, T. B. Cooper, J. J. Mann, R. L. Van Heertum, J. M. Gorman, and M. Laruelle. Increased baseline occupancy of D2 receptors by dopamine in schizophrenia. *Proceedings of the National Academy of Sciences of the United States of America*, 97(14):8104–9, Jul 2000.

[4] J. E. Ahlskog, M. D. Muenter, P. A. Bailey, and P. M. Miller. Parkinson's disease monotherapy with controlled-release MK-458 (PHNO): double-blind study and comparison to carbidopa/levodopa. *Clinical Neuropharmacology*, 14(3):214–27, Jun 1991.

[5] R. L. Ahsan, R. Allom, I. S. Gousias, H. Habib, F. E. Turkheimer, S. Free, L. Lemieux, R. Myers, J. S. Duncan, D. J. Brooks, M. J. Koepp, and A. Hammers. Volumes, spatial extents and a probabilistic atlas of the human basal ganglia and thalamus. *Neuroimage*, 38(2):261–70, Nov 2007.

[6] G. E Alexander and M. D. Crutcher. Functional architecture of basal ganglia circuits: neural substrates of parallel processing. *Trends in Neurosciences*, 13(7):266–71, Jul 1990.

[7] P. Aljabar, R. A. Heckemann, A. Hammers, J. V. Hajnal, and D. Rueckert. Multi-atlas based segmentation of brain images: atlas selection and its effect on accuracy. *Neuroimage*, 46(3):726–38, Jul 2009.

[8] J. Andersson., M. Jenkinson, and S. Stephen. Non-linear registration aka spatial normalisation. Technical report, FMRIB, University of Oxford, 2007.

[9] J. Andersson, M. Richter, W. Richter, S. Skare, R. G. Nunes, M. Robson, and T. E. J. Behrens. Effects of susceptibility distortions on tractography. In *Proceedings of the ISMRM 12th Scientific Meeting and Exhibition, Kyoto*, page 87, 2004.

[10] J. Andersson, S. Skare, and J. Ashburner. How to correct susceptibility distortions in spin-echo echo-planar images: application to diffusion tensor imaging. *Neuroimage*, 20(2):870–88, Oct 2003.

[11] B. A. Ardekani, M. Braun, B. F. Hutton, I. Kanno, and H. Iida. A fully automatic multimodality image registration algorithm. *Journal of Computer Assisted Tomography*, 19(4):615, Jul-Aug 1995.

[12] J. Ashburner. A fast diffeomorphic image registration algorithm. *Neuroimage*, 38(1):95–113, Oct 2007.

[13] J. A. D. Aston, V. J. Cunningham, M. Asselin, A. Hammers, A. C. Evans, and R. N. Gunn. Positron emission tomography partial volume correction: estimation and algorithms. *Journal of Cerebral Blood Flow & Metabolism*, 22(8):1019–34, Aug 2002.

[14] B. B. Avants, C. L. Epstein, M. Grossman, and J. C. Gee. Symmetric diffeomorphic image registration with cross-correlation: evaluating automated labeling of elderly and neurodegenerative brain. *Medical Image Analysis*, 12(1):26–41, Feb 2008.

[15] M. Axer, K. Amunts, D. Grässel, C. Palm, J. Dammers, H. Axer, U. Pietrzyk, and K. Zilles. A novel approach to the human connectome: ultra-high resolution mapping of fiber tracts in the brain. *Neuroimage*, 54(2):1091–101, Jan 2011.

[16] A. J. Bartsch, A. Biller, and G. A. Homola. *Diffusion MRI, from quantitative measurement to in vivo neuroanatomy*, chapter 19: Tractography for Sugical Targeting. Elsevier, 2009.

[17] M. Beckmann, H. Johansen-Berg, and M. F. S. Rushworth. Connectivity-based parcellation of human cingulate cortex and its relation to functional specialization. *The Journal of Neuroscience*, 29(4):1175–90, Jan 2009.

[18] T. E. J. Behrens and S. Jbabdi. *Diffusion MRI: from quantitative measurement to in-vivo neuroanatomy*, chapter MR diffusion tractography. Academic Press, 2009.

[19] T. E. J. Behrens, H. Johansen-Berg, S. Jbabdi, M. F. S. Rushworth, and M. W. Woolrich. Probabilistic diffusion tractography with multiple fibre orientations: What can we gain? *Neuroimage*, 34(1):144–55, Jan 2007.

[20] T. E. J. Behrens, H. Johansen-Berg, M. W. Woolrich, S. M. Smith, C. A. M. Wheeler-Kingshott, P. A. Boulby, G. J. Barker, E. L. Sillery, K. Sheehan, O. Ciccarelli, A. J. Thompson, J. M. Brady, and P. M. Matthews. Non-invasive mapping of connections between human thalamus and cortex using diffusion imaging. *Nature Neuroscience*, 6(7):750–757, Jul 2003.

[21] T. E. J. Behrens, M. W. Woolrich, M. Jenkinson, H. Johansen-Berg, R. G. Nunes, S. Clare, P. M. Matthews, J. M. Brady, and S. M. Smith. Characterization and propagation of uncertainty in diffusion-weighted MR imaging. *Magnetic Resonance in Medicine*, 50(5):1077–88, Nov 2003.

[22] H. Bernheimer, W. Birkmayer, O. Hornykiewicz, K. Jellinger, and F. Seitelberger. Brain dopamine and the syndromes of Parkinson and Huntington. Clinical, morphological and neurochemical correlations. *Journal of the Neurological Sciences*, 20(4):415–455, Dec 1973.

[23] F. Bloch, W. W. Hansen, and M. Packard. Nuclear induction. *Physical Review*, 70(7-8):460–474, 1946.

[24] G. Blomqvist, S. Pauli, L. Farde, L. Ericksson, A. Persson, and C. Halldin. Dynamic models of reversible ligand binding. *Clinical Research and Clinical Diagnosis*, pages 35–44, 1989.

[25] I. Bohanna, N. Georgiou-Karistianis, and G. F. Egan. Connectivity-based segmentation of the striatum in Huntington's disease: vulnerability of motor pathways. *Neurobiology of Disease*, 42(3):475–81, Jun 2011.

[26] I. Boileau, M. Guttman, P. Rusjan, J. R. Adams, S. Houle, J. Tong, O. Hornykiewicz, Y. Furukawa, A. A. Wilson, S. Kapur, and S. J. Kish. Decreased binding of the D3 dopamine receptor-preferring ligand [11C]-(+)-PHNO in drug-naive Parkinson's disease. *Brain*, 132(Pt 5):1366–75, May 2009.

[27] M. L. Bouthenet, E. Souil, M. P. Martres, P. Sokoloff, B. Giros, and J. C. Schwartz. Localization of dopamine D3 receptor mRNA in the rat brain using in situ hybridization histochemistry: comparison with dopamine D2 receptor mRNA. *Brain Research*, 564(2):203–19, Nov 1991.

[28] M. P. Brazell, S. N. Mitchell, M. H. Joseph, and J. A. Gray. Acute administration of nicotine increases the in vivo extracellular levels of dopamine, 3,4-dihydroxyphenylacetic acid and ascorbic acid preferentially in the nucleus accumbens of the rat: comparison with caudate-putamen. *Neuropharmacology*, 29(12):1177–85, Dec 1990.

[29] A. Breier, T. P. Su, R. Saunders, R. E. Carson, B. S. Kolachana, A. de Bartolomeis, D. R. Weinberger, N. Weisenfeld, A. K. Malhotra, W. C. Eckelman, and D. Pickar. Schizophrenia is associated with elevated amphetamine-induced synaptic dopamine concentrations: evidence from a novel positron emission tomography method. *Proceedings of the National Academy of Sciences of the United States of America*, 94(6):2569–74, Mar 1997.

[30] H. Bridge, O. Thomas, S. Jbabdi, and A. Cowey. Changes in connectivity after visual cortical brain damage underlie altered visual function. *Brain*, 131(Pt 6):1433–44, Jun 2008.

[31] R. B Buxton. *Introduction to functional magnetic resonance imaging. Principles and techniques*. Cambridge University Press, 2002.

[32] R. Calzavara, P. Mailly, and S. N. Haber. Relationship between the corticostriatal terminals from areas 9 and 46, and those from area 8a, dorsal and rostral premotor cortex and area 24c: an anatomical substrate for cognition to action. *European Journal of Neuroscience*, 26(7):2005–24, Oct 2007.

[33] C. Cavada and P. S. Goldman-Rakic. Posterior parietal cortex in rhesus monkey: II. evidence for segregated corticocortical networks linking sensory and limbic areas with the frontal lobe. *Journal of Comparative Neurology*, 287(4):422–45, Sep 1989.

[34] C. Cavada and P. S. Goldman-Rakic. Topographic segregation of corticostriatal projections from posterior parietal subdivisions in the macaque monkey. *Neuroscience*, 42(3):683–96, 1991.

[35] H. Chang and J. M. Fitzpatrick. A technique for accurate magnetic resonance imaging in the presence of field inhomogeneities. *IEEE Transactions on Medical Imaging*, 11:319–329, 1992.

[36] M. M. Chiavaras and M. Petrides. Orbitofrontal sulci of the human and macaque monkey brain. *Journal of Comparative Neurology*, 422(1):35–54, Jun 2000.

[37] O. Ciccarelli, M. Catani, H. Johansen-Berg, C. Clark, and A. Thompson. Diffusion-based tractography in neurological disorders: concepts, applications, and future developments. *The Lancet Neurology*, 7(8):715–727, Aug 2008.

[38] B. J. Ciliax, G. W. Drash, J. K. Staley, S. N. Haber, C. J. Mobley, G. W. Miller, E. J. Mufson, D. C. Mash, and A. I. Levey. Immunocytochemical localization of the dopamine transporter in human brain. *Journal of Comparative Neurology*, 409(1):38–56, Jun 1999.

[39] M. X. Cohen, J. C. Schoene-Bake, C. E. Elger, and B. Weber. Connectivity-based segregation of the human striatum predicts personality characteristics. *Nature Neuroscience*, 12(1):32–4, Jan 2009.

[40] W. M. Cowan, T. C. Südhof, and C. F. Stevens. *Synapses*. Johns Hopkins University Press, 2003.

[41] P. L. Croxson, H. Johansen-Berg, T. E. J. Behrens, M. D. Robson, M. A. Pinsk, C. G. Gross, W. Richter, M. C. Richter, S. Kastner, and M. F. S. Rushworth. Quantitative investigation of connections of the prefrontal cortex in the human and macaque using probabilistic diffusion tractography. *The Journal of Neuroscience*, 25(39):8854–66, Sep 2005.

[42] V. J. Cunningham, S. P. Hume, G. R. Price, R. G. Ahier, J. E. Cremer, and A. K. P. Jones. Compartmental analysis of diprenorphine binding to opiate receptors in the rat in vivo and its comparison with equilibrium data in vitro. *Journal of Cerebral Blood Flow & Metabolism*, 11(1):1–9, Jan 1991.

[43] M. Defrise, P. E. Kinahan, D. W. Townsend, C. Michel, M. Sibomana, and D. F. Newport. Exact and approximate rebinning algorithms for 3-D PET data. *IEEE Transactions on Medical Imaging*, 16(2):145–58, Apr 1997.

[44] N. Del Campo, R. J. Tait, J. Acosta-Cabronero, Y. T. Hong, D. Izquierdo-Garcia, R. Smith, F. I. Aigbirhio, B. J. Sahakian, U. Müller, T. W. Robbins, and T. D. Fryer. Quantification of receptor-ligand binding potential in substriatal domains using probabilistic and template regions of interest. *Neuroimage*, 55(1):101–12, Mar 2011.

[45] S. L. Dewey, J. Logan, A. P. Wolf, J. D. Brodie, B. Angrist, J. S. Fowler, and N. D. Volkow. Amphetamine induced decreases in (18F)-N-methylspiroperidol binding in the baboon brain using positron emission tomography (PET). *Synapse*, 7(4):324–327, Oct 1991.

[46] S. L. Dewry, J. D. Brodie, J. S. Fowler, R. R. MacGregor, D. J. Schlyer, P. T. King, D. L. Alexoff, N. D. Volkow, C. Y. Shiue, and A. P. Wolf. Positron emission tomography (PET) studies of dopaminergic/cholinergic interaction in the baboon brain. *Synapse*, 6(4):321–327, May 1990.

[47] G. Di Chiara. On the preferential release of mesolimbic dopamine by amphetamine. *Neuropsychopharmacology*, 5(4):243–7, Dec 1991.

[48] G. Di Chiara and A. Imperato. Drugs abused by humans preferentially increase synaptic dopamine concentrations in the mesolimbic system of freely moving rats. *Proceedings of the National Academy of Sciences of the United States of America*, 85(14):5274–8, Jul 1988.

[49] G. Di Chiara and A. Imperato. Opposite effects of mu and kappa opiate agonists on dopamine release in the nucleus accumbens and in the dorsal caudate of freely moving rats. *Journal of Pharmacology and Experimental Therapeutics*, 244(3):1067–80, Mar 1988.

[50] L. R. Dice. Measures of the amount of ecologic association between species. *Ecology*, 26(3):297–302, Jul 1945.

[51] J. Diedrichsen. A spatially unbiased atlas template of the human cerebellum. *Neuroimage*, 33(1):127–38, Oct 2006.

[52] B. Draganski, F. Kherif, S. Klöppel, P. A. Cook, D. C. Alexander, G. J. M. Parker, R. Deichmann, J. Ashburner, and R. S. J. Frackowiak. Evidence for segregated and integrative connectivity patterns in the human basal ganglia. *The Journal of Neuroscience*, 28(28):7143–52, Jul 2008.

[53] B. Drayer, P. Burger, R. Darwin, S. Riederer, R. Herfkens, and G. A. Johnson. MRI of brain iron. *American Journal of Roentgenology*, 147(1):103–110, Jul 1986.

[54] W. C. Drevets, J. C. Price, D. J. Kupfer, P. E. Kinahan, B. Lopresti, D. Holt, and C. A. Mathis. PET measures of amphetamine-induced dopamine release in ventral versus dorsal striatum. *Neuropsychopharmacology*, 21(6):694–709, Dec 1999.

[55] H. M. Duvernoy. *The human brain: surface, three-dimensional sectional anatomy with MRI, and blood supply*. Springer, 1991.

[56] M. Eapen, D. H. Zald, J. C. Gatenby, Z. Ding, and J. C. Gore. Using high-resolution MR imaging at 7T to evaluate the anatomy of the midbrain dopaminergic system. *American Journal of Neuroradiology*, 32(4):688–94, Apr 2011.

[57] S. B. Eickhoff, K. E. Stephan, H. Mohlberg, C. Grefkes, G. R. Fink, K. Amunts, and K. Zilles. A new SPM toolbox for combining probabilistic cytoarchitectonic maps and functional imaging data. *Neuroimage*, 25(4):1325–1335, May 2005.

[58] L. Farde, E. Ehrin, L. Eriksson, T. Greitz, H. Hall, C. G. Hedström, J. E. Litton, and G. Sedvall. Substituted benzamides as ligands for visualization of dopamine receptor binding in the human brain by positron emission tomography. *Proceedings of the National Academy of Sciences of the United States of America*, 82(11):3863–7, Jun 1985.

[59] L. Farde, H. Hall, S. Pauli, and C. Halldin. Variability in D2-dopamine receptor density and affinity: a PET study with [11C]raclopride in man. *Synapse*, 20(3):200–208, Jul 1995.

[60] L. Farde, A. L. Nordström, F. A. Wiesel, S. Pauli, C. Halldin, and G. Sedvall. Positron emission tomographic analysis of central D1 and D2 dopamine receptor occupancy in patients treated with classical neuroleptics and clozapine. Relation to extrapyramidal side effects. *Archives of General Psychiatry*, 49(7):538–44, Jul 1992.

[61] C. François, J. Yelnik, G. Parcheron, and G. Fenelon. Topographic distribution of the axonal endings from the sensorimotor and associative striatum in the macaque pallidum and substantia nigra. *Experimental Brain Research*, 102(2):305–318, Dec 1994.

[62] S. B. Freedman, S. Patel, R. Marwood, F. Emms, G. R. Seabrook, M. R. Knowles, and G. McAllister. Expression and pharmacological characterization of the human D3 dopamine receptor. *Journal of Pharmacology and Experimental Therapeutics*, 268(1):417–26, Jan 1994.

[63] J. L. Fudge, K. Kunishio, P. Walsh, C. Richard, and S. N. Haber. Amygdaloid projections to ventromedial striatal subterritories in the primate. *Neuroscience*, 110(2):257–75, Mar 2002.

[64] J. Gallezot, J. D. Beaver, R. N. Gunn, N. Nabulsi, D. Weinzimmer, T. Singhal, M. Slifstein, K. Fowles, Y. Ding, Y. Huang, M. Laruelle, R. E. Carson, and E. A. Rabiner. Affinity and selectivity of [11C]-(+)-PHNO for the D3 and D2 receptors in the rhesus monkey brain in vivo. *Synapse*, 66(6):489–500, Jun 2012.

[65] N. Ginovart, L. Galineau, M. Willeit, R. Mizrahi, P. M. Bloomfield, P. Seeman, S. Houle, S. Kapur, and A. A. Wilson. Binding characteristics and sensitivity to endogenous dopamine of [11C]-(+)-PHNO, a new agonist radiotracer for imaging the high-affinity state of D2 receptors in vivo using positron emission tomography. *Journal of Neurochemistry*, 97(4):1089–103, May 2006.

[66] A. Graff-Guerrero, L. Redden, W. Abi-Saab, D. A. Katz, S. Houle, P. Barsoum, A. Bhathena, R. Palaparthy, M. D. Saltarelli, and S. Kapur. Blockade of [11C](+)-PHNO binding in human subjects by the dopamine D3 receptor antagonist ABT-925. *The International Journal of Neuropsychopharmacology*, 13(3):273–87, Apr 2010.

[67] G. Grunder. *Molecular imaging in the clinical neurosciences*. Humana Press, 2012.

[68] R. N. Gunn, S. R. Gunn, and V. J. Cunningham. Positron emission tomography compartmental models. *Journal of Cerebral Blood Flow & Metabolism*, 21(6):635–652, Jun 2001.

[69] R. N. Gunn, A. A. Lammertsma, S. P. Hume, and V. J. Cunningham. Parametric imaging of ligand-receptor binding in PET using a simplified reference region model. *Neuroimage*, 6(4):279–287, Nov 1997.

[70] Q. Guo. *Improving the discovery of molecular imaging probes through biomathematical modelling.* PhD thesis, Oxford University, 2010.

[71] E. V. Gurevich and J. N. Joyce. Distribution of dopamine D3 receptor expressing neurons in the human forebrain: comparison with D2 receptor expressing neurons. *Neuropsychopharmacology*, 20(1):60–80, Jan 1999.

[72] S. N. Haber. The primate basal ganglia: parallel and integrative networks. *Journal of Chemical Neuroanatomy*, 26(4):317–30, Dec 2003.

[73] S. N. Haber. Parallel and integrative processing through the basal ganglia reward circuit: lessons from addiction. *Biological Psychiatry*, 64(3):173–4, Aug 2008.

[74] S. N. Haber, J. L. Fudge, and N. R. McFarland. Striatonigrostriatal pathways in primates form an ascending spiral from the shell to the dorsolateral striatum. *The Journal of Neuroscience*, 20(6):2369–82, Mar 2000.

[75] S. N. Haber, K. Kim, P. Mailly, and R. Calzavara. Reward-related cortical inputs define a large striatal region in primates that interface with associative cortical connections, providing a substrate for incentive-based learning. *The Journal of Neuroscience*, 26(32):8368–76, Aug 2006.

[76] S. N. Haber and B. Knutson. The reward circuit: linking primate anatomy and human imaging. *Neuropsychopharmacology*, 35(1):4–26, Jan 2010.

[77] S. N. Haber, E. Lynd, C. Klein, and H. J. Groenewegen. Topographic organization of the ventral striatal efferent projections in the rhesus monkey: an anterograde tracing study. *Journal of Comparative Neurology*, 293(2):282–98, Mar 1990.

[78] S. N. Haber and N. R. McFarland. The concept of the ventral striatum in nonhuman primates. *Annals of the New York Academy of Sciences*, 877:33–48, Jun 1999.

[79] E. L. Hahn. Spin echoes. *Physical Review*, 80:580–594, Nov 1950.

[80] H. Hall, G. Sedvall, O. Magnusson, J. Kopp, C. Halldin, and L. Farde. Distribution of D1- and D2-dopamine receptors, and dopamine and its metabolites in the human brain. *Neuropsychopharmacology*, 11(4):245–56, Dec 1994.

[81] A. Hammers, R. Allom, M. J. Koepp, S. L. Free, R. Myers, L. Lemieux, T. N. Mitchell, D. J. Brooks, and J. S. Duncan. Three-dimensional maximum probability atlas of the human brain, with particular reference to the temporal lobe. *Human Brain Mapping*, 19(4):224–247, May 2003.

[82] L. N. Hazrati and A. Parent. The striatopallidal projection displays a high degree of anatomical specificity in the primate. *Brain Research*, 592(1-2):213–27, Oct 1992.

[83] R. A. Heckemann, J. V. Hajnal, P. Aljabar, D. Rueckert, and A. Hammers. Automatic anatomical brain MRI segmentation combining label propagation and decision fusion. *Neuroimage*, 33(1):115–26, Oct 2006.

[84] J. C. Hedreen and M. R. DeLong. Organization of striatopallidal, striatonigral, and nigrostriatal projections in the macaque. *Journal of Comparative Neurology*, 304(4):569–95, Feb 1991.

[85] L. Heimer. A new anatomical framework for neuropsychiatric disorders and drug abuse. *The American Journal of Psychiatry*, 160(10):1726–39, Oct 2003.

[86] V. M. Ho, J. Lee, and K. C. Martin. The cell biology of synaptic plasticity. *Science*, 334(6056):623–628, Nov 2011.

[87] D. M. Jackson and A. Westlind-Danielsson. Dopamine receptors: molecular biology, biochemistry and behavioural aspects. *Pharmacology & therapeutics*, 64(2):291–370, 1994.

[88] S. Jbabdi and H. Johansen-Berg. Tractography: where do we go from here? *Brain Connectivity*, 1(3):169–183, Aug 2011.

[89] M. Jenkinson, P. Bannister, M. Brady, and S. Smith. Improved optimization for the robust and accurate linear registration and motion correction of brain images. *Neuroimage*, 17(2):825–41, Oct 2002.

[90] M. Jenkinson, C. F. Beckmann, T. E. J. Behrens, M. W. Woolrich, and S. M. Smith. FSL. *Neuroimage*, 62(2):782–90, Aug 2012.

[91] H. Johansen-Berg and T. E. J. Behrens. *Diffusion MRI: from quantitative measurement to in-vivo neuroanatomy*. Academic Press, 2009.

[92] H. Johansen-Berg, T. E. J. Behrens, E. Sillery, O. Ciccarelli, A. J. Thompson, S. M. Smith, and P. M. Matthews. Functional-anatomical validation and individual variation of diffusion tractography-based segmentation of the human thalamus. *Cerebral Cortex*, 15(1):31–9, Jan 2005.

[93] H. Johansen-Berg and M. F. S. Rushworth. Using diffusion imaging to study human connectional anatomy. *Annual Review of Neuroscience*, 32:75–94, Jul 2009.

[94] D. K. Jones. *Diffusion MRI: from quantitative measurement to in-vivo neuroanatomy*, chapter Gaussian modeling of the diffusion signal. Academic Press, 2009.

[95] D. K. Jones. *Diffusion MRI: theory, methods, and applications*. OUP USA, 2011.

[96] J. H. Jones, P. S. Anderson, J. J. Baldwin, B. V. Clineschmidt, D. E. McClure, G. F. Lundell, W. C. Randall, G. E. Martin, M. Williams, and J. M. Hirshfield. Synthesis of 4-substituted 2h-naphth[1,2-b]-1,4-oxazines, a new class of dopamine agonists. *Journal of Medicinal Chemistry*, 27(12):1607–13, Dec 1984.

[97] J. A. Kauer and R. C. Malenka. Synaptic plasticity and addiction. *Nature Reviews Neuroscience*, 8(11):844–858, Sep 2007.

[98] J. M. Kemp and T. P. Powell. The cortico-striate projection in the monkey. *Brain*, 93(3):525–46, 1970.

[99] J. M. Kemp and T. P. Powell. The connexions of the striatum and globus pallidus: synthesis and speculation. *Philosophical transactions of the Royal Society of London. Series B, Biological sciences*, 262(845):441–57, Sep 1971.

[100] Z. U. Khan, A. Gutiérrez, R. Martín, A. Peñafiel, A. Rivera, and A. De La Calle. Differential regional and cellular distribution of dopamine D2-like receptors: an immunocytochemical study of subtype-specific antibodies in rat and human brain. *Journal of Comparative Neurology*, 402(3):353–71, Dec 1998.

[101] J. Kittler, M. Hatef, R. P. W. Duin, and J. Matas. On combining classifiers. *IEEE Transactions on Pattern Analysis and Machine Intelligence*, 20(3):226–239, Mar 1998.

[102] A. Klein, J. Andersson, B. A. Ardekani, J. Ashburner, B. Avants, M. Chiang, G. E. Christensen, D. L. Collins, J. Gee, P. Hellier, J. H. Song, M. Jenkinson, C. Lepage, D. Rueckert, P. Thompson, T. Vercauteren, R. P. Woods, J. J. Mann, and R.V. Parsey. Evaluation of 14 nonlinear deformation algorithms applied to human brain MRI registration. *Neuroimage*, 46(3):786–802, Jul 2009.

[103] J. Knierim. Neuroscience online, cerebellum, University of Texas. http://neuroscience.uth.tmc.edu/, Date of access: 6/Jul/2013.

[104] M. J. Koepp, R. N. Gunn, A. D. Lawrence, V. J. Cunningham, A. Dagher, T. Jones, D. J. Brooks, C. J. Bench, and P. M. Grasby. Evidence for striatal dopamine release during a video game. *Nature*, 393(6682):266–267, May 1998.

[105] K. M. Koochesfahani, R. De la Fuente-Fernández, V. Sossi, M. Schulzer, L. N. Yatham, T. J. Ruth, S. Blinder, and A. J. Stoessl. Oral methylphenidate fails to elicit significant changes in extracellular putaminal dopamine levels in Parkinson's disease patients: positron emission tomographic studies. *Movement Disorders*, 21(7):970–975, Jul 2006.

[106] M. L. Kringelbach and E. T. Rolls. The functional neuroanatomy of the human orbitofrontal cortex: evidence from neuroimaging and neuropsychology. *Progress in Neurobiology*, 72(5):341–72, Apr 2004.

[107] M. J. Kuhar. In vitro autoradiography. *Current Protocols in Pharmacology*, Chapter 8:Unit 8.1, May 2001.

[108] A. A. Lammertsma and S. P. Hume. Simplified reference tissue model for PET receptor studies. *Neuroimage*, 4(3 Pt 1):153–158, Dec 1996.

[109] E. M. Landaw and J. J. DiStefano. Multiexponential, multicompartmental, and noncompartmental modeling. II. data analysis and statistical considerations. *American Journal of Physiology-Regulatory, Integrative and Comparative Physiology*, 246(5):665–677, May 1984.

[110] M. Laruelle. Imaging synaptic neurotransmission with in vivo binding competition techniques: a critical review. *Journal of Cerebral Blood Flow & Metabolism*, 20(3):423–51, Mar 2000.

[111] M. Laruelle. Measuring dopamine synaptic transmission with molecular imaging and pharmacological challenges: The state of the art. In Gerhard Grunder

and Wolfgang Walz, editors, *Molecular Imaging in the Clinical Neurosciences*, volume 71 of *Neuromethods*, pages 163–203. Humana Press, 2012.

[112] M. Laruelle, A. Abi-Dargham, C. H. van Dyck, R. Gil, C. D. D'Souza, J. Erdos, E. McCance, W. Rosenblatt, C. Fingado, S. S. Zoghbi, R. M. Baldwin, J. P. Seibyl, J. H. Krystal, D. S. Charney, and R. B. Innis. Single photon emission computerized tomography imaging of amphetamine-induced dopamine release in drug-free schizophrenic subjects. *Proceedings of the National Academy of Sciences of the United States of America*, 93(17):9235–40, Aug 1996.

[113] M. Laruelle, R. N. Iyer, M. S. Al-Tikriti, Y. Zea-Ponce, R. Malison, S. S. Zoghbi, R. M. Baldwin, H. F. Kung, D. S. Charney, P. B. Hoffer, R. B. Innis, and C. W. Bradberry. Microdialysis and SPECT measurements of amphetamine-induced dopamine release in nonhuman primates. *Synapse*, 25(1):1–14, Jan 1997.

[114] D. Le Bihan and P. Van Zijl. From the diffusion coefficient to the diffusion tensor. *NMR in Biomedicine*, 15(7-8):431–434, Nov-Dec 2002.

[115] S. E Leh, A. Ptito, M. M. Chakravarty, and A. P Strafella. Fronto-striatal connections in the human brain: a probabilistic diffusion tractography study. *Neuroscience Letters*, 419(2):113–8, May 2007.

[116] S. Lehéricy, M. Ducros, P. Van de Moortele, C. Francois, L. Thivard, C. Poupon, N. Swindale, K. Ugurbil, and D. Kim. Diffusion tensor fiber tracking shows distinct corticostriatal circuits in humans. *Annals of Neurology*, 55(4):522–9, Apr 2004.

[117] C. Lenglet, A. Abosch, E. Yacoub, F. De Martino, G. Sapiro, and N. Harel. Comprehensive in vivo mapping of the human basal ganglia and thalamic connectome in individuals using 7T MRI. *PLoS One*, 7(1):e29153, Jan 2012.

[118] A. I. Levey, S. M. Hersch, D. B. Rye, R. K. Sunahara, H. B. Niznik, C. A. Kitt, D. L. Price, R. Maggio, M. R. Brann, and B. J. Ciliax. Localization of D1 and D2 dopamine receptors in brain with subtype-specific antibodies. *Proceedings of the National Academy of Sciences of the United States of America*, 90(19):8861–5, Oct 1993.

[119] E. Lynd-Balta and S. N. Haber. The organization of midbrain projections to the striatum in the primate: sensorimotor-related striatum versus ventral striatum. *Neuroscience*, 59(3):625–640, Apr 1994.

[120] E. Lynd-Balta and S. N. Haber. The organization of midbrain projections to the ventral striatum in the primate. *Neuroscience*, 59(3):609–623, Apr 1994.

[121] R. T. Malison, K. Y. Mechanic, H. Klummp, R. Baldwin, T. R. Kosten, J. P. Seibyl, and R. B. Innis. Reduced amphetamine-stimulated dopamine release in cocaine addicts as measured by [123I]IBZM SPECT. *Journal of Nuclear Medicine*, 40(5 suppl):110, 1999.

[122] A. Malmberg and N. Mohell. Characterization of [3H]quinpirole binding to human dopamine D2 and D3 receptors: effects of ions and guanine nucleotides. *Journal of Pharmacology and Experimental Therapeutics*, 274(2):790–7, Aug 1995.

[123] L. Marner, N. Gillings, R. A. Comley, W. F. C. Baaré, E. A. Rabiner, A. A. Wilson, S. Houle, S. G. Hasselbalch, C. Svarer, R. N. Gunn, et al. Kinetic modeling of [11C]-SB207145 binding to 5-HT4 receptors in the human brain in vivo. *Journal of Nuclear Medicine*, 50(6):900–908, Jun 2009.

[124] J. H. Martin, H. J. Radzyner, and M. E. Leonard. *Neuroanatomy: text and atlas*. Elsevier, 1989.

[125] S. J. Martin, P. D. Grimwood, and R. G. M. Morris. Synaptic plasticity and memory: an evaluation of the hypothesis. *Annual review of neuroscience*, 23(1):649–711, Aug 2000.

[126] D. Martinez, R. Narendran, R. Foltin, M. Slifstein, D. R. Hwang, A. Broft, Y. Huang, T. Cooper, M. Fischman, H. Kleber, et al. Amphetamine-induced dopamine release: markedly blunted in cocaine dependence and predictive of the choice to self-administer cocaine. *American Journal of Psychiatry*, 164(4):622–629, Apr 2007.

[127] D. Martinez, M. Slifstein, A. Broft, O. Mawlawi, D. Hwang, Y. Huang, T. Cooper, L. Kegeles, E. Zarahn, A. Abi-Dargham, S. N. Haber, and M. Laruelle. Imaging human mesolimbic dopamine transmission with positron emission tomography. Part II: amphetamine-induced dopamine release in the functional subdivisions of the striatum. *Journal of Cerebral Blood Flow & Metabolism*, 23(3):285–300, Mar 2003.

[128] P. M. Matthews, E. A. Rabiner, J. Passchier, and R. N. Gunn. Positron emission tomography molecular imaging for drug development. *British Journal of Clinical Pharmacology*, 73(2):175–86, Feb 2012.

[129] O. Mawlawi, D. Martinez, M. Slifstein, A. Broft, R. Chatterjee, D. R. Hwang, Y. Huang, N. Simpson, K. Ngo, R. Van Heertum, and M. Laruelle. Imaging human mesolimbic dopamine transmission with positron emission tomography: I. accuracy and precision of D2 receptor parameter measurements in ventral striatum. *Journal of Cerebral Blood Flow & Metabolism*, 21(9):1034–57, Sep 2001.

[130] J. H. Meador-Woodruff, A. Mansour, J. R. Bunzow, H. H. Van Tol, S. J. Watson, Jr, and O. Civelli. Distribution of D2 dopamine receptor mRNA in rat

brain. *Proceedings of the National Academy of Sciences of the United States of America*, 86(19):7625–8, Oct 1989.

[131] J. H. Meador-Woodruff, A. Mansour, O. Civelli, and S. J. Watson. Distribution of D2 dopamine receptor mRNA in the primate brain. *Progress in Neuro-Psychopharmacology & Biological Psychiatry*, 15(6):885–93, 1991.

[132] M. A. Mintun, M. E. Raichle, M. R. Kilbourn, G. F. Wooten, and M. J. Welch. A quantitative model for the in vivo assessment of drug binding sites with positron emission tomography. *Annals of Î İeurology*, 15(3):217–227, 1984.

[133] C. Missale, S. R. Nash, S. W. Robinson, M. Jaber, and M. G. Caron. Dopamine receptors: from structure to function. *Physiological Reviews*, 78(1):189–225, Jan 1998.

[134] R. Mizrahi, S. Houle, I. Vitcu, A. Ng, and A. A. Wilson. Side effects profile in humans of (11)C-(+)-PHNO, a dopamine D(2/3) agonist ligand for PET. *Journal of Nuclear Medicine*, 51(3):496–7, Mar 2010.

[135] A. M. Murray, H. L. Ryoo, E. Gurevich, and J. N. Joyce. Localization of dopamine D3 receptors to mesolimbic and D2 receptors to mesostriatal regions of human forebrain. *Proceedings of the National Academy of Sciences of the United States of America*, 91(23):11271–5, Nov 1994.

[136] R. Narendran, W. G. Frankle, N. S. Mason, C. M. Laymon, B. J. Lopresti, J. C. Price, S. Kendro, S. Vora, M. Litschge, J. M. Mountz, et al. Positron emission tomography imaging of D2/3 agonist binding in healthy human subjects with the radiotracer [11C]-N-propyl-norapomorphine: Preliminary evaluation and reproducibility studies. *Synapse*, 63(7):574–584, Jul 2009.

[137] R. Narendran, N. S. Mason, C. M. Laymon, B. J. Lopresti, N. D. Velasquez, M. A. May, S. Kendro, D. Martinez, C. A. Mathis, and W. G.

Frankle. A comparative evaluation of the dopamine D2/3 agonist radiotracer [11C](-)-N-Propyl-norapomorphine and antagonist [11C]Raclopride to measure amphetamine-induced dopamine release in the human striatum. *Journal of Pharmacology and Experimental Therapeutics*, 333(2):533–539, May 2010.

[138] R. Narendran, M. Slifstein, O. Guillin, Y. Hwang, D. Hwang, E. Scher, S. Reeder, E. A. Rabiner, and M. Laruelle. Dopamine D2/3 receptor agonist positron emission tomography radiotracer [11C]-(+)-PHNO is a D3 reeptor preferring agonist in vivo. *Synapse*, 60(7):485–495, Dec 2006.

[139] D. N. Pandya and E. H. Yeterian. Comparison of prefrontal architecture and connections. *Philosophical transactions of the Royal Society of London. Series B, Biological sciences*, 351(1346):1423–32, Oct 1996.

[140] A. Parent and L. Hazrati. Multiple striatal representation in primate substantia nigra. *The Journal of Comparative Neurology*, 344(2):305–320, Oct 1994.

[141] A. Parent and L. N. Hazrati. Functional anatomy of the basal ganglia. I. the cortico-basal ganglia-thalamo-cortical loop. *Brain Research Reviews*, 20(1):91–127, Jan 1995.

[142] R. V. Parsey, M. Slifstein, D. R. Hwang, A. Abi-Dargham, N. Simpson, O. Mawlawi, N. N. Guo, R. Van Heertum, J. J. Mann, and M. Laruelle. Validation and reproducibility of measurement of 5-HT1A receptor parameters with [carbonyl-11C]WAY-100635 in humans: comparison of arterial and reference tissue input functions. *Journal of Cerebral Blood Flow & Metabolism*, 20(7):1111–1133, Jul 2000.

[143] R. E. Passingham. *The frontal lobes and voluntary action*. Oxford University Press, New York, 1993.

[144] B. Patenaude, S. M. Smith, D. N. Kennedy, and M. Jenkinson. A bayesian model of shape and appearance for subcortical brain segmentation. *Neuroimage*, 56(3):907–922, 2011.

[145] G. Percheron and M. Filion. Parallel processing in the basal ganglia: up to a point. *Trends in Neurosciences*, 14(2):55–9, Feb 1991.

[146] M. Petrides. Lateral prefrontal cortex: architectonic and functional organization. *Philosophical transactions of the Royal Society of London. Series B, Biological sciences*, 360(1456):781–95, Apr 2005.

[147] P. P. Piccini. Dopamine transporter: basic aspects and neuroimaging. *Movement Disorders*, 18(S7):3–8, Oct 2003.

[148] E. M. Purcell, H. C. Torrey, and R. V. Pound. Resonance absorption by nuclear magnetic moments in a solid. *Physical Review*, 69(1-2):37, Dec 1946.

[149] D. Purves, G. J. Augustine, and D. Fitzpatrick. *Neuroscience: Circuits within the Basal Ganglia System.* Sunderland (MA): Sinauer Associates, 2nd edition, 2001.

[150] Eugenii A Rabiner, E. A., M. Slifstein, J. Nobrega, C. Plisson, M. Huiban, R. Raymond, M. Diwan, A. A. Wilson, P. McCormick, G. Gentile, R. N. Gunn, and M. Laruelle. In vivo quantification of regional dopamine-D3 receptor binding potential of (+)-PHNO: studies in non-human primates and transgenic mice. *Synapse*, 63(9):782–93, Sep 2009.

[151] J. O. Rinne, J. Hietala, U. Ruotsalainen, E. Säkö, A. Laihinen, K. Någren, P. Lehikoinen, V. Oikonen, and E. Syvälahti. Decrease in human striatal dopamine D2 receptor density with age: a PET study with [11C]raclopride. *Journal of Cerebral Blood Flow & Metabolism*, 13(2):310–4, Mar 1993.

[152] E. T. Rolls. The orbitofrontal cortex and reward. *Cerebral Cortex*, 10(3):284–94, Mar 2000.

[153] E. T. Rolls. A theory of emotion, and its application to understanding the neural basis of emotion. *Behavioral and Brain Sciences*, 23(2):177–91; discussion 192–233, Apr 2000.

[154] O. G. Rousset, Y. Ma, and A. C. Evans. Correction for partial volume effects in PET: principle and validation. *Journal of Nuclear Medicine*, 39(5):904–11, May 1998.

[155] G. Searle, J. D. Beaver, R. A. Comley, M. Bani, A. C. Tziortzi, M. Slifstein, M. Mugnaini, C. Griffante, A. A. Wilson, E. Merlo-Pich, S. Houle, R. Gunn, E. A. Rabiner, and M. Laruelle. Imaging dopamine D3 receptors in the human brain with positron emission tomography, [11C]PHNO, and a selective D3 receptor antagonist. *Biological Psychiatry*, 68(4):392 – 399, Aug 2010.

[156] G. E. Searle, J. D. Beaver, R. A. Tziortzi, A. C.and Comley, M. Bani, G. Ghibellini, E. Merlo-Pich, E. A. Rabiner, M. Laruelle, and R. N. Gunn. Mathematical modelling of [11C]PHNO human competition studies. *NeuroImage*, May 2012.

[157] L. D. Selemon and P. S. Goldman-Rakic. Longitudinal topography and interdigitation of corticostriatal projections in the rhesus monkey. *The Journal of Neuroscience*, 5(3):776–94, Mar 1985.

[158] L. D. Selemon and P. S. Goldman-Rakic. Topographic intermingling of striatonigral and striatopallidal neurons in the rhesus monkey. *The Journal of Comparative Neurology*, 297(3):359–376, Jul 1990.

[159] S. Shapiro and M. Wilk. An analysis of variance test for normality (complete samples). *Biometrika*, 52:591–611, Dec 1965.

[160] M. Shidahara, C. Tsoumpas, A. Hammers, N. Boussion, D. Visvikis, T. Suhara, I. Kanno, and F. E. Turkheimer. Functional and structural synergy for resolution recovery and partial volume correction in brain PET. *Neuroimage*, 44(2):340–8, Jan 2009.

[161] M. Shidahara, C. Tsoumpas, C. J. McGinnity, T. Kato, H. Tamura, A. Hammers, H. Watabe, and F. E. Turkheimer. Wavelet-based resolution recovery using an anatomical prior provides quantitative recovery for human population phantom PET [11C]raclopride data. *Physics in Medicine and Biology*, 57(10):3107–22, May 2012.

[162] P. Shotbolt, A. C. Tziortzi, G. E. Searle, A. Colasanti, J. Van der Aart, S. Abanades, C. Plisson, S. R. Miller, M. Huiban, J. D. Beaver, R. N. Gunn, M. Laruelle, and E. A. Rabiner. Within-subject comparison of [11C]-(+)-PHNO and [11C]raclopride sensitivity to acute amphetamine challenge in healthy humans. *Journal of Cerebral Blood Flow & Metabolism*, 32(1):127–136, Jan 2012.

[163] D. R. Sibley, A. De Lean, and I. Creese. Anterior pituitary dopamine receptors. Demonstration of interconvertible high and low affinity states of the D2 dopamine receptor. *The Journal of Biological Chemistry*, 257(11):6351–61, Jun 1982.

[164] D. R. Sibley and F. J. Monsma, Jr. Molecular biology of dopamine receptors. *Trends in Pharmacological Sciences*, 13(2):61–9, Feb 1992.

[165] S. M. Smith. Fast robust automated brain extraction. *Human Brain Mapping*, 17(3):143–55, Nov 2002.

[166] P. Sokoloff, B. Giros, M. P. Martres, M. Andrieux, R. Besancon, C. Pilon, M. L. Bouthenet, E. Souil, and J. C. Schwartz. Localization and function of the D3 dopamine receptor. *Arzneimittelforschung*, 42(2A):224–30, Feb 1992.

[167] P. Sokoloff, B. Giros, M. P. Martres, M. L. Bouthenet, and J. C. Schwartz. Molecular cloning and characterization of a novel dopamine receptor D3 as a target for neuroleptics. *Nature*, 347(6289):146–51, Sep 1990.

[168] P. Sokoloff and J. C. Schwartz. Novel dopamine receptors half a decade later. *Trends in Pharmacological Sciences*, 16(8):270–5, Aug 1995.

[169] J. K. Staley and D. C. Mash. Adaptive increase in D3 dopamine receptors in the brain reward circuits of human cocaine fatalities. *The Journal of Neuroscience*, 16(19):6100–6, Oct 1996.

[170] I. P. Stolerman, editor. *Encyclopedia of psychopharmacology, Volume 2.* Springer, Aug 2010.

[171] A. Sudhyadhom, I. U. Haq, K. D. Foote, M. S. Okun, and F. J. Bova. A high resolution and high contrast MRI for differentiation of subcortical structures for DBS targeting: the fast gray matter acquisition T1 inversion recovery (FGATIR). *Neuroimage*, 47 Suppl 2:44–52, Aug 2009.

[172] R. K. Sunahara, H. C. Guan, B. F. O'Dowd, P. Seeman, L. G. Laurier, G. Ng, S. R. George, J. Torchia, H. H. Van Tol, and H. B. Niznik. Cloning of the gene for a human dopamine D5 receptor with higher affinity for dopamine than D1. *Nature*, 350(6319):614–9, Apr 1991.

[173] M. Suzuki, Y. L. Hurd, P. Sokoloff, J. C. Schwartz, and G. Sedvall. D3 dopamine receptor mRNA is widely expressed in the human brain. *Brain Research*, 779(1-2):58–74, Jan 1998.

[174] M. Tanner, G. Gambarota, T. Kober, G. Krueger, D. Erritzoe, J. P. Marques, and R. Newbould. Fluid and white matter suppression with the MP2RAGE sequence. *Journal of Magnetic Resonance Imaging*, 35(5):1063–1070, May 2012.

[175] C. Traynor, R. A. Heckemann, A. Hammers, J. O'Muircheartaigh, W. R. Crum, G. J. Barker, and M. P. Richardson. Reproducibility of thalamic segmentation based on probabilistic tractography. *Neuroimage*, 52(1):69–85, Aug 2010.

[176] C. Tsoumpas, F. E. Turkheimer, and K. Thielemans. Study of direct and indirect parametric estimation methods of linear models in dynamic positron emission tomography. *Medical Physics*, 35:1299, 2008.

[177] C. Tsoumpas, F. E. Turkheimer, and K. Thielemans. A survey of approaches for direct parametric image reconstruction in emission tomography. *Medical Physics*, 35:3963, 2008.

[178] University of Oxford. FMRIB58_FA standard space image. http://fsl.fmrib.ox.ac.uk/fsl/fsl4.0/tbss/FMRIB58_FA.html, Date of access: 6/Jul/2013.

[179] A. A. Utter and Michele A. Basso. The basal ganglia: an overview of circuits and function. *Neuroscience & Biobehavioral Reviews*, 32(3):333–42, 2008.

[180] A. G. Van der Kolk, J. Hendrikse, J. J. M. Zwanenburg, F. Visser, and P. R. Luijten. Clinical applications of 7T MRI in the brain. *European Journal of Radiology*, 2011.

[181] G. W. Van Hoesen, E. H. Yeterian, and R. Lavizzo-Mourey. Widespread corticostriate projections from temporal cortex of the rhesus monkey. *Journal of Comparative Neurology*, 199(2):205–19, Jun 1981.

[182] L. A. Van Vliet, N. Rodenhuis, D. Dijkstra, H. Wikström, T. A. Pugsley, K. A. Serpa, L. T. Meltzer, T. G. Heffner, L. D. Wise, M. E. Lajiness, R. M. Huff, K. Svensson, S. Sundell, and M. Lundmark. Synthesis and pharmacological evaluation of thiopyran analogues of the dopamine D3 receptor-selective agonist (4aR,10bR)-(+)-trans-3,4,4a,10b-tetrahydro-4-n-propyl-2H,5H

[1]b enzopyrano[4,3-b]-1,4-oxazin-9-ol (PD 128907). *Journal of Medicinal Chemistry*, 43(15):2871–82, Jul 2000.

[183] A. N. Voineskos, T. K. Rajji, N. J. Lobaugh, D. Miranda, M. E. Shenton, J. L. Kennedy, B. G. Pollock, and B. H. Mulsant. Age-related decline in white matter tract integrity and cognitive performance: a DTI tractography and structural equation modeling study. *Neurobiology of Aging*, 33(1):21–34, Jan 2012.

[184] N. D. Volkow, G. J. Wang, J. S. Fowler, J. Logan, S. J. Gatley, R. Hitzemann, A. D. Chen, S. L. Dewey, and N. Pappas. Decreased striatal dopaminergic responsiveness in detoxified cocaine-dependent subjects. *Nature*, 386(6627):830–3, Apr 1997.

[185] H. N. Wagner Jr, H. D. Burns, R. F. Dannals, D. F. Wong, B. Langstrom, T. Duelfer, J. J. Frost, H. T. Ravert, J. M. Links, S. B. Rosenbloom, et al. Imaging dopamine receptors in the human brain by positron tomography. *Science*, 221(4617):1264–1266, Sep 1983.

[186] J. D. Wallis. Orbitofrontal cortex and its contribution to decision-making. *Annual Review of Neuroscience*, 30:31–56, 2007.

[187] M. Willeit, N. Ginovart, S. Kapur, S. Houle, D. Hussey, P. Seeman, and A. A. Wilson. High-affinity states of human brain dopamine D2/3 receptors imaged by the agonist [11C]-(+)-PHNO. *Biological Psychiatry*, 59(5):389–94, Mar 2006.

[188] A. A. Wilson, P. McCormick, S. Kapur, M. Willeit, A. Garcia, D. Hussey, S. Houle, P. Seeman, and N. Ginovart. Radiosynthesis and evaluation of [11C]-(+)-4-propyl-3,4,4a,5,6,10b-hexahydro-2H-naphtho[1,2-b][1,4]oxazin-9-ol as a potential radiotracer for in vivo imaging of the dopamine D2 high-affinity state with positron emission tomography. *Journal of Medicinal Chemistry*, 48(12):4153–60, Jun 2005.